Coupled Modes Analysis of SRS Backscattering, with Langmuir Decay and Possible Cascadings

by

Ante Salcedo

Submitted to the Department of Electrical Engineering and Computer Science
in partial fulfillment of the requirements for the degree of

Doctor of Philosophy

at the

MASSACHUSETTS INSTITUTE OF TECHNOLOGY

December 2001

© Massachusetts Institute of Technology 2001. All rights reserved.

Author ....
Department of Electrical Engineering and Computer Science
December 11, 2001

Certified by ....
Abraham Bers
Professor of Electrical Engineering & Computer Science
Thesis Supervisor

Accepted by ....
Arthur C. Smith
Chairman, Department Committee on Graduate Students

.

Coupled Modes Analysis of SRS Backscattering, with Langmuir Decay and Possible Cascadings

by

Ante Salcedo

Abstract

Recent experiments aimed at understanding stimulated Raman scattering (SRS) in ICF laser-plasma interactions, suggest that SRS is coupled to the Langmuir decay interaction (LDI). The effects of LDI on the saturation of the SRS backscattering have been investigated, considering typical parameters from recent experiments. Detailed simulations with the coupled mode equations in a finite length plasma, with real wave envelopes and no wave dephasing, are explored here for the first time. A detailed description and analysis of such simulations is provided. The excitation of LDI is found to reduce the SRS reflectivity; the reduction is appreciable in the weak EPW damping limit. The reflectivity is also observed to increase with the damping of ion acoustic waves, the length of the plasma, the intensity of the laser, and the initial amplitude of the noise fluctuations. Possible cascadings of LDI have also been investigated. While the cascading of LDI is found to increase the SRS backscattering, the cascading of SRS is found to reduce it. Considering only the coupling to LDI, our model fails to quantitatively predict the experimental SRS backscattering; however, the calculated backscattering is found to vary in a manner similar to the experimental observations, and our simulations explain interesting physics in the ICF laser-plasma interactions.

Thesis Supervisor: Abraham Bers
Title: Professor of Electrical Engineering & Computer Science

.

Acknowledgments

I give thanks to all the people who have trusted, supported and taught me, during this difficult and significant passage of my life. I would not have done it without you!

First of all I thank my parents, Tere and Javier, my sister Dara and my brother Bruno, for their infinite love and support. I give thanks to my mentors, Prof. A. Bers, Dr. Abhay Ram and Dr. Steve Schultz, for all their teaching and patience, and for guiding me through the complex, riddling ways of the plasma electrodynamics. I thank Prof. J. A. Kong for leading me into the fascinating world of electromagnetism, and to the MIT staff who believed in me and gave me the opportunity to continue, even in the hardest of times: Prof. J. L. Kirtley Jr., Prof. S. Devadas, Marilyn A. Pierce and Monica B. Bell.

I want to give special thanks to Kate Baty, the *"sunshine with teeth"*, for whom I have no words to thank enough; and also thanks to my host families the Kennedy's and the Baty's. Thanks a lot Judy, Dan and Gordon.

Many thanks to my very special friends: Marcos, Gerardo, Jorge, Carlos, Vico, Raymundo and both Jose Luises (Cordova and Cravioto), and to many more whom I cannot mention in this brief space. I am sorry that I have disappeared from your lives for so long, and I promise to make up for it. I would also like to thank my very dear friend: Mtra. Artemisa, for her counseling words, cheers, and invaluable friendship.

To the Mexican institutions CONACyT and UNAM, I express my gratitude for their financial support, which enabled me to carry on my doctoral program.

And last but not least, I thank God because I have always found an answer to my prayers.

.

"As the light increased, I discovered around me an ocean of mist."

- Henry David Thoreau -

.

Contents

.

Table of Abbreviations Used

BEMW	Backscattered electromagnetic wave in SRS
BEPW	Backscattered electron plasma wave in the principal LDI
CEPW	Cascade electron plasma wave
CIAW	Cascade ion acoustic wave
COM	Coupled mode equations
DT	Deuterium-tritium
EMWc	Electromagnetic wave in the SRS cascading
EPW	Electron plasma wave in SRS and the principal LDI
EPWc	Electron plasma wave in the SRS cascading
FEPWc	Electron plasma wave in the LDI cascading of the EPWc
IAW	Ion acoustic wave in the principal LDI
IAWc	Ion acoustic wave in the LDI cascading of the EPWc
IST	Inverse Scattering Transform
ICF	Inertial confinement fusion
LANL	Los Alamos National Laboratory
LDI	Langmuir decay interaction
LLNL	Lawrence Livermore National Laboratory
SBS	Stimulated Brillouin scattering
SRS	Stimulated Raman scattering
STC	Spatio-temporal chaos
TPD	Two plasmon decay
3COM	Three wave coupled mode equations
5COM	Five wave coupled mode equations
7COM	Seven wave coupled mode equations
3WI	Three wave interactions

.

List of Figures

17

.

List of Tables

.

Chapter 1

Introduction

Inertial confinement fusion (ICF) is a proposed technology aimed to produce controlled fusion of deuterium and tritium (DT), as an alternative source of energy for future generation of electrical power [1, 2, 3]. In the *direct-drive ICF* (illustrated in Figure 1-1) several laser beams are used to compress and heat the fusion fuel, which (in the simplest configuration) is contained in a $\sim 100~\mu m$ spherical-glass shell that acts as an *ablator*. The laser beams produce a rapid expansion of the ablator, such that the fuel is compressed and heated to reach fusion conditions [2]. In an alternative approach known as *indirect-drive ICF*, the fuel container is placed inside a case made of gold, which is know as *hohlraum* (see Figure 1-2). Several laser beams are driven to the walls of the hohlraum to produce X-rays, which in turn propagate to the ablator to heat it and induce its rapid expansion [3]. The hohlraum is usually filled with a highly compressed gas to prevent the gold from reaching the fuel.

One of the major problems to achieve efficient indirect-drive ICF is the nonlinear scattering produced by the interaction of the beams and the plasma created when the hohlraum gas-fill ionizes [2]. Due to the nonlinear nature of the plasma dynamics in electromagnetic fields, the laser excites backscattered electromagnetic waves that scatter the laser energy away from the target (thus reducing the efficiency of the process) and produces hot electrons that may preheat the fuel (making it more difficult to compress). A significant source of scattering that has been identified in several

a) Initial setup   b) Compression of the fuel   c) Fusion occurs.
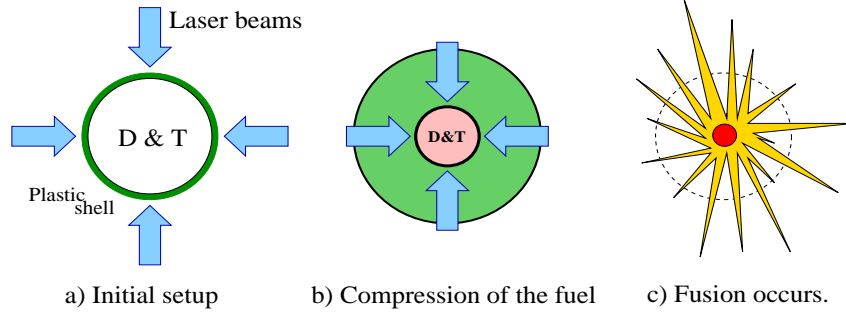
Figure 1-1: Direct Drive – Inertial Confinement Fusion

experiments, is the nonlinear coupling between triplets of resonant linear plasma modes. This kind of nonlinear coupling, known as *three wave interactions* (3WI), is the basis of interactions studied in my thesis.

I have investigated the laser backscattering produced by a nonlinear process known as *stimulated Raman scattering* (SRS), where the plasma electromagnetic wave (externally excited by the laser) nonlinearly couples to a backscattered electromagnetic wave and a longitudinal plasma wave. This phenomenon is a nonlinear 3WI that has been observed in recent ([4] - [14]) and past ([15] - [22]) experiments, aimed at understanding its implications to ICF. The excitation of SRS degrades the efficiency in ICF because the scattering of the laser reduces the amount of energy that can reach the fuel, and the production of energetic electrons (by the longitudinal plasma wave) inhibits the compression of the fuel. Based on the *coupled modes equations* [23] – [31], I have set up [and numerically solved] a model that describes the coupling of SRS to other 3WI, such as *Langmuir decay interaction* (LDI), *first Langmuir cascade*, and *first SRS cascade*. I have focused my investigation to understand the dependence of SRS on the *damping of ion acoustic waves*, the electron plasma density and the intensity of the laser - parameters which have been studied experimentally ([4] – [6]).

Although SRS backscattering in characteristic ICF plasmas has been observed in many experiments and investigated for a long time, it has not been fully understood yet. In recent experiments [6, 10, 12, 13] a laser beam was focused to a small region inside an ICF characteristic plasma to create a "single hot-spot" (or "single speckle"),
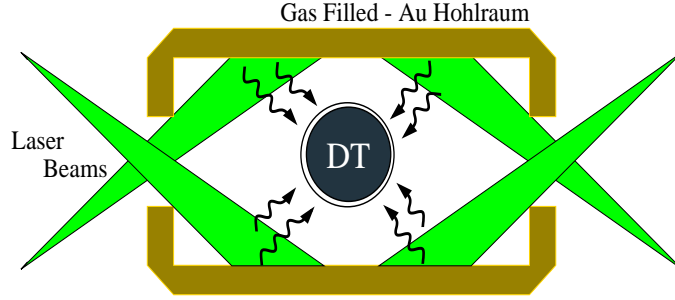
Figure 1-2: Indirect Drive – Inertial Confinement Fusion

where the laser intensity can be considered uniform and the plasma homogeneous. Motivated by these experiments, my investigation with the COM equations is of particular interest because it attains a simple model for the SRS backscattering, and allows an understanding of the laser-plasma interactions with relatively simple physics. Alternative models, also proposed to investigate the SRS backscattering in single-speckle experiments ([32] – [45]), tend to be more general but also more complex than the COM equations. Such models are only amenable to numerical investigation, and it is difficult to extract the important physics from them. In this thesis I present and discuss numerical simulations with the COM equations, that correspond to recent ICF experimental parameters and attempt to explain some of the experimental observations.

The present chapter contains a brief introduction to the relevant 3WI processes ([46] – [52]) and to some recent experimental observations that have motivated my research ([4] – [7]). An outline of the chapters in rest of the thesis is provided in Section (1.3).

1.1 Nonlinear Coupling of Modes in ICF Plasmas

As explained before, the nonlinear nature of the plasma electrodynamics inside the hohlraum produces undesirable consequences from the coupling between linear plasma modes. Before any further analysis, the linear modes that can be excited in such plasmas are reviewed first.

Considering a non magnetized plasma (as in ICF), a linearization of the Maxwell-fluid equations that describe the plasma electrodynamics (discussed in Chapter 3) lead to three fundamental linear plasma waves: the *electromagnetic waves* (EMW), the *electron plasma waves* (EPW), and the *ion acoustic waves* (IAW). Ignoring damping and collisions, and assuming small $k\lambda_{De}$, the real frequency and real wavenumber of the characteristic modes (ω and k respectively) are given by the approximate *dispersion relations* in Table (1.1).[46] In this Table, the electron plasma frequency $f_{pe} = \omega_{pe}/2\pi$ [$\omega_{pe}^2 = q_e^2 n_e/\epsilon_o m_e$], the electron thermal velocity v_{Te} [$v_{Te}^2 = \kappa T_e/m_e$], and the speed of sound in the plasma c_a [$c_a^2 = (1 + 3T_i/Z_i T_e)Z_i \kappa T_e/m_i$] are plasma parameters that depend on the equilibrium electron temperature (T_e), ion temperature (T_i) and electron density ($n_e = \sum_i Z_i n_i$). The parameters m_e, m_i and Z_i are the electron and ion masses and the ratio of ion to electron charges, respectively.

	Dispersion Relation
EMW	$\omega^2 \approx \omega_{pe}^2 + c^2 k^2$
EPW	$\omega^2 \approx \omega_{pe}^2 + 3v_{Te}^2 k^2$
IAW	$\omega^2 \approx c_a^2 k^2$

Table 1.1: Linear dispersion relations.

In the nonlinear plasma electrodynamics the characteristic linear plasma modes can become coupled in many different ways ([47] - [50]). A particularly strong coupling that has been observed experimentally, occurs between triplets of linear plasma modes that satisfy the *resonance conditions*:

$$k_\ell = k_m + k_n, \tag{1.1}$$

$$\omega_\ell = \omega_m + \omega_n. \tag{1.2}$$

Among the many possible interactions between wave triplets, this thesis is particularly concerned with two of them: the nonlinear coupling between two electromagnetic waves and an electron plasma wave (SRS), and the coupling between two electron plasma waves and an ion acoustic wave, known as the *Langmuir decay inter-*
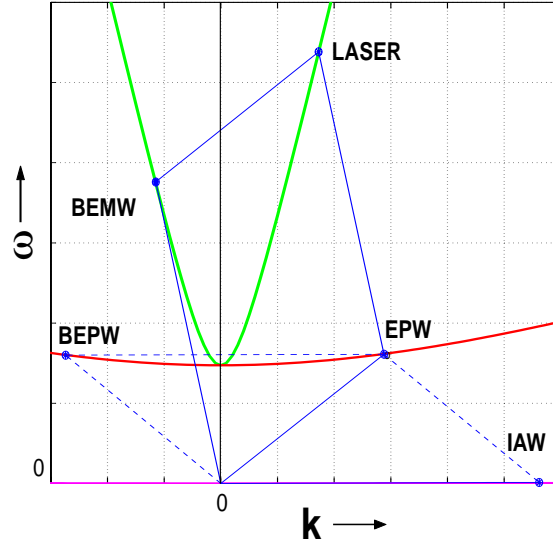
Figure 1-3: SRS and LDI, with a common electron plasma wave.

action (LDI). The possible coupling of SRS to LDI through a common electron plasma wave, relevant to the modeling of the laser-plasma interactions in ICF experiments, is the central topic of this thesis. To illustrate such coupling, Figure (1-3) shows the phase matching conditions for SRS coupled to LDI.

Considering an externally driven high frequency electromagnetic wave (designated as the *laser*), in one dimensional dynamics relevant to the SRS backscattering, Figure (1-3) illustrates the coupling of the laser to a lower frequency backscattered electromagnetic wave (BEMW) and a forward scattered electron plasma wave (EPW). In turn, the EPW further couples to a backscattered electron plasma wave (BEPW) and an ion acoustic wave (IAW). As can be appreciated from the figure, SRS can only be excited if the laser frequency is at least twice as large as the plasma frequency ($\omega_{laser} > 2\omega_{pe}$). This means that the electron plasma density must be below one quarter of the *critical density* ($n_{cr} = n_e\omega_{laser}^2/\omega_{pe}^2$), which is well satisfied in all the ICF experiments that are considered in the present work.

When the nonlinear effects can be considered weak (see discussion in Chapter 2), the 3WI only produces a space/time amplitude modulation of the fields in the coupled

modes. Such modulation is characteristic of a narrow spread of the spectrum (in ω and k), centered at the natural frequency and wavenumber of the coupled waves. This has been observed in experiments ([4, 6, 10] for example) and therefore motivated the investigation of such kind of wave-wave interactions.

In this thesis the investigation of SRS/LDI interactions is restricted to homogeneous plasmas. In the past, particularly for direct drive, inhomogeneities played an important role. However, in recent "single-speckle" experiments, as well as in the wave-wave interactions that take place in the hohlraum-fill plasma (in indirect–drive ICF), the inhomogeneities are weak and the plasma is considered to be homogeneous. Other three wave interactions like *stimulated Brillouin scattering*[46]–[50] (SBS) and *two plasmon decay*[46]–[50] (TPD), which also involve the coupling of the laser beams to electron plasma and ion acoustic waves, are not considered in this thesis. The effects of such 3WI on the laser SRS backscattering are left as work for the future. Furthermore, the effects of filamentation (ponderomotive and thermal) [55] are also not considered in this thesis.

1.2   Recent Experimental Observations

Among the numerous experiments that have been aimed to understand the laser-plasma interactions in ICF, few of them are specifically aimed to the understanding of the space/time evolution, saturation and possible control of SRS. These experiments have explored the dependence of the SRS backscattering on the different ICF laser-plasma parameters ([4] - [22]), such as: the laser intensity, plasma temperature and density gradients, plasma flow velocity, plasma geometry and plasma composition. The detailed physics behind the observed SRS backscattering, however, remain unclear.

This thesis does not aim to explain all the observed results, which have been obtained for widely differing experimental conditions. Instead, it focuses on recent experiments that show the coupling of SRS to LDI. In a first series of experiments [4, 5] carried out at Lawrence Livermore National Laboratory (LLNL), the depen-

a) Experiments at LLNL (λ_o = 350 nm) b) Experiments at LANL (λ_o = 527 nm)
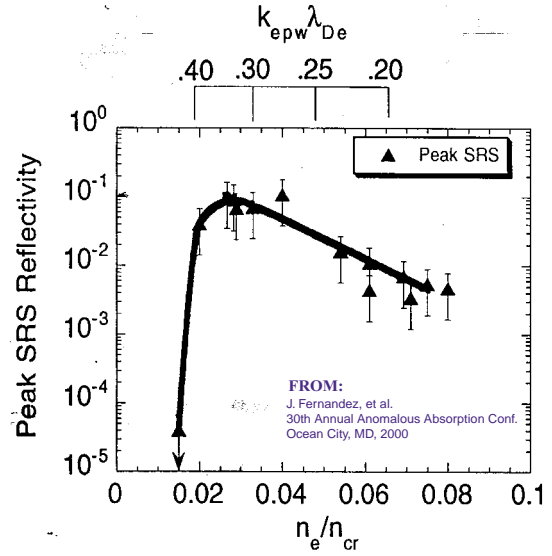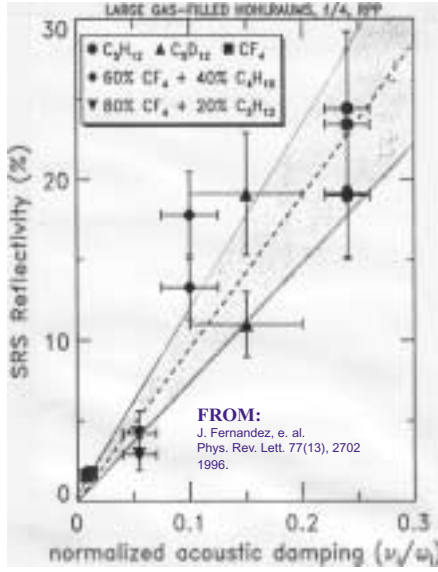
Figure 1-4: Experimental observations of SRS reflectivity

dence of the SRS backscattering on the damping of ion acoustic waves was investigated. As illustrated in Figure (1-4.a), the SRS backscattering was found to increase as the damping of ion acoustic waves (ν_i/ω_i) was increased. In a second series of experiments [6, 12, 13] carried at Los Alamos National Laboratory (LANL), the SRS backscattering as a function of the plasma density was investigated in a single hot-spot configuration (discussed in Chapter 4). The reflectivity observed in such experiments is illustrated in Figure(1-4.b). Figure (1-5), on the other hand, shows the measured spectrum of the SRS backscattering [4], which exhibits a narrow spread of the spectrum (in $\lambda = 2\pi/k$) centered at the wavelength of the SRS backscattered electromagnetic wave: $\lambda_{BEMW} = 580 nm$.

In most previous ICF laser-plasma experiments, the high-power laser incident on the plasma had numerous hot-spots/speckles, which were randomly distributed over its cross section. The laser-plasma interactions in such circumstances are difficult to investigate (theoretically and computationally). The much simpler experimental conditions in the recent single hot-spot experiments, however, have partly motivated my investigation of the coupled modes equations, as a possible way to approximately
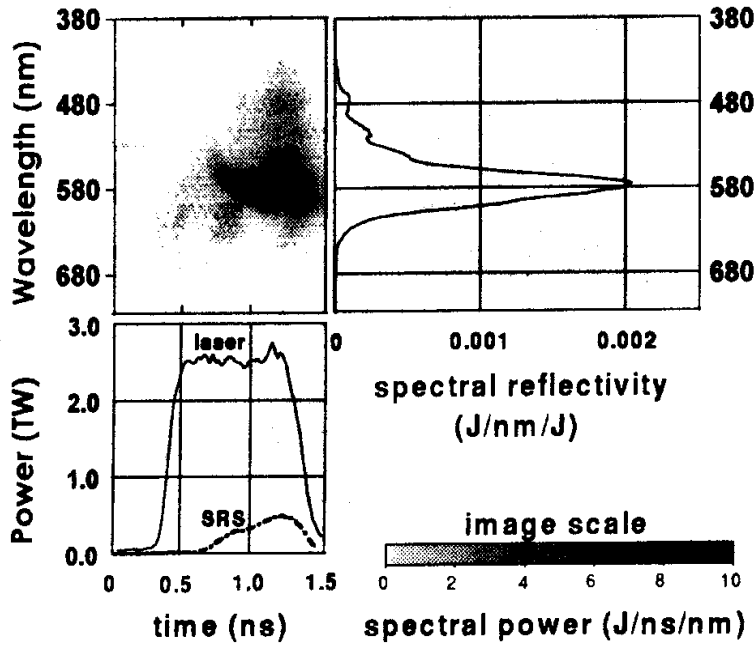
Figure 1-5: Observed spectrum of the SRS backscattering (see [4]).

model the laser-plasma interactions in ICF characteristic plasmas. In these experiments the narrow spectrum spreading (Fig. 1.5) clearly indicates the slow modulation characteristic of 3WI, and the dependence of the SRS backscattering on the damping of ion acoustic waves (Fig. 1.4.a) shows the coupling between SRS and LDI.

Since the experimental reflectivity shown in Figure (1-4) was obtained for varying plasma parameters that are not readily available, a numerical investigation of the SRS reflectivity cannot be directly compared with experiments (as discussed in Chapters 4 and 7). Furthermore, the saturation of SRS-backscattering may also be affected by nonlinear aspects (trapping) associated with the EPWs, as well as by other 3WIs - both of which are not considered in this thesis. However, I have found that the COM equations with typical experimental parameters, lead to an SRS reflectivity which varies with ion acoustic wave damping, electron plasma density and laser intensity, in a qualitatively similar manner to that observed in the above experiments [4, 5, 6, 12, 13].

More recent experiments have also confirmed the existence of LDI, identifying the

28

forward propagating electron plasma waves that result from the further coupling of LDI to subsequent 3WI processes (cascading). These experiments [10], however, are not considered in the present work.

1.3   Outline of Thesis Chapters

The basic theory behind the nonlinear three wave interactions (3WI) is reviewed in Chapter 2. In this chapter I also describe and analyze the Landau damping of longitudinal modes [46, 48], which is a fundamental parameter to study the coupling of SRS and LDI. Chapter 3 reviews the different modeling paths that have been taken in the investigation of the laser-plasma electrodynamics, relevant to ICF experiments ([23] – [45]). A special attention is given to the "coupled modes equations" (COM), which constitute the main approach used in this thesis. A discussion on the previous works and the peculiarities of my investigation are also provided in Chapter 3. Chapter 4 investigates the effects that Langmuir decay interaction (LDI) produces on the stimulated Raman scattering (SRS), considering typical data from the the single hot-spot experiments described in [6]. Detailed numerical simulations with the five-wave COM equations (5COM) are carried out for the first time, revealing interesting results on the saturation of LDI and its effect on SRS. The dependence of the SRS reflectivity on the different parameters, like the ion acoustic wave damping, the initial amplitude of the noise, and the laser intensity, are investigated in Chapter 5. In Chapter 6, the 5COM equations are extended to incorporate the possible cascadings of SRS and LDI. Here I investigate, numerically, the modification of SRS backscattering by consecutive 3WI processes. Finally, in Chapter 7, the significant results I have obtained are summarized. The detailed derivations of the models used in this thesis are given in Appendices A and B. The numerical procedure is described in Appendix C.

.

Chapter 2

Three Wave Interactions

The nonlinear three wave interactions occur in plasma physics, nonlinear optics and hydrodynamics [53, 63, 64], when three linear waves [with frequencies ω_ℓ, ω_m, ω_n, and wavenumbers $\overline{k}_\ell$, $\overline{k}_m$, $\overline{k}_n$] coexist and approximately satisfy the *resonance conditions*:

$$\omega_\ell \approx \omega_m + \omega_n, \tag{2.1}$$

$$\overline{k}_\ell \approx \overline{k}_m + \overline{k}_n. \tag{2.2}$$

In such kind of wave-wave interactions, which are prominent in systems that are weakly nonlinear (and the lowest order nonlinearity is quadratic in the field amplitudes), the nonlinearity can be manifested as the coupling between the slowly varying amplitudes of the resonant modes. The slow variation is characteristic of a narrow spreading of the spectrum, in the vicinity of the real frequencies and wavenumbers of the coupled modes.

Considering one dimensional dynamics along $\hat{x}$, as derived in Appendix B, the 3WI equations are [28]:

$$\left(\frac{\partial}{\partial t_s} + v_{g\ell} \frac{\partial}{\partial x_s} + \nu_\ell \right) a_\ell = -K a_m a_n e^{i\delta_k x} e^{-i\delta_\omega t}, \tag{2.3}$$

$$\left(\frac{\partial}{\partial t_s} + v_{gm} \frac{\partial}{\partial x_s} + \nu_m \right) a_m = K^* a_\ell a_n^* e^{-i\delta_k x} e^{i\delta_\omega t}, \tag{2.4}$$

$$\left(\frac{\partial}{\partial t_s} + v_{gn}\frac{\partial}{\partial x_s} + \nu_n\right)a_n = K^*a_\ell a_m^* e^{-i\delta_k x}e^{i\delta_\omega t}; \tag{2.5}$$

where the a's are the slowly varying complex wave envelopes, the v's are the group velocities, the ν's stand for the damping $(\nu > 0)$ or growth $(\nu < 0)$ of the linear uncoupled waves, and K is a coupling coefficient. The mismatch in the resonance conditions is given by $\delta_\omega = \omega_\ell - \omega_m - \omega_n$ and $\delta_k = k_\ell - k_m - k_n$. The subscript "$s$" indicates the slowly varying nature of the wave envelopes: $|(\partial/\partial t_s)a_\beta| \ll |\omega_\beta a_\beta|$ and $|(\partial/\partial x_s)a_\beta| \ll |k_\beta a_\beta|$, for $\beta = \ell,\ m$ and n. The highest frequency wave is referred as the "parent" or "pump", and the other two waves are referred as the "daughters".

When the requirements for the resonant 3WI are met exactly $(\delta_\omega = 0$ and $\delta_k = 0)$ and the nonlinear coupling is conservative $(\gamma_\beta = 0)$, the equations for the coupling of positive energy wave-envelopes in a homogeneous plasma reduce to [49, 63, 28]:

$$\left(\frac{\partial}{\partial t} + v_{g\ell}\frac{\partial}{\partial x}\right)a_\ell = -Ka_m a_n, \tag{2.6}$$

$$\left(\frac{\partial}{\partial t} v_{gm}\frac{\partial}{\partial x}\right)a_m = K^*a_\ell a_n^*, \tag{2.7}$$

$$\left(\frac{\partial}{\partial t} + v_{gn}\frac{\partial}{\partial x}\right)a_n = K^*a_\ell a_m^*. \tag{2.8}$$

The above form of the 3WI equations can be integrated with the *inverse scattering transform* (IST), to obtain a soliton solution [53]. There is no analytic solution, however, when the system is not conservative $(\gamma_\beta \neq 0)$ and/or the resonance conditions are not satisfied exactly $(\delta_\omega \neq 0$ or $\delta_k \neq 0)$. The nonconservative space/time evolution of the 3WI has been investigated mainly numerically ([23] – [31]), and with the aid of nonlinear (soliton) perturbation theory [53].

2.1 Three Wave Parametric Interactions

Considering an initial situation where the amplitudes of the daughter waves are sufficiently small and the high frequency wave is externally driven, the nonlinear term in equation (2.6) can be initialy neglected. In this case, the amplitude of the pump wave

can be taken as approximately constant: $a_\ell(x,t) \approx a_o$, with a_o being the externally driven amplitude. For one dimensional dynamics with propagation in $\hat{x}$, and perfect frequency matching $\delta_\omega = \delta_k = 0$, the linear equations governing the slowly varying amplitude of the daughter waves become:

$$\left(\frac{\partial}{\partial t_s} + v_{gm}\frac{\partial}{\partial x_s} + \nu_m\right)a_m = K^* a_o a_n^*, \tag{2.9}$$

$$\left(\frac{\partial}{\partial t_s} + v_{gn}\frac{\partial}{\partial x_s} + \nu_n\right)a_n = K^* a_o a_m^*; \tag{2.10}$$

where positive $\nu_\beta \equiv -\gamma_\beta$ (for $\beta = m,\ n$) is introduced as the damping of mode β. In the rest of this thesis positive ν will denote damping coefficients, and positive γ the growth rates.

In an infinitely extended plasma, the Fourier/Laplace transformation $[\partial/\partial t_s \rightarrow -i\tilde{\omega}$ and $\partial/\partial x_s \rightarrow i\tilde{k}]$ of Eqs. (2.9)-(2.10), with initial and boundary conditions being zero, leads to the dispersion relation:

$$\left(\tilde{\omega} - v_{gm}\tilde{k} + i\nu_m\right)\left(\tilde{\omega} - v_{gn}\tilde{k} + i\nu_n\right) + |Ka_o|^2 = 0. \tag{2.11}$$

Here, $\tilde{\omega}$ and $\tilde{k}$ are the characteristic frequency and wavenumber of the envelopes, satisfying $|\tilde{\omega}| \ll |\omega|$ and $|\tilde{k}| \ll |k|$. The daughter envelopes, in this case, are:

$$a_m(x_s, t_s) = a_{mo}e^{i\tilde{k}x_s}e^{-i\tilde{\omega}t_s}, \tag{2.12}$$

$$a_n(x_s, t_s) = a_{no}e^{i\tilde{k}x_s}e^{-i\tilde{\omega}t_s}. \tag{2.13}$$

Equation (2.11) clearly shows that the stability of the system depends on the unperturbed pump wave amplitude (a_o) and the damping of the daughter waves (ν_β). When $\tilde{\omega}_i(\tilde{k}_r) > 0$ the daughters grow unstable in time and the 3WI is known as a "*parametric instability*". In particular, when the system is conservative ($\nu_m = \nu_n = 0$) the daughter waves have a maximum time growth rate $\gamma \equiv |Ka_o|$, which is known as "*parametric growth rate*" [49, 50].

When the damping of the daughter waves is non-zero, the *threshold condition* for

instability is given by [49]:

$$|\gamma|^2 = |Ka_o|^2 > \nu_m\nu_n \equiv \gamma_c^2. \tag{2.14}$$

If $v_{gm}v_{gn} > 0$, the instability is convective, and when $v_{gm}v_{gn} < 0$ the threshold condition for absolute instability is [49]:

$$|\gamma|^2 = |Ka_o|^2 > \frac{|v_{gm}v_{gn}|}{4}\left(\frac{\nu_m}{|v_{gm}|} + \frac{\nu_n}{|v_{gn}|}\right)^2 \equiv \gamma_a^2. \tag{2.15}$$

The damping of the daughter waves, a fundamental parameter in the stability criteria, needs to be evaluated from the corresponding linear dispersion relations. The characteristic damping of longitudinal plasma modes, which is relevant to the ICF laser-plasma interaction experiments, is reviewed at the end of this chapter.

2.2   Energy conservation relations

Since the wave energy densities are given by $w_\beta = \omega_\beta|a_\beta|^2$ (for $\beta = \ell$, m and n), as considered in Appendices A and B, the equations for the wave energy density flow can be found multiplying Eqs. (2.3), (2.4) and (2.5) by $\omega_\ell a_\ell^*$, $\omega_m a_m^*$ and $\omega_n a_n^*$, respectively. Assuming one dimensional dynamics along $\hat{x}$, with no wave de-phasing ($\delta_\omega = \delta_k = 0$), the equations for the *energy density flow* $[watts/m^3]$ are:

$$\left(\frac{\partial}{\partial t_s} + v_{g\ell}\frac{\partial}{\partial x_s} + 2\nu_\ell\right)w_\ell \equiv \dot{W}_\ell = 2K\omega_\ell a_\ell^* a_m a_n. \tag{2.16}$$

$$\left(\frac{\partial}{\partial t_s} + v_{g\ell}\frac{\partial}{\partial x_s} + 2\nu_m\right)w_m \equiv \dot{W}_\ell = -2K^*\omega_m a_\ell a_m^* a_n^*. \tag{2.17}$$

$$\left(\frac{\partial}{\partial t_s} + v_{g\ell}\frac{\partial}{\partial x_s} + 2\nu_n\right)w_n \equiv \dot{W}_\ell = -2K^*\omega_n a_\ell a_m^* a_n^*. \tag{2.18}$$

The left hand sides of these equations describe the time variation of the power density in the resonant modes (along their characteristics), and the right hand sides give the nonlinear coupling of energy.

From the energy density flow equations we obtain the *Manley-Rowe relations*, which give the conservation of the energy density flow [49]. With a real coupling coefficient K and real wave envelopes a_β, the Manley-Rowe relations are

$$\frac{\dot{W}_\ell}{\omega_\ell} = -\frac{\dot{W}_m}{\omega_m}, \tag{2.19}$$

$$\frac{\dot{W}_\ell}{\omega_\ell} = -\frac{\dot{W}_n}{\omega_n}, \tag{2.20}$$

$$\frac{\dot{W}_m}{\omega_m} = +\frac{\dot{W}_n}{\omega_n}; \tag{2.21}$$

where $\dot{W}_\beta \equiv (\partial_t + v_{g\beta}\partial_x + \nu_\beta)\mathrm{w}_\beta$, for $\beta = \ell$, m and n [as in Equations (2.16)–(2.18)].

Considering a finite length of interaction ($0 < x < L$), the energy conservation relations for the total energy in the system are found by integration of (2.19)–(2.21), over the interaction length and the interaction time [i.e., $0 < t' < t$]. For clarity we begin integrating $\dot{W}_\ell$ only (left side of Eq. 2.16), to obtain:

$$I_\ell = \left[\int_0^L \mathrm{w}_\ell(t', x)dx\right]_{t'=t} - \left[\int_0^L \mathrm{w}_\ell(t', x)dx\right]_{t'=0} + 2\nu_\ell \int_0^t dt' \int_0^L dx\mathrm{w}_\ell(t', x)$$
$$+ v_{g\ell}\int_0^t dt' \left[\mathrm{w}_\ell(t', x = L) - \mathrm{w}_\ell(t', x = 0)\right]. \tag{2.22}$$

In the one dimensional approximation considered here, an integration over the transverse directions (y and z) leads to a constant cross section area (A). Considering that $A = 1$, the first two terms in Eq. (2.22), $[\int \mathrm{w}_\ell dx]_{t'=t}$ and $[\int \mathrm{w}_\ell dx]_{t'=t}$, stand for the total energy [in *Joules*] contained by the ℓ mode, in the region of interaction, at times $t' = 0$ and $t' = t$. The last term, $v_{g\ell}\int[\mathrm{w}_\ell(t', x = L) - \mathrm{w}_\ell(t', x = 0)]dt'$, gives the total energy that that was carried across the boundaries ($x = L$ and $x = 0$) by mode ℓ, between $t' = 0$ and $t' = t$. And the remaining term, $2\nu_\ell \int dt' \int dx[\mathrm{w}_\ell]$, stands for the total energy dissipated by the ℓ mode [within the interaction time/length].

A direct integration of the Manley-Rowe relations [(2.19)–(2.21)] over x and t', from 0 to L and 0 to t, leads to the following equations for the conservation of energy

density [in $Joules/m^2$]:

$$I_m = -\frac{\omega_m}{\omega_\ell} I_\ell, \tag{2.23}$$

$$I_n = -\frac{\omega_n}{\omega_\ell} I_\ell, \tag{2.24}$$

$$I_n = +\frac{\omega_m}{\omega_n} I_m. \tag{2.25}$$

Once again, an integration over the transverse directions (y and z) leads to a constant cross section area (A), which can be factored out. Therefore, considering that $A = 1$, Equations (2.23)–(2.25) also constitute the equations for the total conservation of energy (in $Joules$). While the different integrals in Eq. (2.22) are positive definite, I_ℓ, I_m and I_n are not necessarily so. This indicates that any mode can gain or lose energy to its coupled modes.

When the three wave frequencies (ω_ℓ, ω_m and ω_n) are positive and the high frequency pump wave (a_ℓ) is externally driven, the energy will initialy transfer to the daughter waves. The conservation relations, Eqs. (2.23)–(2.25), are important in verifying the numerical schemes that are used to solve the equations.

2.3 Stimulated Raman Scattering (SRS)

Stimulated Raman scattering is the nonlinear coupling between two electromagnetic waves and an electron plasma wave, whose wave envelopes are described by Eqs. (2.6)–(2.8). Looking at backscattering only, we restrict to the one dimensional framework explained in Appendix B (where the SRS coupling is maximum) and consider no resonance de-phasing.

For a high frequency electromagnetic wave (mode ℓ) coupled to a backscattered electromagnetic wave (mode m) and a forward propagating electron plasma wave (mode n), representing the SRS coupling of a laser beam propagating through a weakly nonlinear plasma, the three wave coupled mode equations are:

$$\left(\frac{\partial}{\partial t_s} + v_{g\ell}\frac{\partial}{\partial x_s} + \nu_\ell\right) a_\ell = -K a_m a_n, \tag{2.26}$$

$$\left(\frac{\partial}{\partial t_s} + v_{gm}\frac{\partial}{\partial x_s} + \nu_m \right) a_m = K^* a_\ell a_n^*, \tag{2.27}$$

$$\left(\frac{\partial}{\partial t_s} + v_{gn}\frac{\partial}{\partial x_s} + \nu_n \right) a_n = K^* a_\ell a_m^*. \tag{2.28}$$

Equations (2.26)–(2.28) contain seven fundamental parameters: the group velocities (v_g's), the wave damping rates (ν's) and the nonlinear coupling coefficient (K). From the electromagnetic and electron plasma wave dispersion relations given in Table (1-1), the group velocities [$v_g = d\omega(k)/dk$] are $v_{g\ell} = c^2 k_\ell/\omega_\ell$, $v_{gm} = c^2 k_m/\omega_m$ and $v_{gn} = 3v_{Te}^2 k_n/\omega_n$, for the EMW, BEMW and EPW, respectively. In ICF experimental parameters $v_{g\ell} \approx c \approx -v_{gm} \gg v_{gn}$.

The damping of the electromagnetic waves is mainly collisional, and is neglected. However, the damping of the electron plasma waves, which is due to Landau damping, can be significantly large and needs to be evaluated carefully (see Section 2.6). Since the EM collisional damping is neglected, the threshold for SRS backscattering is zero, and a relatively small unperturbed laser amplitude can produce significant SRS backscattering.

The coupling coefficient for SRS backscattering, as derived in Appendices A and B, is

$$K \approx \sqrt{\frac{2}{\epsilon_o}} \frac{e}{m_e} \frac{k_n}{4} \left(\frac{\omega_{pe}^2}{\omega_\ell \omega_m \omega_n} \right)^{1/2}. \tag{2.29}$$

The maximum SRS parametric growth rate $\gamma_{SRS} = |Ka_o|$ is then given by:

$$(\gamma_{SRS})_{max} = \frac{k_n}{4}|v_{o\ell}|\sqrt{\frac{\omega_n}{\omega_m}}, \tag{2.30}$$

where $|v_{o\ell}| = e|E_\ell|/m_e\omega_\ell$ is the electron quiver velocity in the field of the pump wave, and $|E_\ell|$ the unperturbed amplitude of the pump electric field in the plasma.

While the wave de-phasing (δ_ω, δ_k) has been neglected in this Section, it may also be significant in the overall behavior of SRS when the plasma cannot be taken as homogeneous [54, 56, 57], or when the wave-particle interactions (like electron trapping) are important [69] – [71]. The investigation of such de-phasing is left as a problem for the future.

37

2.4 Langmuir decay interaction (LDI)

LDI is a slightly different 3WI process, in which the high frequency wave (mode ℓ) is an electron plasma wave that decays into a backscattered electron plasma wave (mode m) and an ion acoustic wave (mode n). In our case the LDI pump wave is taken to be the electron plasma wave driven by SRS.

The group velocities are now: $v_{g\ell} = 3v_{Te}^2 k_\ell/\omega_\ell$, $v_{gm} = 3v_{Te}^2 k_m/\omega_m$ and $v_{gn} = c_s^2 k_n/\omega_n$. Similar to SRS, $v_{g\ell} \approx -v_{gm} \gg v_{gn}$. Unlike SRS, the Landau damping coefficients of all the waves can be significantly large, so that the threshold condition for convective instability is given by: $\gamma_c = \sqrt{\nu_m \nu_n}$.

The LDI coupling coefficient, as derived in Appendices A and B, is

$$K \approx \sqrt{\frac{2}{\epsilon_o}} \frac{e}{m_e} \frac{\omega_{pe}}{4v_{Te}} \left(\frac{\omega_n}{\omega_\ell \omega_m} \right)^{1/2}.$$ (2.31)

The maximum growth rate for the LDI is:

$$(\gamma_{LDI})_{max} \approx \frac{1}{4} \frac{|v_{o\ell}|}{v_{Te}} \sqrt{\omega_m \omega_n},$$ (2.32)

where $|v_{o\ell}| = e|E_\ell|/m_e\omega_\ell$ is the electron quiver velocity in the field of the pump wave, and $|E_\ell|$ is the unperturbed amplitude of the pump electron plasma wave.

2.5 Landau damping

While the amplitude of Landau damping depends on the wavelength of the wave (i.e., it is nonlocal), in the slowly varying amplitude approximation - where only a narrow spread of the spectrum occurs - the Landau damping can be taken as approximately constant for the range of wavelengths that is considered. Therefore, the Landau damping can be evaluated at the real wavenumber of each linear longitudinal wave. To calculate this damping [48], one needs to consider the kinetic plasma dispersion relation (described in Chapter 3), finding the roots $[\omega(k_r) = \omega_r(k_r) + i\omega_i(k_r)]$ for a real wavenumber $k = k_r$. The Landau damping is then given by the imaginary part
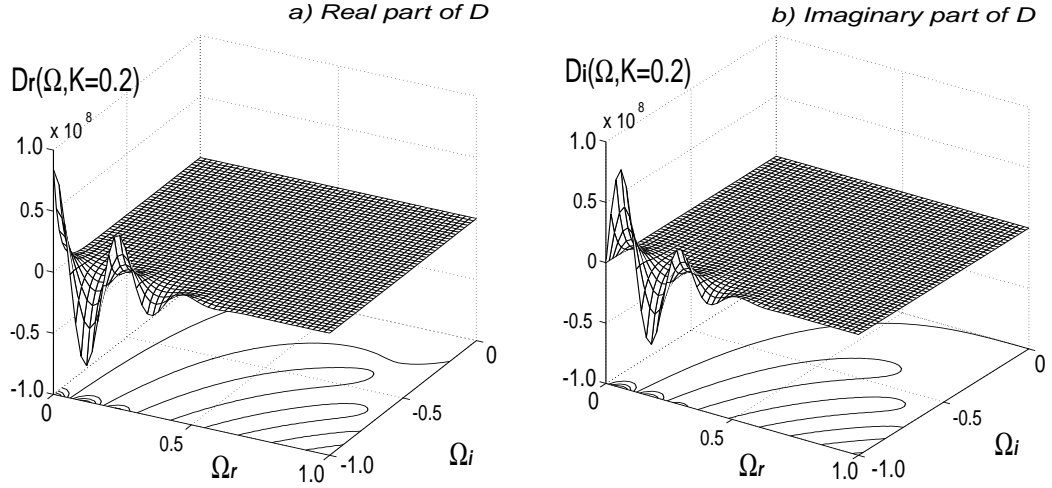
Figure 2-1: EPW kinetic dispersion relation function, for $K = k\lambda_{De} = 0.2$.

of the complex frequency associated to k_r $[\omega_i(k_r)]$.

For a *Maxwellian distribution* (assuming thermal equilibrium) [48]:

$$f_{s_M}(w) = \frac{n_{so}}{v_{Ts}\sqrt{2\pi}} exp\left(-\frac{w^2}{2v_{Ts}^2}\right),\tag{2.33}$$

the kinetic dispersion relation is given by [48]:

$$D_L(k,\omega) = 1 - \frac{Z'(\zeta_e)}{2k_r^2\lambda_{De}^2} - \sum_\beta \frac{Z'(\zeta_\beta)}{2k_r^2\lambda_{D\beta}^2} = 0.\tag{2.34}$$

Here, $\lambda_{Ds} = v_{Ts}/\omega_{ps}$ is the particle Debye length, $\zeta = \omega/\sqrt{2}|k_r|v_{Ts}$, and $Z(\zeta)$ is the *plasma dispersion function* [59, 60]:

$$Z(\zeta) = i2e^{-\zeta^2}\int_{-\infty}^{i\zeta} e^{-t^2}dt = -i\sqrt{\pi}e^{-\zeta^2}\left[1 + erf(i\zeta)\right].\tag{2.35}$$

To gain some insight on the nature of the kinetic dispersion relation, Figure (2-1) shows a picture of $D_L(K,\Omega)$, where the arguments (k,ω) have been normalized to: $K = k\lambda_{De}$ and $\Omega = \omega/\omega_{pe}$. Only electron plasma waves ($\omega_r \sim \omega_{pe}$) are studied in the figure, so that the low frequency ion dynamics $[\sum_\beta Z'(\zeta_\beta)/(2k_r^2\lambda_{D\beta}^2)]$ have been neglected. Figure (2-1.a) shows the real part of the dispersion relation for a particular $K = 0.2$, and Figure (2-1.b) the imaginary part.
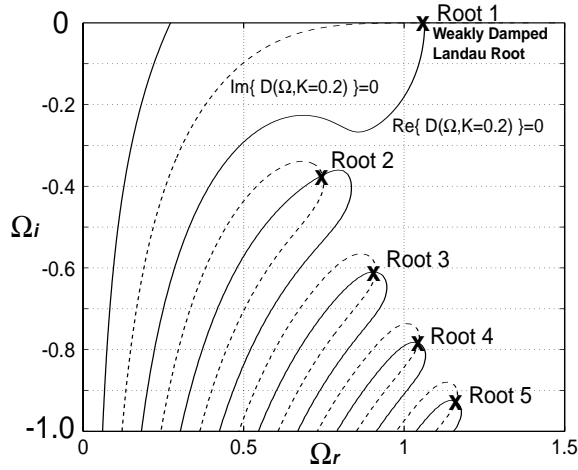
Figure 2-2: Roots of the EPW dispersion relation function (with $K = 0.2$).

The kinetic dispersion relation has an infinite number of roots [48], some of which are illustrated in Fig. (2-2). In this figure the contour lines for $\mathcal{R}e\{D_L(\Omega, K = 0.2)\} = 0$ are plotted as solid lines, and the contour lines for $\mathcal{I}m\{D_L(\Omega, K = 0.2)\} = 0$ are plotted as dashed lines. The intersections in the figure correspond to the roots of $D_L(K, \Omega) = 0$, labeled as "Root1", "Root2", etc.

The k_r dependence of the frequencies in the first seven modes in the electron plasma range of frequencies are illustrated in Figure (2.3). The first mode is weakly damped even if k_r is changed, and the real frequency of this mode approaches the plasma frequency ($\omega_r \to \omega_{pe}$) as k_r goes to zero . Because of its weaker damping, the first mode is time asymptotically dominant in the plasma, and therefore it is referred as the "*principal mode*". For small $k\lambda_{De}$, the real frequency of the principal mode approximately satisfies the linearized dispersion relation for electron plasma waves (given in Chapter 1):

$$\omega_r^2 \approx \omega_{pe}^2 + 3v_{Te}^2 k_r^2. \tag{2.36}$$

Different asymptotic approximations can be obtained to calculate the electron plasma wave damping in the limit of $K \equiv k\lambda_{De} \ll 1$ [48, 61, 62]. However, all the Landau damping coefficients reported on this thesis are calculated locally (in k_r) from the exact kinetic dispersion relation (Eq. 2.33).

40
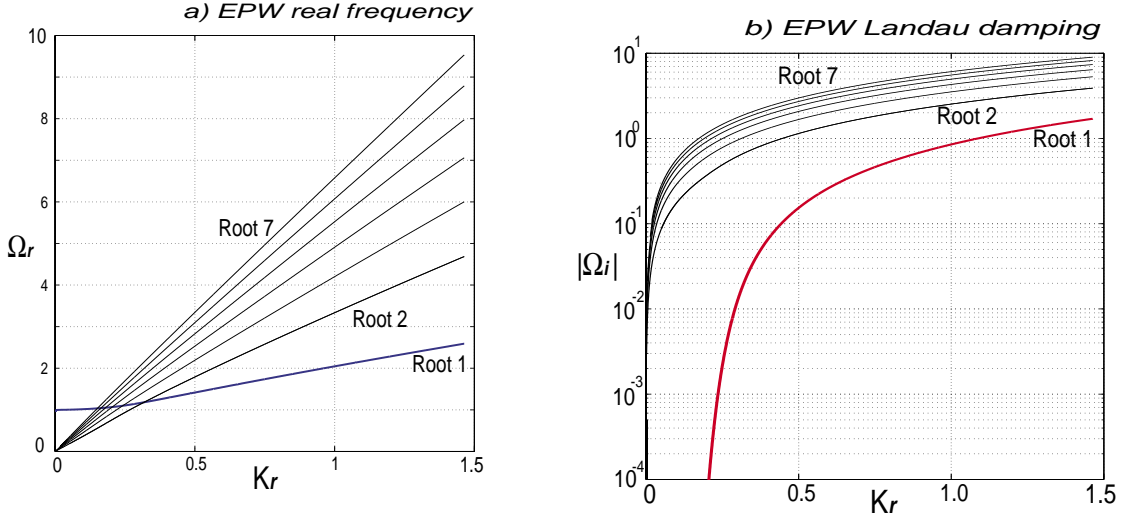
Figure 2-3: Dispersion relation of electron plasma waves with real K.

The Landau damping of the ion acoustic waves can also be calculated from Equation (2.33); however, in this case the ion dynamics cannot be neglected. When ion dynamics are considered, the kinetic dispersion relation exhibits new series of roots at lower frequencies ($\omega_r \ll \omega_{pe}$), which correspond to the linear ion acoustic plasma modes. Again, only one of these lower frequency modes is weakly damped, and it is referred as the "*principal ion acoustic wave*".

The dispersion relation of the principal IAW is illustrated in Figures (2-4) and (2-5), for a carbon and hydrogen plasma. Figure (2-4) shows the principal IAW dispersion relation for different ratios of the ion to electron temperatures ($\theta = T_i/T_e$), considering an ion composition of 70% H and 30% C. As can be noticed in Figure (2-4.b), the Landau damping of the ion acoustic waves is sensitive to the particle temperatures, even for small $k\lambda_{De}$ (see also [62]).

For $k\lambda_{De} \ll 1$, the real frequency of the principal IAW is approximately given by:

$$\omega_r^2 \approx (1 + 3T_i/Z_iT_e)c_s^2k_r^2, \tag{2.37}$$

where $c_s = (Z_i\kappa T_e/m_i)^{1/2}$.

The Landau damping of the principal IAW is also very sensitive to the plasma ion

41
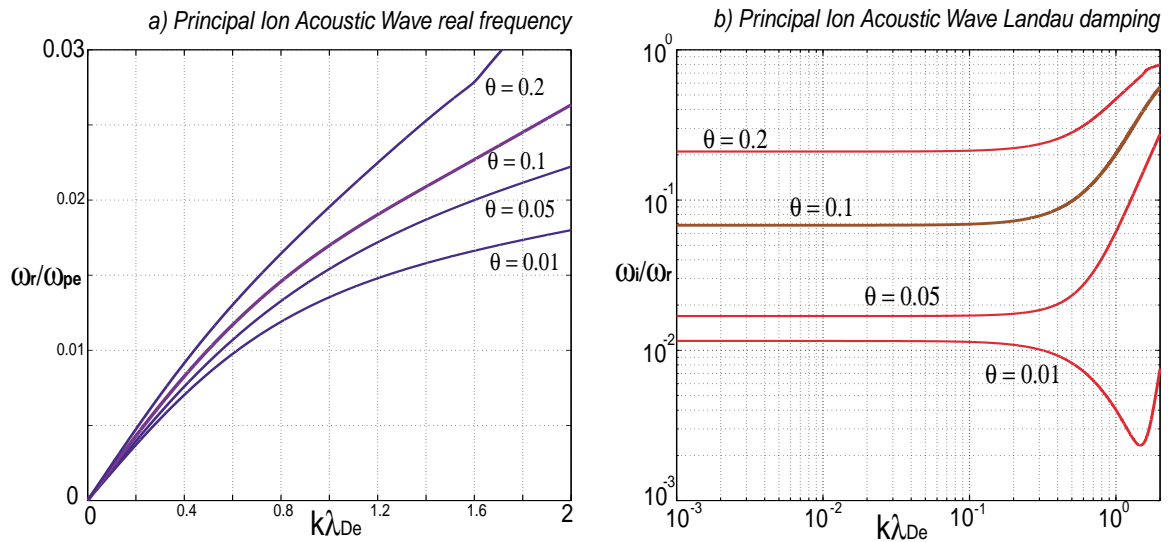
Figure 2-4: Principal Ion Acoustic Wave vs. Ion/Electron Temperature Ratio.

species composition (see also [61]). Figure (2-5) shows the principal IAW dispersion relation for different hydrogen/carbon concentrations, considering $\theta = 0.1$. The dispersion relation for 70% hydrogen and 30% carbon has been highlighted in the figure. A small change in the ion density composition can produce a significant change of the IAW damping.
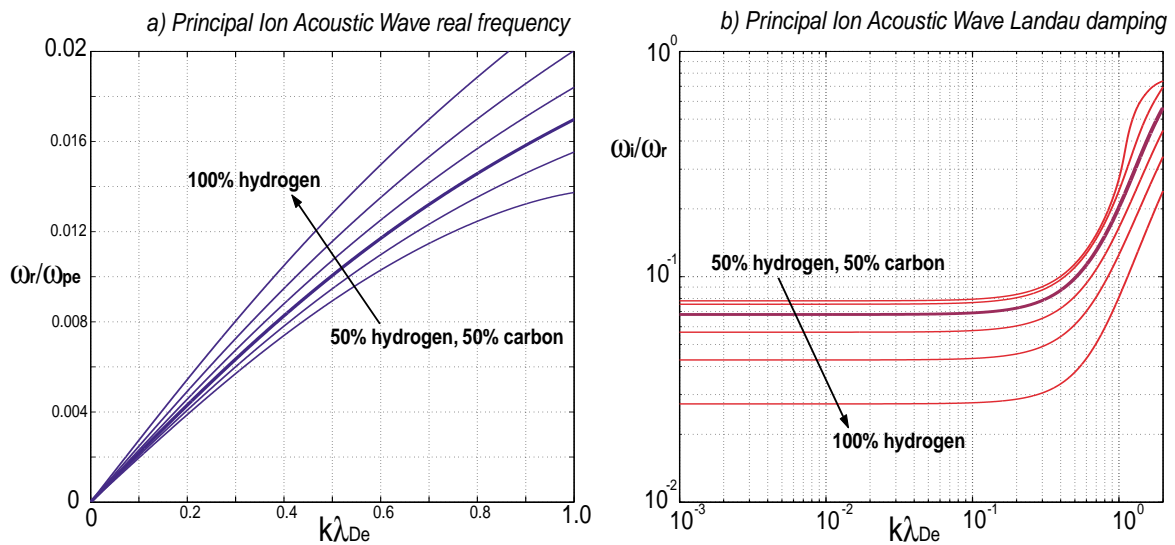
Figure 2-5: Principal Ion Acoustic Wave vs. Ion Species Composition.

Chapter 3

Nonlinear Laser-plasma Electrodynamics in ICF

The different models to describe the SRS reflectivity as a function of various problem parameters observed in ICF experiments ([23] – [45]) are described and analyzed in this chapter. The coupled modes approximation ([23] – [31]), described in Section (3.3), is the main approach used in the thesis.

Due to the complexity of the laser-plasma interactions that occur in ICF experiments, all the models used for their investigation need to be somehow approximated. While the approximate models cannot be expected to entirely explain the experimental observations, their importance should not be discarded because they can lead to the understanding of some aspects of the overall problem, and provide a qualitative description of the observations. Many approximate models that are available in literature are derived from the Maxwell equations and the Vlasov-kinetic plasma equations ([32]-[35]). This models however, are frequently further approximated by the multifluid plasma equations ([37]-[45]).

As a guide to the reader, Figure (3-1) shows a simple map of the main modeling paths that have been pursued in the description of the SRS backscattering in ICF plasmas. The Maxwell-Vlasov equations are either studied numerically, by direct numerical integration [32, 33] or with the "particle in cell" approach [34, 35], or they
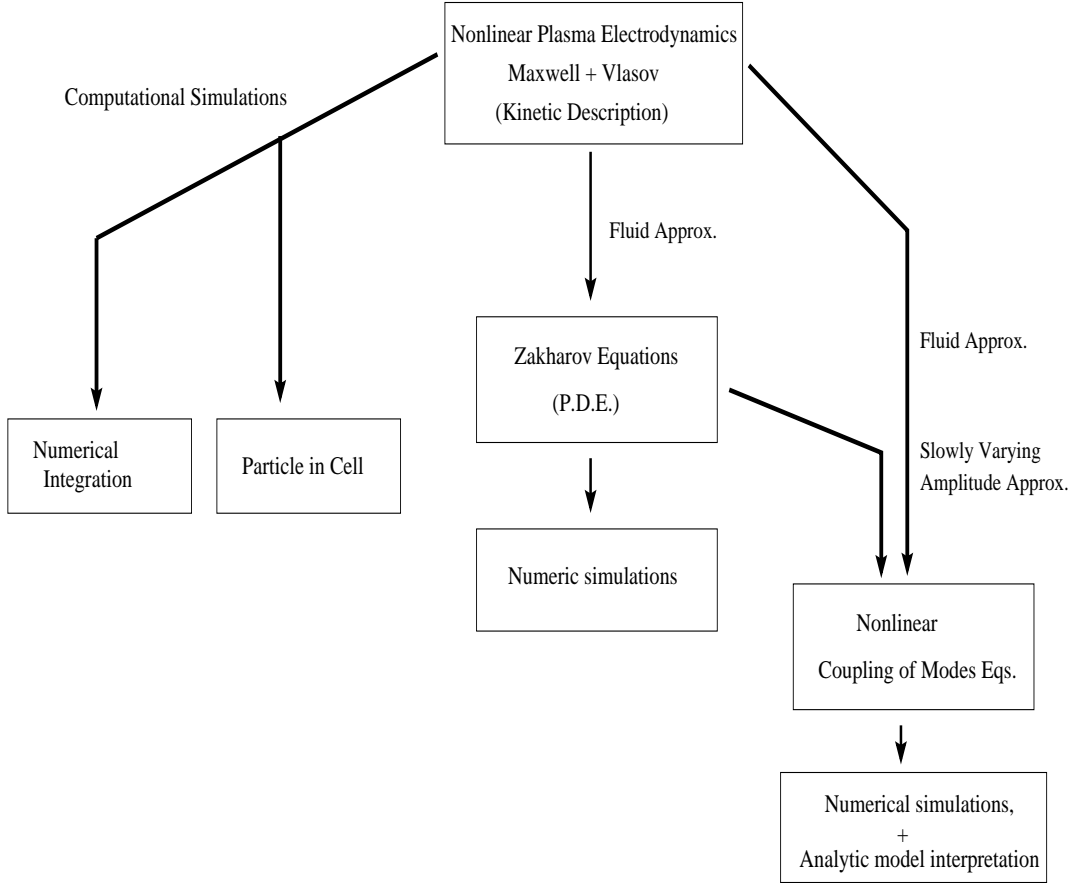
Figure 3-1: Map of models for laser backscattering in ICF plasmas

are first reduced to the multifluid model ([37] – [45]). Some other computational approaches (not treated here), are mixed kinetic and fluid [36].

Zakharov equations (derived in Appendix B) follow from a separation of time scales in the multi-fluid model, considering small perturbations of an initial equilibrium state and an expansion in orders of amplitudes (generally up to the second order). They are second order partial differential equations, describing the nonlinear coupling between natural linear plasma modes, which are usually investigated numerically ([37] – [45]) or even further reduced to the "coupled modes equations". Apart from the second order in amplitude expansion, the coupled modes equations (derived in Appendices A and B) also consider that the amplitudes of the coupled waves are slowly varying in time and space. These are first order partial differential equations

that only describe the nonlinear coupling between the wave envelopes, and constitute one of the simplest available models. The COM equations can be integrated numerically [23] – [31], or further reduced so analytic solutions are possible [49] – [53]. Much insight can be gained from the linear and nonlinear analytic solutions, that help in understanding and guiding numerical solutions of more complex equations.

A brief description of the basic Maxwell-Vlasov plasma model is given next, followed by a discussion on the Maxwell-fluid models used to understand ICF laser-plasma experimental results.

3.1 Maxwell-Vlasov Formulation

The Maxwell-Vlasov equations describe the self-consistent charge and current densities, and the electric and magnetic fields, in a collisionless plasma with particle distribution functions $f_s(\overline{w}, \overline{r}, t)$, which are time ($t$), space ($\overline{r}$) and particle velocity ($\overline{w}$) dependent. The fluid density of a particle species s $[n_s(\overline{r}, t)]$ is given by:

$$n_s(\overline{r}, t) = \int_{-\infty}^{\infty} f_s(\overline{w}, \overline{r}, t) d^3\overline{w}. \tag{3.1}$$

The self consistent macroscopic electromagnetic fields, $\overline{E}$ and $\overline{B} = \mu_o \overline{H}$, satisfy Maxwell equations:

$$\nabla \times \overline{E} + \frac{\partial \overline{B}}{\partial t} = 0, \tag{3.2}$$

$$\nabla \times \overline{B} - \frac{1}{c^2} \frac{\partial \overline{E}}{\partial t} - \mu_o \overline{J} = 0, \tag{3.3}$$

$$\epsilon_o \nabla \cdot \overline{E} = \rho, \tag{3.4}$$

$$\nabla \cdot \overline{B} = 0; \tag{3.5}$$

and the Vlasov-kinetic equation:

$$\frac{\partial f_s}{\partial t} + \overline{w} \cdot \frac{\partial f_s}{\partial \overline{r}} + \frac{q_s}{m_s}(\overline{E} + \overline{w} \times \overline{B}) \cdot \frac{\partial f_s}{\partial \overline{w}} = 0. \tag{3.6}$$

The charge ρ and current $\overline{J}$ densities are, respectively, given by

$$\rho = \sum_s q_s \int f_s d^3\overline{w}, \qquad (3.7)$$

$$\overline{J} = \sum_s q_s \int \overline{w} f_s d^3\overline{w}. \qquad (3.8)$$

In the above equations, ϵ_o, μ_o and $c = (\mu_o\epsilon_o)^{-1/2}$ are the permitivity, permeability and speed of light in vacuum, respectively. The electric charge and mass of the plasma particle species s are q_s and m_s, respectively.

The Maxwell-Vlasov equations for appropriate ICF laser-plasma conditions are extremely difficult to solve, partly because they are a nonlinear set of partial differential-integral equations with generally not well-defined boundary conditions.

Prior attempts have been made to solve the Maxwell-Vlasov equations numerically [32, 33]; however, computer simulations are difficult because of the wide range of scales. The details of these codes are omitted in this review because they are not directly relevant.

3.2   Maxwell-Fluid Formulation

Due to the complexity of solving Eqs. (3.2)–(3.8), alternative reduced models have been explored. A significant simplification is obtained when the kinetic equations are reduced to the multi-fluid plasma approximation [48], by taking the velocity moments of the Vlasov equation.

The zeroth velocity moment of the Vlasov equation [Eq. (3.6)] leads to the continuity equation:

$$\frac{\partial}{\partial t}n_s + \nabla \cdot (n_s\overline{v}_s) = 0, \qquad (3.9)$$

and the first velocity moment, $\langle\overline{w}\rangle$, gives the momentum conservation equation:

$$\frac{\partial}{\partial t}\overline{v}_s + \overline{v}_s \cdot \nabla\overline{v}_s = \frac{q_s}{m_s}(\overline{E} + \overline{v}_s \times \overline{B}) - \frac{1}{m_s n_s}\nabla p_s. \qquad (3.10)$$

In Eqs. (3.9) and (3.10), $\overline{v}_s = \langle \overline{w} \rangle$, n_s and ∇p_s, are the average velocity, density and pressure gradient, respectively, of species s. While the pressure involves higher order velocity moments, the *equation of state* can be used as an alternative equation to close the system:

$$p_s = \gamma_s n_s \kappa T_s. \tag{3.11}$$

Here, the "gas constant" (γ_s) is set to $\gamma_s = 1$ for isothermal dynamics, or $\gamma_s = (d_s + 2)/d_s$ for adiabatic particles with d_s degrees of freedom.

The plasma fluid equations are simply connected to the Maxwell equations through the charge and current densities:

$$\rho = \sum_s q_s n_s, \tag{3.12}$$

$$\overline{J} = \sum_s q_s n_s \overline{v}_s. \tag{3.13}$$

The multifluid plasma equations, though much simpler than the kinetic equations, are still quite difficult to solve numerically for the ICF laser-plasma conditions [40].

Further simplification of the Maxwell-fluid equations leads to the *Zakharov equations*, and the *coupled modes equations*. The Zakharov and COM models are still too complex for analytic investigation, but both of them can be readily studied numerically. The detailed derivation of both models is given in Appendices A and B.

3.2.1 Zakharov's equations

Proposed in 1972, the Zakharov equations have been widely used to study the SRS backscattering ([37]-[45]). The model basically consists of three second order partial differential equations, which describe the nonlinear coupling on three different time scales: 1) the fast frequency variations of the electromagnetic waves [EMW], 2) the intermediate time scale of longitudinal electron plasma waves [EPW], and 3) the slow frequency variations of the longitudinal ion acoustic waves [IAW].

Zakharov equations describe the dynamics in perturbations of an initial steady

state characterized by a non-drifting ($v_{eo} = v_{io} = 0$), neutral, homogeneous plasma ($n_{eo} = Z_i n_{io} = constant$), with no electromagnetic fields ($\overline{E}_o = \overline{B}_o = 0$). For one dimensional dynamics with propagation in the $\hat{x}$ direction, linearly polarized transverse modes in $\hat{y}$, and small perturbations that are constant in (y, z) the total electron density (n_e), ion density (n_i), electron velocity ($\overline{v}_e$), ion velocity ($\overline{v}_i$) and electric field ($\overline{E}$), are given by:

$$n_e(x,t) = n_{eo} + n_{eh}(x,t) + n_{e\ell}(x,t), \tag{3.14}$$

$$n_i(x,t) = n_{io} + n_{i\ell}(x,t), \tag{3.15}$$

$$\overline{v}_e(x,t) = \hat{x}\left[v_{exh}(x,t) + v_{ex\ell}(x,t)\right] + \hat{y}v_{ey}(x,t), \tag{3.16}$$

$$\overline{v}_i(x,t) = \hat{x}v_{ix\ell}(x,t), \tag{3.17}$$

$$\overline{E}(x,t) = \hat{x}[E_{xh}(x,t) + E_{x\ell}(x,t)] + \hat{y}E_y(x,t). \tag{3.18}$$

Where, n_{eh}, $n_{e\ell}$, $n_{i\ell}$, v_{exh}, $v_{ex\ell}$, v_{ey}, $v_{ix\ell}$, E_{xh}, $E_{x\ell}$ and E_y, are small perturbations of the steady state. The subscript "h" stands for high frequency oscillations of the order of the EPW time-scale, and subscript "ℓ" for slow oscillations of the order of the IAW time-scale. The $\hat{y}$ components of the fields oscillate with the characteristic frequency of the EMW, corresponding to the fastest time scale in the system.

The full Zakharov equations are derived from the Maxwell-fluid equations with the perturbation expansion in (3.14)-(3.18). Then, the Zakharov equations as obtained in Appendix A [Eqs. (A.44)-(A.46)] are:

$$\left(\frac{\partial^2}{\partial t^2} - c^2\frac{\partial^2}{\partial x^2} + 2\nu_E\frac{\partial}{\partial t} + \omega_{pe}^2\right)v_{ey} = -\omega_{pe}^2\left(\frac{n_{eh}}{n_{eo}}v_{ey}\right) - \omega_{pe}^2\left(\frac{n_{e\ell}}{n_{eo}}v_{ey}\right), \tag{3.19}$$

$$\left(\frac{\partial^2}{\partial t^2} - 3v_{Te}^2\frac{\partial^2}{\partial x^2} + 2\nu_L\frac{\partial}{\partial t} + \omega_{pe}^2\right)E_{xh} = -\omega_{pe}^2\frac{n_{e\ell}}{n_{eo}}E_{xh} - \frac{q_e n_{eo}}{2\epsilon_o}\frac{\partial}{\partial x}\left(\frac{|v_{ey}|^2}{2}\right), \tag{3.20}$$

$$\left(\frac{\partial^2}{\partial t^2} - c_a^2\frac{\partial^2}{\partial x^2} + 2\nu_A\frac{\partial}{\partial t}\right)n_{e\ell} = Z_i\frac{m_e}{m_i}n_{eo}\frac{\partial^2}{\partial x^2}\left(\frac{|v_{ey}|^2 + |v_{exh}|^2}{2}\right). \tag{3.21}$$

The coefficients $v_{Te} = 3(\kappa T_e/m_e)^{1/2}$, $c_s \approx (\kappa T_e/m_i)^{1/2}$ and $\omega_{pe} = (q_e^2 n_{eo}/\epsilon_o m_e)^{1/2}$,

are the electron thermal velocity, the speed of sound in the plasma, and the electron plasma frequency, respectively. E_{xh}, v_{ey} and $n_{e\ell}$, are the amplitudes of the electric field of the electron plasma waves, the electron transverse velocity, and the low frequency electron component of the electron density, respectively. The damping coefficient of electromagnetic waves (ν_E) is considered to be collision Al, and the damping coefficients of longitudinal modes (ν_L and ν_A) is due to Landau damping (treated in Chapter 2).

The left hand sides of the Zakharov equations describe second order linear modes for the three different time scales. The right hand sides give the approximate nonlinear coupling between these modes.

As mentioned before, the Zakharov equations in the frame of ICF plasmas are usually studied numerically, with further approximations. To illustrate the nature of these approximations, the reduced equations by T. Kolber, et. al. [42], are discussed next.

Zakharov-Kolber reduced model

Kolber, et al. [42], have set up a model, derived from the full wave Zakharov equations. This model describes the coupling between four linear waves: a high frequency electromagnetic wave (with $\omega \approx \omega_o$), the SRS backscattering electromagnetic wave (with $\omega \approx \omega_1 \approx \omega_o - \omega_{pe}$), an electron plasma wave ($\omega \approx \omega_{pe}$), and a low frequency ion acoustic wave [42, 43].

Considering that both electromagnetic waves have a slowly varying amplitude, the total electron transverse velocity (i.e., the linear superposition of both electromagnetic waves) is given by:

$$v_{ey} = \frac{1}{2} \sum_{\beta=0,1} [\Psi_\beta(x,t)e^{-i\omega_\beta t} + C.C.].\tag{3.22}$$

The electron plasma wave, on the other hand, is also considered to have a slowly varying amplitude and a frequency $\omega_{EPW} \approx \omega_{pe}$. Therefore, the EPW electric field is given by:

$$E_{xh} = \frac{1}{2}[\mathcal{E}(x,t)e^{-i\omega_{pe}t} + C.C.].\tag{3.23}$$

The slowly varying amplitudes Ψ_o, Ψ_1 and $\mathcal{E}$, in Eqs. (3.22) and (3.23), stand for the slow amplitude modulations in time. They satisfy the slowly varying conditions: $|\partial_t \Psi_o| \ll |\omega_o \Psi_o|$, $|\partial_t \Psi_1| \ll |\omega_1 \Psi_1|$ and $|\partial_t \mathcal{E}| \ll |\omega_{pe} \mathcal{E}|$.

Also derived in Appendix A, the model proposed in [42] results from combining Eqs. (3.19)–(3.23) and neglecting the direct coupling between electromagnetic and ion acoustic waves $[n_{e\ell} v_{ey}$ in Eq. (3.19), and $\partial_{xx}|v_{ey}|^2$ in Eq. (3.21)]. Grouping together all the resonant terms (with frequencies ω_o, ω_1 and ω_{pe}), one finds the following set of equations:

$$i\frac{\partial}{\partial t}\Psi_o + i\nu_E \Psi_o + \frac{c^2}{2\omega_o}\frac{\partial^2}{\partial x^2}\Psi_o - \frac{\omega_{pe}^2 - \omega_o^2}{2\omega_o}\Psi_o = \frac{\omega_{pe}^2}{2\omega_o}\frac{n_{e\ell}}{n_{eo}}\Psi_o - \frac{e}{4\omega_o m_e}\left(\frac{\partial}{\partial x}\mathcal{E}\right)\Psi_1, \quad (3.24)$$

$$i\frac{\partial}{\partial t}\Psi_1 + i\nu_E \Psi_1 + \frac{c^2}{2\omega_1}\frac{\partial^2}{\partial x^2}\Psi_1 - \frac{\omega_{pe}^2 - \omega_1^2}{2\omega_1}\Psi_1 = \frac{\omega_{pe}^2}{2\omega_o}\frac{n_{e\ell}}{n_{eo}}\Psi_1 - \frac{e}{4\omega_o m_e}\left(\frac{\partial}{\partial x}\mathcal{E}\right)\Psi_o, \quad (3.25)$$

$$i\frac{\partial}{\partial t}\mathcal{E} + i\nu_L \mathcal{E} + \frac{3}{2}\frac{v_{Te}^2}{\omega_{pe}}\frac{\partial^2}{\partial x^2}\mathcal{E} - \frac{\omega_{pe}}{2}\frac{n_{e\ell}}{n_{eo}}\mathcal{E} = \frac{e n_{eo}}{4\omega_{pe}\epsilon_o}\frac{\partial}{\partial x}\Psi_o \Psi_1^*, \quad (3.26)$$

$$\left(\frac{\partial^2}{\partial t^2} - c_s^2\frac{\partial^2}{\partial x^2} + 2\nu_A\frac{\partial}{\partial t}\right)n_{e\ell} = \frac{n_{eo}}{2}\frac{m_e}{m_i}\frac{\partial^2}{\partial x^2}(\Psi_o^2 + \Psi_1^2) + \frac{\epsilon_o}{4m_i}\frac{\partial^2}{\partial x^2}\mathcal{E}^2. \quad (3.27)$$

Once again, the damping coefficients ν_E, ν_L, and ν_A, are the collisional damping of the electromagnetic waves, the local Landau damping of the electron plasma wave, and the Landau damping of the ion acoustic waves, respectively.

Kolber, et al., studied the time evolution of the SRS reflectivity, the spectral distribution of the ion acoustic and electron plasma waves, and the space/time evolution of $n_{e\ell}(x,t)$ and $\mathcal{E}(x,t)$. Considering a variety of ICF experimental plasma parameters [42], they found that the SRS backscattering saturates in a time that is much shorter than the experimental duration of the laser pulses. The EPW was numerically found to evolve into a turbulent steady state (with a broad spectral distribution around the resonant frequency). This result however, contradicts the initial assumption of $\omega_{EPW} \approx \omega_{pe}$, and the assumption of constant (local) Landau damping. They did not investigate the effects of Landau damping on the SRS reflectivity.

3.3 Coupled Modes Equations

The COM equations constitute a simpler model to investigate the SRS backscattering, and its possible coupling to LDI [23] - [27]. Since ICF experiments clearly suggest the coupling of SRS and LDI (see Chapters 1 and 2), we have chosen this model to investigate the laser-plasma electrodynamics in such ICF experiments. While there are many nonlinear effects that are not included in our investigation [like the wave-particle interactions], the COM equations allow us to get a qualitative understanding of some of the important physics behind the SRS backscattering observations.

In the slowly varying amplitude approximation, considering the one dimensional framework explained in Appendix B, the electric field of a linear mode with real frequency and real wave number (ω_ℓ, k_ℓ) is given by:

$$E_\ell = \frac{1}{2} \left\{ \mathcal{E}_\ell(x_s, t_s) e^{-i\omega_\ell t} e^{ik_\ell x} \right\}. \tag{3.28}$$

Where the slowly varying function $\mathcal{E}_\ell$ satisfies $|\partial_{x_s} \mathcal{E}_\ell| \ll |k_\ell \mathcal{E}_\ell|$ and $|\partial_{t_s} \mathcal{E}_\ell| \ll |\omega_r \mathcal{E}_\ell|$.

The three wave COM equations derived in Appendix B can easily be extended to account for the coupling between the five waves in SRS and LDI (see also Appendix A, for a derivation from the full wave Zakharov equations). These five-wave coupled modes equations are:

$$\left(\frac{\partial}{\partial t} + v_{g1} \frac{\partial}{\partial x} + \nu_1 \right) a_1 = -K_{SRS} a_2 a_3 e^{-i(\delta_S \omega)t} e^{i(\delta_S k)x}, \tag{3.29}$$

$$\left(\frac{\partial}{\partial t} + v_{g2} \frac{\partial}{\partial x} + \nu_2 \right) a_2 = K_{SRS}^* a_1 a_3^* e^{i(\delta_S \omega)t} e^{-i(\delta_S k)x}, \tag{3.30}$$

$$\left(\frac{\partial}{\partial t} + v_{g3} \frac{\partial}{\partial x} + \nu_3 \right) a_3 = K_{SRS}^* a_1 a_2^* e^{i(\delta_S \omega)t} e^{-i(\delta_S k)x} - K_{LDI} a_4 a_5 e^{-i(\delta_L \omega)t} e^{i(\delta_L k)x}, \tag{3.31}$$

$$\left(\frac{\partial}{\partial t} + v_{g4} \frac{\partial}{\partial x} + \nu_4 \right) a_4 = K_{LDI}^* a_3 a_5^* e^{i(\delta_L \omega)t} e^{-i(\delta_L k)x}, \tag{3.32}$$

$$\left(\frac{\partial}{\partial t} + v_{g5} \frac{\partial}{\partial x} + \nu_5 \right) a_5 = K_{LDI}^* a_3 a_4^* e^{i(\delta_L \omega)t} e^{-i(\delta_L k)x}. \tag{3.33}$$

Where a_ℓ, for $\ell = 1... 5$, stand for the amplitudes of the laser, backscattered EM wave (BEMW), SRS induced electron plasma wave (EPW), LDI induced backscattered electron plasma wave (BEPW), and LDI induced ion acoustic wave (IAW), respectively. For positive frequencies ($\omega_\ell.0$) the wave action density is given by $|a_\ell|^2 = \mathrm{w}_\ell/\omega_\ell$. The parameters w_ℓ, $v_{g\ell}$ and ν_ℓ are the wave energy density, group velocity and damping rate of the ℓ_{th} mode, respectively. In the slowly varying amplitude approximation, it is required that $\nu_\ell \ll \omega_\ell$. The de-phasing terms, $(\delta_S\omega) = \omega_1 - \omega_2 - \omega_3$, $(\delta_S k) = k_1 - k_2 - k_3$, $(\delta_L\omega) = \omega_3 - \omega_4 - \omega_5$, and $(\delta_L k) = k_3 - k_4 - k_5$, also need to be small $[(\delta_{S,L}\omega) \ll \omega_\ell$ and $(\delta_{S,L}k) \ll k_\ell]$ to be consistent with the slowly varying amplitude approximation.

The coupling coefficients (K_{SRS} and K_{LDI}), derived in Appendices A and B, are:

$$K_{SRS} = -\frac{k_3}{4}\sqrt{\frac{2}{\epsilon_o}}\left(\frac{e}{m_e}\right)\left[\frac{\omega_{pe}^2}{\omega_1\omega_2\omega_3}\right]^{1/2}, \qquad (3.34)$$

$$K_{LDI} = -\sqrt{\frac{2}{\epsilon_o}}\left(\frac{e}{m_e}\right)\frac{\omega_{pe}}{4v_{Te}}\left(\frac{\omega_5}{\omega_3\omega_4}\right)^{1/2}. \qquad (3.35)$$

The main topic of my research is to investigate the effects of LDI on the SRS backscattering by solving the coupled modes equations [49]. While limited aspects of this model (with further approximations) have been investigated by other authors, no detailed attempt has been made to explain the experimental data. Below we review some of the previous work on COM.

Previous work with COM equations

The use of the five wave coupled mode equations (5COM) in the modeling of SRS coupled to LDI was first proposed by Heikkinen and Karttunen, in 1980. They studied the relation between the SRS reflectivity and the intensity of the laser pump [23, 24, 25]. In their investigation, Heikkinen and Karttunen neglected the time derivatives that appear in Eqs. (3.29) and (3.30),[23] finding numerical solutions for a reduced version of their model. They considered a single species homogeneous plasma, zero wave de-phasing and typical ICF laser-plasma parameters $[n/n_{cr} = 0.1,$

$T_e \sim 1keV$, $\lambda_o = 1.6\mu m$, interaction length $L_{int} \sim 15\lambda_o$, and laser intensity from $\mathcal{I}_o = 5 \times 10^{14}$ to 3×10^{16} W/cm^2].

According to their simulations at low laser intensities the SRS reflectivity increases with intensity, and at high laser intensities the reflectivity becomes "temporally spiky and chaotic". Their SRS reflectivity $[\sim O(10^{-3}\%)]$ however, is practically nil, and they do not provide any comparison with experimental observations. Also their simulations are not applicable to the single speckle exp eriments, where the interaction length is $L_{int} \sim 400\lambda_o$.

An alternative approach, also based on the coupled modes equations, was pursued by Chow et al., in 1992 [26]-[29]. Following some numerical investigations of the two-fluid equations for SRS, by Bonnaud et al. [40], Chow, et al., assumed that the large growth rate of LDI (compared to the growth of SRS) produced the rapid saturation of the electron plasma wave that is common to SRS and LDI (EPW). This saturation was considered to occur before the laser pump depleted at all. Considering no wave de-phasing and real wave envelopes, Chow et al., solved the three wave COM equations that correspond to LDI only, considering a growth rate that was estimated from the SRS parametric equations $(\gamma_{_{SRS}} = |K_{_{SRS}}|a_o)$. Including an ad-hoc diffusion term to represent some nonlocal Landau damping, Chow's model for LDI is:

$$\left(\frac{\partial}{\partial t} + v_{g3}\frac{\partial}{\partial x} - \gamma_{_{SRS}}\right)a_3 = -K_{_{LDI}}a_4 a_5 + D\frac{\partial^2}{\partial x^2}a_3, \qquad (3.36)$$

$$\left(\frac{\partial}{\partial t} + v_{g4}\frac{\partial}{\partial x} + \nu_4\right)a_4 = K_{_{LDI}}a_3 a_5, \qquad (3.37)$$

$$\left(\frac{\partial}{\partial t} + v_{g5}\frac{\partial}{\partial x} + \nu_5\right)a_5 = K_{_{LDI}}a_3 a_5, \qquad (3.38)$$

where D is the diffusion coefficient.

For periodic boundary conditions, Chow found that LDI rapidly saturated via *spatio temporal chaos* (STC).[26] Once saturated, the randomized amplitude of the LDI-EPW $[a_3(x,t)]$ was used in the parametric linear equation for the SRS-BEMW (see Chapter 2). The resulting equation was then integrated with the assumption

that the laser amplitude remained essentially unperturbed [$a_1 = a_o$, with a_o the unperturbed laser amplitude]:[29]

$$\left(\frac{\partial}{\partial t} + v_{g2}\frac{\partial}{\partial x}\right)a_2 = K_{SRS}a_o a_3. \tag{3.39}$$

With this approach, the SRS reflectivity was found to scale with the laser intensity, in a manner similar to that observed in some experiments [29, 19, 18]. However, the diffusion term, which was necessary for the model to reach saturation, remained as an unclear parameter. The assumption of a constant growth rate in Eq.(3.34) [which is not consistent with the space/time evolution of the wave amplitudes in SRS], the EPW would cascade to shorter wavelengths, without reaching a steady state. Only with the diffusion term included in Eq. (3.36) the cascading to shorter wavelengths is stopped, and a stable solution found.

In an early stage of my research, I continued Chow's investigation by trying to extend his model to more recent experimental parameters. However, I found that for the recent experiments (in which $k_{EPW}\lambda_{De}$ was smaller), the diffusion coefficient was not large enough to restrict cascading and the growth of short wavelengths. Trying to improve Chow's approach with a better description of the nonlocal Landau damping, I investigated the following model for LDI [30]:

$$\left(\frac{\partial}{\partial t} + v_{g3}\frac{\partial}{\partial x} - \gamma_{Net}\right)a_3 = -K_{LDI}a_4 a_5 + iV\frac{\partial}{\partial x}a_3 + D\frac{\partial^2}{\partial x^2}a_3, \tag{3.40}$$

$$\left(\frac{\partial}{\partial t} + v_{g4}\frac{\partial}{\partial x} + \nu_4\right)a_4 = K_{LDI}a_3 a_5, \tag{3.41}$$

$$\left(\frac{\partial}{\partial t} + v_{g5}\frac{\partial}{\partial x} + \nu_5\right)a_5 = K_{LDI}a_3 a_5, \tag{3.42}$$

where the wave amplitudes (a_3, a_4 and a_5) are complex variables. Considering an expansion of the Landau damping near $k_3 \equiv k_{EPW}$, the nonlocal damping of the electron plasma wave is approximated as [$\nu_3 a_3$] $= -(\nu_{L3} + iV\partial_x + D\partial_x^2)a_3$, with $\nu_{L3} = |\omega_{i3}(k_3)|$, $V = |d\omega_{i3}(k)/dk|_{k_3}$ and $D = |d^2\omega_{i3}(k)/dk^2|_{k_3}$. Considering the

coupling to SRS, the "net growth" of the electron plasma wave was estimated to be: $\gamma_{Net} = (\nu_{L3} - \sqrt{\nu_{L3} - 4\gamma_{SRS}})/2$.

With Equations (3.40)–(3.42), following the same procedure as in [29], I did achieve a steady state for the experimental parameters in [4]. I then found that the variation in the SRS reflectivity due to variations in the damping of ion acoustic waves was qualitatively consistent with experimental observations [30]. However, I could not find a way to verify the conservation of energy in the model equations. The assumption of periodic boundary conditions and a constant laser amplitude ($a_1 = a_o$) were not consistent with experiments.

Motivated by more recent single speckle experiments [6, 13, 12] I decided to pursue a numeric solution of the five-wave coupled mode equations [(3.29)–(3.33)] in a finite extent plasma geometry. The interesting results are discussed in Chapters 4, 5 and 6.

3.4   Discussion

Since the full wave Zakharov equations consider the coupling between all resonant plasma waves, and the COM equations only the coupling between the slowly varying amplitudes of some of these waves, the Zakharov equations are valid for a wider range of parameters. They encompass many nonlinear effects that are not included in the COM formulation, such as: *cascading*, *wave collapse* and *Langmuir turbulence*.

The COM equations can be readily extended to include cascades (see Chapter 6), and allow for an easy understanding and interpretation of the coupling between SRS and LDI. The numerical results can also be readily checked for energy conservation, or to approach analytic solutions (in certain limits). Also, the COM equations lead to The Zakharov equations are only amenable to numerical investigation, and it is difficult to extract the important physics related to the saturation of SRS. The Zakharov model is also far too complex for any analytical analysis.

While the COM equations have been investigated before, in this thesis I present, for the first time, numerical solutions for parameters relevant to recent experiments.

The numerical simulations lead to interesting results regarding to the effects of ion acoustic wave damping, electron plasma wave damping and laser intensity, on the saturation of the SRS backscattering.

Chapter 4

SRS Coupling to LDI

The five wave coupled mode equations describing the coupling of SRS and LDI are studied in this chapter. We consider one dimensional dynamics for backscattering, with a finite region of interaction in a homogeneous plasma. Starting from an estimated initial noise level, the five wave envelopes are evolved numerically in time and space, to find the SRS backscattering. We restrict ourselves to the case of real wave envelopes with no wave de-phasing, to simplify computations. As will be demonstrated, the system exhibits complex dynamics, and reveals the interesting phenomena that is reported in Chapters 4, 5 and 6.

4.1   Five Wave COM Equations

The five waves in the coupling of SRS and LDI, and their cold plasma dispersion relations are: 1) the electromagnetic plasma wave externally excited by the laser $[\omega_1^2 = \omega_{pe}^2 + c^2 k_1^2]$, 2) the backscattered electromagnetic wave $[\omega_2^2 = \omega_{pe}^2 + c^2 k_2^2]$, 3) the electron plasma wave shared by SRS and LDI, $[\omega_3^2 = \omega_{pe}^2 + 3v_{Te}^2 k_3^2]$, 4) the backscattered electron plasma wave $[\omega_4^2 = \omega_{pe}^2 + 3v_{Te}^2 k_4^2]$, and 5) the LDI ion acoustic wave $[\omega_5^2 = c_a^2 k_5^2]$.

The real frequencies and wave numbers satisfy the phase matching conditions: $\omega_1 = \omega_2 + \omega_3$, $k_1 = k_2 + k_3$, $\omega_3 = \omega_4 + \omega_5$, and $k_3 = k_4 + k_5$. Such frequencies and wavenumbers are illustrated in Fig. (1-3), where the abbreviations BEMW, EPW,

BEPW and IAW, stand for the SRS backscattered electromagnetic wave, the SRS electron plasma wave, the LDI backscattered electron plasma wave, and the LDI excited ion acoustic wave, respectively. For convenience, the pump electromagnetic wave, externally excited by the laser, is referred to as the "LASER".

For one dimensional dynamics, with no wave de-phasing and real wave amplitudes, the five wave coupled mode equations [Eqs. (3.29)–(3.33)] reduce to:

$$\left(\frac{\partial}{\partial t} + v_{g1}\frac{\partial}{\partial x} + \nu_1\right) a_1 = -|K_{SRS}|a_2 a_3, \tag{4.1}$$

$$\left(\frac{\partial}{\partial t} + v_{g2}\frac{\partial}{\partial x} + \nu_2\right) a_2 = |K_{SRS}|a_1 a_3, \tag{4.2}$$

$$\left(\frac{\partial}{\partial t} + v_{g3}\frac{\partial}{\partial x} + \nu_3\right) a_3 = |K_{SRS}|a_1 a_2 - |K_{LDI}|a_4 a_5, \tag{4.3}$$

$$\left(\frac{\partial}{\partial t} + v_{g4}\frac{\partial}{\partial x} + \nu_4\right) a_4 = |K_{LDI}|a_3 a_5, \tag{4.4}$$

$$\left(\frac{\partial}{\partial t} + v_{g5}\frac{\partial}{\partial x} + \nu_5\right) a_5 = |K_{LDI}|a_3 a_4, \tag{4.5}$$

where $|a_\ell|^2 = w_\ell/\omega_\ell$, w_ℓ, $v_{g\ell}$ and ν_ℓ are the wave action density, wave energy density, group velocity and damping, respectively, of the ℓ_{th} mode. The subscripts $\ell = 1, 2,$ 3, 4, 5 represent the LASER, BEMW, EPW, BEPW and IAW, respectively.

Assuming a conservative coupling system, as in Section B.5, the coupling coefficients are (Appendices A and B):

$$|K_{SRS}| \approx \sqrt{\frac{2}{\epsilon_o}}\frac{e}{m_e}\frac{k_3}{4}\left(\frac{\omega_{pe}^2}{\omega_1\omega_2\omega_3}\right)^{1/2}, \tag{4.6}$$

$$|K_{LDI}| \approx \sqrt{\frac{2}{\epsilon_o}}\frac{e}{m_e}\frac{\omega_{pe}}{4v_{Te}}\left(\frac{\omega_5}{\omega_3\omega_4}\right)^{1/2}. \tag{4.7}$$

The parametric growth-rates are: $\gamma_{SRS} = |K_{SRS}|a_1 = (k_3 v_{o1}/4)\sqrt{\omega_3/\omega_2}$ and $\gamma_{LDI} = |K_{LDI}|a_3 = (k_5 v_{o3}/4)\sqrt{\omega_5/\omega_4}$, where $|v_{o\ell}| = e|E_\ell|/m_e\omega_\ell$ is the electron quiver velocity in the field of the ℓ_{th} mode.

Using an approach similar to that in Chapter 2 for the 3WI, the following conservation relations can be derived from Eqs. (4.1)–(4.5):

$$I_2 = -\frac{\omega_2}{\omega_1}I_1, \tag{4.8}$$

$$I_5 = \frac{\omega_5}{\omega_4}I_4, \tag{4.9}$$

$$I_3 = -\frac{\omega_3}{\omega_1}I_1 - \frac{\omega_3}{\omega_5}I_5, \tag{4.10}$$

where I_ℓ, for $\ell = 1...5$, is given by:

$$I_\ell = \left[\int_0^L \mathrm{w}_\ell(t', x)dx\right]_{t'=t} - \left[\int_0^L \mathrm{w}_\ell(t', x)dx\right]_{t'=0} + 2\nu_\ell \int_0^t dt' \int_0^L dx\mathrm{w}_\ell(t', x)$$
$$+ v_{g\ell}\int_0^t dt'\left[\mathrm{w}_\ell(t', x = L) - \mathrm{w}_\ell(t', x = 0)\right]. \tag{4.11}$$

The Manley-Rowe relations for the total time variation of the wave energy densities along their characteristics are:

$$\frac{\dot{W}_1}{\omega_1} = -\frac{\dot{W}_2}{\omega_2}, \tag{4.12}$$

$$\frac{\dot{W}_4}{\omega_4} = \frac{\dot{W}_5}{\omega_5}, \tag{4.13}$$

$$\frac{\dot{W}_1}{\omega_1} = -\frac{\dot{W}_3}{\omega_3} - \frac{\dot{W}_5}{\omega_5}; \tag{4.14}$$

where $\dot{W}_\ell = (\partial_t + v_{g\ell}\partial_x + 2\nu_\ell)\,\mathrm{w}_\ell$.

The energy conservation relations are used as a check of the numerical results. As described in Appendix C, the error in the conservation of the total energy [Eqs.(C.10)–(C.14)] was calculated during numerical simulations, at every time step.

4.2   Experimental Parameters and Normalization

We consider recent experiments carried at Los Alamos National Laboratory [6], where the SRS backscattering from a *single speckle interaction* was investigated. In these experiments a plastic foil was initialy blasted with an intense laser pulse (incident
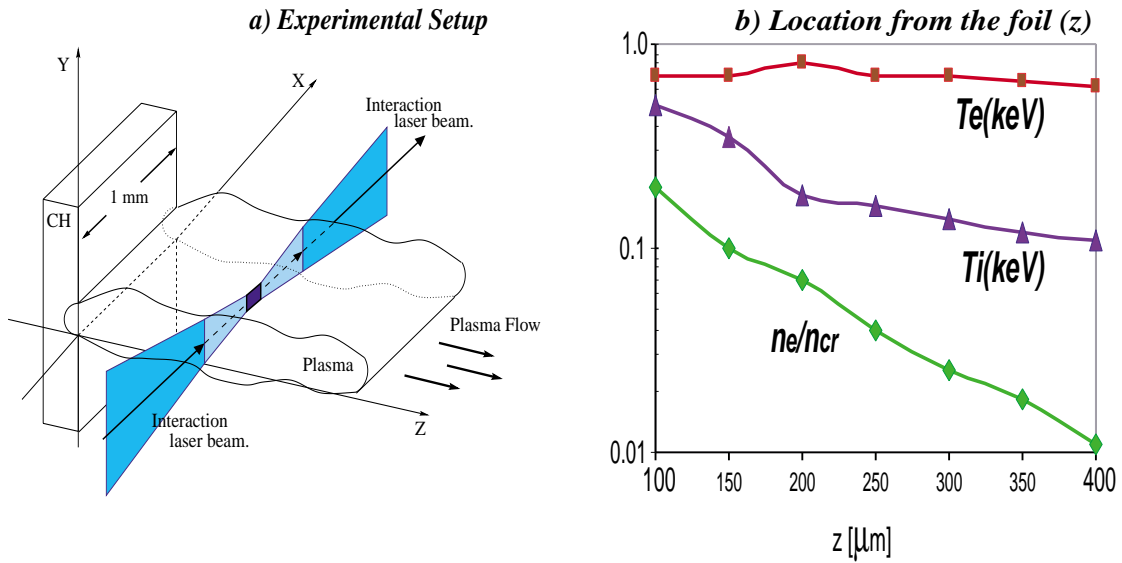
Figure 4-1: Single hot-spot experiments [6]: a) experimental setup and b) measured plasma characteristics. Laser wavelength $\lambda_o = 527\ nm$ and best focus intensity $\mathcal{I}_o \sim 10^{15}\ Watts/cm^2$.

in the $-z$ direction), to create an ICF characteristic plasma. Once the *formation beam* was turned off, and the plasma created, a second laser pulse (the *interaction beam*) was focused into the formed plasma to study SRS. Figure (4-1.a) illustrates the interaction beam only, propagating across the direction of plasma flow. As illustrated, the interaction beam was carefully focused (diffraction limited) to a small region in the plasma, to create an interaction "*hot spot*", or equivalently, a "*single speckle*" interaction region. The hot-spot, where the plasma density and the field intensity can be taken as homogeneous, is illustrated in Figure (4-1.a) using a dark square in the center of the plasma.

The wavelength and duration of the interaction beam are $\lambda_o = 0.527\mu m$ and $T_o \sim 1nsec$, respectively. Considering a diffraction limited Gaussian beam with an $f8$ focal lens, the length of the hot-spot is $L \approx 8f^2\lambda_o \approx 225\mu m$, and the width $F\lambda_o \approx 4\mu m$ [6].

In a series of experiments the interaction beam was pointed at different distances away from the plastic foil (different points in $\hat{z}$) to investigate the SRS backscattering

60

induced in different regimes.[6] In Figure (4-1.b) the electron density is always below one quarter of the critical density $[n_{cr} = n_e\omega_1^2/\omega_{pe}^2 \sim 10^{27}m^{-3}]$, which is a necessary requirement for SRS to be excited (see Chapter 1). The electron temperature is approximately $700eV$ and the ion temperature ranges between $T_i \approx 100eV$ to $T_i \approx 500eV$, and the electron plasma angular frequency (ω_{pe})is in the range of 5×10^{14} to 8×10^{14} rad/sec.

The experimentally observed SRS backscattering is illustrated in Figure (1-4.b), which shows a collection of data from various similar experiments with different laser intensities. Presumably when the laser intensity is above a certain level, the SRS reflectivity saturates independently of the laser intensity [7]. The investigation of such probable saturation of the SRS backscattering with laser intensity ($\mathcal{I}_o$) is discussed in Chapter 5. Meanwhile, a typical best focus laser intensity of $\mathcal{I}_o = 6\times10^{15}[Watts/cm^2]$ (see [6]) is taken to investigate the dependence of the SRS backscattering on the electron plasma density.

The real frequencies of the electromagnetic waves (ω_{1r} and ω_{2r}), normalized to the plasma frequency, are shown in Table (4.1). A necessary condition for SRS to take place is that $\omega_1 > 2\omega_{pe}$. On the other hand, $\omega_2 > 2\omega_{pe}$ not only indicates the low density (relative to critical) of the plasma, but also satisfies the condition for further nonlinear SRS cascade (exciting a forward propagating electromagnetic wave and a backscattered electron plasma wave). The SRS cascading is discussed in Chapter 6.

As explained in Chapter 2, the dampings of the longitudinal waves need to be estimated from the kinetic dispersion relation (Eq. 2.33). Considering a charge neutral plasma with three charged species in thermal equilibrium [electrons, hydrogen ions and carbon ions], Equation (2.33) was used to calculate the real frequency and the Landau damping associated to the real wavenumber (k_r), for each longitudinal mode. The calculated real frequency was compared within 5% of the frequency obtained from the cold plasma dispersion relation. The Landau damping frequency is found to be much smaller than the real frequency, so that we can assume slowly varying amplitude approximation explained in Chapter 2.

z [μm]	n_e/n_{cr}	ω_{1r}/ω_{pe}	ω_{2r}/ω_{pe}	$k_3\lambda_{De}$	ω_{3i}/ω_{3r}	ω_{4i}/ω_{4r}	ω_{5i}/ω_{5r}	ω_b/ω_{pe}
230	0.05	4.47	3.35	0.283	0.0072	0.004	0.359	0.69
240	0.043	4.82	3.68	0.308	0.013	0.009	0.359	0.725
250	0.04	5	3.85	0.319	0.017	0.012	0.359	0.74
260	0.036	5.27	4.11	0.339	0.024	0.018	0.359	0.76
270	0.033	5.5	4.32	0.356	0.032	0.024	0.359	0.78
280	0.03	5.77	4.58	0.375	0.041	0.033	0.359	0.8
290	0.027	6.08	4.47	0.398	0.053	0.044	0.359	0.832
300	0.025	6.32	5.09	0.416	0.064	0.053	0.359	0.84
310	0.023	6.59	5.34	0.435	0.075	0.064	0.359	0.86
370	0.015	8.16	6.78	0.548	0.149	0.135	0.359	0.95

Table 4.1: Plasma parameters in single hot-spot experiments for $\lambda_o = 527\ nm$, $\mathcal{I}_o = 6 \times 10^{15}\ Watts/cm^2$, $T_e \approx 700eV$, n_e/n_{cr} ranging from 0.015 to 0.05, and T_i ranging from 117 to 165 eV.

Table (4.1) shows the calculated EPW wavenumbers $k_3\lambda_{De}$, which can be compared to the ones provided in Figure (1-4.b) to notice the discrepancy that results from the uncertain experimental data (T_e for example). An idea of the possible error in the Landau damping due to variations in $k\lambda_{De}$, particle temperature ratios (T_i/T_e), or even in the particle species concentrations, can be obtained from the Figures (2-4) and (2-5).

At sufficient EPW amplitudes (a_3, a_4), the resonant wave-particle interactions can lead to the nonlinear phenomenon of *electron trapping* [48]. In such case, electrons with velocity $w \approx v_p$ (where v_p is the phase velocity) bounce around in the potentials of the wave, with a characteristic *bounce frequency* ω_b given by:

$$\omega_b = \left(\frac{e}{m_e} k_3 E_3 \right)^{1/2}. \tag{4.15}$$

Considering the Manley-Rowe relations [Eq. (2.22) in particular], the bounce frequencies for the extreme case of $E_3 = (\omega_3/\omega_1)^{1/2} E_o$ and E_o the unperturbed amplitude of the laser, are shown in Table (4.1). In such extreme case the electron bounce frequencies scale with the EPW frequency $\omega_3 \approx \omega_{pe}$. Therefore, electron trapping could lead to a frequency shift of the waves [69, 70] and a possible modification of the

Parameter	Symbol	Dimensions	Normalization
Time	t	$[sec]$	$\gamma_b t$
Space	x	$[m]$	$\gamma_b x/v_{g3}$
Field amplitudes	a_ℓ	$[(J \cdot sec/m^3)^{1/2}]$	a_ℓ/a_o
Group velocities	$v_{g\ell}$	$[m/sec]$	$v_{g\ell}/v_{g3}$
Damping rates	ν_ℓ	$[rad/sec]$	ν_ℓ/γ_b
SRS Coupling	$|K_{SRS}|$	$[(J \cdot sec/m^3)^{-1/2}/sec]$	$G = |K_{SRS}|/|K_{LDI}|$
LDI coupling	$|K_{LDI}|$	$[(J \cdot sec/m^3)^{-1/2}/sec]$	1

Table 4.2: Table of normalizations

Landau damping, even if the EPW phase velocity is large compared to the thermal velocity $v_{p3}/v_{Te} = (\omega_3/\omega_{pe})(k_3\lambda_{De})^{-1} \approx (k_3\lambda_{De})^{-1} \gg 1$ (i.e., only few electrons are trapped). The effects of wave-particle interactions require further investigation, and are left as a problem for the future.

The 5COM equations are normalized as described in Table (4.2), where $\gamma_b = |K_{LDI}|a_o$ has been taken as an estimation of the fastest growth rate in the system ($\gamma_b > \gamma_{LDI} > \gamma_{SRS}$). The normalized group velocities are $v_{g1} \approx -v_{g2} \approx 30$, $v_{g3} \approx -v_{g4} \approx 1$ and $v_{g5} \approx 0$. The normalized 5COM equations, with boundary conditions at $x = -L/2$ and $x = L/2$, are:

$$\left(\frac{\partial}{\partial t} + 30\frac{\partial}{\partial x}\right) a_1 = -Ga_2 a_3, \tag{4.16}$$

$$\left(\frac{\partial}{\partial t} - 30\frac{\partial}{\partial x}\right) a_2 = Ga_1 a_3, \tag{4.17}$$

$$\left(\frac{\partial}{\partial t} + \frac{\partial}{\partial x} + \nu_3\right) a_3 = Ga_1 a_2 - a_4 a_5, \tag{4.18}$$

$$\left(\frac{\partial}{\partial t} - \frac{\partial}{\partial x} + \nu_4\right) a_4 = a_3 a_5, \tag{4.19}$$

$$\left(\frac{\partial}{\partial t} + \nu_5\right) a_5 = a_3 a_4; \tag{4.20}$$

where the small collisional damping of electromagnetic waves has been neglected.

This damping is given by $\nu_{1,2} = \omega_{pe}^2/\omega_{1,2}^2\nu_{ei}$ [47], where ν_{ei} is the electron-ion

z [μm]	n_e/n_{cr}	$k_3\lambda_{De}$	γ_b/ω_{pe}	ν_1	ν_2	ν_3	ν_4	ν_5	G
230	0.05	0.283	0.055	0.226	0.127	0.146	0.0816	0.0792	0.619
240	0.043	0.308	0.0599	0.229	0.134	0.257	0.165	0.081	0.5882
250	0.04	0.319	0.062	0.233	0.139	0.314	0.21	0.082	0.5724
260	0.036	0.339	0.066	0.234	0.142	0.433	0.311	0.082	0.5535
270	0.033	0.356	0.069	0.235	0.145	0.547	0.411	0.082	0.5389
280	0.03	0.375	0.0724	0.236	0.148	0.685	0.535	0.082	0.5228
290	0.027	0.398	0.0765	0.237	0.152	0.851	0.687	0.082	0.5046
300	0.025	0.416	0.079	0.238	0.154	0.98	0.808	0.082	0.4915
310	0.023	0.435	0.083	0.238	0.156	1.13	0.949	0.082	0.478
370	0.015	0.548	0.099	0.244	0.169	1.99	1.78	0.082	0.4117

Table 4.3: Normalized parameters used in the numerical simulations. Laser wavelength $\lambda_o = 527\ nm$ and best focus intensity $\mathcal{I}_o = 6 \times 10^{15}\ Watts/cm^2$.

collisional frequency:

$$\nu_{ei} \approx 2 \times 10^{-6} \frac{Z n_{eo} ln\Lambda}{T_{eV}^{3/2}}, \qquad (4.21)$$

with $\Lambda \equiv \lambda_{De}/r_o$ and $r_o = (e^2/4\pi\epsilon_o\kappa Te)$. The normalized collisional dampings $(\nu_{1,2}/\gamma_b)$ are shown in Table (4.3).

For laser intensity of $\mathcal{I}_o = 6 \times 10^{15}[Watts/cm^2]$, one picosecond of real time corresponds to approximately 44 normalized time units (NtU), and one micro meter correspond to about four normalized space units (NxU). The normalized length of the hot-spot is $\approx 900NxU$ and the time for the laser to transit through the hot-spot is $\approx 30NtU$. The normalized growth and dampings are shown in Table (4-3).

From Table (4-3), we note the normalized damping of the ion acoustic wave (ν_5) and the growth rate (G) are almost constant. The dampings of electron plasma waves (ν_3 and ν_4), on the other hand, change by approximately one order of magnitude. The normalized parameter γ_b is much smaller than the plasma frequency ($\omega_{pe} \sim 10^{14}$ rad/sec), and the normalized SRS growth rate (G) is much smaller than the SRS frequencies (ω_1, ω_2 and ω_3). This scalings are consistent with the slowly varying amplitude approximation.

4.3 Space-Time Evolution ($k\lambda_{De} = 0.319$)

We study the simulations for a plasma with $n_e/n_{cr} = 0.04$ ($k\lambda_{De} = 0.319$). For this case, $z = 250 \ \mu m$, the normalized growth rate and damping coefficients are $G \approx 0.6$, $\nu_3 \approx 0.3$, $\nu_4 \approx 0.2$ and $\nu_5 \approx 0.08$ (Table 4.3).

The numerical results are obtained with two different numerical techniques. One is based on the method of characteristics [72] and the other on the Lax-Wendroff integration scheme [73]. Since both techniques give almost identical results (Appendix C) no further distinction of the results from the two methods is made.

In the numerical evolution of the wave envelopes, we need to specify the initial and boundary conditions, for the wave amplitudes. To this purpose, we set the initial amplitudes (at $t = 0$) to an estimated noise level. The boundary conditions of all waves (except for the laser) are also set to the estimated amplitude of the noise. While the initial noise level is not known from experiments, we estimated it considering that the spatial amplification in the strong damping limit is very small. In such case, the initial noise amplitude was chosen to be 0.0005 (normalized amplitude units), so the numerical simulations of the reflectivity with $n_e/n_{cr} = 0.015$ (strongest damping limit) approximately matched the experimental observations [the first point, $n_e/n_{cr} = 0.015$, in Figure (1-4.b)]. The exact same noise level was taken in following simulations; because a primary objective of this work was to investigate the effects of Landau damping on the SRS. A discussion on the effects of the noise amplitude on the saturated SRS reflectivity is given in Chapter 5 (Section 5.2).

Figure (4-2) illustrates the interaction region, the initial and boundary conditions, and the direction of propagation of the wave envelopes. The $900NxU$ finite region of interaction is set to span from $x = -450$ to $x = 450 \ NxU$. The boundary conditions for the positive group velocity waves are set at $x = -450$, and for the negative group velocity waves at $x = 450$. All the boundary conditions are set to the estimated noise level except for the laser, which is set to $a_1(x = -450, t) = 1$. The boundary conditions are illustrated with circles in the figure. [1]

---

[1]For convenience, even though the plasma is much larger than the region of interaction (see
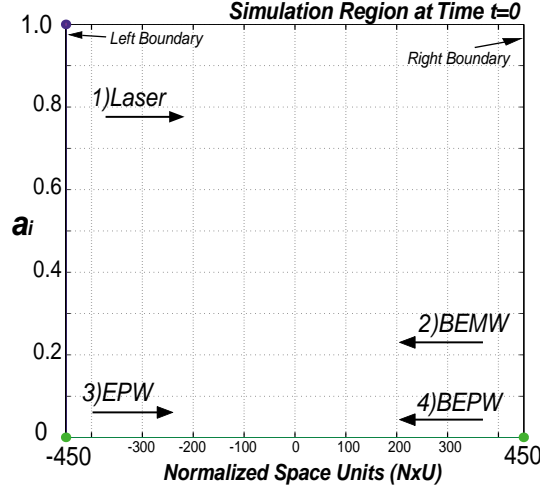
Figure 4-2: Interaction region, initial condition and boundary conditions.

The wave amplitudes are evolved in time for about $1500NtU \approx 35psec$ till a saturated steady state is observed. This time is shorter than the experimental duration of the pulse, and larger than the laser transit time $(30NtU)$ and the electron plasma period $(T_{pe} = 2\pi/\omega_{pe} = 0.39NtU)$. If the coupling coefficients were set to zero, the space/time evolution of the wave envelopes would only exhibit the propagation of the boundary conditions through the plasma (with their corresponding group velocities). However, when the coupling is non zero, the energy of the laser couples to the BEMW and EPW waves, leading to SRS. As time increases, the BEMW and EPW amplitudes grow from their initial noise levels in localized regions of the plasma, in which the laser envelope locally depletes. When the amplitude of the EPW (a_3) reaches the LDI threshold for instability $(LDI_{th} = \sqrt{\nu_4 \nu_5})$, the LDI daughters are also excited. The LDI interactions occur only in that region of the plasma where the amplitude of the EPW exceeds the LDI threshold. This in turn produce a local depletion of the EPW, leading to a transitory regime that exhibits oscillations in time and space, and eventually settles to a steady state (in about $500NtU$). To illustrate the above sequence of events, Figure (4-3) shows the field amplitudes within the plasma, at various instances of time.

At time $t = 24$ NtU, shown in Figure (4-3.a), the edge of the laser pulse has

Figure 4-1.a), from here on we refer to the interaction region as "the plasma".

not reached the other boundary (the transit time is 30 NtU). The laser amplitude exhibits a small depletion localized near the left boundary, where the amplitude of the SRS daughter waves is significantly above noise.

At $t = 36NtU$, when the laser has transitted the plasma, see Figure (4-3.b), the laser depletion has become very significant. Near the left boundary ($x = -450$), the SRS daughter waves have large amplitudes that produce the rapid depletion of the laser. This depletion contributes to the localization of the strongest SRS interactions to a narrow region near the left boundary ($x = -450$) where the EPW has the largest amplitude. The LDI daughters have also grown to amplitudes that are now observable.

It is important to remember that the squared amplitudes of the waves (a_ℓ^2) measure the wave action densities $w_\ell = |a_\ell|^2/\omega_\ell$ $[J/m^3]$. Therefore, while the amplitude of the longitudinal plasma wave is large, relative to the amplitude of the laser, the wave energy density of the waves is smaller than that of the laser. The reason for this, is that the laser frequency is much larger than the frequency of the electrostatic wave.

As time continues the five wave interactions remain localized near the left boundary. When the LDI daughters grow to a sufficiently large amplitude, thereby weakening the SRS interaction ($|K_{SRS}|a_2a_3$ in Eq. 4.1, and $|K_{SRS}|a_1a_3$ in Eq. 4.2). Then the laser amplitude recovers once again. The local depletion of the EPW also produces a localized reduction of the parametric LDI growth rate. Then, a_4 and a_5 start to decay in time (in the regions where a_3 has been depleted). This happens because the weakened nonlinear LDI interaction [$K_{LDI}a_3a_5$ in Eq.(4.4) and $K_{LDI}a_3a_4$ in (4.5)] cannot sustain the growth of the heavily Landau damped LDI daughter waves.

In this fashion a transitory stage is established [see Figs. (4-3.c) – (4-3.f)]. SRS produces the localized growth of the EPW, which then excites LDI. This leads to the depletion of the EPW. The competition between SRS and LDI, and the space–time evolution of the wave envelopes, lead to the localized space/time oscillations near the left boundary, that are observed in Figure (4-3.c) [at time $t = 50$ NtU]. The numerical simulations show that the system eventually reaches a steady state illustrated in Figure (4-4).
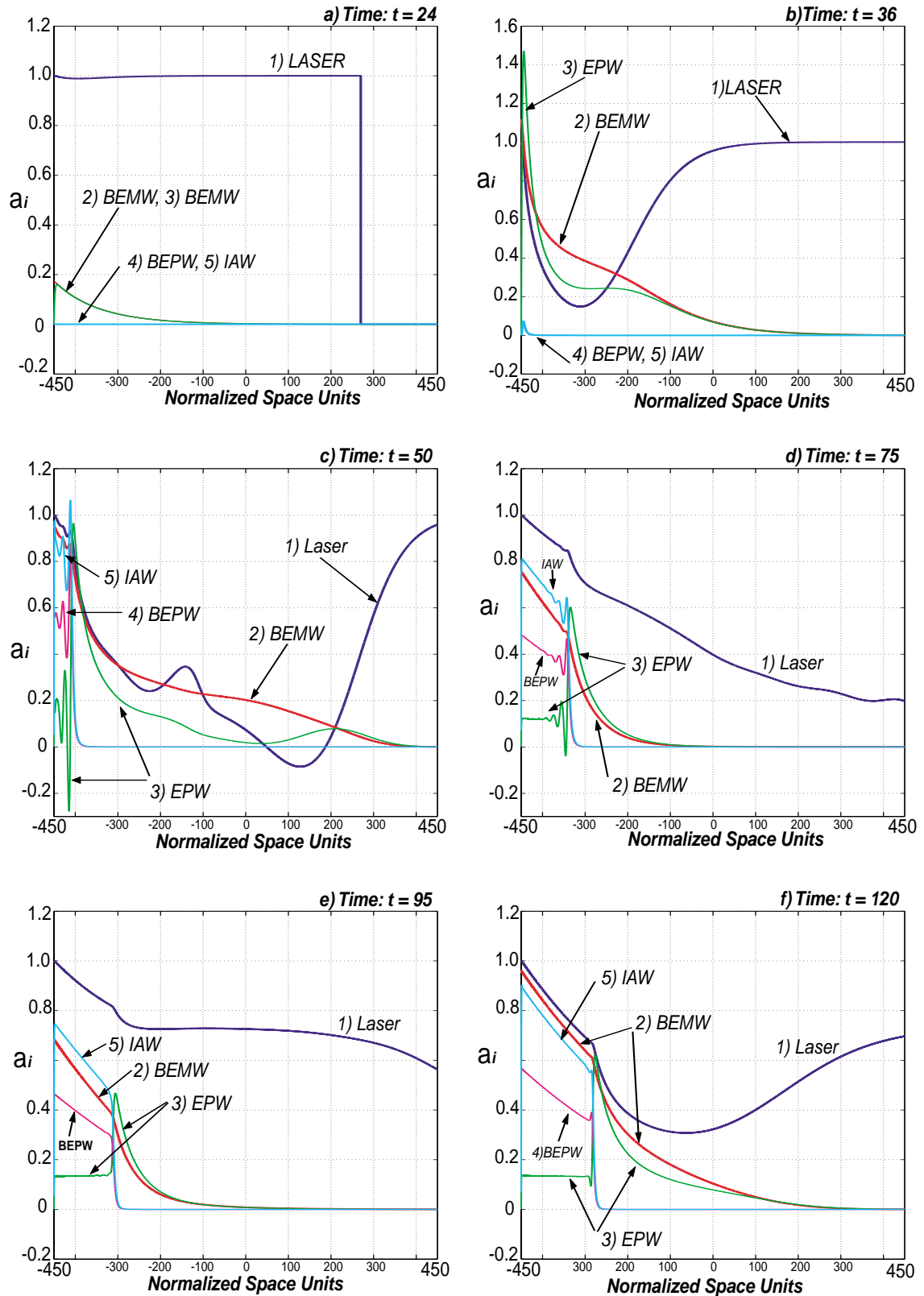
Figure 4-3: Early space-time evolution of the field amplitudes, for $k\lambda_{De} = 0.319$ ($z = 250 \ \mu m$, $n_e/n_{cr} = 0.04$, $T_e = 700eV$ and $T_i = 160eV$).
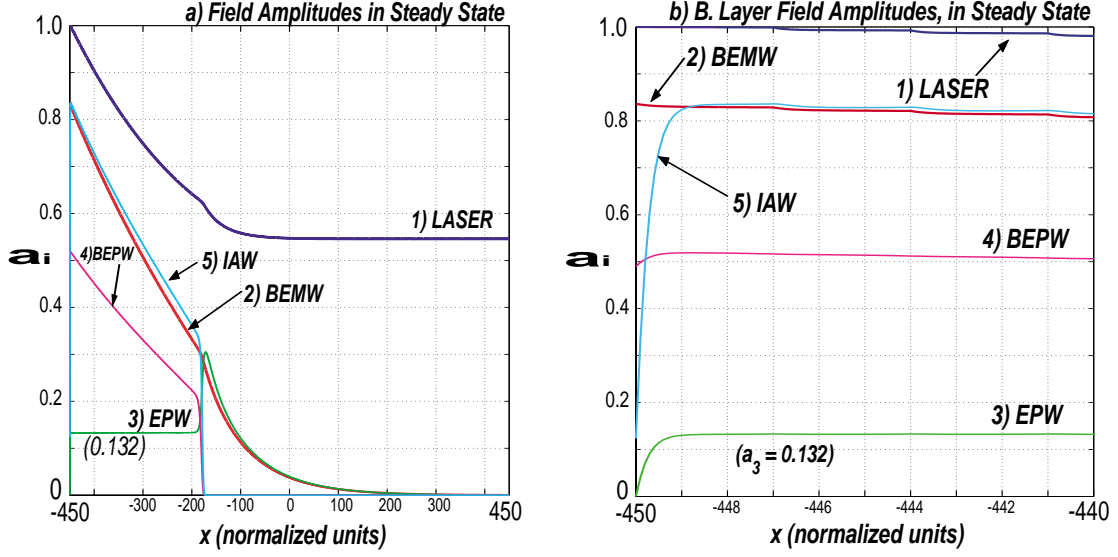
Figure 4-4: Field amplitudes in steady state for $k\lambda_{De} = 0.319$ ($z = 250\ \mu m$, $n_e/n_{cr} = 0.04$, $T_e = 700eV$ and $T_i = 160eV$). Laser intensity $\mathcal{I}_o = 6 \times 10^{15}\ Watts/cm^2$ and wavelength $\lambda_o = 527\ nm$.

Five Wave Steady State Solution

While the steady state in Figure (4-4) is established within $t \sim 500NtU \approx 10psec$, the numerical simulations were continued until $t \sim 1500NtU$ to make certain that the wave envelopes do not evolve further in time. In the steady state the nonlinear interaction between the five waves in SRS and LDI remains localized near the left boundary. In this region, the amplitude of the EPW is fixed at an amplitude which is slightly above the LDI threshold for instability ($a_3 = \sqrt{\nu_4\nu_5} = 0.132$).

The steady state exhibits four characteristic regions: (1) a boundary layer, shown in detail in Figure 4-4.b, (2) a region where the five wave interactions of SRS coupled to LDI occur $[-448 < x < -180]$, (3) a transition region $[-180 < x < -120]$, and (4) a region where SRS is independent of LDI because the EPW amplitude is below the LDI threshold condition $[x > -120]$.

In order to understand the steady state, it is convenient to look at the spatial variation of the EPW amplitude from the right boundary to the left. The EPW propagates from left to right, and its group velocity is relatively small (by a factor of 30) compared to the electromagnetic waves. Therefore, it grows locally according to

the amplitude of the BEMW, which grows from right to left as it propagates through the plasma.

Starting from a small amplitude at $x = 450 NxU$, the EPW exhibits a spatial growth towards the left. While $a_3(x)$ is below the LDI threshold condition $[x > -120]$, SRS is completely independent of LDI. In such region, the amplitude of the laser remains almost constant and the SRS daughters grow to the left with the SRS parametric growth rate (see Chapter 2). Considering that $a_3(x) = a_3(x = 450)exp[\Gamma_s(450 - x)]$, the EPW reaches the LDI threshold $[a_3(x_p) = \sqrt{\nu_4 \nu_5}]$ at $x = x_p$:

$$x_p = 450 - \frac{1}{|\Gamma_s|} ln \left(\frac{\sqrt{\nu_4 \nu_5}}{a_3(x = 450)} \right), \tag{4.22}$$

where the spatial SRS parametric growth rate Γ_s is given by [49]:

$$\Gamma_s = -\frac{\nu_3}{2} \pm \frac{1}{2} \left(\nu_3^2 + 4\frac{|Ga_1|^2}{|v_{g2}|} \right)^{1/2}. \tag{4.23}$$

For a saturated laser amplitude $a_1 \approx 0.55$ and $a_3(x = 450) = 0.00033$ [as obtained numerically], and $|\Gamma_s| = 0.011$ the EPW reaches the LDI threshold at $x_p \approx -150$ NxU, which approximately matches the numerical result. The nonlinear interactions between the five waves in SRS and LDI are localized to the left of this point.

A transitory region in $-180 < x < -150$ NxU is observed first. In this region the amplitudes of the LDI daughters (a_4, a_5) are not large enough to modify the EPW growth, which is sustained by SRS. Therefore, a_3 continues growing to the left until it suddenly depletes at $x \approx -180$. The rapid depletion observed at $x = -180$ NxU suggests an internal boundary layer, due to the transition from 3COM to 5COM.

In $-448 < x < -180$ NxU, the full interaction between the five waves in SRS and LDI is very clear. The amplitude of the EPW saturates slightly above the threshold for the LDI instability, at the equilibrium point between the growth induced by SRS and the nonlinear effective damping due to LDI. If this equilibrium is slightly perturbed increasing the amplitude of a_3, the LDI daughters (a_4 and a_5) grow and bring a_3 back to the equilibrium. If a_3 is instead reduced, it becomes independent of a_4 and a_5,

70

and the interaction with a_2 and a_1 (in SRS) would produce its growth to eventually return it to the equilibrium point.

In steady state ($\partial/\partial t \to 0$), when $a_3 \approx \sqrt{\nu_4 \nu_5}$ Equations (4.19) and (4.20) give:

$$a_5(x) = \frac{a_3}{\nu_5} a_4(x) \approx \sqrt{\frac{\nu_4}{\nu_5}} a_4(x). \tag{4.24}$$

This condition has been verified in our numerical simulations, in the regions where a_3 saturates at the LDI threshold.

The boundary layer shown in detail in Figure (4-4.b) results from the boundary condition that is imposed to a_3 at $x = -450$, the small EPW group velocity $|v_{g3}|$ (relative to $|v_{g2}|$) and the discontinuity of K_{SRS} at the left boundary [$K_{SRS}(x < -450) = 0$ and $K_{SRS}(x > -450) \neq 0$]. In the boundary layer the amplitude of the EPW grows from the boundary condition as it propagates into the plasma, until it catches up with the saturated amplitude that is imposed by the interactions in SRS and LDI.

Time evolution of the SRS reflectivity

The time evolution of the field amplitudes at the boundaries and the SRS reflectivity are illustrated in Figure (4-5). At the left boundary ($x = -450$), shown in the upper plot of Figure (4-5.a), the laser amplitude remains constant at its boundary condition. The amplitude of the BEMW, on the other hand, grows from the initial noise level until it clearly saturates at $t \approx 500$ NtU ($\sim 10psec$). The transitory oscillations that are observed before the saturation have a periodicity of $\sim 71 NtU$, which is a slow variation compared to the periodicity of the BEMW ($2\pi/\omega_2 \sim 1.6 NtU$). For clarity purposes the amplitude of the BEPW (a_4) is not plotted and the other wave amplitudes remain fixed at 0.0005 (their boundary condition).

At the right boundary ($x = 450$), shown in the lower plot of Figure (4-5.a), all the wave amplitudes remain at the noise level, except for the laser. This can also be observed in Figures (4-3) and (4-4.a). The laser amplitude is zero until $t = 30 NtU$, which is the laser transit time. After such time, the laser amplitude shows transitory
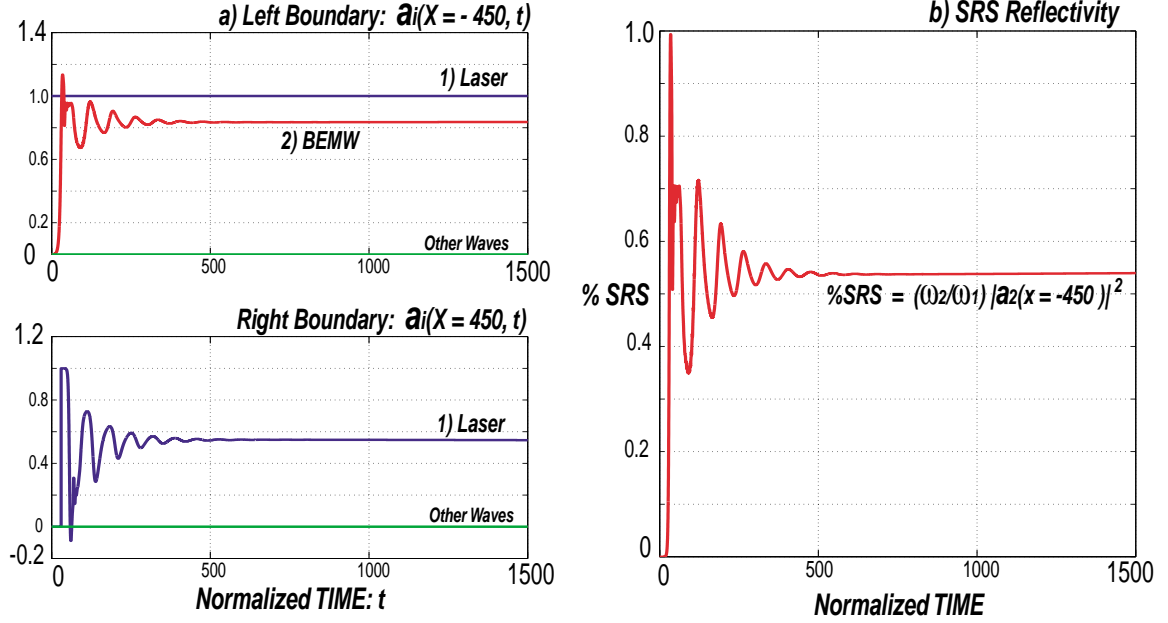
Figure 4-5: Wave amplitudes at the two boundaries and SRS reflectivity for $k\lambda_{De} = 0.319$ ($n_e/n_{cr} = 0.04$, $T_e = 700eV$ and $T_i = 160eV$). Laser intensity $\mathcal{I}_o = 6 \times 10^{15}$ $Watts/cm^2$ and wavelength $\lambda_o = 527\ nm$.

oscillations that eventually lead to a saturated state. A closer look shows that the growing a_2, in the upper plot, corresponds to a decaying a_1 in the lower plot (shifted by $\sim 25\ NtU$ which is approximately the laser transit time). The negative value of a_1 at $t \sim 60\ NtU$ (lower plot in Figure 4-5.a) implies that the laser changes its phase by 180 degrees.

Figure (4-5.b) shows the total SRS backscattering as a function of time:

$$SRS_r(t) = \frac{s_2}{s_1} = \frac{|v_{g2}|w_2}{|v_{g1}|w_1} \approx \frac{\omega_2|a_2(x=-450,t)|^2}{\omega_1|a_1(x=-450,t)|^2} = \frac{\omega_2}{\omega_1}|a_2(x=-450,t)|^2, \quad (4.25)$$

where s_ℓ is the wave energy flow density, w_ℓ the wave energy density, $a_1(x=-450) = 1$ is laser amplitude at the left boundary, and $v_{g2} = -v_{g1}$ are the EM wave group velocities.

For $\omega_2/\omega_1 \approx 0.77$, the SRS backscattering saturates at $\approx 50\%$. The saturated numerical reflectivity is larger than the experimental observations ($\sim 5\%$). This difference, however, is discussed later in this chapter.

ERROR in Energy Conservation

$I_2/\omega_2 + I_1/\omega_1$

$I_5/\omega_5 + I_3/\omega_3 + I_1/\omega_1$

$I_4/\omega_4 + I_5/\omega_5$

Normalized Time
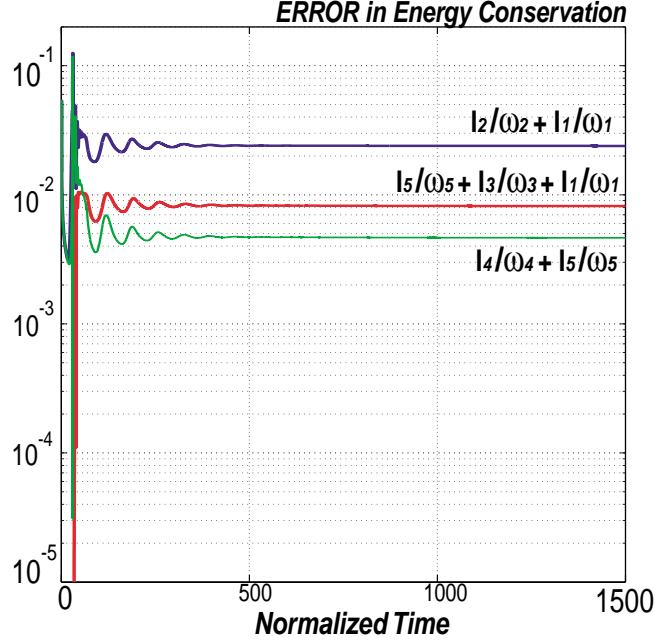
Figure 4-6: Calculated error in the total energy conservation [Eqs. (C.10)–(C.14)].

Error in the Conservation of Energy

The calculated error as a function of time, defined in Appendix C [Eqs. (C.10)–(C.15)], is shown in Figure (4.6) as a function of time. This error, combines the numerical errors due to the evolution of the wave envelopes and due to the evaluation of the integrals in the conservation relations (Eqs. 4.12 - 4.14). The error is found to be smaller than $\sim 10^{-2}$.

The error can be compared with the total amount of energy that is supplied to the system during each time step (E_{step}). Considering a constant cross section of area $A = 1$ (as explained in Section 2-3), such energy is calculated as $E_{step} \sim s_o \Delta x \Delta t$, with s_o being the unperturbed laser energy flow density: $s_o = v_{g1} \mathrm{w}_o = v_{g1} \omega_1 |a_o|^2$.

With $\Delta t = \Delta x = 0.1$ (as in the simulations), $E_{step} = 0.3$ and the numeric error of $O(10^{-2})$ can be taken as small. A glitch of amplitude 0.15 can be observed at $t = 30$, corresponding to the maximum possible error that is obtained with the trapezoidal rule of integration (when the laser front reaches the right boundary).

4.4 Other regimes of $k\lambda_{De}$ (n_e/n_{cr}, T_e and T_i)

For all of the parameters in Table (4.3), the early space/time evolution is found to be similar to the one detailed in Section 4.3; therefore, it is not described further. However, the final saturated state is found to evolve to one of three different states. This final states can be classified as: (1) strong, (2) intermediate and (3) weak EPW damping. For $0.3 < k\lambda_{De} < 0.4$ (intermediate damping) the system evolves into a steady state like the one explained in Section 4.3 (where $k\lambda_{De} = 0.319$). For $k\lambda_{De} > 0.4$ (strong electron plasma wave damping) the system evolves to a steady state where the amplitude of the EPW (a_3) is always below the LDI threshold condition. In such case LDI is not excited at all. For $k\lambda_{De} < 0.3$ (weak EPW damping) the system evolves into a saturated state where the EPW amplitude exhibits chaotic (incoherent) space-time structures near the left boundary.

4.4.1 Strong EPW damping limit ($k\lambda_{De} > 0.4$)

The saturation of SRS coupled to LDI in the strong damping limit is studied here, considering the plasma parameters at $z = 290 \ \mu m$ ($k\lambda_{De} = 0.4$). In this case, the normalized growth rate and damping coefficients are $G \approx 0.5$, $\nu_3 \approx 0.851$, $\nu_4 \approx 0.687$ and $\nu_5 \approx 0.08$ (see Table 4-3). Once again, the group velocities are $v_{g1} \approx -v_{g2} \approx 30$, $v_{g3} \approx -v_{g4} \approx 1$ and $v_{g5} \approx 0$. Starting with an initial amplitude of $0.0005a_o$ the wave envelopes evolved to the steady state shown in Figure (4-7).

As shown in Figure (4-7.a) the amplitude of the EPW (a_3) barely reaches the LDI threshold condition ($\sqrt{\nu_4\nu_5} = 0.23$), near the left boundary. Otherwise a_3 is always below the LDI threshold, and the the LDI daughters (a_4 and a_5) never grow from their initial amplitude. Therefore, in the steady state SRS is completely independent of LDI.

With the laser amplitude saturated at $a_1 \approx 0.89$ (as in Figure 4-7.a), Equations (4.21)-(4.22) indicate that $a_3(x)$ reaches the LDI threshold ($\sqrt{\nu_4\nu_5} = 0.23$) at $x = x_p \approx -415 \ NxU$. This point is consistent with the numerical result shown in Figure (4-7). and corroborates that a_3 remains under the LDI threshold almost until it
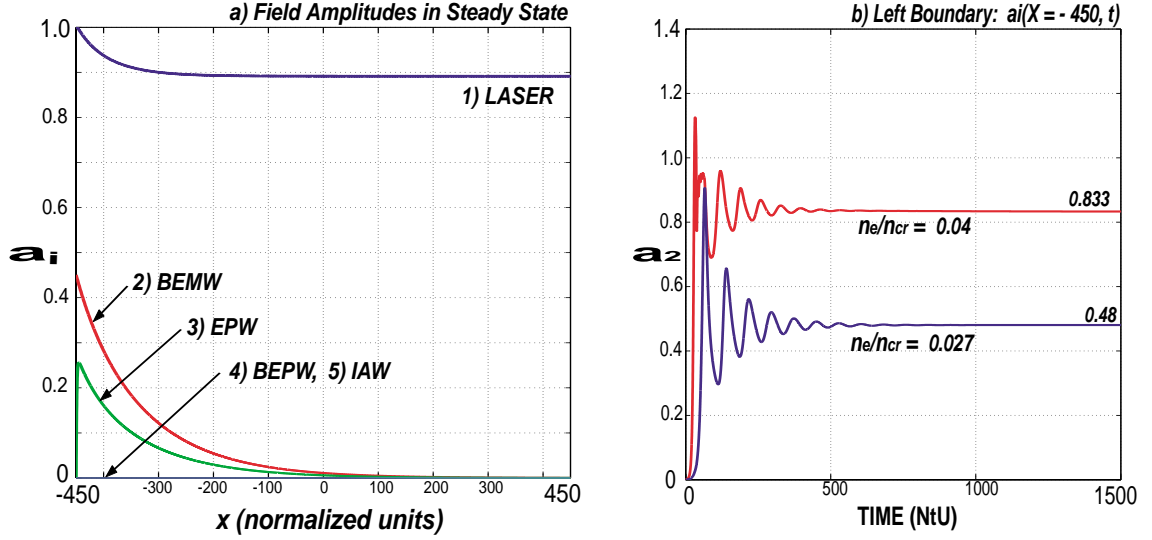
Figure 4-7: Steady state in the strong EPW damping limit $k\lambda_{De} = 0.4$ ($z = 290 \ \mu m$, $n_e/n_{cr} = 0.027$, $T_e = 700eV$ and $T_i = 142eV$).

reaches the left boundary. The narrow region where $a_3 > 0.23$ is not long enough to allow the transition from SRS only to SRS with LDI (which is explained in Section 4.3). As the damping of the electron plasma waves is increased a_3 the spatial growth of a_3 is reduced, and a_3 never reaches the LDI threshold (unless the length of the plasma is increased).

We have also evolved the three weave coupled mode equations that correspond to SRS only, obtaining the exact same steady state solution shown in Figure (4-7.a), to corroborate that SRS is indeed independent of LDI.

The time evolution of the BEMW amplitude at the left boundary $[a_2(x = -450, t)]$, is shown in Figure (4-7.b). As a reference, the BEMW amplitude corresponding to $k\lambda_{De} = 0.319$ (see Section 4.3) is given in the figure. The time oscillations due to the transition from the initial condition to the steady state are observed once again. After $t \sim 1000 \ NtU$ the BEMW settles to a saturated amplitude $a_2(x = -450, t > 1000) \approx 0.48$, which is below the the saturated amplitude obtained in the previous section (≈ 0.88). With $\omega_2/\omega_1 \approx 0.8$, the SRS reflectivity is: $\%SRS = \omega_2/\omega_1|a_2(x = -450, t)|^2 \approx 16\%$.

The above numerical results indicate that an increment in the damping of the
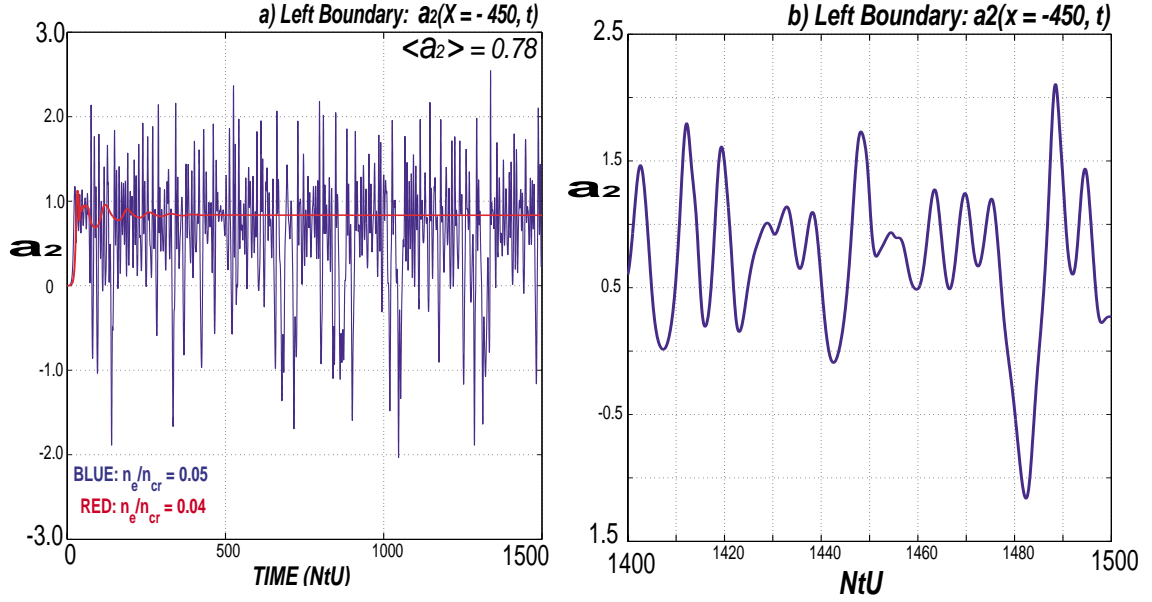
Figure 4-8: SRS saturation in the weak EPW damping limit $k\lambda_{De} = 0.28$ ($z = 230$ μm $n_e/n_{cr} = 0.05$, $T_e = 720eV$ and $T_i = 165eV$).

electron plasma waves, leads to a reduction of the SRS backscattering. The probable reason is analyzed in Section (4.6).

4.4.2   Weak EPW damping limit $(k\lambda_{De} < 0.3)$

The saturation in the weak damping limit is investigated here, considering plasma parameters at $z = 230$ μm ($k\lambda_{De} = 0.28$, $n_e/n_{cr} = 0.05$, $T_e = 700$ and $T_i = 165$). The corresponding normalized growth rate and dampings are $G \approx 0.62$, $\nu_3 \approx 0.146$, $\nu_4 \approx 0.08$ and $\nu_5 \approx 0.075$ (see Table 4-3). Evolving the wave envelopes from an initial amplitude of $0.0005a_o$ the system evolved into a saturated state where the EPW (a_3) exhibits incoherent space/time fluctuations near the left boundary (instead of the saturation at the LDI threshold observed before). The space/time fluctuations are slowly varying, and the backscattering $a_2(x = -450, t)$ remains constant on the time average.

Figure (4-8.a) shows the time variation of the BEMW at the left boundary [$a_2(x = -450, t)$]. For easy comparison, the corresponding evolution with plasma parameters with $k\lambda_{De} = 0.319$ (see Section 4.3) is also shown in the figure. Even if no definitive
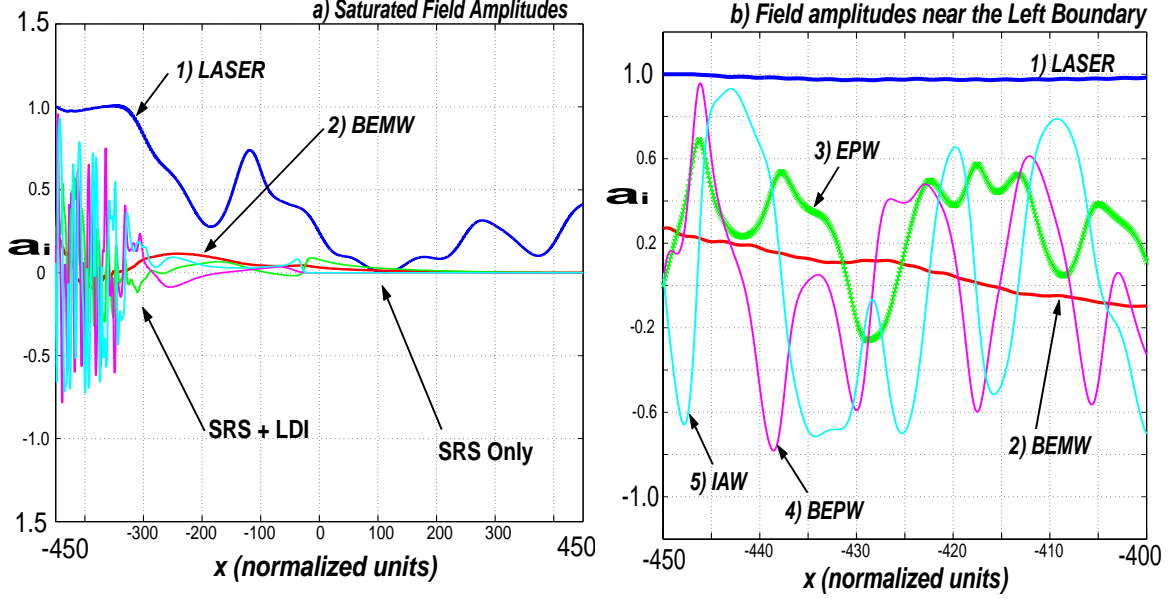
Figure 4-9: Detailed view of the spatial field-amplitudes fluctuations ($k\lambda_{De} = 0.28$).

steady state is established, the backscattering is saturated (i.e., on the average a_2 does not grow, nor decay, with time). A detailed view of the time variations in $a_2(x = -450, t)$ is shown in Figure (4-8.b), showing that the time fluctuations order with $T \sim O(5NtU)$, which is a larger than the BEMW temporal periodicity ($T_{BEMW} = 2\pi/\omega_2 \approx 0.2\ NtU$).

With $\omega_2/\omega_1 \approx 0.75$, the average backscattering $\langle |a_2(x = -450, t)| \rangle \approx 0.78$ leads to an average SRS reflectivity of $\langle \%SRS \rangle \approx 45.5\%$. This reflectivity is below the one obtained in Section (4.3) for $k\lambda_{De} = 0.0319$ ($\sim 50\%$).

Figure (4-9) shows a picture of the spatial structure of the waves, at an arbitrary moment in the saturated state. While this picture changes with time, it can help in understanding the saturated state. The waves in LDI (a_3, a_4 and a_5) exhibit space-time fluctuations only near the left boundary, and otherwise remain at noise level. A detailed view of the field amplitude spatial fluctuations is shown in Figure (4-9.b), where the wave envelopes are observed to have a slow spatial variation compared to the actual wavelength. The scaling of the spatial variations of a_3 [$\sim O(10NxU)$], for example, is long compared to the wavelength of the electron plasma wave ($\lambda_{EPW} = 2\pi/k_3 \approx 1.2\ NxU$). The magnitude of a_3 at the different grid-

a) Space-time fluctuations in the EPW

b) EPW space-time correlation near the left boundary
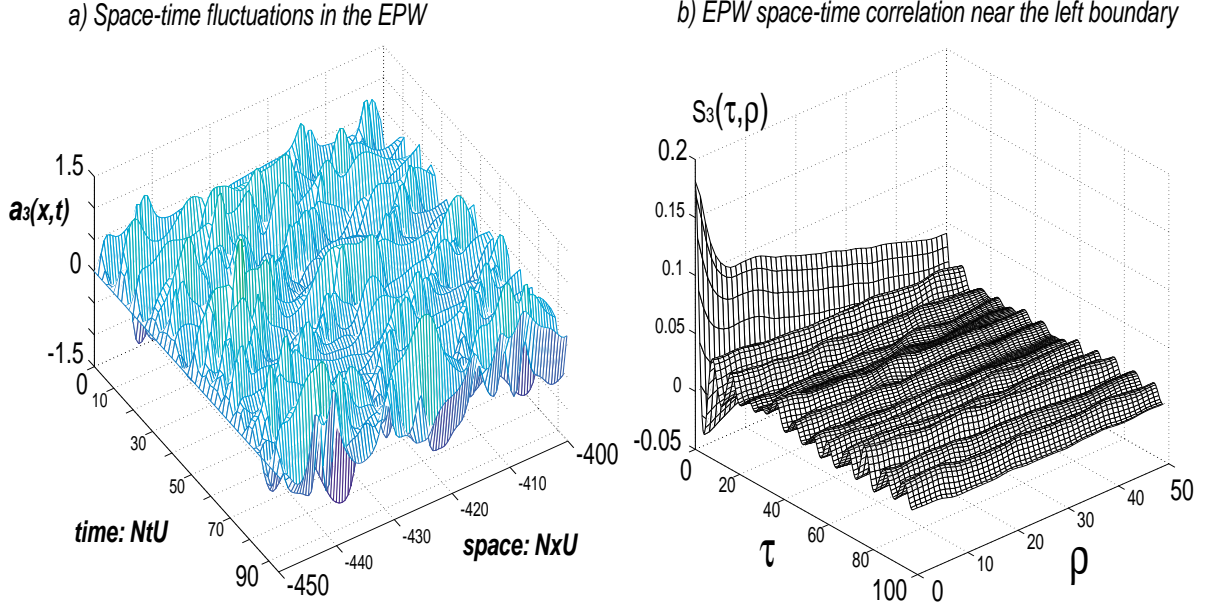
Figure 4-10: Space-time EPW amplitude fluctuations and correlation ($k\lambda_{De} = 0.28$).

points has been highlighted with crosses in the figure, to show that the number of grid-points in the numerical simulation is enough to resolve the spatial fluctuations.

The space-time fluctuations in a_3 (in $-450 < x < -300$) produce an effective de-phasing, which in turn explains the reduction of the SRS backscattering (from that in Section 4.3, where no fluctuations occur).

Figure (4-10.a) shows in detail the EPW space-time fluctuations near the left boundary. This figure resembles the pictures of the spatio-temporal chaos (STC) that were first observed in a periodic-space simulation of LDI, by Carson Chow, et. al. (see Chapter 3).[26, 28] At first glance, the reader may notice the apparent chaotic behavior of coherent structures in time and space, which is the clear signature of the STC. A closer look however, indicates that in this finite length simulation the structures are not completely chaotic. Instead they are created at approximately regular intervals (in time and space), and then propagate into the plasma with an approximately constant velocity ($v \approx v_{g3} = 1$).

The correlation and spectrum of the EPW fluctuations are necessary to better understand the nature of the space-time structures. To this purpose, Figure (4-10.b)

78
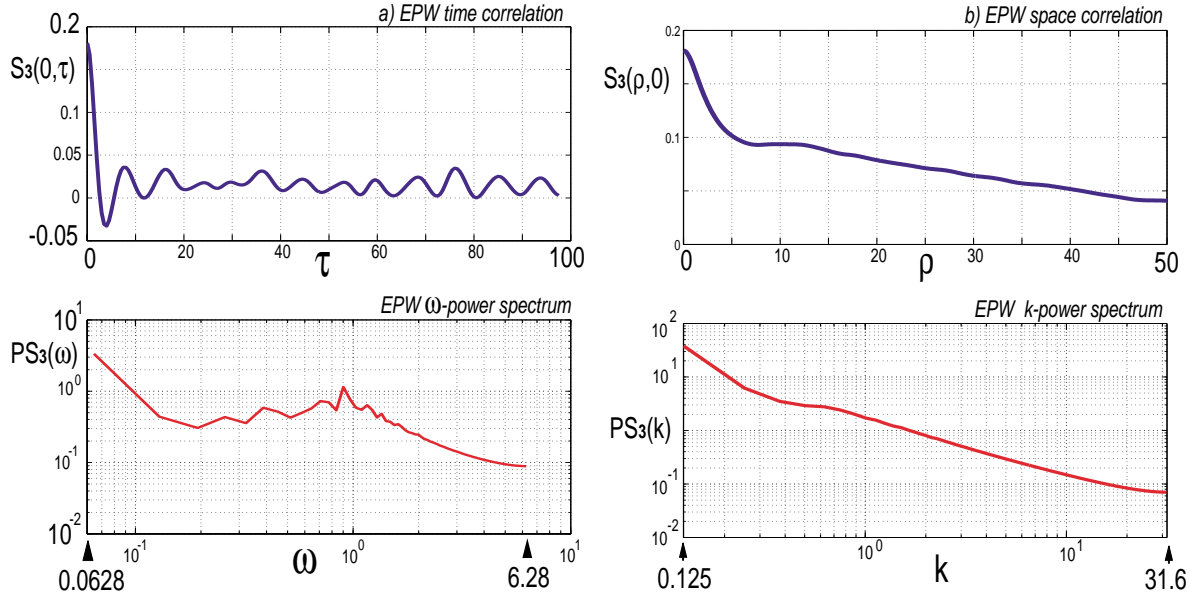
Figure 4-11: a) EPW power spectrum in ω, and b) EPW power spectrum in k.

shows the correlation function of the fluctuations in a_3, which is calculated as:

$$S_3(\rho, \tau) = \frac{1}{RT} \int_0^R d\rho \int_0^T d\tau\, a_3(x,t) a_3(x + \rho, t + \tau). \qquad (4.26)$$

The correlation function $S_3(\rho, \tau)$ exhibits a single major peak of finite width at $\rho = \tau = 0$, which may be a slight indication of STC. However, the correlation does not decay away completely. Instead, it exhibits clear oscillations in time, which indicate that similar structures (of size $\sim 10NxU$) repeat at regular time intervals (of $\sim 8NtU$). The behavior in space, on the other hand, is harder to understand, because of the narrow sample of space fluctuations that is available.

The τ dependence of the space-autocorrelation function $S_3(\rho = 0, \tau)$, and its Fourier transform (the frequency power spectrum), are shown in Figure (4-11.a). The autocorrelation shown in the upper plot, clearly shows a τ-periodicity of about $100/13 \approx 7.6\ NtU$, which approximately corresponds to the time spacing between the structures in Figure (4-10.a). This periodicity is corroborated in the frequency power spectrum, which exhibits a peak at $\omega \approx 2\pi/7.6 = 0.82$. The power spectrum also peaks at $\omega \approx 0$ because of the offset level in the correlation function, which
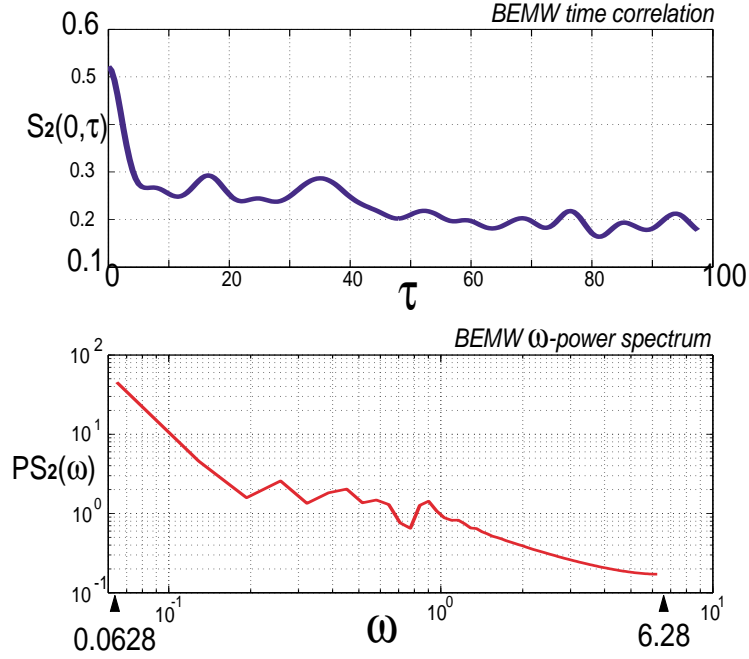
Figure 4-12: Frequency power spectrum of the SRS backscattering $[a_2(x = -450, t)]$.

mainly indicates that the amplitude of a_3 is positive most of the time (a negative amplitude implies a 180 degrees de-phasing). The band-width of the frequency power spectrum is $\delta\omega \sim 2$, which is narrow in comparison with the EPW frequency $\omega_3 \approx 1.1(\omega_{pe}/\gamma_b) = 20$ (normalized frequency units).

The ρ variation of the time-autocorrelation function $S_3(\rho, \tau = 0)$, and its Fourier transform (the k-power spectrum), are illustrated in Figure (4-11.b). The k-power spectrum $[PS_3(k) \sim k^{-\alpha}]$ shows a maximum at $k = 0$, followed by a rapid decay ($\alpha \approx 150$) to a plateau, and then a slow decay ($\alpha \approx 1$). The k power spectrum peaks at $k = 0$ because of the offset in the autocorrelation function $[S_3(\rho, \tau) > 0]$, and exhibits a plateau at $k \approx 0.5$ because of the spatial structures observed in Figure (4-10.a). A longer sample of the randomized EPW amplitude (a_3) is necessary to better resolve the plateau. Such sample, however, is not available because the structures are confined to a narrow region near the left boundary. The band-width of the k-power spectrum, $\delta k \approx 1$ (after the plateau), is again found to be narrow in comparison to the EPW wavenumber $k_3 = 2\pi/\lambda_3 \approx 4$ (in normalized units).

The BEMW autocorrelation function $[S_2(\rho = 0, \tau)]$ and its frequency power spec-

trum, are illustrated in Figure(4-12). In the upper plot, $S_2(\rho = 0, \tau)$ exhibits a peak at $\tau \approx 0$, followed by a slow decay in τ. The power spectrum, in the lower plot, peaks at $\omega \approx 0$ (because of the offset in S_2) and the exhibits a slow decay in ω. The bandwidth of the power spectrum is $\delta\omega \approx 2$, which again is narrow compared to the BEMW frequency $\omega_2 \approx 3.35(\omega_{pe}/\gamma_b) = 60$ (normalized frequency units).

The periodicity in τ of the EPW power spectrum (PS_3) indicates a long scale correlation, which opposes the idea of chaotic motion of the structures in a_3. This long scale correlation appears to be consistent with the observed movement of the structures along their characteristics (see Figure 4-10.a). While the motion of the structures is apparently non chaotic, the space where the structures develop is not long enough to determine whether the motion is chaotic or not; therefore further investigation (with different laser-plasma parameters) is necessary to determine the chaotic/incoherent nature of the space-time fluctuations in a_3.

4.5   SRS variation with Electron Plasma Density

Figure (4-13) illustrates the numerical SRS backscattering as a function of the electron plasma density n_e/n_{cr}. As shown in Table (4-3), $k\lambda_{De}$ decreases when n_e/n_{cr} increases, so the dampings of the electron plasma waves are reduced while the rest of the parameters in the simulation remain approximately constant. The numerical simulations with the parameters in Table (4-3) show that the SRS backscattering increases as the EPW damping is reduced, until the damping is so small that the EPW develops incoherent/chaotic amplitude fluctuations. In this case ($n_e/n_{cr} \sim 0.05$), the fluctuations in a_3 produce a de-phasing of the nonlinear SRS interactions, which in turn appreciably reduces the SRS backscattering.

Figure (4-13) also shows the SRS backscattering obtained from three wave coupled mode equations (3COM) for SRS only (without LDI). The comparison of the numeric reflectivities (with and without LDI) suggests that LDI works as an effective nonlinear-damping for the EPW, because it reduces the SRS reflectivity as if ν_3 was
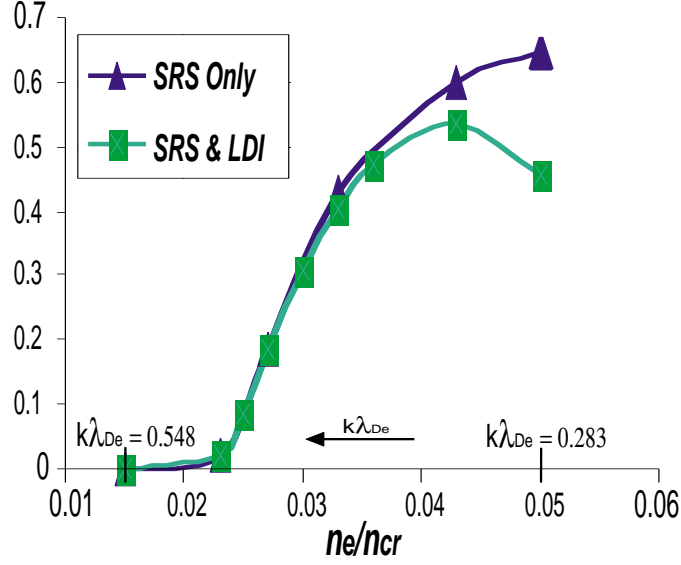
Figure 4-13: Variation of the SRS reflectivity with electron plasma density.

increased (n_e/n_{cr} reduced). This effect can be better appreciated in Figure (4-14.a), where the steady state EPW amplitudes, for the different electron plasma densities, are illustrated. The figure clearly shows that the onset of LDI (near the left boundary) forces down the amplitude of the EPW (to the LDI threshold condition $\sqrt{\nu_4\nu_5}$). As the density increases, ν_4 is reduced, and a_3 saturates at a lower level.

In Figure (4-14.b), on the other hand, the spatial growth of the BEMW (from right to left) is clearly modified in the regions where LDI has been excited. Such modification of the BEMW spatial growth rate (the break in the curves), becomes stronger when the electron plasma density increases (i.e., ν_3 and saturated a_3 decrease). The reason for this is that a smaller a_3 produces a weaker interaction between the laser and the BEMW [a_2a_3 in Eq. 4.15 and a_1a_3 in Eq. 4.16]. In this fashion, the figure also shows that the SRS parametric growth rate (in the rightmost region of the plasma) is reduced when n_e/n_{cr} is reduced, which corresponds to a stronger depletion of the laser (consistent with a strong a_3 near the left boundary).

The effective nonlinear damping produced by LDI, is remarkably strong when $n_e/n_{cr} = 0.05$. As explained in Section (4.4), the amplitude of the electron plasma wave exhibits chaotic/incoherent space-time fluctuations (due to LDI), producing a de-phasing in SRS. Such de-phasing in turn debilitates the nonlinear interaction
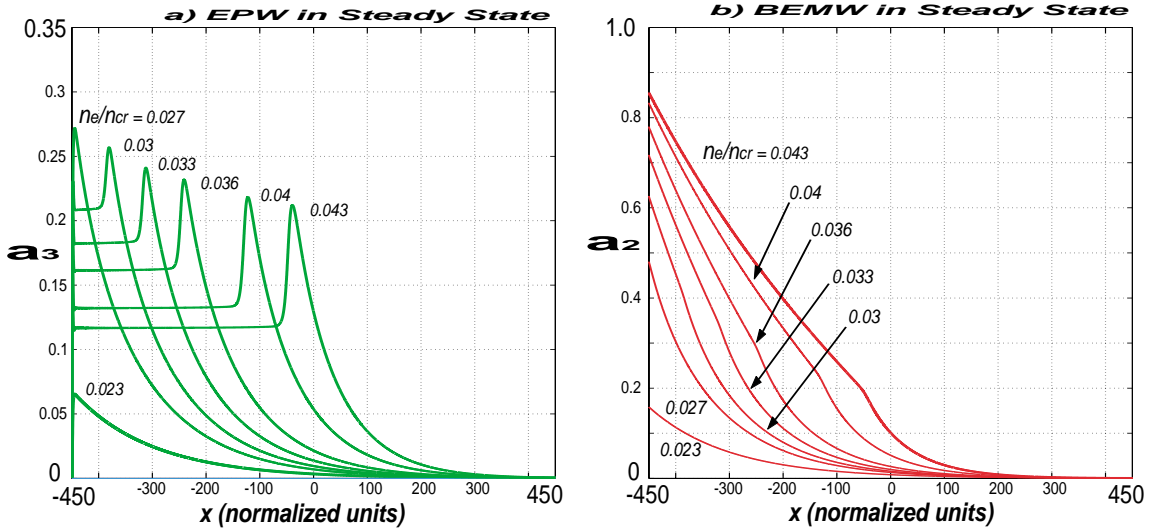
Figure 4-14: Variation of the steady state EPW and BEMW amplitudes with n_e/n_{cr}.

between the laser and the BEMW, leading to a significant reduction of the SRS backscattering.

A comparison between Figures (4-13) and (1-4.b), shows that the numerical SRS reflectivity varies with the electron plasma density (n_e/n_{cr}) in a manner similar to the experimental observations. The reflectivity grows for $n_e/n_{cr} < 0.04$, and then begins to decrease when $n_e/n_{cr} > 0.04$ (due to the onset of incoherent fluctuations of a_3). The maximum numeric reflectivity $SRSr \sim 50\%$ [at $n_e/n_{cr} = 0.043$], however, is very large compared to the experimental measurement of $SRS_r \sim 5\%$. The reduction of the SRS reflectivity due to the wave dephasing (when $n_e/n_{cr} = 0.05$), on the other hand, is not sufficient to explain the experiments. The reason for such discrepancies is not easy to understand, and requires further investigation. While other nonlinear phenomena that are not modeled in the 5COM equations may play an important role, the inaccuracy in parameters obtained from certain experimental measurements (in particular the plasma temperature) may also be responsible for the discrepancy.

The dependence of the numerical SRS reflectivity upon different parameters of the problem is investigated in Chapter 5. Then the effects of the SRS and LDI cascadings are investigated in Chapter 6. The discussion on the validity of the coupling of modes equations, is continued in such chapters.

83

.

Chapter 5

Dependence of SRS/LDI on Different System Parameters

The dependence of the SRS backscattering investigated in Chapter 4, on the possible variation of the laser-plasma parameters, is explored in this chapter. Section (5.1) considers variations on the ion acoustic wave damping, Section (5.2) variations on the initial amplitude of the noise, and Section (5.3) the variations on the laser intensity. Since the work in the present Chapter extends the investigation reported in Chapter 4, the same nomenclature and terminology are used, unless otherwise specifically specified.

5.1 Ion Acoustic Wave Damping

In a series of experiments at Lawrence Livermore National Laboratory (LLNL) the SRS backscattering was found to increase with the damping of ion acoustic waves [4, 5]. This observation was very surprising at the time, because people expected instead that SRS was independent of the IAW damping [4]. While the observed dependence has not been completely understood, it suggests the coupling of SRS to LDI, or to other processes that involve ion acoustic waves (like stimulated Brillouin scattering). We investigate the SRS backscattering as a function of IAW damping, using the five wave coupled modes equations for SRS and LDI, in a finite homogeneous plasma
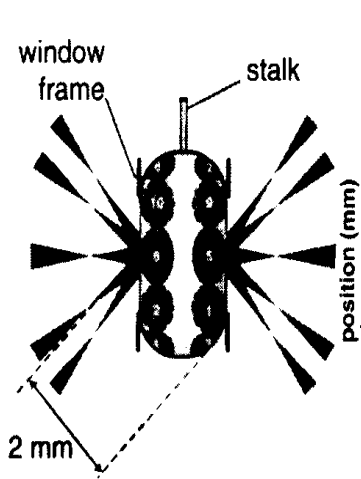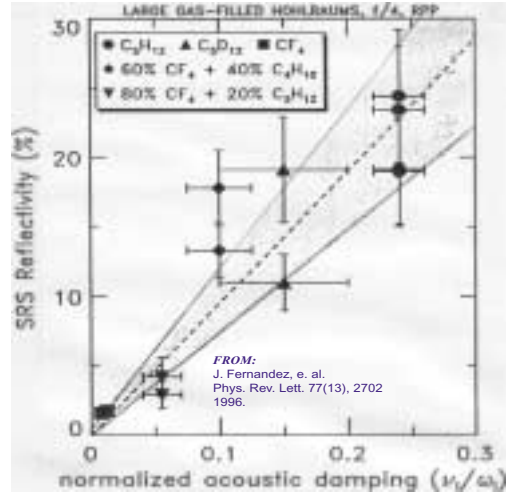
a) Experimental Set up   b) Experimental Observations

Figure 5-1: Experimental investigation of SRS backscattering with IAW damping [4, 5]. Laser wavelength $\lambda_o = 350\ nm$ and intensity $\mathcal{I}_o = 5 \times 10^{14}\ Watts/cm^2$.

geometry. As in Chapter 4, our investigation is restricted to real wave envelopes, with no wave de-phasing.

Considering that stimulated Brillouin scattering (SBS) is significantly reduced with increased IAW damping [5], SBS is left out of the investigation. To consider the effects of SBS, the 5COM equations can be extended by incorporating the equations for the SBS coupled waves (similar to Chapter 6, where cascadings of LDI are incorporated to the model).

5.1.1 Experimental observations

In the experiments at LLNL, several laser beams were pointed to a gas-bag containing a gas-mixture (see Figure 5-1.a), to create a plasma where the SRS backscattering could be investigated. The composition of the gas-mixture was changed to obtain plasmas with different ion acoustic wave dampings, keeping the other plasma parameters approximately constant [4, 5] (i.e., only $k\lambda_{Di}$ was changed). Then, an interaction laser beam was focused to the plasma and the SRS backscattering was observed.

Different from the single hot-spot experiments considered in Chapter 4, the inter-

action beams were not diffraction limited into the plasma. Instead, a random phase plate (RPP) was used to smooth out the intensity of the interaction beam, creating a collection of many single hot-spots at random positions in the plasma [5].

The wavelength of the interaction beam was $\lambda_o = 350\ nm$ and the intensity $\mathcal{I}_o \sim 5 * 10^{14}\ Watts/cm^2$. With a typical electron temperature of $T_e \sim 1\ keV$ and electron plasma density $n_e/n_{cr} \sim 0.075$ ($n_{cr} \sim 10^{28}\ m^{-3}$), the laser frequency was $\omega_1 \approx 3.6\omega_{pe}$, and the BEMW frequency $\omega_2 \approx 2.55\omega_{pe}$. The duration of the interaction beam was approximately 1 $nsec$, and the path of the laser through the plasma approximately 2 mm long. The measured SRS backscattering, which was collected from similar experiments with different IAW dampings, is shown in Figure (5-1.b). The backscattering ranges from 1% to 30%, while the damping of the ion acoustic waves changes from $\nu_5/\omega_{r5} \sim 0.01$ to 0.3.

With the above parameters $k_3\lambda_{De} \approx 0.259$, and the Landau dampings of the electron plasma waves (Eq. 2.33) are $\nu_3/\omega_{r3} \sim 0.0036$ and $\nu_4/\omega_{r4} \sim 0.00115$. Since the IAW damping is $\nu_5/\omega_{r5} < 0.3$, the slowly varying amplitude approximation (considered in the coupled mode equations) is well satisfied for the EPW, and marginally so for IAW.

With the same normalization used in Chapter 4 [see Table (4.2)], the normalized parameters are $v_{g1} \approx -v_{g2} \approx 30$, $v_{g4} \approx -v_{g3} = -1$, $v_{g5} \approx 0$, $\nu_3 = 0.39$, $\nu_4 = 0.15$ and $G = 0.699$. The normalized damping of the ion acoustic wave ranges from $\nu_5 = 0.0156$ to $\nu_5 = 0.468$ normalized units (which correspond to $\nu_5/\omega_{r5} \sim 0.01$ and $\nu_5/\omega_{r5} \sim 0.3$, respectively). We consider an initial amplitude of the noise of $0.0005a_o$. All the boundary conditions are set to this amplitude, except for the laser pump (which is externally driven through the left boundary).

Since the purpose of our investigation is not to predict the experimental SRS backscattering, but rather to understand how it is modified by the IAW damping, we consider an interaction length $L \sim 430\lambda_o$ (similar to the hot-spot in Chapter 4). This interaction length ($0.15mm$) is much smaller than the actual size of the plasma in experiments ($2mm$). The investigation of the SRS backscattering in longer plasmas,

87

probably with many single hot-spots at random positions, is left as a problem for the future. In normalized units, the length of interaction region is 200 NxU (0.15 mm) spanning from -100 to $100NxU$, and the laser "transit time" (to cruise through the plasma) is ~ 6 NtU.

The geometry of the plasma in the gas-bag is difficult to model, and the uncertainty in the laser-plasma parameters is very significant. Therefore, it would be too ambitious to expect the numerical simulations to accurately predict the experimentally observed reflectivity.

5.1.2 Numerical Results

Equations (4.16)-(4.20) were integrated numerically to evolve the slowly varying wave envelopes, in 1D space and time.

The wave envelopes always evolved into a definitive steady state, similar to Sections (4.3) and (4.4.1), in a time $t < 100$ $psec$. The detailed description of the early space/time evolution (before the onset of the steady state) is omitted, because the evolution is similar to the one described in section (4.3) and there is nothing new to learn from it.

Two different scenarios were observed in the steady state,. In the first scenario, observed when $\nu_5/\omega_5 \geq 0.15$, LDI is not excited at all, due to the heavy damping of the IAW. As an illustration, Figure (5-2.a) shows the wave envelopes in steady state for $\nu_5/\omega_5 = 0.15$ ($\nu_5/\gamma_b = 0.234$). The EPW amplitude, growing from right to left (as in Chapter 4), reaches the LDI threshold ($\sqrt{\nu_4\nu_5} = 0.18$) at $x = x_p = -60$. The LDI daughters are barely excited near the left boundary, where a_3 is above the LDI threshold. For a larger IAW damping, the LDI daughters are never excited, and SRS is completely independent of LDI (same as in Section 4.4.1).

In the second steady state scenario, observed when $\nu_5/\omega_5 < 0.15$, the saturated LDI is observed near the left boundary (similar to simulations in Section 4.3). As an illustration, Figure (5-2.b) shows the wave envelopes in steady state, for $\nu_5/\omega_5 = 0.01$ ($\nu_5/\gamma_b = 0.0156$ normalized damping units). LDI is localized in $x < -30$, where
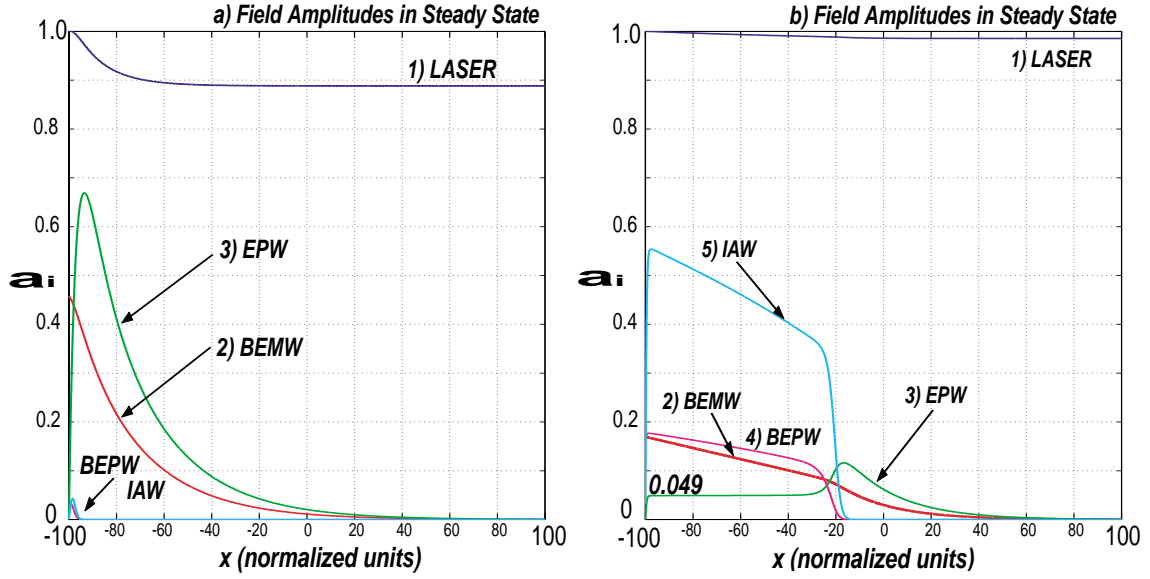
Figure 5-2: Field amplitudes in steady state: a) $\nu_5/\omega_5 = 0.15$ and b) $\nu_5/\omega_5 = 0.01$.

the EPW amplitude (a_3) has a constant value slightly above the LDI threshold:
$a_3 = \sqrt{\nu_5\nu_4} = \sqrt{0.0156 * 0.15} \approx 0.049$.

When LDI is excited ($\nu_5/\omega_5 < 0.15$) the steady state exhibits the four characteristic regions explained in Section (4.3). In Figure (5-2.b), for example, the LDI daughters remain at the noise level in $x > 0$, where the EPW and BEMW grow towards the left with the SRS parametric growth rate [Eqs. (4.21) – (4.22)]. A transition region occurs in $-30 < x < 0$, where a_3 shows an overshoot between its SRS parametric growth and the sudden saturation to the LDI threshold. Following the transition region, in $-99 < x < -40$, the EPW is saturated at an amplitude just above the LDI threshold (as in Section 4.3). Finally, very close to the left boundary, a boundary layer occurs, where the amplitude a_3 changes from its boundary condition $[a_3(x = -100, t) = 0.0005]$ to the saturated amplitude due to SRS/LDI.

Figure (5-3) shows the time variation of the SRS reflectivity, for different ion acoustic wave dampings. Again, the SRS reflectivity is calculated with:

$$SRS_\mathbf{r}(t) = (\omega_2/\omega_1)|a_2(x = -450, t)|^2. \tag{5.1}$$

As shown in the figure, the backscattering always reaches a saturated state in
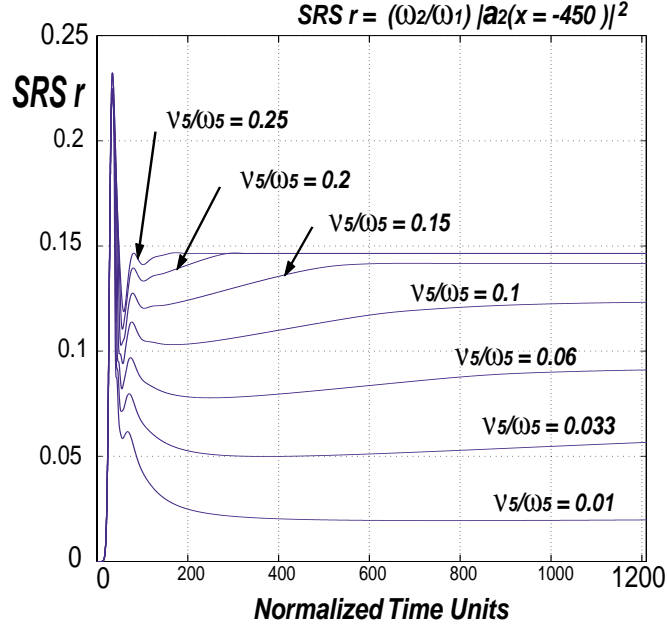
Figure 5-3: Time dependence of SRS reflectivity, for the different IAW dampings.

$t < 800 NtU \approx 66 psec$ (which is a short time compared to the duration of the laser pulse). An initial overshoot is observed in all the simulations. In the weak IAW damping limit the BEMW never grows after the overshoot because LDI kicks in, producing the saturation of the EPW amplitude [at the LDI threshold], which in turn weakens the nonlinear interaction in SRS [$Ga_2 a_3$ in Eq. 4.16, and $Ga_1 a_3$ in Eq. 4.17]. As the IAW damping increases, the saturation of a_3 near the left boundary occurs at larger amplitudes, thus leading to a higher SRS backscattering ($Ga_1 a_3$ in Eq. 4.17 is larger near the left boundary).

When the IAW damping is too large ($\nu_5/\omega_5 \geq 0.15$) LDI is not excited at all, and SRS saturates independently of the IAW damping (see Figure 5-3). In this case, the saturated SRS backscattering in steady state is exactly the same obtained with the 3COM equations for SRS only. No matter what is the damping of the ion acoustic waves, the SRS/LDI backscattering (5COM) is always smaller or equal, than the SRS backscattering with no LDI (3COM). Increasing the IAW damping reduces the effects of LDI on SRS, thus producing a reflectivity that approaches to the one obtained with the 3COM equations for SRS only.

Figure (5-4) shows the steady state amplitudes of the IAW (a_5) and the EPW

90
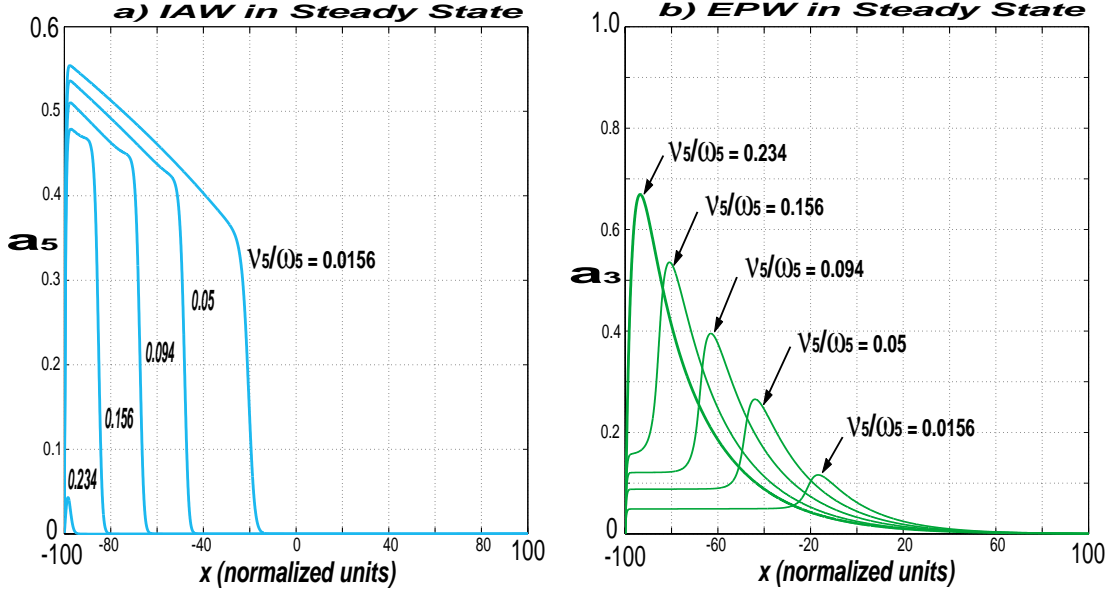
Figure 5-4: Steady state EPW and IAW, for the different IAW dampings

(a_3), for the different IAW dampings. The amplitude of the IAW, in figure (5-4.a), decreases near the left boundary as the IAW damping is increased. On the other hand, the saturated amplitude of the EPW near the left boundary, in Figure (5-4.b), increases when the IAW damping is increased (i.e., the LDI threshold is increased). A larger amplitude of a_3 reinforces the nonlinear SRS interaction, because of the larger Ga_2a_3 in Eq. 4.16, and Ga_1a_3 in Eq. 4.17. The stronger SRS interaction near the left boundary produces the larger SRS reflectivity.

The dependence of the SRS backscattering on the IAW damping, is illustrated in Figure (5-5). This is the same as Figure (5-3) at time $t = 1200$ (steady state). In the figure, the SRS backscattering is observed to increase with the IAW damping, until a clear saturation occurs at $\nu_5/\omega_5 \geq 0.15$.

Considering that the gas-bag plasma geometry in experiments is difficult to model and the uncertainty in the laser-plasma parameters is significantly large, even if typical experimental parameters have been considered, no direct comparison with experiments is possible. However, even if different laser-plasma parameters would lead to a different SRS backscattering, the increasing trend with damping of ion acoustic waves would remain the same (as well as the physics behind it).
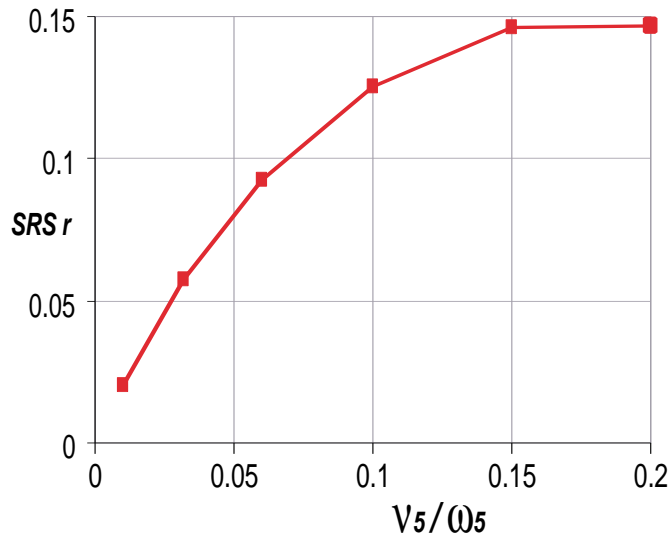
Figure 5-5: Numerical SRS Reflectivity Vs. IAW damping.

The numerical reflectivities found in this section are much smaller than the reflectivities in Chapter 4, mainly because of the shorter length of the interaction region. While most of the normalized parameters scale similar in both chapters, the length of interaction is very different ($L = 200NxU$ in Chapter 5, and $L = 900NxU$ in Chapter 4). Such a big difference in the normalized plasma lengths, results from the different laser wavelengths and intensities that are used in each chapter ($\lambda_o = 527$ nm, $\mathcal{I}_o \sim 10^{15}$ $Watts/cm^2$ in Chapter 4, and $\lambda_o = 350$ nm, $\mathcal{I}_o \sim 10^{14}$ $Watts/cm^2$ in Chapter 5).

The difference in the plasma lengths (considered in Chapters 4 and 5) is relevant to our investigation, because it demonstrates the sensitivity of the numeric SRS backscattering on the estimated length of the plasma.

5.2 Amplitude of the Noise

The dependence of the SRS reflectivity on the amplitude of the noise is investigated in this section. To this purpose, we simply calculate the SRS backscattering for different amplitudes of the noise.
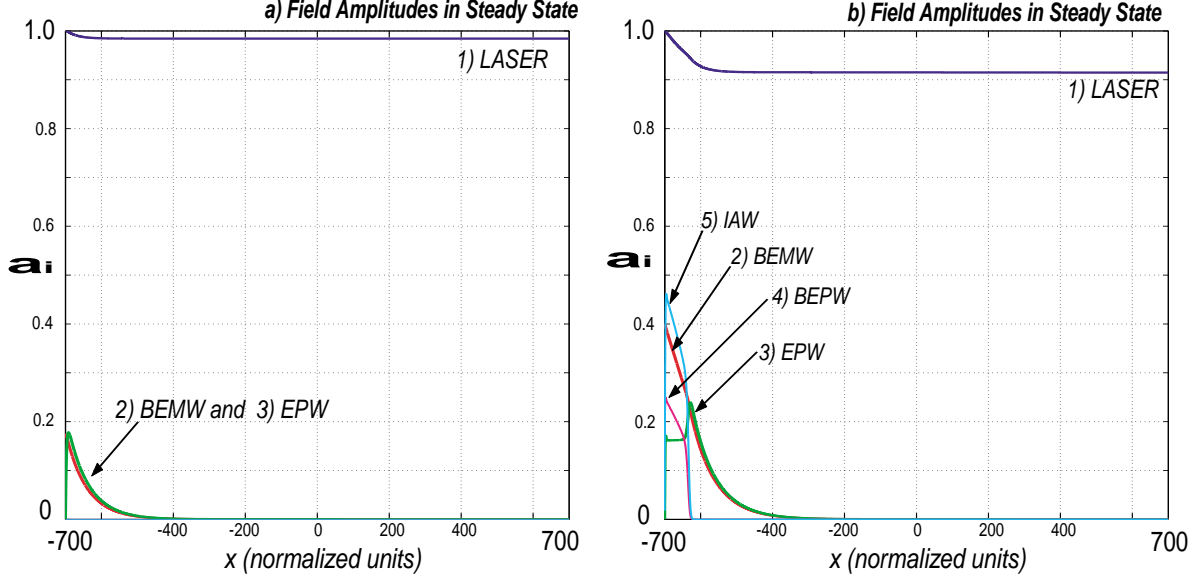
Figure 5-6: Steady state for: a) $N = 1E - 11a_o$ and b)$N = 1E - 9a_o$.

In anticipation to section (5.3), we consider the laser plasma parameters: $\lambda_o = 527nm$, $\mathcal{I}_o = 6 \times 10^{15} \ watts/cm^2$, $T_e = 500eV$, $T_i = 150eV$ and $n_e/n_{cr} = 0.025$. A hot-spot length of 225 μm is considered, for easy comparison with Chapter 4.

With the normalization in Table 4.2, the normalized length of the interaction region is $1400NxU$. The normalized group velocities are $v_{g1} \approx -v_{g2} \approx 30$, $v_{g3} \approx -v_{g4} \approx 1$ and $v_{g5} \approx 0$. The laser transit time is approximately $47NtU$, and the normalized growth and dampings are: $G = 0.449$, $\nu_3 = 0.4$, $\nu_4 = 0.298$ and $\nu_5 = 0.086$. The 5COM equations (4.15)–(4.19) were integrated numerically, for different noise levels (N) ranging from $N = 10^{-13}a_o$ to $N = 10^{-3}a_o$.

The wave envelopes always evolved into a definitive steady state (like in Sections 4.3 and 4.4.1). When the noise level is $N < 5 \times 10^{-11}a_o$ LDI was not excited at all. As an illustration, Figure (5-6.a) shows the field amplitudes in steady state, for $N = 1 \times 10^{-11}a_o$.

For a larger amplitude of the noise, a_3 grows to the LDI threshold within the region of interaction and therefore excites LDI. In this case, as explained in Chapter 4, a_3 saturates at the LDI threshold in the region where LDI develops (i.e., near the left boundary). Figure (5-6.b), for example, shows the wave envelopes in the steady
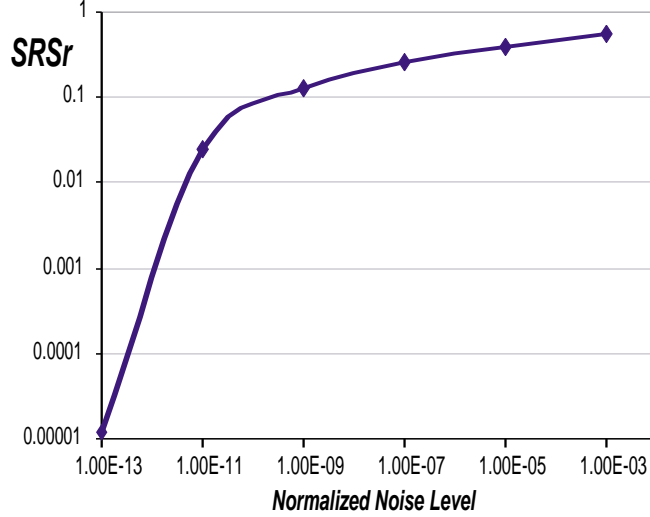
Figure 5-7: Numerical SRS reflectivity vs. initial noise level.

state, for $N = 1 \times 10^{-9} a_o$. Near the left boundary, a_3 clearly saturates at the LDI threshold ($\sqrt{\nu_4 \nu_5} = 1.6$).

With $\omega_2 / \omega_1 = 0.08$, Figure (5-7) illustrates the calculated SRS reflectivity (Eq. 5.1) as a function of the noise level (N). As observed, the SRS reflectivity increases with the amplitude of the noise. The rate at which the reflectivity increases, is modified at $N \sim 5 \times 10^{-11} a_o$, because of the onset of LDI. At $N = 5 \times 10^{-4} a_o$, a large SRS reflectivity of about 50% is found in agreement with the calculations presented in Chapter 4.

In the framework of the single hot-spot experiments, Figure (5-7) shows that a very small reflectivity can be obtained, if the noise level is sufficiently reduced. For example, if the noise level is reduced to $10^{-10} a_o$, a reflectivity of 10% (similar to experiments) can be obtained. While some analytic attempts to investigate the amplitude of the noise have been made [66, 67], it has not been measured in experiments. Considering thermal electron fluctuations in a plasma (with immobile ions), one can estimate the total energy density in the essentially undamped portion of the fluctuating spectrum as: $\langle E_N^2 \rangle = 0.215 \kappa T_e / 2\pi^2 \epsilon_o \lambda_{De}^3$ [68]. With plasma parameters at $z = 250 \mu m$, the electron fluctuations energy density leads to a noise level: $E_N / E_o \sim 1 * 10^{-7}$.

$\mathcal{I}_o$ [W/m^2]	L [NxU]	N/a_o	ν_3	ν_4	ν_5	G
$4E10^{15}$	1100	1.3e-11	0.49	0.36	0.105	0.449
$5E10^{15}$	1250	1.1e-11	0.444	0.326	0.094	0.449
$6E10^{15}$	1400	1.0e-11	0.4	0.298	0.086	0.449
$8E10^{15}$	1600	0.86e-11	0.35	0.258	0.074	0.449
$1E10^{16}$	1800	0.77e-11	0.31	0.231	0.066	0.449

Table 5.1: Normalized parameters for numerical simulations with varying laser intensity ($\mathcal{I}_o$). Laser wavelength $\lambda_o = 527\ \mu m$, and plasma parameters: $T_e = 500eV$, $T_i = 150eV$ and $n_e/n_{cr} = 0.025$.

Such noise level, is a function of the temperature and density of the plasma. It may be enhanced (depending of the amplitude and wavelength of the laser [66]), and may also be a function of time, space or even the other laser-plasma parameters. In this section, all the wave envelopes have been considered to start from the same noise level, which may not be entirely accurate, but allows an easy investigation of the main physics of the system. The estimation of the initial amplitude of the noise is a rather difficult problem, which requires further investigation.

5.3 Laser Intensity

The effects of the laser intensity are investigated in this section. From the recent single hot-spot experiments in [6], we consider the laser-plasma parameters: $\lambda_o = 527nm$, $T_e = 500eV$, $T_i = 150eV$ and $n_e/n_{cr} = 0.025$. With such parameters ($k\lambda_{De} = 0.35$), we calculated the SRS backscattering for different values of the laser intensity ($\mathcal{I}_o$) ranging from 4×10^{15} to 1×10^{16} [$Watts/cm^2$]. Again, a plasma length of $L = 225\mu m$ is taken in the calculation of the reflectivities.

Considering the numerical results in Section (5.2), we assume an amplitude of the noise, so the maximum SRS reflectivity in the order of 10%. To this purpose, the noise level is set to $1 \times 10^{-11} E_o$, with E_o the unperturbed amplitude of the electric field at 6×10^{15} [$Watts/cm^2$]. Such amplitude of the noise, however, is not realistic because it is below the amplitude of the thermal noise.
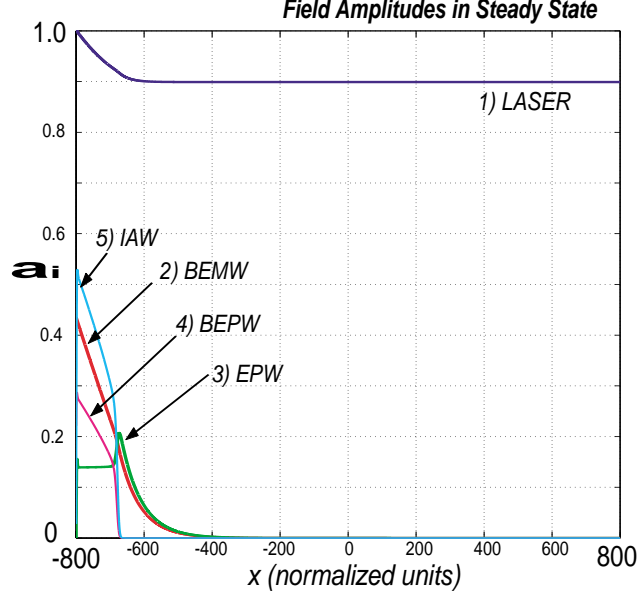
Figure 5-8: Steady state for $\mathcal{I}_o = 8 \times 10^{15} \ Watts/cm^2$.

With the above parameters and the normalization in Table 4.2, the normalized group velocities are $v_{g1} \approx -v_{g2} \approx 30$, $v_{g3} \approx -v_{g4} \approx 1$ and $v_{g5} \approx 0$. The normalization parameter $\gamma_b = |K_{LDI} a_o|$ is now dependent on the laser intensity $\mathcal{I}_o$ (see Chapter 4). Therefore, the normalized dampings (ν_ℓ), noise level (N) and time/space units (NxU and NtU), are now dependent on the laser intensity. The normalized SRS coupling coefficient $[G \sim |K_{SRS}|/|K_{LDI}|]$, on the other hand, is independent of $\mathcal{I}_o$. The normalized parameters corresponding to the different laser intensities are given in Table (5-1).

Same as before, the wave envelopes were numerically evolved in time and space, and always were found to reach a definitive steady state – similar to Sections (4.3) and (4.4.1). Again, the early space/time evolution of the field amplitudes, before the onset of the steady state, is omitted here for brevity purposes.

The steady state field amplitudes for $\mathcal{I}_o = 6 \times 10^{15}$ and for $8 \times 10^{15} \ [Watts/cm^2]$ are illustrated in Figures (5-6.a) and (5-8), respectively. In Figure (5-6.a), the amplitude of the electron plasma wave (a_3) remains below the LDI threshold condition throughout the simulation region, and LDI is not excited at all (as already explained). Such kind of steady state is observed when the laser intensity is $\mathcal{I}_o < 6 \times 10^{15} Watts/cm^2$.
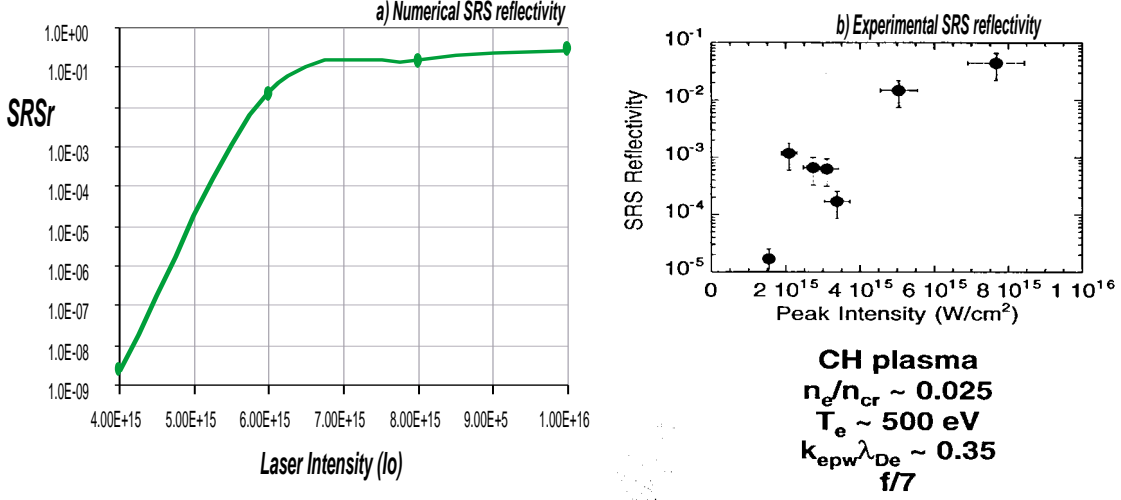
Figure 5-9: SRS reflectivity vs. laser intensity ($\mathcal{I}_o$).

When the laser intensity is larger $[\mathcal{I}_o > 6 \times 10^{15} Watts/cm^2]$ LDI is excited within the plasma, thus leading to the steady state where the EPW amplitude (a_3) saturates at the LDI threshold (near the left boundary).

With $\omega_2/\omega_1 \approx 0.8$, the calculated SRS reflectivity (Eq. 4.22) is shown in Figure (5-9). In this figure, the SRS reflectivity increases with the laser intensity, and then saturates after $\mathcal{I}_o \approx 6 \times 10^{15} Watts/cm^2$ (due to the excitation of LDI). As a reference to the reader, the experimental observation of the SRS reflectivity with similar laser-plasma parameters [6] is shown in Figure (5-9.b).

The numerical SRS reflectivity fails to accurately predict the experiments, probably because of the many other nonlinear effects that are not considered in the 5COM equations (like cascading, wave de-phasing, laser filamentation, and electron trapping). The numerical SRS reflectivity, however, is observed to vary with the laser intensity, in a manner similar to the experimental observations.

5.4 Discussion

The dependence of the SRS reflectivity on the ion acoustic wave damping, the initial noise level and the laser intensity, was investigated. The reflectivity is found to increase when any of the above parameters increases. The SRS backscattering is

97

also found to be sensitive to the length of the interaction region, which has not been accurately modeled with the abrupt finite length.

The numeric simulations with the 5COM equations fail to accurately predict the experimentally observed reflectivity. The reason for this, is not clear. While the uncertain experimental data may be an important source of discrepancy, the many approximations (that are implicit in the model) may also be responsible for the error. Further investigations is required to clear such issues.

While possible discrepancies in the experimental data may change the calculated SRS backscattering, the trends explained in this chapter (which are similar to those in experiments) would not be changed. Nor the physics behind them.

Chapter 6

Cascadings of LDI and SRS

In this Chapter, the 5COM equations [Eqs. (4.1)–(4.5)] are extended to investigate the effects of the SRS and LDI cascadings. To this purpose, we use seven coupled mode equations (7COM) to model the *first cascading of LDI*, and nine wave coupled mode equations (9COM) for the cascading of SRS. The coupled mode equations are solved in a finite, homogeneous plasma, using the method of characteristics [72] and the Lax-Wendroff scheme [73], with experimental parameters from the single hot-spot experiments explained in Chapter 4.

6.1 First Cascade of LDI

The first cascading of LDI occurs when the backscattered electron plasma wave in LDI decays into a secondary LDI process. When this happens, two new waves appear in the system: a forward propagating electron plasma wave (referred as the CEPW), and a cascade ion acoustic wave (CIAW).

Keeping the nomenclature used in Chapter 4, the new waves satisfy:

$$\omega_4 = \omega_6 + \omega_7, \tag{6.1}$$

$$k_4 = k_6 + k_7, \tag{6.2}$$

where the subscripts 6 and 7 refer to the cascading waves CEPW and CIAW, re-
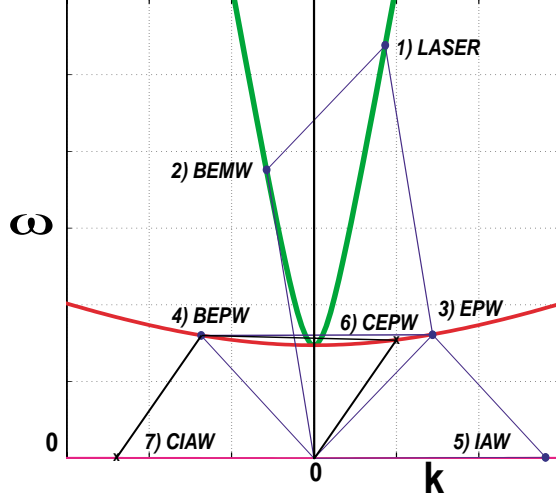
Figure 6-1: SRS coupled to LDI and first LDI cascade.

spectively. The subscripts 1 through 5, refer to the LASER, BEMW, EPW, BEPW and IAW, respectively. Figure (6-1) illustrates the dispersion relations and the phase matching conditions of the seven coupled waves.

Considering real wave envelopes and no wave de-phasing, the seven coupled modes equations are:

$$\left(\frac{\partial}{\partial t} + v_{g1}\frac{\partial}{\partial x} + \nu_1\right) a_1 = -K_{SRS} a_2 a_3, \tag{6.3}$$

$$\left(\frac{\partial}{\partial t} + v_{g2}\frac{\partial}{\partial x} + \nu_2\right) a_2 = K_{SRS} a_1 a_3, \tag{6.4}$$

$$\left(\frac{\partial}{\partial t} + v_{g3}\frac{\partial}{\partial x} + \nu_3\right) a_3 = K_{SRS} a_1 a_2 - K_{LDI} a_4 a_5, \tag{6.5}$$

$$\left(\frac{\partial}{\partial t} + v_{g4}\frac{\partial}{\partial x} + \nu_4\right) a_4 = K_{LDI} a_3 a_5 - K_{casc} a_6 a_7, \tag{6.6}$$

$$\left(\frac{\partial}{\partial t} + v_{g5}\frac{\partial}{\partial x} + \nu_5\right) a_5 = K_{LDI} a_3 a_4, \tag{6.7}$$

$$\left(\frac{\partial}{\partial t} + v_{g6}\frac{\partial}{\partial x} + \nu_6\right) a_6 = K_{casc} a_4 a_7, \tag{6.8}$$

$$\left(\frac{\partial}{\partial t} + v_{g7}\frac{\partial}{\partial x} + \nu_7\right) a_7 = K_{casc} a_4 a_6; \tag{6.9}$$

were $|a_\ell|^2 = \mathrm{w}_\ell/\omega_\ell$, w_ℓ, $v_{g\ell}$ and ν_ℓ are the wave action density, wave energy density,

100

group velocity and damping rate of the ℓ_{th} mode (for $\ell = 1 \rightarrow 7$).

The coupling coefficients for SRS and LDI are given in Chapter 4, in Eqs. (4.6) and (4.7), and the coupling coefficient for the first LDI cascade is

$$|K_{casc}| \approx \sqrt{\frac{2}{\epsilon_o}} \frac{e}{m_e} \frac{\omega_{pe}}{4 v_{Te}} \left(\frac{\omega_7}{\omega_4 \omega_6} \right)^{1/2} . \tag{6.10}$$

In the above model, the equations for the waves belonging to more than one triad have multiple nonlinear coupling terms (one for each triad). The EPW amplitude (a_3), in Equation (6.5),is coupled to the waves in SRS (a_1, a_2) and the waves in LDI (a_4, a_5). In Equation (6.6), on the other hand, the BEPW amplitude (a_4) is coupled to the waves in LDI (a_3, a_5) and the waves in the first LDI cascade (a_6, a_7).

Equations (6.3)–(6.9) assume that the EPW (a_3) and CEPW (a_6) are not directly coupled. However, as shown in Figure (6-1), their frequencies, wave numbers and group velocities are very similar, so a_3 and a_6 may be correlated (if their growth rates overlap). An alternative approach to consider the effects of the first LDI cascading would be to find the four coupled mode equations (instead of three) for the coupling of the slowly varying amplitudes of the EPW, BEPW, IAW and CIAW. These equations, however, need to be derived as in Appendix B, considering perturbations up to the third order in the field amplitudes. This investigation was done by D. Watson [52].

The energy conservation relations for the seven coupled waves are derived from Equations (6.3)–(6.9), just like it is done in Chapter 2 for the three waves problem. These relations are:

$$I_2 + \frac{\omega_2}{\omega_1} I_1 = 0, \tag{6.11}$$

$$I_7 + \frac{\omega_7}{\omega_6} I_6 = 0, \tag{6.12}$$

$$I_3 + \frac{\omega_3}{\omega_1} I_1 + \frac{\omega_3}{\omega_5} I_5 = 0, \tag{6.13}$$

$$I_5 + \frac{\omega_5}{\omega_4} I_4 + \frac{\omega_5}{\omega_6} I_6 = 0, \tag{6.14}$$

$$I_4 + \frac{\omega_4}{\omega_1} I_1 + \frac{\omega_4}{\omega_3} I_3 + \frac{\omega_4}{\omega_6} I_6 = 0. \tag{6.15}$$

As before, the integrals I_ℓ (for $\ell \to 1..7$) are defined by:

$$I_\ell = \left[\int_0^L \mathrm{w}_\ell(t',x)dx \right]_{t'=t} - \left[\int_0^L \mathrm{w}_\ell(t',x)dx \right]_{t'=0} + 2\nu_\ell \int_0^t dt' \int_0^L dx \mathrm{w}_\ell(t',x)$$

$$+ v_{g\ell} \int_0^t dt' \left[\mathrm{w}_\ell(t',x=L) - \mathrm{w}_\ell(t',x=0) \right], \quad (6.16)$$

where w_ℓ is the wave energy density in the ℓ_{th}. The meaning of the integrals in (6.16) is discussed in Chapter 2 (Section 2.3).

The error in the conservation relations [Eqs. (C.10)-(C.14), in Appendix C] has been evaluated throughout all the simulations, to assume the validity of the numerical results.

With the same normalization used in Chapter 4 (see Table 4.2) the normalized 7COM equations are:

$$\left(\frac{\partial}{\partial t} + v_{g1} \frac{\partial}{\partial x} \right) a_1 = -G a_2 a_3, \quad (6.17)$$

$$\left(\frac{\partial}{\partial t} + v_{g2} \frac{\partial}{\partial x} \right) a_2 = G a_1 a_3, \quad (6.18)$$

$$\left(\frac{\partial}{\partial t} + \frac{\partial}{\partial x} + \nu_3 \right) a_3 = G a_1 a_2 - a_4 a_5, \quad (6.19)$$

$$\left(\frac{\partial}{\partial t} - \frac{\partial}{\partial x} + \nu_4 \right) a_4 = a_3 a_5 - G_c a_6 a_7, \quad (6.20)$$

$$\left(\frac{\partial}{\partial t} + v_{g5} \frac{\partial}{\partial x} + \nu_5 \right) a_5 = a_3 a_4. \quad (6.21)$$

$$\left(\frac{\partial}{\partial t} + v_{g6} \frac{\partial}{\partial x} + \nu_6 \right) a_6 = G_c a_4 a_7, \quad (6.22)$$

$$\left(\frac{\partial}{\partial t} + v_{g7} \frac{\partial}{\partial x} + \nu_7 \right) a_7 = G_c a_4 a_6; \quad (6.23)$$

where $G_c = |K_{casc}|/|K_{LDI}|$.

Considering the single hot-spot experiments explained in Chapter 4, the group velocities are $v_{g1} \approx -v_{g2} \approx 30$, $v_{g3} \approx v_{g6} \approx -v_{g4} = 1$, and $v_{g5} \approx v_{g7} \approx 0$. The length of the interaction region is taken to be 225 μm (900 NxU) and the laser transit

$z\ [\mu m]$	ω_{6i}/ω_{6r}	ω_{7i}/ω_{7r}	ν_3	ν_4	ν_5	ν_6	ν_7	G	G_c
230	0.002	0.33	0.146	0.082	0.079	0.04	0.073	0.619	0.969
240	0.005	0.34	0.257	0.165	0.081	0.096	0.076	0.5882	0.971
250	0.007	0.34	0.314	0.21	0.081	0.131	0.076	0.5724	0.971
260	0.012	0.34	0.433	0.311	0.081	0.211	0.076	0.5535	0.973
270	0.018	0.34	0.547	0.411	0.081	0.295	0.076	0.5389	0.974
280	0.025	0.34	0.685	0.535	0.081	0.404	0.076	0.5228	0.975
290	0.035	0.34	0.851	0.687	0.081	0.54	0.076	0.5046	0.976
300	0.043	0.34	0.98	0.808	0.081	0.65	0.076	0.4915	0.977
310	0.053	0.34	1.13	0.949	0.081	0.78	0.076	0.478	0.978
370	0.122	0.34	1.99	1.78	0.081	1.58	0.076	0.4117	0.981

Table 6.1: Normalized parameters in the seven wave simulations, for $\lambda_o = 527\ nm$ and $\mathcal{I}_o = 6 \times 10^{15}\ Watts/cm^2$.

time (to cruise through the plasma) is approximately 30 NtU. All simulations were run for about 1500 NtU ($\sim 35\ psec$). The damping of the longitudinal waves is calculated from from the exact kinetic dispersion, Eq. (2.33), considering a neutral plasma with two ion species in thermal equilibrium (70% hydrogen and 30% carbon). The normalized dampings and coupling coefficients, for the different parameters in Figure (4-1.b), are summarized in Table (6.1). In such table, ν_3, ν_4, ν_5 and G, are just the same used in Chapter 4 (they are repeated here for convenience). While the damping of the ion acoustic waves and the coupling coefficients are almost constant, the dampings of electron plasma waves change by almost one order of magnitude. In all cases, the Landau damping of the cascading daughters is smaller than the real frequency, in agreement with the slowly varying amplitude approximation.

Numerical Results

The real wave envelopes (a_ℓ) are evolved numerically in time and one dimensional space, starting from an initial noise level, which was set to $0.0005a_o$ (for easy comparison with Chapter 4).

The detailed description of the early space/time evolution of the coupled waves is omitted here (it is similar to the one explained in Chapter 4). Instead, we focus
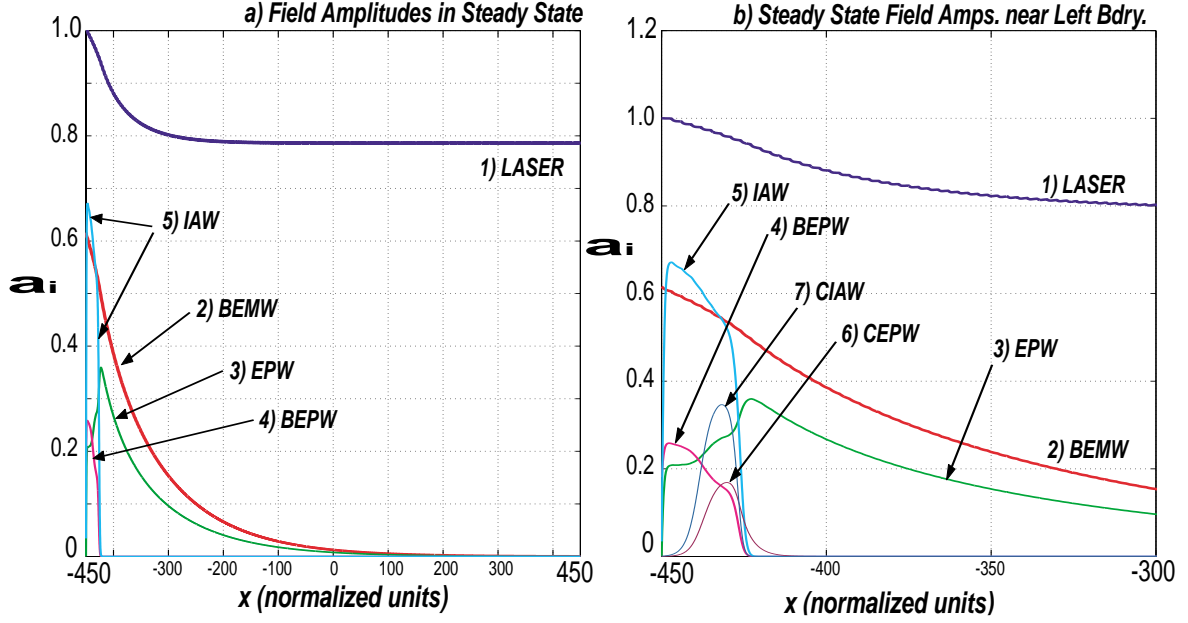
Figure 6-2: Field amplitudes in steady state for $k\lambda_{De} = 0.398$ ($z = 290~\mu m$, $n_e/n_{cr} = 0.027$, $T_e = 700eV$ and $T_i = 142eV$). Laser intensity $\mathcal{I}_o = 6 \times 10^{15}~Watts/cm^2$ and wavelength $\lambda_o = 527~nm$.

our efforts to understand the nature of the steady state, and the effects that the first cascading of LDI produces on the saturated SRS backscattering. Similar to Chapter 4, during early times of the simulations one basically observes that SRS grows locally, in a narrow region near the left boundary (where the laser enters the plasma). The EPW locally decays to LDI (wherever it surpasses the threshold condition $\sqrt{\nu_4\nu_5}$), giving place to a series of space/time oscillations that eventually evolve into a steady state. The main difference with Chapter 4 is that now the BEPW (a_4) also decays locally into the first LDI cascade (a_6 and a_7), whenever a_4 surpasses the threshold for the LDI cascading $\sqrt{\nu_6\nu_7}$.

Figure (6-2) illustrates the field amplitudes in the steady state, for plasma parameters at $z = 290~\mu m$ ($k\lambda_{De} = 0.398$). For clarity, Figure(6-2.a) only shows the amplitudes of the five waves in SRS and LDI (a_1 to a_5) throughout the plasma, and Figure (6-2.b) shows all the seven waves in a small region near the left boundary ($x = -450~NxU$).

The steady state is very similar to the one observed in Chapter 4 (in which no

cascading was considered). As before, the BEMW (a_2) and the EPW (a_3) grow towards the left with the SRS characteristic growth-rate (Eq. 4.21). In such fashion, the rightmost part of the interaction region ($x > -400 \ NxU$) exhibits only SRS, while the EPW amplitude (a_3) is below the LDI threshold ($\sqrt{\nu_4 \nu_5} \approx 0.236$). Once a_3 exceeds the LDI threshold, an overshoot is observed (towards the left), followed by the saturation of a_3. The overshoot and saturation of a_3 can be better appreciated in Figure (6-2.b), which is a detailed view of the region near the left boundary.

In Figure(6-2.b), the overshoot and saturation of a_3 are similar to Chapter 4. However, different from before, a_3 does not saturate to the LDI threshold. A clear modification of a_3 can be observed in $-440 < x < -430 NxU$, where the LDI cascading daughters (CEPW and CIAW) have grown to an appreciable amplitude. To explain this modification, we look at the steady states obtained with other plasma parameters, corresponding to different dampings of the electron plasma waves (i.e., different $k\lambda_{De}$).

First of all, when $k\lambda_{De} > 0.4$ (large EPW damping) the EPW wave envelope (a_3) is always below the LDI threshold, unless the size of the plasma is increased. In this case, SRS is completely independent of LDI and LDI cascading. In the steady state, the amplitudes a_1, a_2 and a_3 are equal to the amplitudes obtained with the 5COM equations (for SRS/LDI), and with the 3COM equations (for SRS only). The details of this kind of saturation have already been explained in Chapter 4 (Section 4.4).

For weaker EPW damping ($k\lambda_{De} < 0.4$) a_3 reaches the LDI threshold within simulation region and excite LDI. If the amplitude of the LDI-BEPW (a_4) grows to a sufficiently large amplitude, the first cascade of LDI is also excited. Figure (6-3), for example, shows the steady state corresponding to the plasma parameters at $z = 250$ μm ($k\lambda_{De} = 0.319$).

In Figure (6-3) a_3 reaches the LDI threshold ($\sqrt{\nu_4 \nu_5} \approx 0.13$) at $x_p \approx -300$, as can be corroborated with Eqs. (4.21)–(4.22). In Figure (6-3.b), on the other hand, when a_3 begins to deplete (towards the left) at $x \approx -360NxU$, a_4 begins to grow (as in Section 4.3). However, the growth of a_4 suddenly settles to a constant amplitude
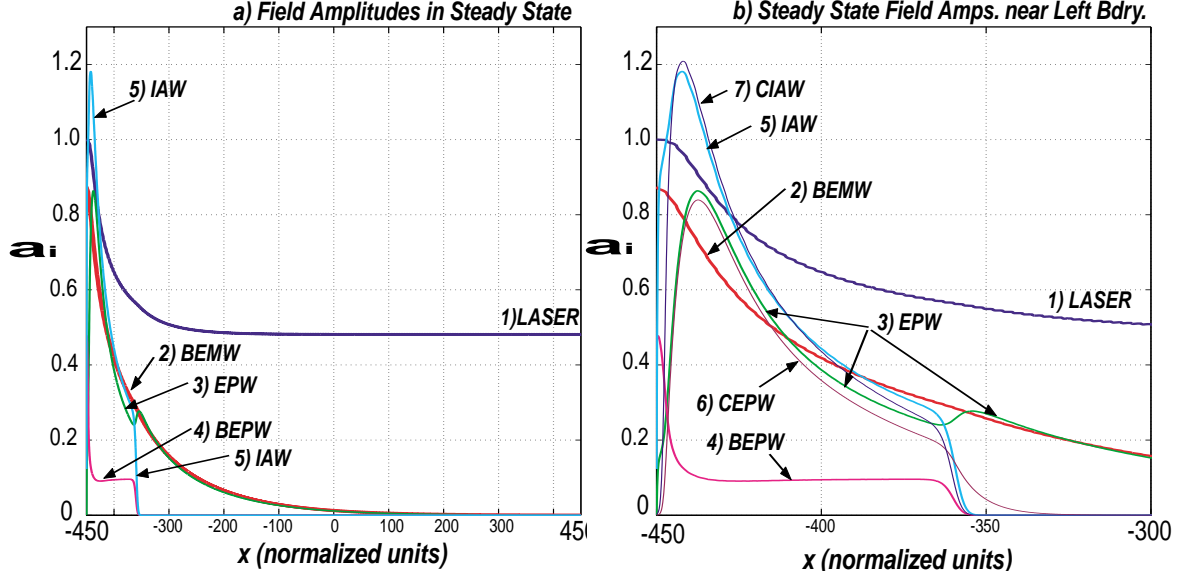
Figure 6-3: Field amplitudes in steady state for $k\lambda_{De} = 0.319$ ($z = 250\ \mu m$, $n_e/n_{cr} = 0.04$, $T_e = 700eV$ and $T_i = 160eV$). Laser intensity $\mathcal{I}_o = 6 \times 10^{15}\ Watts/cm^2$ and wavelength $\lambda_o = 527\ nm$.

(where the cascading daughters have become visible), and a_3 begins to grow again. The excitation of the LDI cascading prevents the BEPW from growing, and therefore weakens LDI (reduces a_4a_5 in Eq. 6.19, and a_4a_3 in Eq. 6.21). A very interesting observation, is that the saturated amplitude of the BEPW (a_4) corresponds exactly to the LDI cascading threshold: $\sqrt{\nu_6\nu_7} \approx 0.1$; this is the equilibrium point between the competition of LDI (that induces the growth of a_4) and LDI cascading (that effectively damps a_4). This saturation of a_4 is similar to the saturation of a_3 explained in Section (4.3).

The plasma parameters at $z = 290$ ($k\lambda_{De} = 0.39$) correspond to the transition between having pure SRS, and having SRS with LDI and LDI cascading. When the cascading is excited, it works as an effective nonlinear damping for the BEPW (prevents a_4 from growing to significant amplitudes), thus annihilating the effects of LDI on SRS. This conclusion is further discussed later in the present section, after a better understanding of the steady state wave-wave interactions has been obtained.

Figure (6-4) compares the EPW (a_3) and BEMW (a_2) obtained with the 5COM equations (see Chapter 4) and the 7COM equations, for $k\lambda_{De} = 0.319$. In Figure
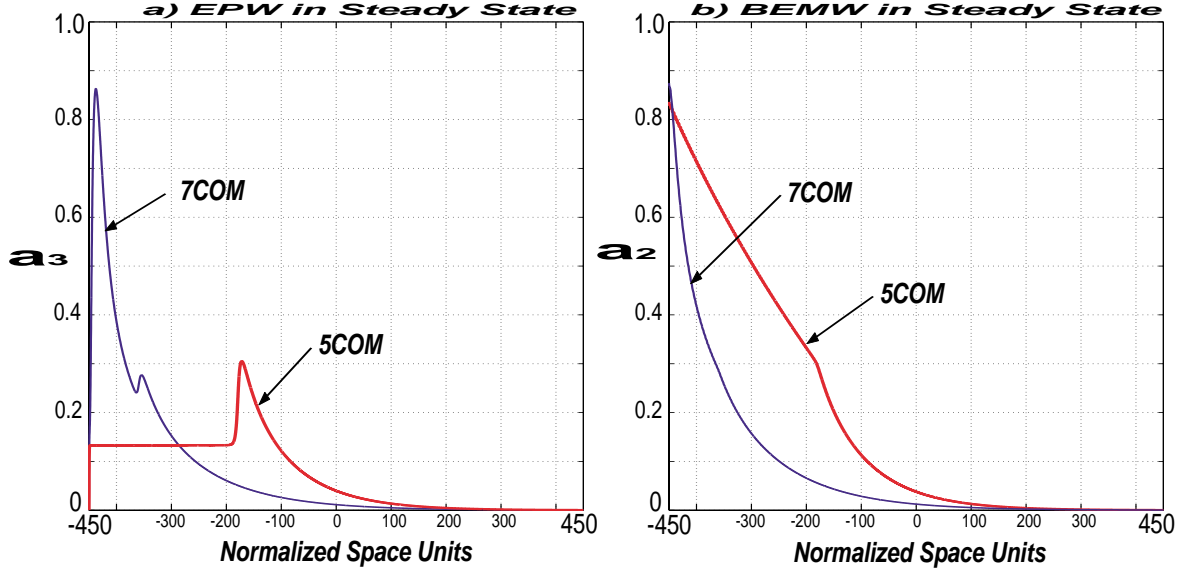
Figure 6-4: Steady state BEMW & EPW in the 5COM and 7COM simulations, for $k\lambda_{De} = 0.319$.

(6-4.a), the 5COM-EPW saturates at the LDI threshold condition ($\sqrt{\nu_4 \nu_5} \approx 0.13$), while the 7COM-EPW continues to grow towards the left (after a small depletion at $x \approx -360 NxU$). The small indentation observed in the 7COM-EPW, corresponds to the excitation of the LDI cascading (see Fig. 6-3.b). When LDI is excited, a_3 depletes and a_4 grows. However, when a_4 saturates at the cascading threshold, a_3 begins to grow again. The figure clearly shows that LDI cascading basically reduces LDI.

In the rightmost section of the plasma, the spatial growth rate (to the left) of the 7COM-EPW is smaller than the growth of the 5COM-EPW. The reason for this, is that the larger a_3 near the left boundary produces a stronger depletion of the laser ($a_3 a_2$ in Eq. 6.17), therefore leading to a weaker parametric SRS in the rightmost part of the plasma (where the laser amplitude remains constant and no LDI or LDI cascading are present). The depletion of the laser can be observed in Figures (6-3.a) and (4-4.a).

Figure (6-4.b) illustrates the steady state amplitude of the BEMW (a_2). When no cascading is considered (5COM), the onset of LDI modifies the SRS parametric growth of a_2. However, when cascading is considered, the effects of LDI are reduced and a_2 continues growing to the left, as if LDI was never excited. If there is any
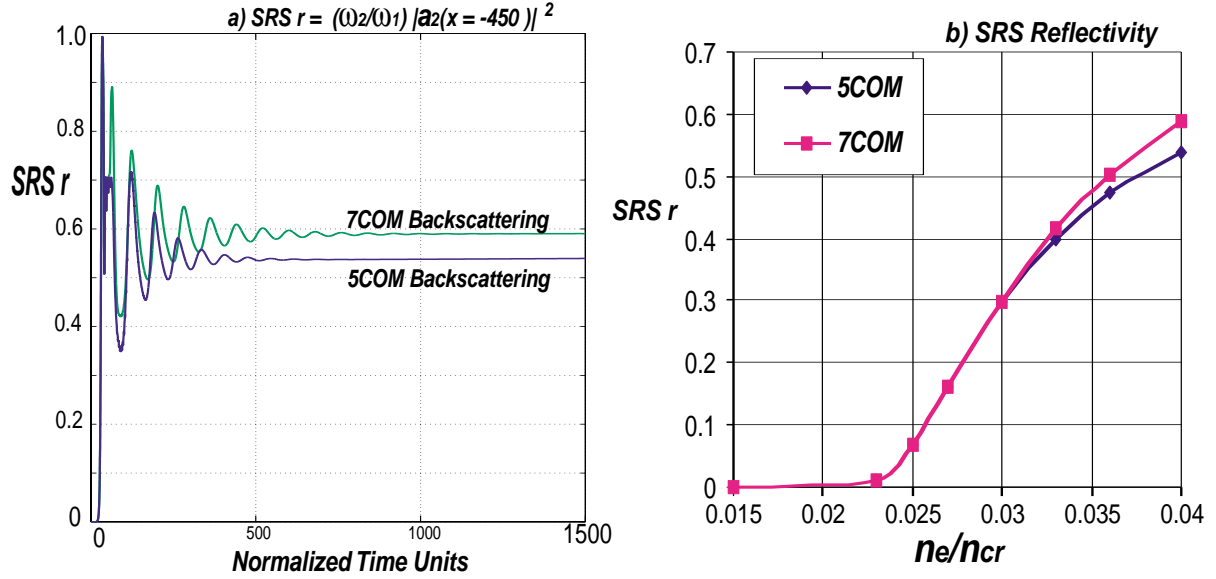
Figure 6-5: SRS backscattering: 7COM vs. 5COM.

modification of the growth, it is not appreciable in the figure.

In summary, the above simulations show that LDI cascading reduces the effects of LDI on SRS, thus producing a larger SRS reflectivity (see Figure 6-4.b). In the 7COM case, the EPW envelope has a bigger amplitude near the left boundary, and in turn the SRS reflectivity is larger.

Time evolution of the SRS backscattering

To conclude Section (6.1), we look at the time variation of the SRS reflectivity (Eq. 4.22). Figure (6-5.a) compares the reflectivities corresponding to the 5COM and 7COM equations, for $k\lambda_{De} = 0.319$). Again, the SRS reflectivity with LDI cascading (7COM) is larger than the reflectivity without cascading (5COM). Different plasma parameters lead to similar pictures, which are not described here. In every case, the saturation of SRS occurs in $t < 1000\ NtU$ ($\sim 22psec$) which is a small time compared to the duration of the experimental laser pulses ($\sim 1nsec$).

Figure (6-5.b) shows the total SRS backscattering obtained with the 5COM equations (lower curve) and with the 7COM equations. While both reflectivities are identical in the lower density limit (large $k\lambda_{De}$), when the density increases (the EPW

damping decreases) the SRS backscattering with the LDI cascading is larger than the backscattering without cascading. In the larger damping limit, LDI and LDI cascading are not excited at all, so the same SRS reflectivity is found with the 7COM, 5COM and 3COM equations (for SRS, SRS/LDI and SRS/LDI/Csc, respectively).

In the framework of my numerical investigation, I find that the first LDI cascading reduces the effects of LDI on SRS, thus leading to an increment of the SRS backscattering. In the same fashion, however, when a second cascading of LDI is allowed (i.e., a_6 can decay into a consecutive LDI) it is likely to reduce the effect of the first LDI cascade, thus leading again to a lower SRS backscattering. But this has not been shown. The SRS reflectivity in the presence of multiple cascades of LDI has not been investigated.

6.2   Cascading of SRS

Now we turn our attention to the possible cascading of SRS, which can occur when the frequency of the BEMW (ω_2) is larger than two times the electron plasma frequency ($\omega_2 > 2\omega_{pe}$). In this case, a_2 can decay into a secondary SRS process, as illustrated in Figure (6-6). We have investigated the implications of such cascading, allowing the electron plasma waves (in both the principal and secondary SRS) to decay into their respective LDIs. To this purpose, the corresponding nine wave coupled mode equations (9COM), have been integrated numerically.

To model the SRS cascading as described above, four new waves need to be considered in the SRS/LDI system that was explained in Chapter 4. These waves are the forward propagating electromagnetic wave due to the cascade of SRS (8: EMWc), the backscattered electron plasma wave in such cascade (9: EPWc), the forward propagating electron plasma wave due to the LDI decay of the EPWc (10: FEPWc) and the ion acoustic wave in such LDI decay (11: IAWc). These waves, as well as their dispersion relations and phase matching conditions, are illustrated in Figure (6-6).

For consistency with the rest of the thesis, the new four waves are numbered with $\ell = 8 \rightarrow 11$, for the EMWc, EPWc, FEPWc and IAWc, respectively. In such way,
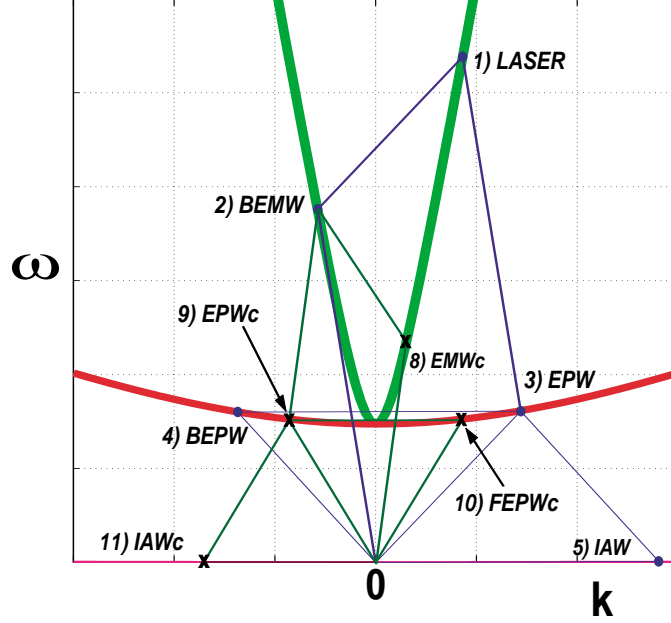
Figure 6-6: SRS with SRS cascading and LDI.

the seven waves considered in Section (6.1) are still numbered with $\ell = 1$ through 7, corresponding to the LASER, BEMW, EPW, BEPW, IAW, CEPW and CIAW, respectively.

Considering the laser-plasma parameters in the single hot-spot experiments [6], real wave envelopes, no wave de-phasing and the normalization in Table (4-2), one obtains the eleven coupled mode equations to model the nonlinear coupling between the wave envelopes of the above eleven modes:

$$\left(\frac{\partial}{\partial t} + v_{g1} \frac{\partial}{\partial x} \right) a_1 = -G_{\scriptscriptstyle SRS} a_2 a_3, \tag{6.24}$$

$$\left(\frac{\partial}{\partial t} + v_{g2} \frac{\partial}{\partial x} \right) a_2 = G_{\scriptscriptstyle SRS} a_1 a_3 - G_{\scriptscriptstyle SRScc} a_8 a_9, \tag{6.25}$$

$$\left(\frac{\partial}{\partial t} + v_{g3} \frac{\partial}{\partial x} + \nu_3 \right) a_3 = G_{\scriptscriptstyle SRS} a_1 a_2 - a_4 a_5 \tag{6.26}$$

$$\left(\frac{\partial}{\partial t} + v_{g4} \frac{\partial}{\partial x} + \nu_4 \right) a_4 = a_3 a_5 - G_{\scriptscriptstyle Casc} a_6 a_7, \tag{6.27}$$

110

$$\left(\frac{\partial}{\partial t} + v_{g5} \frac{\partial}{\partial x} + \nu_5 \right) a_5 = a_3 a_4, \tag{6.28}$$

$$\left(\frac{\partial}{\partial t} + v_{g6} \frac{\partial}{\partial x} + \nu_6 \right) a_6 = G_{Casc} a_4 a_7, \tag{6.29}$$

$$\left(\frac{\partial}{\partial t} + v_{g7} \frac{\partial}{\partial x} + \nu_7 \right) a_7 = G_{Casc} a_4 a_6, \tag{6.30}$$

$$\left(\frac{\partial}{\partial t} + v_{g8} \frac{\partial}{\partial x} + \nu_8 \right) a_8 = G_{SRScc} a_2 a_9, \tag{6.31}$$

$$\left(\frac{\partial}{\partial t} + v_{g9} \frac{\partial}{\partial x} + \nu_9 \right) a_9 = G_{SRScc} a_2 a_8 - G_{LDIscc} a_{10} a_{11}, \tag{6.32}$$

$$\left(\frac{\partial}{\partial t} + v_{g10} \frac{\partial}{\partial x} + \nu_{10} \right) a_{10} = G_{LDIscc} a_9 a_{11}, \tag{6.33}$$

$$\left(\frac{\partial}{\partial t} + v_{g11} \frac{\partial}{\partial x} + \nu_{11} \right) a_{11} = G_{LDIscc} a_9 a_{10}. \tag{6.34}$$

Again, $|a_\ell|^2 = \mathrm{w}_\ell / \omega_\ell$, w_ℓ, $v_{g\ell}$ and ν_ℓ are the wave action density, wave energy density, group velocity and damping rate of mode ℓ. Since the cascading of LDI is excluded from the investigation in this Section, the cascading coupling coefficient is set to zero ($G_{Casc} \equiv 0$). The normalized coupling coefficients for the SRS cascading and the LDI of the EPWc, are $G_{SRScc} = |K_{SRScc}/K_{LDI}|$ and $G_{LDIscc} = |K_{LDIscc}/K_{LDI}|$, where:

$$|K_{SRScc}| \approx \sqrt{\frac{2}{\epsilon_o}} \frac{e}{m_e} \frac{k_9}{4} \left(\frac{\omega_{pe}^2}{\omega_2 \omega_8 \omega_9} \right)^{1/2}, \tag{6.35}$$

$$|K_{LDIscc}| \approx \sqrt{\frac{2}{\epsilon_o}} \frac{e}{m_e} \frac{\omega_{pe}}{4 v_{Te}} \left(\frac{\omega_{11}}{\omega_9 \omega_{10}} \right)^{1/2}. \tag{6.36}$$

Considering the single hot-spot experimental parameters (see Figure 4-1.b), and the normalization of Equations (6.24)-(6.34), the group velocities are again: $v_{g1} \approx v_{g8} \approx -v_{g2} \approx 30$, $v_{g3} \approx v_{g10} \approx -v_{g4} = 1$, $v_{g5} \approx v_{g11} \approx 0$. The length of the interaction region is 900 NxU, and the laser transit time 30 NtU (same as in Chapter 4). The collisional damping of the EMWc (ν_8) is taken as $\nu_8 = 0$. The Landau dampings of the EPWc, FEPWc and IAWc, as well as the coupling coefficients (G_{SRScc} and G_{LDIscc}), are given in Table (6.2).

$z\ [\mu m]$	n_e/n_{cr}	$k_3\lambda_{De}$	ω_2/ω_{pe}	ν_9	ν_{10}	ν_{11}	G_{SRScc}	G_{LDIscc}
230	0.05	0.283	3.35	0.0008	0.0001	0.0488	0.619	0.832
240	0.043	0.308	3.68	0.0069	0.0017	0.0517	0.593	0.847
250	0.04	0.319	3.85	0.0142	0.0044	0.053	0.579	0.853
260	0.036	0.339	4.11	0.0377	0.0157	0.054	0.562	0.862
270	0.033	0.356	4.32	0.071	0.035	0.053	0.549	0.8678
280	0.03	0.375	4.58	0.125	0.073	0.0533	0.534	0.874
290	0.027	0.398	4.87	0.208	0.136	0.054	0.517	0.8803
300	0.025	0.416	5.09	0.283	0.19	0.056	0.505	0.884
310	0.023	0.435	5.34	0.377	0.279	0.057	0.492	0.888
370	0.015	0.548	6.78	1.03	0.87	0.057	0.428	0.905

Table 6.2: Normalized parameters in the SRS cascading problem, for $\lambda_o = 527\ nm$ and $\mathcal{I}_o = 6 \times 10^{15}\ Watts/cm^2$.

As shown in the Table, the frequency of the BEMW (ω_2) is always larger than twice the plasma frequency: $\omega_2/\omega_{pe} > 2$. The Landau dampings of electron plasma waves (ν_9 and ν_{10}), on the other hand, change by approximately an order of magnitude, increasing when n_e/n_{cr} is reduced (larger $k_3\lambda_{De}$). The normalized coupling coefficients (G_{SRScc} and G_{LDIscc}) and the IAW damping (ν_{11}), are almost constant in the Table. With such parameters, the eleven wave envelopes were evolved in time and space, using the two numerical techniques explained in Appendix C. Again, both techniques gave almost identical results and they are not discussed any longer.

Like in Chapter 4, all the boundary conditions were set to an estimated noise level, except for the laser's boundary condition, which was set to $a_1(x = -450) = 1$ (considering that it is externally driven through the left boundary). The initial noise level was again set to 0.0005 (normalized amplitude units), for easy comparison with the numerical results in Chapter 4.

Since G_{Casc} was set to zero, the space/time evolution of the daughter waves in the first LDI cascade (a_6 and a_7), is independent of the other waves in the system and only exhibits an amplitude decay (due to their non zero dampings). The other nine waves evolved in time and space until reaching a clear saturation.

For reasons of brevity, the discussion of the early time evolution (before the sat-
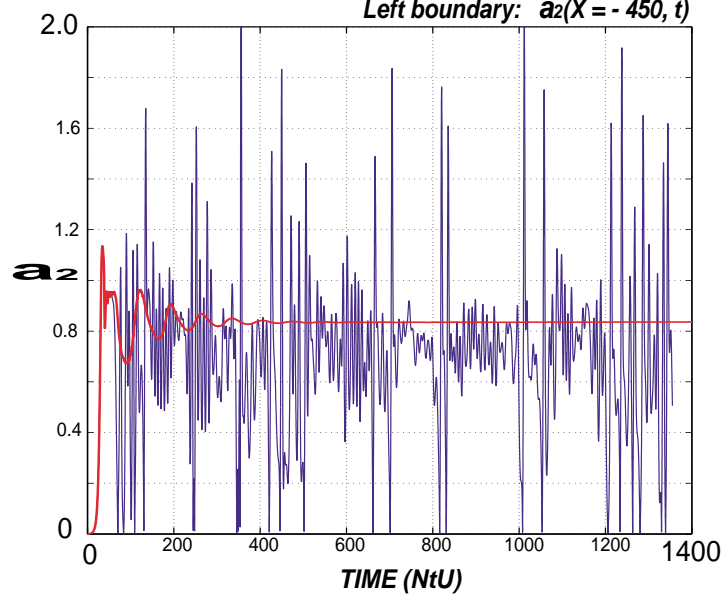
Figure 6-7: Time evolution of $a_2(x = -450, t)$ in SRS cascade with LDI, for $k\lambda_{De} = 0.319$ ($z = 250~\mu m$, $n_e/n_{cr} = 0.04$, $T_e = 700 eV$ and $T_i = 160 eV$). Laser intensity $\mathcal{I}_o = 6 \times 10^{15}~Watts/cm^2$ and wavelength $\lambda_o = 527~nm$.

uration of SRS) is not provided. The attention of the reader is instead directed to understand the nature of the saturated state, which always occurred in $t < 200 NtU$ ($t < 10~psec$). In such saturated state, the wave envelopes exhibit space/time fluctuations near the left boundary (where the laser enters the plasma), similar to the case of weak EPW damping (explained in Section 4.5). In spite of the space/time fluctuations, on the average the envelopes remained constant.

Figure (6-7) illustrates the time evolution of the BEMW amplitude at the left boundary [$a_2(x = -450, t)$]. As it can be observed, $a_2(x = -450, t)$ exhibits oscillations in time, but remains constant on the average. As a reference to the reader, the corresponding evolution, obtained with the 5COM equations (see Section 4.3), is also provided. While at early times ($t < 100 NtU$) both amplitudes are almost identical (they overlap), the amplitude with no SRS cascading rapidly reaches a steady state, and the amplitude with SRS cascading begins to oscillate in time. The average amplitude of $a_2(x = -450, t)$ with SRS cascading, is below the steady state amplitude obtained with no SRS cascading. Therefore, the cascading of SRS has resulted in a reduction of the above SRS reflectivity.
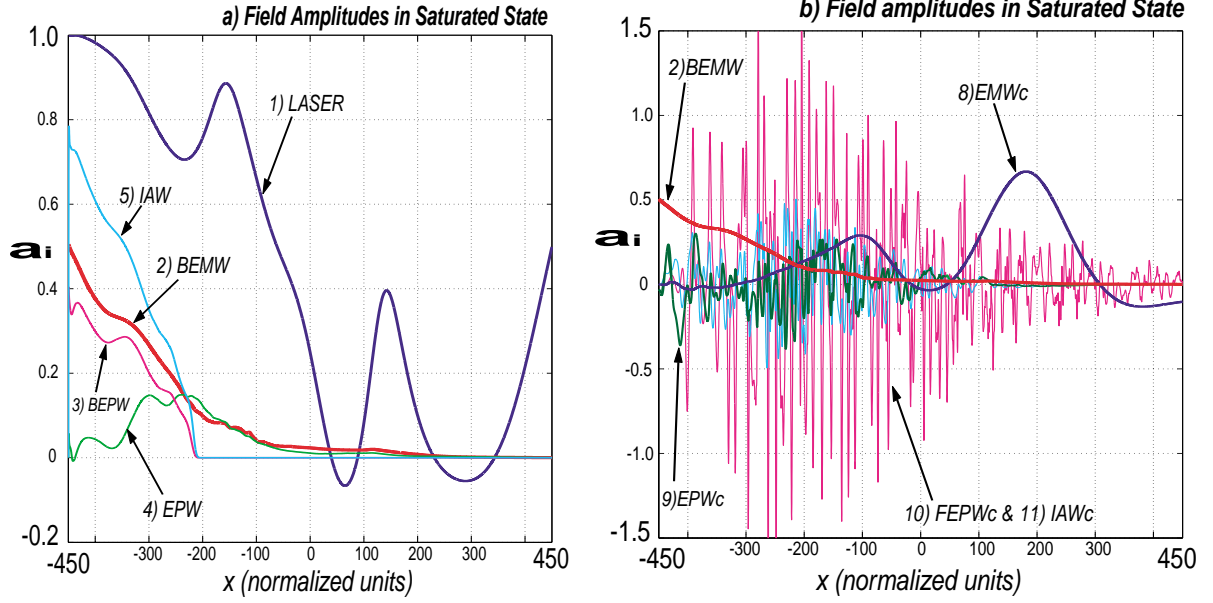
Figure 6-8: Saturated wave envelopes at time $t = 1350NtU$, for $k\lambda_{De} = 0.319$ ($z = 250 \ \mu m$, $n_e/n_{cr} = 0.04$, $T_e = 700eV$ and $T_i = 160eV$). Laser intensity $\mathcal{I}_o = 6 \times 10^{15}$ $Watts/cm^2$ and wavelength $\lambda_o = 527 \ nm$.

A sample of the wave amplitudes in the saturated state, is shown in Figure (6-8) for all the waves in SRS cascading with LDI. For clarity purposes, Figure (6-8.a) shows only the envelopes of the five waves in the SRS coupled to LDI that was investigated in Chapter 4 (see Figure 4-4.a). Figure (6-8.b), on the other hand, illustrates the envelopes of the five waves in the SRS cascading and its LDI (a_2, a_8, a_9, a_{10} and a_{11}). While the illustrated field amplitudes change with time, the figures should be useful to explain some important aspects of the wave-wave interactions in space. However, since the main purpose of this Section is to investigate the overall effects of SRS cascading on the SRS reflectivity, no detailed description of the space/time fluctuations is provided.

First of all, in Figure (6-8.a) the laser amplitude (a_1) is observed to decay as the laser propagates through the plasma (from left to right). Even if a_1 exhibits oscillations in space, within the simulation region, its amplitude is reduced because the laser loses energy (to a_2 and a_3) as it propagates through the plasma. The space fluctuations observed in a_1, indicate that rapid oscillations of the field amplitudes occur near the left boundary. The time scaling of such oscillations, needs to be smaller

114
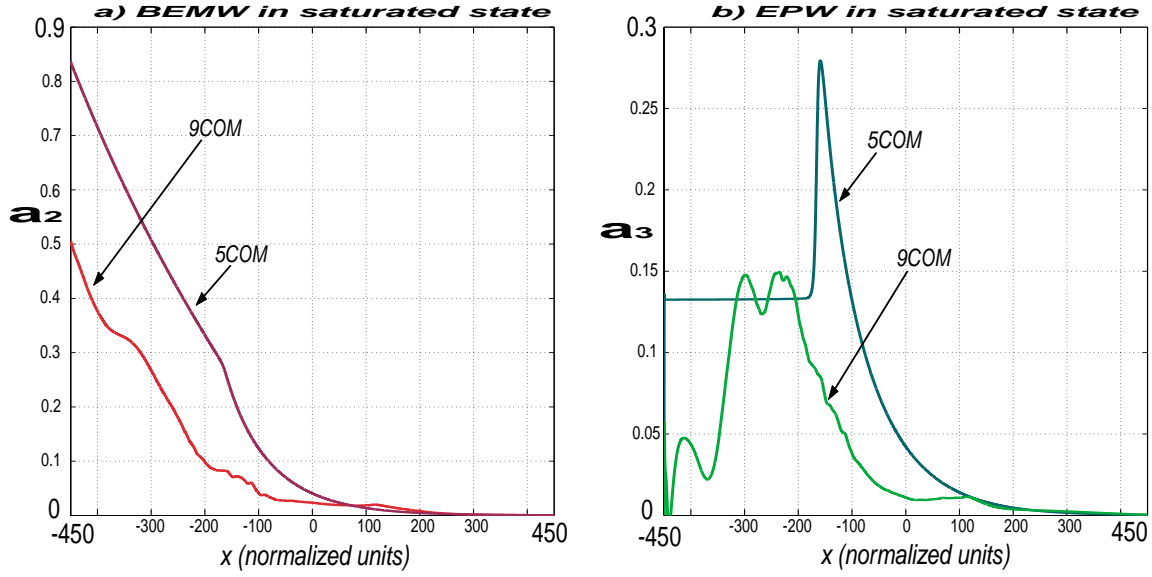
Figure 6-9: BEMW & EPW in the 5COM and 9COM simulations ($k\lambda_{De} = 0.319$).

than $30NtU$, to show up in the amplitude of the laser (before it transits through). The amplitude of the BEMW, on the other hand, grows towards the left, starting from the initial noise level at the right boundary (its boundary condition). The growing amplitude of the BEMW (a_2) excites the cascading of SRS (a_8 and a_9), as illustrated in Figure (6.8-b). In this figure, the amplitude of the EMWc (a_8) grows from left to right, as it propagates through the plasma and takes energy from a_2 (Eqs. 6.25 and 6.31). The amplitude of the EPWc (which can be considered almost stationary) exhibits a larger amplitude in $-300 < x < -100$, where it decays into a secondary LDI (a_{10} and a_{11}). The excitation of the SRS cascading leads to a modification of the BEMW, which instead of growing with the parametric SRS growth rate (as in Chapter 4), now grows with a perturbed growth rate that changes with time. The modified growth of the BEMW, produces a modification of the LDI-EPW, which instead of saturating at the LDI threshold, now oscillates in time (accordingly with the oscillations of the BEMW, that are produced in the SRS cascading).

A better idea of the way that SRS cascading modifies the BEMW (a_2) and EPW (a_3), can be obtained from Figure (6-9). Here the wave envelopes a_3 and a_2 from Figure (6-8.a), are compared to their 5COM steady state counterparts (see Figure 4-4.a). While in steady state the 5COM amplitude a_2 is completely independent
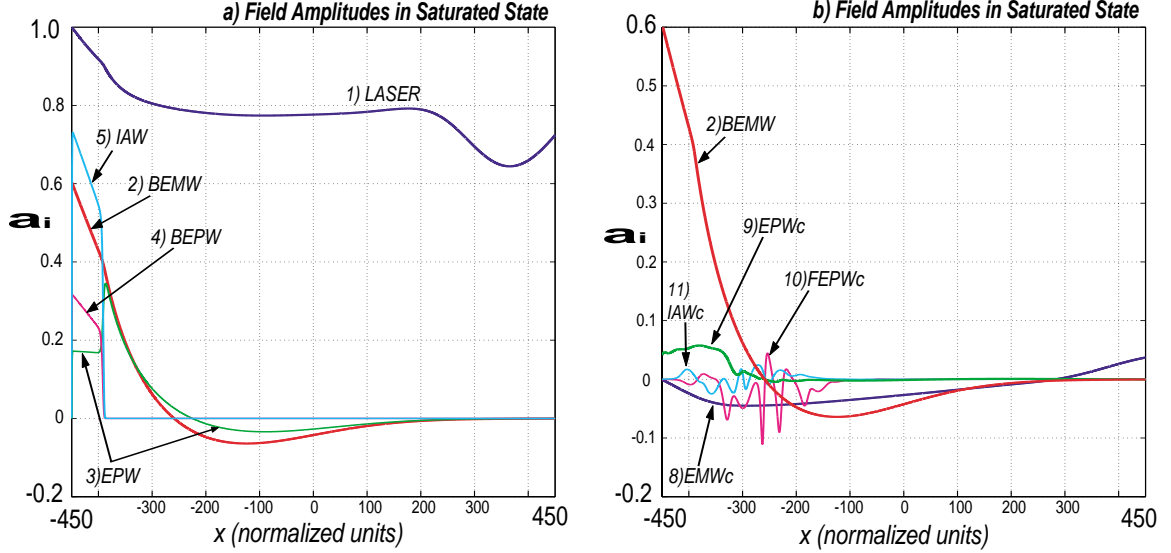
Figure 6-10: Saturated wave envelopes in SRS cascade with LDI, for $k\lambda_{De} = 0.356$ ($z = 270 \ \mu m$, $n_e/n_{cr} = 0.033$, $T_e = 700 eV$ and $T_i = 150 eV$). Laser intensity $\mathcal{I}_o = 6 \times 10^{15} \ Watts/cm^2$ and wavelength $\lambda_o = 527 \ nm$.

of time (steady state), the 9COM amplitude fluctuates with a periodicity of ~ 15 NtU. In spite of the fluctuations, Figure (6-9.a) clearly shows that the excitation of SRS cascading perturbs the parametric spatial growth rate (to the left) of a_2 (which was observed in Chapter 4). Such modification of the BEMW, modifies in turn, the amplitude of the EPW (a_3), as shown in Figure (6-9.b). Again, a_3 does not saturate to the LDI threshold condition, and instead, is oscillates in time and space.

When the dampings of the electron plasma waves are increased, the effects of the SRS cascading are reduced. To illustrate this remark, Figure (6-10) shows the field amplitudes with $z = 270\mu m$ ($n_e/n_{cr} = 0.033$, $k\lambda_{De} = 0.356$). In Figure (6-10.b), the amplitude of the oscillations in the SRS cascading (and its LDI) have been clearly reduced. The amplitudes of the original five waves ($a_1 \rightarrow a_5$), exhibit a saturation which resembles the steady state explained in Chapter 4. Again, there is no definitive steady state, and the wave envelopes illustrated in Figure (6-10.a) are time dependent. The time oscillations of the BEMW at the left boundary, $a_2(x = -450, t)$, are shown in Figure (6-11). In this figure, the oscillations (due to the SRS cascading) are not as large and fast, as in Figure (6-7), which corresponds to a weaker damping $[k\lambda_{De} = 0.319]$.
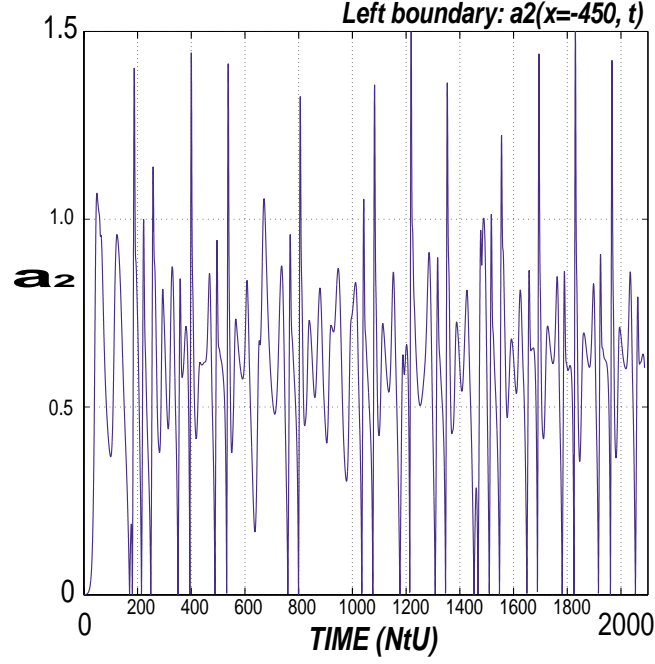
Figure 6-11: Time evolution of $a_2(x = -450, t)$ in SRS cascade with LDI, for $k\lambda_{De} = 0.356$ ($z = 270~\mu m$, $n_e/n_{cr} = 0.033$, $T_e = 700eV$ and $T_i = 150eV$). Laser intensity $\mathcal{I}_o = 6 \times 10^{15}~Watts/cm^2$ and wavelength $\lambda_o = 527~nm$.

When the dampings of the longitudinal modes are further increased, the effects of SRS cascading are completely annihilated. The reason for this is that a_9 remains at low amplitudes (due to the large ν_9), therefore weakening the nonlinear interaction in the SRS cascading (reducing $a_9 a_8$ in Eq. 6.25, and $a_9 a_2$ in Eq. 6.31). The SRS reflectivity as a function of the electron plasma density (n_e/n_{cr}) is shown in Figure (6.12). As a reference to the reader, the SRS backscattering obtained with the 5COM equations is also provided in this figure. It can be observed that at low n_e/n_{cr} (large $k\lambda_{De}$) the effects of SRS cascading are negligible. However, as the density increases ($k\lambda_{De}$ reduced), the SRS cascading produces a significant reduction of the total SRS reflectivity.

The significant reduction of the backscattering that was observed in Chapter 4, when $n_e/n_{cr} = 0.05$, is not observed any more. The space/time structures in the EPW amplitude that produced a wave de-phasing (see Section 4.5), are destroyed by the SRS cascading.
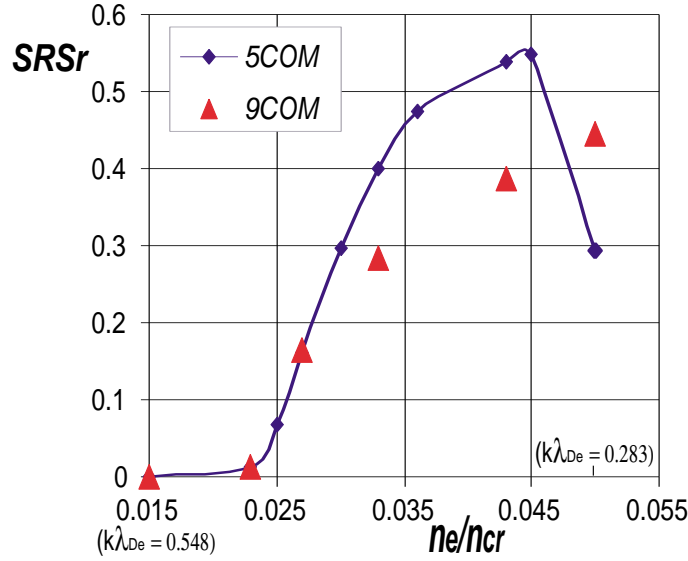
Figure 6-12: SRS Backscattering: 9COM vs. 5COM.

6.3 Analysis and Discussion

The effects of the possible cascadings of SRS and LDI, have been investigated throughout the present chapter.

It is found that the first cascading of LDI increases the SRS reflectivity, because it annihilates the effects of the principal LDI (which, as explained in Chapter 4, reduce the SRS backscattering). When the first LDI cascade is allowed in the SRS/LDI system, the amplitude of the BEPW (a_4) is weakened by its decay to the cascading daughters (a_6 and a_7). A weaker a_4, in turn, debilitates the nonlinear interactions in the principal LDI ($a_4 a_5$ in Eq. 4.17), and therefore reinforces SRS [i.e. a_3 does not saturate at the LDI threshold].

The investigation of multiple LDI cascadings has been left as a problem for the future. While the first cascade of LDI annihilates the principal LDI, a further cascade would annihilate the effects of the first cascade (therefore allowing the principal LDI to develop as if there where no cascades at all).

The possible cascading of SRS was also investigated. While such cascading has not been observed or perhaps looked for experimentally, we find that it is probable to

118

occur, because of the low electron plasma density ($n_e/n_{cr} \ll 0.25$). In the framework of numeric simulations, it is found that the SRS cascading produces a significant reduction of the SRS backscattering, when $k\lambda_{De}$ is small (i.e., weak Landau damping). While it appears that such cascading has not been investigated before, it should not be discarded, because it may have a strong effect on the saturation of SRS. Such cascading can also couple to the two-plasmon decay [39], and this needs further study.

.

Chapter 7

Conclusions

The research presented in this thesis has been inspired by recent experiments on the stimulated Raman backscattering in ICF laser-plasma interactions, which have suggested the coupling of SRS to the Langmuir decay interaction (LDI). I have studied the nonlinear interaction between SRS and LDI, and the subsequent saturation of SRS, based upon the simplest description of nonlinear coupled mode equations and for three different experimental regimes of the electron plasma wave damping: 1) strong damping, 2) moderate damping, and 3) weak damping. Towards this end, I have studied in detail the space-time evolution of the coupled modes equations (COM) in a finite length plasma. With these equations, I have investigated the coupling of SRS to LDI, and also their cascadings.

I have carried out detailed simulations using two different numerical techniques, which are based on the Lax-Wendroff integration scheme and the method of characteristics, respectively. The numerical results have been checked to ensure that the energy conservation relations (Manley-Rowe) are satisfied at all times.

My numerical simulations reveal some interesting physics responsible for the saturation of SRS with LDI. First, I find that the onset of LDI reduces the SRS reflectivity, and that the damping of EPW plays an important role in the saturation of SRS. When damping of the electron plasma waves is increased, the effects of LDI on SRS are reduced, and the SRS reflectivity increases. In the strong EPW damping limit, LDI is

not excited at all and SRS becomes completely independent of LDI.

For a moderate EPW damping, LDI is found to be localized near the boundary where the laser enters the plasma, and the amplitude of the SRS electron plasma wave (a_3) saturates just above the threshold for LDI. This threshold determines the balance between SRS (which tends to increase a_3) and LDI (which damps a_3). When the EPW damping is reduced, the LDI threshold is reduced as well. In the weak EPW damping limit, a_3 is found to exhibit incoherent space-time fluctuations in the region where LDI is excited. The associated wave de-phasing produces an appreciable reduction of the SRS backscattering.

Experiments show that the SRS reflectivity increases with IAW damping, which can be understood within the framework of my numerical simulations. The backscattering is also found to be sensitive to the intensity of the laser, the initial amplitude of the noise and the length of the interaction region. While the laser intensity is known from experimental data, the length of the plasma and the intensity of the noise have been only roughly estimated. Further investigation is necessary to better model these parameters, and this has been left as a problem for the future.

I have studied the possible cascadings of SRS and LDI by extending the 5COM equations to the 7COM and 9COM equations. As far as I can determine, these investigation has never been carried out before. I find that the onset of the first LDI cascade weakens the principal LDI, thereby increasing the SRS reflectivity. While further cascadings have not been investigated in detail, it is likely that a second cascade of LDI would weaken the effects of the first cascade.

The cascading of SRS into a secondary SRS leads to a significant reduction in the backscattering. This is primarily due to the direct draining of energy from the backscattered electromagnetic wave (a_2). The effects of SRS cascading are specially strong in the weak damping limit (small $k\lambda_{De}$). In the strong damping limit (large $k\lambda_{De}$), on the other hand, the electron plasma waves inhibits the secondary SRS process.

The calculated SRS reflectivity has been found to vary in a manner similar to

experiments. However, an absolute comparison with experiments is difficult because, for a given experiment, not all the necessary plasma parameters are known. The inclusion of other effects, like the possible coupling to stimulated Brillouin scattering (SBS) and the extension of the model to 2D (or even 3D), are left for the future. Other effects not included in my investigation, but important for future research, are the effects of electron trapping and filamentation.

In conclusion, by considering various systems of coupled mode equations describing the nonlinear interaction of SRS and LDI, and their possible cascades, I have studied the scaling of the SRS backscatter interaction as a function of various plasma parameters. Some of the most important cases that I have considered in my simulations have shown variations in backscattering consistent with experiments. The coupled modes equations have helped me to clarify the relevant physics necessary to understand the coupling of SRS and LDI, and the effect of various plasma parameters on the SRS backscattering.

.

Appendix A

Derivation of Zakharov's Equations & Reduction to COM Equations

A detailed derivation of the full wave Zakharov's equations is provided in this Appendix. Following the derivation by W. Rozmus, et al.,[39] we begin with the well known Maxwell equations and the multi-fluid plasma relations:

$$\nabla \times \overline{E} + \frac{\partial \overline{B}}{\partial t} = 0, \tag{A.1}$$

$$\nabla \times \overline{B} - \frac{1}{c^2}\frac{\partial \overline{E}}{\partial t} - \mu_o \overline{J} = 0, \tag{A.2}$$

$$\epsilon_o \nabla \cdot \overline{E} = \rho, \tag{A.3}$$

$$\nabla \cdot \overline{B} = 0, \tag{A.4}$$

and,

$$\rho = \sum_s q_s n_s, \tag{A.5}$$

$$\overline{J} = \sum_s q_s n_s \overline{v}_s, \tag{A.6}$$

$$\frac{\partial}{\partial t} n_s + \nabla \cdot (n_s \overline{v}_s) = 0, \tag{A.7}$$

$$\frac{\partial}{\partial t}\overline{v}_s + \overline{v}_s \cdot \nabla \overline{v}_s = \frac{q_s}{m_s}(\overline{E} + \overline{v}_s \times \overline{B}) - \frac{\gamma_s \kappa T_s}{m_s n_s}\nabla n_s. \tag{A.8}$$
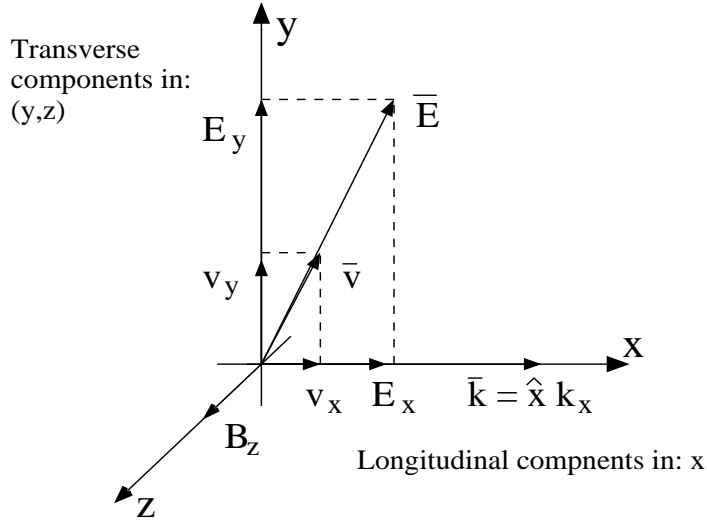
Figure A-1: Reference frame and field polarizations.

Relevant to SRS backscattering, the derivation of the Zakharov equations that is provided in this Appendix, is restricted to one dimensional dynamics. It is considered that all waves propagate in the $\hat{x}$ direction, so $\overline{k} = \hat{x}k$, $\partial_y = \partial_z = 0$, and $\nabla \rightarrow \hat{x}\partial_x$. The transverse (electromagnetic) electric field is assumed to be linearly polarized along the $\hat{y}$ direction, the electrostatic (longitudinal) field along $\hat{x}$ and the magnetic field along $\hat{z}$ ($\overline{B} = \hat{z}B_z$). The total electric field is given by $\overline{E} = \hat{x}E_x + \hat{y}E_y$. The reference frame and polarization of the fields are illustrated in Figure A-1.

Zakharov's equations assume an initial steady state, and small perturbations added to it. At time $t = 0$, the steady state consists of a non-drifting [$\overline{v}_e(x, t = 0) = \overline{v}_i(x, t = 0) = 0$], homogeneous [$n_{eo} = constant$] and neutral [$Z_i n_{io} = n_{eo}$] plasma; which is free of electric and magnetic fields [$\overline{E}_o = \overline{B}_o = 0$]. The electron density [$n_e(x, t)$], ion density [$n_i(x, t)$], electron velocity [$\overline{v}_e(x, t)$], ion velocity [$\overline{v}_i(x, t)$], electric field [$\overline{E}(x, t)$] and magnetic field [$\overline{B}(x, t)$], are those in steady state, modified by the small perturbations: n_{eh}, $n_{e\ell}$, $n_{i\ell}$, v_{exh}, $v_{ex\ell}$, v_{ey}, $v_{ix\ell}$, E_{xh}, $E_{x\ell}$, E_y and B_z:

$$n_e(x, t) = n_{eo} + n_{eh}(x, t) + n_{e\ell}(x, t), \tag{A.9}$$

$$n_i(x, t) = n_{io} + n_{i\ell}(x, t), \tag{A.10}$$

$$\overline{v}_e(x,t) = \hat{x}\left[v_{exh}(x,t) + v_{ex\ell}(x,t)\right] + \hat{y}v_{ey}(x,t), \tag{A.11}$$

$$\overline{v}_i(x,t) = \hat{x}v_{ix\ell}(x,t), \tag{A.12}$$

$$\overline{E}(x,t) = \hat{x}[E_{xh}(x,t) + E_{x\ell}(x,t)] + \hat{y}E_y(x,t). \tag{A.13}$$

$$\overline{B}(x,t) = \hat{z}B_z(x,t). \tag{A.14}$$

Two different kinds of perturbations are considered: those which change with a frequency similar to the EPW (the low-frequency, fast perturbations), and those oscillating with a frequency similar to the IAW (the low-frequency, slow perturbations). In Equations (A.11)-(A.14) the subindex ℓ stands for low-frequency slow oscillations, and the subindex h for low-frequency fast perturbations. The $\hat{y}$ and $\hat{z}$ components of the fields oscillate with a frequency similar to the electromagnetic waves – which is the fastest oscillation in the system.

The Maxwell-fluid equations need to be decomposed into their longitudinal and transverse components; however, before this is carried out, the momentum conservation equation (A.8) is simplified, showing that for the given initial conditions $\overline{v}_s \cdot \nabla \overline{v}_s - (q_s/m_s)\overline{v} \times \overline{B} \to \nabla |\overline{v}_s|^2/2$.

Starting with the vector identity:

$$\overline{v}_s \cdot \nabla \overline{v}_s = \nabla \frac{|\overline{v}_s|^2}{2} - \overline{v}_s \times (\nabla \times \overline{v}_s), \tag{A.15}$$

the momentum conservation equation (A.8) rewrites as:

$$\frac{\partial}{\partial t}\overline{v}_s + \nabla \frac{|\overline{v}_s|^2}{2} - \frac{q_s}{m_s}\overline{E} + \frac{\gamma_s \kappa T_s}{m_s n_s}\nabla n_s = \overline{v}_s \times (\nabla \times \overline{v}_s) + \frac{q_s}{m_s}(\overline{v}_s \times \overline{B}). \tag{A.16}$$

Since $\nabla \cdot \overline{B} = 0$, the magnetic field is $\overline{B} = \nabla \times \overline{A}$ (where $\overline{A}$ is a vector potential), so Eq. (A.16) becomes:

$$\frac{\partial}{\partial t}\overline{v}_s + \nabla \frac{|\overline{v}_s|^2}{2} - \frac{q_s}{m_s}\overline{E} + \frac{\gamma_s \kappa T_s}{m_s n_s}\nabla n_s = \frac{1}{m_s}\overline{v}_s \times \nabla \times \left(m_s \overline{v}_s + q_s \overline{A}\right). \tag{A.17}$$

It can be shown that $\partial_t \left[\nabla \times \overline{P}\right] = 0$, where $\overline{P} = m_s \overline{v}_s + q_s \overline{A}$, is the *canonic*

momentum. To show this,

$$\frac{\partial}{\partial t}\left[\nabla \times \overline{P}\right] = \nabla \times \left[m_s \frac{\partial \overline{v}}{\partial t} + q_s \frac{\partial \overline{A}}{\partial t}\right]; \tag{A.18}$$

where $\partial \overline{v}/\partial t$ is given by Eq. (A.17), and $\partial \overline{A}/\partial t$ by Faraday's law [Eq.(A.1)]:

$$\nabla \times \left(\overline{E} + \frac{\partial \overline{A}}{\partial t}\right) = 0. \tag{A.19}$$

Since $\nabla \times (\nabla \phi) = 0$, for a scalar potential ϕ, Eq. (A.19) leads to:

$$\frac{\partial \overline{A}}{\partial t} = -\overline{E} - \nabla \phi. \tag{A.20}$$

Then, substitution of Eqs. (A.17) and (A.20) into (A.18), gives:

$$\frac{\partial}{\partial t}\left[\nabla \times \overline{P}\right] = \nabla \times \left[\overline{v}_s \times \nabla \times \overline{P}\right]. \tag{A.21}$$

Equation (A.21) shows that an initial $\overline{P} = 0$, leads to $\partial_t \left[\nabla \times \overline{P}\right] = 0$, so $\nabla \times \overline{P}$ remains at zero all the time. Therefore, given the initial steady state where: $\overline{v}_s = \overline{B} = 0$, the momentum conservation equation can be rewritten as:

$$\frac{\partial}{\partial t}\overline{v}_s + \nabla \frac{|\overline{v}_s|^2}{2} - \frac{q_s}{m_s}\overline{E} + \frac{\gamma_s \kappa T_s}{m_s n_s}\nabla n_s = 0. \tag{A.22}$$

Now, with $\partial_y = \partial_z = 0$ and $\nabla \to \hat{x}\partial_x$, we proceed to decompose the Maxwell-fluid equations into their longitudinal an transverse components. Substitution of (A.9)-(A.14) into Equations (A.1)-(A.7) and (A.22), and separation in $(\hat{x}, \hat{y})$ components, leads to the equations for the transverse (electromagnetic) fields [corresponding to the $\hat{y}$ component]:

$$\left[\frac{\partial^2}{\partial t^2} - c^2 \frac{\partial^2}{\partial x^2}\right]E_y = -\sum_s \frac{q_s}{\epsilon_o}\frac{\partial}{\partial t}\left(n_s v_{sy}\right), \tag{A.23}$$

$$\frac{\partial}{\partial t}\left(v_{sy}\right) = \frac{q_s}{m_s}E_y; \tag{A.24}$$

128

and the equations for the longitudinal (electrostatic) fields [corresponding to the $\hat{x}$ component]:

$$\frac{\partial}{\partial x} E_x = \sum_s \frac{q_s n_s}{\epsilon_o}, \tag{A.25}$$

$$\frac{\partial}{\partial t}(v_{sx}) = \frac{q_s}{m_s} E_x - \frac{1}{2}\frac{\partial}{\partial x}|v_s|^2 - \gamma_s \frac{\kappa T_s}{m_s n_s}\frac{\partial}{\partial x} n_s, \tag{A.26}$$

$$\frac{\partial}{\partial t} n_s + \frac{\partial}{\partial x} n_s v_{sx} = 0. \tag{A.27}$$

Zakharov's equation for the electromagnetic waves, follows from equations (A.23) and (A.24). Since the ion transverse velocity is $v_{iy} = 0$ [EM waves have $\omega \gg \omega_{pi}$], from Eq. (A.23):

$$\left[\frac{\partial^2}{\partial t^2} - c^2 \frac{\partial^2}{\partial x^2}\right] E_y = -\frac{q_e}{\epsilon_o}\frac{\partial}{\partial t}(n_e v_{ey}). \tag{A.28}$$

Then, from Eqs. (A.24) $[E_y = (m_e/q_e)\partial_t v_{ey}]$ and (A.28), one finds:

$$\left(\frac{\partial^2}{\partial t^2} - c^2\frac{\partial^2}{\partial x^2} + \omega_{pe}^2\right) v_{ey} = -\frac{e^2 n_{eh}}{\epsilon_o m_e} v_{ey} - \frac{e^2 n_{e\ell}}{\epsilon_o m_e} v_{ey}; \tag{A.29}$$

where $\omega_{pe}^2 = q_e^2 n_{eo}/m_e \epsilon_o$. The nonlinear terms $n_{eh} v_{ey}$ and $n_{e\ell} v_{ey}$, stand for the coupling between high frequency oscillations (electromagnetic time scale) and low frequency oscillations. In three wave interactions where two electromagnetic waves interact with a lower frequency wave (like in SRS or SBS), these nonlinear terms give rise to the corresponding coupling [as shown in Section A.1].

Zakharov's equations for the longitudinal modes are a bit more trickier. To derive them, it is first necessary to separate the longitudinal equations [(A.25)-(A.27)], into the fast varying (EPW time-scale) and slowly varying (IAW time-scale) components. The equations for the high frequency EPW-dynamics are:

$$\frac{\partial}{\partial x} E_{xh} = \frac{q_e}{\epsilon_o} n_{eh}, \tag{A.30}$$

$$\frac{\partial}{\partial t} v_{exh} = -\frac{1}{2}\frac{\partial}{\partial x}|v_e|^2 - \gamma_e \frac{\kappa T_e}{m_e n_e}\frac{\partial}{\partial x}n_{eh} + \frac{q_e}{m_e}E_{xh}, \tag{A.31}$$

$$\frac{\partial}{\partial t}n_{eh} + \frac{\partial}{\partial x}n_e v_{exh} = 0; \tag{A.32}$$

and for the slow frequency IAW dynamics:

$$\frac{\partial}{\partial x}E_{x\ell} = \frac{q_e}{\epsilon_o}\left(n_{e\ell} + Z_i n_{i\ell}\right), \tag{A.33}$$

$$\frac{\partial}{\partial t}v_{ex\ell} = -\frac{1}{2}\frac{\partial}{\partial x}|v_e|^2 - \gamma_e \frac{\kappa T_e}{m_e n_e}\frac{\partial}{\partial x}n_{e\ell} + \frac{q_e}{m_e}E_{xh}, \tag{A.34}$$

$$\frac{\partial}{\partial t}v_{ix\ell} = -\frac{1}{2}\frac{\partial}{\partial x}|v_i|^2 - \gamma_i \frac{\kappa T_i}{m_i n_i}\frac{\partial}{\partial x}n_{i\ell} + \frac{q_i}{m_i}E_{xh}, \tag{A.35}$$

$$\frac{\partial}{\partial t}n_{e\ell} + \frac{\partial}{\partial x}n_e v_{ex\ell} = 0, \tag{A.36}$$

$$\frac{\partial}{\partial t}n_{i\ell} + \frac{\partial}{\partial x}n_i v_{ix\ell} = 0. \tag{A.37}$$

Zakharov's equation for the **electron plasma waves**, is derived from Eqs. (A.30)–(A.32). From Eq. (A.30), one finds

$$\frac{\partial n_{eh}}{\partial x} = \frac{\epsilon_o}{q_e}\frac{\partial^2 E_{xh}}{\partial x^2}. \tag{A.38}$$

Then, from Eqs. (A.30) and (A.32),

$$\frac{\partial}{\partial t}(n_e v_{exh}) = -\frac{\epsilon_o}{q_e}\frac{\partial^2 E_{xh}}{\partial t^2}; \tag{A.39}$$

where

$$\frac{\partial}{\partial t}(n_e v_{exh}) = n_e \frac{\partial}{\partial t}v_{exh} + v_{exh}\frac{\partial}{\partial t}(n_{eh} + n_{e\ell}). \tag{A.40}$$

In Equation (A.40), $v_{exh}\partial_t(n_{eh} + n_{e\ell})$ is ordered with $[\omega_{pe}v_{exh}(n_{eh} + n_{e\ell})]$, and $n_e\partial_t v_{exh}$ is ordered with $[\omega_{pe}v_{exh}(n_{eo} + n_{eh} + n_{e\ell})]$. Since $n_{eo} \gg n_{eh}$ & $n_{e\ell}$, the term $[v_{exh}\partial_t(n_{eh} + n_{e\ell})]$ can be neglected to obtain (as in [39]):

$$\frac{\partial}{\partial t}(n_e v_{exh}) \approx n_e \frac{\partial}{\partial t}v_{exh}. \tag{A.41}$$

130

Then, multiplying Eq. (A.31) by n_e, and considering equations (A.38), (A.39) and (A.41); the Zakharov equation for electron plasma waves is obtained:

$$\left(\frac{\partial^2}{\partial t^2} - 3\frac{\kappa T_e}{m_e}\frac{\partial^2}{\partial x^2} + \omega_{pe}^2 \right) E_{xh} = -\omega_{pe}^2 \frac{n_{exh} + n_{e\ell}}{n_{eo}} E_{xh} + \frac{q_e n_e}{2\epsilon_o}\frac{\partial}{\partial x}\left(\frac{|v_e|^2}{2} \right); \quad (A.42)$$

where $\gamma_e = 3$ for one degree freedom electrons.

Finally, the Zakharov equation for the **ion acoustic waves** follows from equations (A.33)–(A.37). While the algebra is omitted for brevity, the steps and approximations are very similar to those in the case of the electron plasma waves. The Zakharov equation for ion acoustic waves turns out to be:

$$\left[\frac{\partial^2}{\partial t^2} - Z_i\frac{\kappa T_e}{m_i}\left(1 + \frac{3T_i}{Z_i T_e} \right)\frac{\partial^2}{\partial x^2} \right] n_{e\ell} = Z_i\frac{m_e}{m_i}n_e\frac{\partial^2}{\partial x^2}\left(\frac{|v_e|^2}{2} \right). \quad (A.43)$$

where $|v_e|^2 = |v_{ey}|^2 + |v_{exh}|^2$, $n_e = n_{eo} + n_{e\ell} + n_{eh}$, $\gamma_e = 1$ and $\gamma_i = 3$, for adiabatic electrons and one degree freedom ions. The nonlinear terms $(\partial_{xx}|v_{ex\ell}|^2)$ and $(\partial_{xx}|v_{ix\ell}|^2)$ have been neglected, as compared to $(\partial_{xx}|v_{exh}|^2)$.

Equations (A.29), (A.42) and (A.43), are the three second order Zakharov equations that model the coupling between the plasma dynamics in the EMW, EPW and IAW time-scales. Equation (A.42) can be further simplified, as neglecting $\partial_x|v_{exh}|^2$ (compared to $\partial_x|v_{ey}|^2$) and neglecting $n_{eh}E_{xh}$ (which gives harmonic generation with $\omega \sim 2\omega_{pe}$). Equation (A.43) can be conveniently simplified as well, neglecting $n_{e\ell}$ and n_{eh} compared to n_{eo}. Considering the previous approximations, and adding phenomenological damping, the Zakharov equations [A.29, A.42 and A.43] can be rewritten as:

$$\left(\frac{\partial^2}{\partial t^2} - c^2\frac{\partial^2}{\partial x^2} + 2\nu_E\frac{\partial}{\partial t} + \omega_{pe}^2 \right) v_{ey} = -\omega_{pe}^2\left(\frac{n_{eh}}{n_{eo}}v_{ey} \right) - \omega_{pe}^2\left(\frac{n_{e\ell}}{n_{eo}}v_{ey} \right), \quad (A.44)$$

$$\left(\frac{\partial^2}{\partial t^2} - 3v_{Te}^2\frac{\partial^2}{\partial x^2} + 2\nu_L\frac{\partial}{\partial t} + \omega_{pe}^2 \right) E_{xh} = -\omega_{pe}^2\frac{n_{e\ell}}{n_{eo}}E_{xh} - \frac{q_e n_e}{2\epsilon_o}\frac{\partial}{\partial x}\left(\frac{|v_{ey}|^2}{2} \right), \quad (A.45)$$

$$\left(\frac{\partial^2}{\partial t^2} - c_a^2 \frac{\partial^2}{\partial x^2} + 2\nu_A \frac{\partial}{\partial t} \right) n_{e\ell} = Z_i \frac{m_e}{m_i} n_{eo} \frac{\partial^2}{\partial x^2} \left(\frac{|v_{ey}|^2 + |v_{exh}|^2}{2} \right), \qquad (A.46)$$

where the coefficients: $\omega_{pe} = (q_e^2 n_{eo}/\epsilon_o m_e)^{1/2}$, $v_{Te} = (\kappa T_e/m_e)^{1/2}$ and $c_a^2 = (\kappa T_e + 3\kappa T_i)/m_i$, are the electron plasma frequency, electron thermal velocity and speed of sound in the plasma.

The phenomenological damping has been added arbitrarily: ν_E for collisional damping of electromagnetic waves, and (ν_L, ν_A) for the Landau damping of electron plasma and ion acoustic waves, respectively. As explained in Chapter 2, Landau damping is a nonlocal effect, which is frequency and wavenumber dependent. When the nonlinearities of the model produce a narrow frequency spreading near the frequency of the waves (i.e. slowly varying amplitudes), the Landau damping can be considered approximately constant, and evaluated at the particular frequency and wave-number of the wave . However, when the nonlinearities produce a wide range of frequencies, the nonlocal nature of the Landau damping has to be considered (which is not an easy task).

In Eqs. (A.44)–(A.46), the left hand sides describe simple linear waves, which are nonlinearly coupled by the terms on the right hand sides. While Zakharov's equations can be written in terms of different variables (which oscillate with the appropriate frequencies), in this Appendix they are written in terms of v_{ey}, E_{xh} and $n_{e\ell}$; which are the perturbation amplitudes of the transverse electron velocity due to electromagnetic waves, the electric field amplitude in electron plasma waves and the electron density due to ion acoustic waves.

Zakharov's equations constitute an approximate nonlinear model for the coupling of waves in laser-plasma interactions, and they have been widely studied in the frame of ICF laser SRS-backscattering. However, there is no analytic solution for them, and they are difficult to solve numerically, so they are frequently simplified for numeric or analytic investigation.

Numerous approximations of Eqs. (A.44)–(A.46) can be found in literature; however, the most popular approximation assumes the slow modulation (in time and space) of the field amplitudes in the electromagnetic and electron plasma waves. As

an example of these reduced versions of the Zakharov's equations, the model proposed by Kolber, et al.,[42] is outlined in the following section (see also [42, 39]).

A.1 Kolber-Zakharov Equations

In their paper [42], Kolber and his colleagues considered two electromagnetic waves (the laser and the SRS backscattering), interacting with an electron plasma wave and an ion acoustic wave. They have set up a model that can be derived from the full Zakharov's equations, considering that the electromagnetic and electron-plasma waves have an amplitude which is slowly varying in time.

In their model, the transverse component of the electron velocity is just the superposition of the transverse electron velocities due to the laser high frequency electromagnetic wave (v_{eyo}) and the SRS backscattering (v_{ey1}); which have frequencies and wavenumbers (ω_o, k_o) and (ω_1, k_1), respectively. Therefore, the total transverse electron velocity is:

$$v_{ey} = v_{eyo} + v_{ey1} = \left(\frac{1}{2}\right) \left[\sum_{\beta=0,1} \Psi_\beta(x,t) e^{-i\omega_\beta t} + c.c. \right] ; \qquad (A.47)$$

where, Ψ_o and Ψ_1 are the slowly varying amplitudes, such that: $\partial_t \Psi_o(x,t) \ll \omega_o$ and $\partial_t \Psi_1(x,t) \ll \omega_1$.

The electric field in the electron plasma wave (E_{xh}) is also considered to be slowly varying in time:

$$E_{xh} = \left(\frac{1}{2}\right) \left[\mathcal{E}(x,t) e^{-i\omega_{pe}t} + c.c. \right], \qquad (A.48)$$

where $\mathcal{E}(x,t)$ is also a slowly varying amplitude $[\partial_t \mathcal{E}(x,t) \ll \omega_{pe}]$, and the wave frequency has been approximated as $\omega \approx \omega_{pe}$.

Using (A.30), Eqs. (A.44) and (A.47) and neglecting, as in [42], the coupling to

IAW's $[n_{e\ell}v_{ey}]$, one gets:

$$\left(\frac{\partial^2}{\partial t^2} - c^2\frac{\partial^2}{\partial x^2} + 2\nu_E\frac{\partial}{\partial t} + \omega_{pe}^2\right)[v_{eyo} + v_{ey1}] = -\frac{\omega_{pe}^2\epsilon_o}{n_{eo}q_e}[v_{eyo} + v_{ey1}]\frac{\partial E_{xh}}{\partial x}; \quad \text{(A.49)}$$

Equation (A.49) is then separated into frequency components, considering (A.47)-(A.48) and the SRS resonance condition: $\omega_o \approx \omega_1 + \omega_{pe}$. The nonresonant crossed terms: $v_{eyo}\partial_x E_{xh}$ and $v_{ey1}^*\partial_x E_{xh}$, which are not in resonance with the main waves, are neglected. Taking only those components with frequency $\omega \approx \omega_o$, one finds the equation for the high frequency EMW:

$$\left(\frac{\partial^2}{\partial t^2} - c^2\frac{\partial^2}{\partial x^2} + 2\nu_E\frac{\partial}{\partial t} + \omega_{pe}^2\right)v_{eyo} = -\frac{\omega_{pe}^2\epsilon_o}{n_{eo}q_e}\left(\frac{\partial E_{xh}}{\partial x}\right)v_{ey1}; \quad \text{(A.50)}$$

and grouping together the terms with frequency $\omega \approx \omega_1$, the equation for for the SRS backscattering:

$$\left(\frac{\partial^2}{\partial t^2} - c^2\frac{\partial^2}{\partial x^2} + 2\nu_E\frac{\partial}{\partial t} + \omega_{pe}^2\right)v_{ey1} = -\frac{\omega_{pe}^2\epsilon_o}{n_{eo}q_e}\left(\frac{\partial E_{xh}}{\partial x}\right)v_{eyo}^*. \quad \text{(A.51)}$$

Evaluating the time derivatives, and neglecting $(\partial^2\Psi_\beta/\partial t^2)$ and $(\nu_E\partial\Psi_\beta/\partial t)$ under the assumptions of slow variation in time and weak damping, one finds the equations used by Kolber, et al., for the electromagnetic modes:

$$i\frac{\partial\Psi_o}{\partial t} + i\nu_E\Psi_o + \frac{c^2}{2\omega_o}\frac{\partial^2\Psi_o}{\partial x^2} - \frac{\omega_p^2 - \omega_o^2}{2\omega_o}\Psi_o - \frac{\omega_p^2}{\omega_o}\frac{n_{io}}{2n_{eo}}N\Psi_o = -\frac{e}{4\omega_o m_e}\frac{\partial\mathcal{E}}{\partial x}\Psi_1, \quad \text{(A.52)}$$

$$i\frac{\partial\Psi_1}{\partial t} + i\nu_E\Psi_1 + \frac{c^2}{2\omega_1}\frac{\partial^2\Psi_1}{\partial x^2} - \frac{\omega_p^2 - \omega_1^2}{2\omega_1}\Psi_1 - \frac{\omega_p^2}{\omega_1}\frac{n_{io}}{2n_{eo}}N\Psi_1 = -\frac{e}{4\omega_1 m_e}\frac{\partial\mathcal{E}^*}{\partial x}\Psi_o. \quad \text{(A.53)}$$

In a similar way, after neglecting the direct coupling between electromagnetic and ion acoustic waves $[\partial|v_{ey}|^2$ in Eq. (A.46)], substitution of (A.47)–(A.48) into (A.45)–(A.46), leads to the equations that Kolber, et al., proposed for the electron plasma

and ion acoustic waves:

$$i\frac{\partial \mathcal{E}}{\partial t} + \frac{3}{2}\frac{v_{Te}^2}{\omega_p}\frac{\partial^2 \mathcal{E}}{\partial x^2} - \frac{1}{2}\omega_p N\mathcal{E} + i\nu_L \cdot \mathcal{E} = \frac{en_{eo}}{4\omega_{pe}\epsilon_o}\frac{\partial}{\partial x}(\Psi_o \Psi_1^*), \qquad (A.54)$$

$$\frac{\partial^2 N}{\partial t^2} - c_s^2\frac{\partial^2 N}{\partial x^2} + 2\nu_A \cdot \frac{\partial N}{\partial t} = \frac{\epsilon_o}{4n_{io}m_i}\frac{\partial^2 |\mathcal{E}|^2}{\partial x^2}, \qquad (A.55)$$

where $N = n_{e\ell}/n_{eo}$.

A.2 Coupled Modes Equations

To conclude this Appendix, the coupling of modes equations are derived from the Zakharov equations, taking in consideration the slowly varying amplitude approximation. Since the Zakharov equations [(A.44)-(A.46)] account for the coupling between electromagnetic, electron plasma and ion acoustic waves, in this section we target the five wave coupled mode equations, for the coupling of SRS and LDI (see Chapter 4).

The nonlinear terms: $n_{e\ell}v_{ey}$ in Eq. (A.44) and $|v_{ey}|^2$ in Eq. (A.46), which are responsible for the direct coupling between electromagnetic and ion-acoustic waves, are neglected. This coupling, results in a different kind of parametric process, known as *stimulated Brillouing scattering* (see [46, 47]); which is not relevant to the contents of this thesis. Considering these approximations, the Zakharov equations are rewritten as:

$$\left(\frac{\partial^2}{\partial t^2} - c^2\frac{\partial^2}{\partial x^2} + 2\nu_E\frac{\partial}{\partial t} + \omega_{pe}^2\right)v_{ey} = -\omega_{pe}^2\left(\frac{n_{eh}}{n_{eo}}v_{ey}\right), \qquad (A.56)$$

$$\left(\frac{\partial^2}{\partial t^2} - 3v_{Te}^2\frac{\partial^2}{\partial x^2} + 2\nu_L\frac{\partial}{\partial t} + \omega_{pe}^2\right)E_{xh} = -\omega_{pe}^2\frac{n_{e\ell}}{n_{eo}}E_{xh} - \frac{q_e n_e}{2\epsilon_o}\frac{\partial}{\partial x}\left(\frac{|v_{ey}|^2}{2}\right), \quad (A.57)$$

$$\left(\frac{\partial^2}{\partial t^2} - c_a^2\frac{\partial^2}{\partial x^2} + 2\nu_A\frac{\partial}{\partial t}\right)n_{e\ell} = Z_i\frac{m_e}{m_i}n_{eo}\frac{\partial^2}{\partial x^2}\left(\frac{|v_{ex}|^2}{2}\right). \qquad (A.58)$$

In the coupling of SRS to LDI, we need to consider five linear modes: 1) the high frequency (induced by the laser) electromagnetic wave with $[\omega_1, k_1]$, 2) the backscattered electromagnetic wave $[\omega_2, k_2]$, 3) the SRS electron plasma wave $[\omega_3, k_3]$, 4) the LDI backscattered EPW (ω_4, k_4) and 5) the LDI excited ion acoustic wave

$[\omega_5, k_5]$. The frequencies and wave numbers approximately satisfy the following *phase matching conditions*:

$$\omega_1 = \omega_2 + \omega_3, \tag{A.59}$$

$$k_1 = k_2 + k_3, \tag{A.60}$$

$$\omega_3 = \omega_4 + \omega_5, \tag{A.61}$$

$$k_3 = k_4 + k_5. \tag{A.62}$$

In the slowly varying amplitude approximation, the linear modes are considered to have a slow modulation in time and space; such that the five waves in SRS-LDI are:

$$v_{ey1} = \frac{1}{2} \left[\mathcal{V}_1(x_s, t_s) e^{-i\omega_1 t} e^{-ik_1 x} + C.C. \right], \tag{A.63}$$

$$v_{ey2} = \frac{1}{2} \left[\mathcal{V}_2(x_s, t_s) e^{-i\omega_2 t} e^{-ik_2 x} + C.C. \right], \tag{A.64}$$

$$E_{xh3} = \frac{1}{2} \left[\mathcal{E}_3(x_s, t_s) e^{-i\omega_3 t} e^{-ik_3 x} + C.C. \right], \tag{A.65}$$

$$E_{xh4} = \frac{1}{2} \left[\mathcal{E}_4(x_s, t_s) e^{-i\omega_4 t} e^{-ik_4 x} + C.C. \right], \tag{A.66}$$

$$n_{el5} = \frac{1}{2} \left[\mathcal{N}_5(x_s, t_s) e^{-i\omega_5 t} e^{-ik_5 x} + C.C. \right]. \tag{A.67}$$

The slowly varying amplitudes of the fields are: $\mathcal{V}_1$, $\mathcal{V}_2$, $\mathcal{E}_3$, $\mathcal{E}_4$ and $\mathcal{N}_5$; which time and space derivatives (∂_{t_s} and ∂_{x_s}) are ordered with $O(\xi^2)$. For consistency with the slowly varying amplitude approximation, the phenomenological damping in equations (A.56)–(A.58) also needs to be ordered with $O(\xi^2)$.

By superposition of the linear modes, the total transverse electron velocity and longitudinal EPW electric field, are:

$$v_{ey} = v_{ey1} + v_{ey2}, \tag{A.68}$$

$$E_{xh} = E_{xh3} + E_{xh4}. \tag{A.69}$$

With $n_{eh} = (\epsilon_o/q_e)\partial_x E_{xh}$ (from Eq. A.30); using Eqs. (A.63)–(A.66) in (A.68)-

(A.69) and Zakharov's equation (A.56), and collecting only those terms with frequency $\omega \approx \omega_1$, [the nonresonant terms are considered later], one finds the following equation:

$$\left[(-i\omega_1)^2 - 2i\omega_1 \frac{\partial}{\partial t_s} + \frac{\partial^2}{\partial t_s^2} \right] \mathcal{V}_1 - c^2 \left[(ik_1)^2 + 2ik_1 \frac{\partial}{\partial x_s} + \frac{\partial^2}{\partial x_s^2} \right] \mathcal{V}_1 +$$

$$2\nu_E \left(-i\omega_1 + \frac{\partial}{\partial t_s} \right) \mathcal{V}_1 + \omega_{pe}^2 \mathcal{V}_1 = -\frac{q_e}{2m_e} \left(ik_3 \mathcal{E}_3 + \frac{\partial}{\partial x_s} \mathcal{E}_3 \right) \mathcal{V}_2. \qquad (A.70)$$

Then, separating into orders of magnitude, the equations for $O(\xi)$ and $O(\xi^2)$, are:

$$\omega_1^2 = c^2 k_1^2 + \omega_{pe}^2, \qquad (A.71)$$

$$\left(\frac{\partial}{\partial t_s} + v_{g1} \frac{\partial}{\partial x_s} + \nu_E \right) \mathcal{V}_1 = \frac{q_e}{4m_e} \left(\frac{k_3}{\omega_1} \right) \mathcal{E}_3 \mathcal{V}_2. \qquad (A.72)$$

Equation (A.71) is simply the dispersion relation of the high frequency electromagnetic wave, and Eq. (A.72) defines the slowly varying amplitude, in terms of the nonlinear coupling to the backscattered electromagnetic wave and the electron plasma wave. Later in this section, Eq. (A.72) is rewritten in terms of the wave action density; however, at this point we continue with the equations for the other linear modes.

Again, using Eqs. (A.63)–(A.66) in (A.68)-(A.69) and Zakharov's equation (A.56); but collecting now those terms with frequency $\omega \approx \omega_2$, one finds:

$$\left[(-i\omega_2)^2 - 2i\omega_2 \frac{\partial}{\partial t_s} + \frac{\partial^2}{\partial t_s^2} \right] \mathcal{V}_2 - c^2 \left[(ik_2)^2 + 2ik_2 \frac{\partial}{\partial x_s} + \frac{\partial^2}{\partial x_s^2} \right] \mathcal{V}_2 +$$

$$2\nu_E \left(-i\omega_2 + \frac{\partial}{\partial t_s} \right) \mathcal{V}_2 + \omega_{pe}^2 \mathcal{V}_2 = -\frac{q_e}{2m_e} \left(ik_3 \mathcal{E}_3 + \frac{\partial}{\partial x_s} \mathcal{E}_3 \right)^* \mathcal{V}_1. \qquad (A.73)$$

As before, separating into orders of magnitude and neglecting terms of order $O(\xi^3)$ or higher, one finds the equations for the first and second order amplitudes:

$$\omega_2^2 = c^2 k_2^2 + \omega_{pe}^2, \qquad (A.74)$$

$$\left(\frac{\partial}{\partial t_s} + v_{g2} \frac{\partial}{\partial x_s} + \nu_E \right) \mathcal{V}_2 = \frac{q_e}{4m_e} \left(\frac{k_3}{\omega_2} \right) \mathcal{V}_1 \mathcal{E}_3^*. \tag{A.75}$$

The equation for the slowly varying amplitude of the electron plasma wave, follows from Eqs. (A.63)–(A.67) and (A.57). While the algebra is omitted, it is straight forward to show that after collecting those terms with frequency $\omega \approx \omega_3$, one obtains:

$$\left[(-i\omega_3)^2 - 2i\omega_3 \frac{\partial}{\partial t_s} + \frac{\partial^2}{\partial t_s^2} \right] \mathcal{E}_3 - 3v_{Te}^2 \left[(ik_3)^2 + 2ik_3 \frac{\partial}{\partial x_s} + \frac{\partial^2}{\partial x_s^2} \right] \mathcal{E}_3 +$$

$$2\nu_L \left(-i\omega_3 + \frac{\partial}{\partial t_s} \right) \mathcal{E}_3 + \omega_{pe}^2 \mathcal{E}_3 = -\frac{q_e n_{eo}}{2\epsilon_o} (ik_3) \mathcal{V}_1 \mathcal{V}_2^* - \frac{\omega_{pe}^2}{2} \left(\frac{\mathcal{N}_5}{n_{eo}} \right) \mathcal{E}_{xh4}. \tag{A.76}$$

Once again, separation into orders of magnitude gives the first order dispersion relation for the electron plasma wave, and an equation for the slowly varying amplitude of the EPW ($\mathcal{E}_3$):

$$\omega_3^2 = 3v_{Te}^2 k_3^2 + \omega_{pe}^2, \tag{A.77}$$

$$\left(\frac{\partial}{\partial t_s} + v_{g3} \frac{\partial}{\partial x_s} + \nu_L \right) \mathcal{E}_3 = \frac{q_e n_{eo}}{4m_e \epsilon_o} \left(\frac{k_3}{\omega_2} \right) \mathcal{V}_1 \mathcal{V}_2^* - i \frac{\omega_{pe}^2}{4\omega_3 n_{eo}} (\mathcal{N}_5 \mathcal{E}_4). \tag{A.78}$$

Same as in the case of the electron plasma wave, but collecting terms with frequency $\omega \approx \omega_4$, one finds those equations for the LDI backscattered electron plasma wave:

$$\omega_4^2 = 3v_{Te}^2 k_4^2 + \omega_{pe}^2, \tag{A.79}$$

$$\left(\frac{\partial}{\partial t_s} + v_{g4} \frac{\partial}{\partial x_s} + \nu_L \right) \mathcal{E}_4 = -i \frac{\omega_{pe}^2}{4\omega_4 n_{eo}} (\mathcal{E}_3 \mathcal{N}_5^*). \tag{A.80}$$

Finally, for the ion acoustic wave, from Eqs. (A.63)–(A.69) and Zakharov's equation (A.58); collecting those terms with frequency $\omega \approx \omega_5$, and using $v_{exh} = (i\epsilon_o \omega_{pe}/q_e n_{eo}) E_{xh}$, one finds:

$$\omega_5^2 = c_a^2 k_5^2, \tag{A.81}$$

and

$$\left(\frac{\partial}{\partial t_s} + v_{g5} \frac{\partial}{\partial x_s} + \nu_A \right) \mathcal{N}_5 = -i Z_i \frac{\epsilon_o}{4m_i} \left(\frac{k_5^2}{\omega_5} \right) \mathcal{E}_3 \mathcal{E}_4^*. \tag{A.82}$$

In summary, the 5 coupled mode equations for the waves in SRS coupled to LDI, are the equations: (A.72), (A.75), (A.78), (A.80) and (A.82). For convenience, and consistency with the rest of the thesis, these equations are next rewritten in terms of the wave amplitudes a_ℓ (for $\ell = 1 : 5$), such that $a_\ell^2 = w_\ell/\omega_\ell$ is the wave action density of the ℓ mode (with w being the wave energy density).

We begin by writing the 5 COM equations in terms of the electric field slowly varying amplitudes. From the Maxwell fluid equations, and considering the slowly varying approximation (A.63)–(A.67), one finds that:

$$\mathcal{V}_1 = i \frac{q_e}{m_e \omega_1} \mathcal{E}_1, \tag{A.83}$$

$$\mathcal{V}_2 = i \frac{q_e}{m_e \omega_2} \mathcal{E}_2, \tag{A.84}$$

$$\mathcal{V}_3 = i \frac{\epsilon_o \omega_{pe}}{q_e n_{eo}} \mathcal{E}_3, \tag{A.85}$$

$$\mathcal{V}_4 = i \frac{\epsilon_o \omega_{pe}}{q_e n_{eo}} \mathcal{E}_4, \tag{A.86}$$

and

$$\mathcal{N}_5 = -i \frac{n_{eo} q_e}{m_e \omega_5} \left(\frac{c_s^2}{v_{Te}^2} \right) \frac{k_5}{\omega_5} \mathcal{E}_5. \tag{A.87}$$

Direct substitution of Eqs. (A.83)–(A.87) into the COM equations gives the five COM equations, in terms of the slowly varying amplitudes of the electric fields:

$$\left(\frac{\partial}{\partial t_s} + v_{g1} \frac{\partial}{\partial x_s} + \nu_E \right) \mathcal{E}_1 = \frac{q_e}{4 m_e} \left(\frac{k_3}{\omega_2} \right) \mathcal{E}_2 \mathcal{E}_3, \tag{A.88}$$

$$\left(\frac{\partial}{\partial t_s} + v_{g2} \frac{\partial}{\partial x_s} + \nu_E \right) \mathcal{E}_2 = -\frac{q_e}{4 m_e} \left(\frac{k_3}{\omega_1} \right) \mathcal{E}_1 \mathcal{E}_3^*, \tag{A.89}$$

$$\left(\frac{\partial}{\partial t_s} + v_{g3} \frac{\partial}{\partial x_s} + \nu_L \right) \mathcal{E}_3 = \frac{q_e}{4 m_e} \frac{\omega_{pe}^2}{\omega_2 \omega_3} \left(\frac{k_3}{\omega_1} \right) \mathcal{E}_1 \mathcal{E}_2^* - \frac{q_e}{4 m_e} \left(\frac{c_s^2}{v_{Te}^2} \frac{\omega_{pe}^2}{\omega_5^2} \right) \frac{k_5}{\omega_3} \mathcal{E}_4 \mathcal{E}_5, \tag{A.90}$$

$$\left(\frac{\partial}{\partial t_s} + v_{g4} \frac{\partial}{\partial x_s} + \nu_L \right) \mathcal{E}_4 = \frac{q_e}{4 m_e} \left(\frac{c_s^2}{v_{Te}^2} \frac{\omega_{pe}^2}{\omega_5^2} \right) \frac{k_5}{\omega_4} \mathcal{E}_3 \mathcal{E}_5^*, \tag{A.91}$$

$$\left(\frac{\partial}{\partial t_s} + v_{g5} \frac{\partial}{\partial x_s} + \nu_A \right) \mathcal{E}_5 = \frac{Z_i \epsilon_o}{4} \left(\frac{m_e}{m_i} \right) \frac{1}{q_e n_{eo}} \frac{v_{Te}^2}{c_s^2} \omega_5 k_5 \mathcal{E}_3 \mathcal{E}_4^*. \tag{A.92}$$

139

Finally, we write the electric field amplitudes in terms of the action density amplitudes:

$$\mathcal{E}_\ell = \sqrt{\frac{2\omega_\ell}{\epsilon_o}} a_\ell, \tag{A.93}$$

for $\ell = 1...4$; and

$$\mathcal{E}_5 = \sqrt{\frac{2\omega_5}{\epsilon_o}} k_5 \lambda_{De} a_5, \tag{A.94}$$

for the ion acoustic wave (see Appendix B).

Direct substitution of (A.91)–(A.92) in (A.86)–(A.90), with the assumption of $\omega_3 \approx \omega_4 \approx \omega_{pe}$, gives the so desired equations:

$$\left(\frac{\partial}{\partial t_s} + v_{g1} \frac{\partial}{\partial x_s} + \nu_E \right) a_1 = -K_{SRS} a_2 a_3, \tag{A.95}$$

$$\left(\frac{\partial}{\partial t_s} + v_{g2} \frac{\partial}{\partial x_s} + \nu_E \right) a_2 = K_{SRS} a_1 a_3^*, \tag{A.96}$$

$$\left(\frac{\partial}{\partial t_s} + v_{g3} \frac{\partial}{\partial x_s} + \nu_L \right) a_3 = K_{SRS} a_1 a_2^* - K_{LDI} a_4 a_5, \tag{A.97}$$

$$\left(\frac{\partial}{\partial t_s} + v_{g4} \frac{\partial}{\partial x_s} + \nu_L \right) a_4 = K_{LDI} a_3 a_5^*, \tag{A.98}$$

$$\left(\frac{\partial}{\partial t_s} + v_{g5} \frac{\partial}{\partial x_s} + \nu_A \right) a_5 = K_{LDI} a_3 a_4^*; \tag{A.99}$$

where:

$$K_{SRS} = -\sqrt{\frac{2}{\epsilon_o}} \frac{e}{m_e} \frac{k_3}{4} \left(\frac{\omega_{pe}^2}{\omega_1 \omega_2 \omega_3} \right)^{1/2}, \tag{A.100}$$

$$K_{LDI} = -\sqrt{\frac{2}{\epsilon_o}} \frac{e}{m_e} \frac{\omega_{pe}}{4 v_{Te}} \left(\frac{\omega_5}{\omega_3 \omega_4} \right)^{1/2}. \tag{A.101}$$

Appendix B

Derivation of the COM equations

The coupling of modes equations are derived in detail, following the derivation by
A. Bers, in [49]. The derivation begins with the Maxwell equations, and assumes
small perturbations of an initial steady state; just like in the derivation of Zakharov's
equations given in Appendix A. Each mode, however, is now treated as an independent
linear wave, which acquires a slowly varying modulation, due to an "external" second
order current density that results from the product of two resonant modes.

Since the coupling of modes results from such an "external" excitation, Maxwell
equations are written with the explicit internal and external, charge and current
densities:

$$\nabla \times \overline{E} + \frac{\partial \overline{B}}{\partial t} = 0, \tag{B.1}$$

$$\nabla \times \overline{B} - \frac{1}{c^2}\frac{\partial \overline{E}}{\partial t} - \mu_o \overline{J}_{int} = \mu_o \overline{J}_{ext}, \tag{B.2}$$

$$\epsilon_o \nabla \cdot \overline{E} - \rho_{int} = \rho_{ext}, \tag{B.3}$$

$$\nabla \cdot \overline{B} = 0; \tag{B.4}$$

where $(\overline{J}_{int},\, \rho_{int})$, are the internal current and charge densities excited in the plasma
by the electromagnetic fields, and $(\overline{J}_{ext},\, \rho_{ext})$ are the sources of external excitation.

The plasma fluid equations, which are used later in this Appendix to find the
"external" current density that gives the coupling of the resonant modes, are the

same as (A.5)-(A.8), repeated here for convenience:

$$\rho = \sum_s q_s n_s, \tag{B.5}$$

$$\overline{J} = \sum_s q_s n_s \overline{v}_s, \tag{B.6}$$

$$\frac{\partial}{\partial t} n_s + \nabla \cdot (n_s \overline{v}_s) = 0, \tag{B.7}$$

$$\frac{\partial}{\partial t} \overline{v}_s + \overline{v}_s \cdot \nabla \overline{v}_s = \frac{q_s}{m_s}(\overline{E} + \overline{v}_s \times \overline{B}) - \frac{\gamma_s \kappa T_s}{m_s n_{so}} \left(\frac{n_s}{n_{so}}\right)^{\gamma_s - 2} \nabla n_s. \tag{B.8}$$

Consistent with the derivation of Zakharov's equations (see Appendix A), the derivation in this Appendix is also restricted to one dimensional dynamics. As before, it is assumed that all waves propagate in the $\hat{x}$ direction ($\partial_y = \partial_z = 0$ and $\nabla \to \hat{x}\partial_x$), and that the total electric field has a longitudinal component in $\hat{x}$ and a linearly polarized transverse component in $\hat{y}$. For consistency, the magnetic component of the electromagnetic wave is linearly polarized in $\hat{z}$ [See Figure A-1].

The initial steady state, at time $t = 0$, consists of a non-drifting [$\overline{v}_e(x, t = 0) = \overline{v}_i(x, t = 0) = 0$], homogeneous [$n_{eo} = constant$], neutral [$Z_i n_{io} = n_{eo}$] plasma, free of electric or magnetic fields [$\overline{E}_o = \overline{B}_o = 0$]. First and second order amplitude perturbations: $n_{e1}, n_{i1}, \overline{v}_{e1}, \overline{v}_{i1}, \overline{E}_1, \overline{B}_1, n_{e2}, n_{i2}, \overline{v}_{e2}$ and $\overline{v}_{i2}$, are considered to modify the steady state. Therefore, the total electron density (n_e), ion density (n_i), electron velocity ($\overline{v}_e$), ion velocity ($\overline{v}_i$), electric field ($\overline{E}$) and magnetic field ($\overline{B}$), are:

$$n_e(x, t) = n_{eo} + n_{e1}(x, t) + n_{e2}(x, t), \tag{B.9}$$

$$n_i(x, t) = n_{io} + n_{i1}(x, t) + n_{i2}(x, t), \tag{B.10}$$

$$\overline{v}_e(x, t) = \hat{x}[v_{ex1}(x, t) + v_{ex2}(x, t)] + \hat{y}[v_{ey1}(x, t) + v_{ey2}(x, t)], \tag{B.11}$$

$$\overline{v}_i(x, t) = \hat{x}[v_{ix1}(x, t) + v_{ix2}(x, t)] + \hat{y}[v_{iy1}(x, t) + v_{iy2}(x, t)], \tag{B.12}$$

$$\overline{E}(x, t) = \overline{E}_1(x, t) = \hat{x}E_{x1}(x, t) + \hat{y}E_{y1}(x, t), \tag{B.13}$$

$$\overline{B}(x,t) = \overline{B}_1(x,t) = \hat{z}B_{z1}(x,t). \tag{B.14}$$

The subindex "1", in the perturbation expansion, stands for perturbations in the order of a small parameter $O(\xi)$; and the subindex "2", for perturbations in the order of $O(\xi^2)$. The second order perturbations are kept Eqs. (B.9)–(B.12), because the external excitation that produces the coupling is considered to be second order.

The underlying assumption, is to consider that the electric field has an amplitude which is slowly varying in time and space, ordered with the coupling to order $O(\xi^2)$:

$$\overline{E}(x,t) = \overline{E}_1(x,t) = \mathcal{R}e\left\{\overline{\mathcal{E}_1}(x_s,t_s)e^{i(k_r x - \omega_r t)}\right\}, \tag{B.15}$$

where

$$\overline{\mathcal{E}}_1(x_s,t_s) = \hat{x}\mathcal{E}_{x1}(x_s,t_s) + \hat{y}\mathcal{E}_{y1}(x_s,t_s), \tag{B.16}$$

and (k_r, ω_r) are the wavenumber and frequency, that satisfy the linear dispersion relation. The *slowly varying amplitude* approximation assumes that $|\partial_{x_s}\mathcal{E}| \ll |k_r\mathcal{E}|$ and $|\partial_{t_s}\mathcal{E}| \ll |\omega_r\mathcal{E}|$.

The internal current density, which determines the linear modes, is found first. In a linear approximation (valid for small amplitude perturbations):

$$\overline{J}_{int}(x,t) = \int dx' \int dt' \overline{\overline{\sigma}}(x',t') \cdot \overline{E}_1(x - x', t - t'), \tag{B.17}$$

where $\overline{\overline{\sigma}}(x,t)$ is the plasma conductivity tensor, that can be evaluated from the fluid (or kinetic) plasma equations.

The slowly-varying electric field envelope is expanded in a Taylor series, near $x_s - x' = x_s$ and $t_s - t' = t_s$, to obtain:

$$\overline{\mathcal{E}}_1(x_s - x', t_s - t') = \overline{\mathcal{E}}_1(x_s,t_s) - x'\left|\frac{\partial\overline{\mathcal{E}}_1}{\partial(x_s)}\right|_{x'=0,t'=0} - t'\left|\frac{\partial\overline{\mathcal{E}}_1}{\partial(t_s)}\right|_{x'=0,t'=0} + O(\xi^3), \tag{B.18}$$

where $(\partial^2\mathcal{E}/\partial t_s^2)$ and $(\partial^2\mathcal{E}/\partial x_s^2)$ are considered of order $O(\xi^3)$; and therefore neglected.

Then, from Eqs. (B.15)-(B.18) and noticing that $\overline{\overline{\sigma}}(x,t)$ is pure real, the internal current density evaluates approximately to be:

$$\overline{J}_{int}(x,t) \approx \mathcal{R}e\left\{\int dx' \int dt' \overline{\overline{\sigma}}(x',t') \cdot \left[\overline{\mathcal{E}}_1(x_s,t_s) - x'\frac{\partial \overline{\mathcal{E}}_1}{\partial x_s} - t'\frac{\partial \overline{\mathcal{E}}_1}{\partial t_s}\right] e^{-i\omega_r(t-t')}e^{ik_r(x-x')}\right\}.$$
(B.19)

From the Fourier/Laplace integrals of $\overline{\overline{\sigma}}(x',t')$, one can readily obtain:

$$\overline{J}_{int}(x,t) \approx \mathcal{R}e\left\{\left[\overline{\overline{\sigma}}(k_r,\omega_r) \cdot \overline{\mathcal{E}}_1(x_s,t_s) - i\frac{\partial \overline{\overline{\sigma}}}{\partial k_r} \cdot \frac{\partial \overline{\mathcal{E}}_1}{\partial x_s} + i\frac{\partial \overline{\overline{\sigma}}}{\partial \omega_r} \cdot \frac{\partial \overline{\mathcal{E}}_1}{\partial t_s}\right] e^{-i\omega_r(t-t')}e^{ik_r(x-x')}\right\}.$$
(B.20)

Assuming that the internal current density is also slowly varying: $\overline{J}_{int}(x,t) = \mathcal{R}e\left\{\overline{\mathcal{J}}_{int}(x_s,t_s)e^{-i(k_r x - \omega_r t)}\right\}$, the slowly varying amplitude is simply:

$$\overline{\mathcal{J}}_{int}(x_s,t_s) \approx \overline{\overline{\sigma}}(k_r,\omega_r) \cdot \overline{\mathcal{E}}_1(x_s,t_s) + \frac{\partial \overline{\overline{\sigma}}}{\partial k_r} \cdot \frac{\partial \overline{\mathcal{E}}_1}{\partial x_s} - \frac{\partial \overline{\overline{\sigma}}}{\partial \omega_r} \cdot \frac{\partial \overline{\mathcal{E}}_1}{\partial t_s}.$$
(B.21)

In first order perturbations, the conductivity tensor is diagonal (i.e., with $\overline{B}_o = 0$):

$$\overline{\overline{\sigma}}(k_r,\omega_r) = \begin{pmatrix} \sigma_T & 0 & 0 \\ 0 & \sigma_T & 0 \\ 0 & 0 & \sigma_L \end{pmatrix},$$
(B.22)

where $\sigma_L(k_r,\omega_r)$ and $\sigma_T(k_r,\omega_r)$ are the internal responses due to longitudinal and transverse electric fields. Therefore, the transverse and longitudinal components can be treated separately. Considering (B.22), Eq. (B.21) gives:

$$(\mathcal{J}_{int})_y \approx \mathcal{E}_{y1}(x_s,t_s)\sigma_T(k_r,\omega_r) + \frac{\partial \mathcal{E}_{y1}}{\partial x_s} \cdot \frac{\partial \sigma_T}{\partial k_r} - \frac{\partial \mathcal{E}_{y1}}{\partial t_s} \cdot \frac{\partial \sigma_T}{\partial \omega_r},$$
(B.23)

and

$$(\mathcal{J}_{int})_x \approx \mathcal{E}_{x1}(x_s,t_s)\sigma_L(k_r,\omega_r) + \frac{\partial \mathcal{E}_{x1}}{\partial x_s} \cdot \frac{\partial \sigma_L}{\partial k_r} - \frac{\partial \mathcal{E}_{x1}}{\partial t_s} \cdot \frac{\partial \sigma_L}{\partial \omega_r}.$$
(B.24)

Consistent with the assumption of one dimensional dynamics ($\nabla \to \hat{x}\partial_x$) and the perturbation approximation, Maxwell's equations are also separated into transverse

144

and longitudinal components:

$$\frac{\partial E_{y1}}{\partial x} = -\frac{\partial B_{z1}}{\partial t}, \tag{B.25}$$

$$\frac{\partial B_{z1}}{\partial x} = -\mu_o \epsilon_o \frac{\partial E_{y1}}{\partial t} - \mu_o (J_{int})_y - \mu_o (J_{ext})_{y2}, \tag{B.26}$$

$$\epsilon_o \frac{\partial E_{x1}}{\partial x} = (J_{int})_x + (J_{ext})_{x2}, \tag{B.27}$$

where the external current density is considered to be second order only.

To find the equation for the slowly varying amplitude of $\overline{E}$, the internal current densities [(B.23)–(B.24)] are incorporated to Maxwell's equations [(B.25)-(B.27)], and then separated order by order. For clarity, longitudinal and transverse equations are treated separately.

B.1 Equations for the Slowly Varying Amplitude of the Transverse Fields

From (B.25) and (B.26), the wave equation for electromagnetic fields is:

$$\left(\frac{\partial^2}{\partial x^2} + \mu_o \epsilon_o \frac{\partial^2}{\partial t^2} \right) E_{y1} \approx \mu_o \frac{\partial}{\partial t} (J_{int})_y + \mu_o \frac{\partial}{\partial t} (J_{ext})_y. \tag{B.28}$$

In the slowly varying amplitude approximation, it is considered that

$$E_{y1} = \mathcal{R}e\{\mathcal{E}_{y1}(x_s, t_s)e^{i(k_r x - \omega_r t)}\}, \tag{B.29}$$

$$(J_{int})_y = \mathcal{R}e\{(\mathcal{J}_{int})_y(x_s, t_s)e^{i(k_r x - \omega_r t)}\}, \tag{B.30}$$

$$(J_{ext})_{y2} = \mathcal{R}e\{(\mathcal{J}_{ext})_{y2}(x_s, t_s)e^{i(k_e x - \omega_e t)}\}; \tag{B.31}$$

where $(\mathcal{J}_{int})_y$ is given by (B.23). Then, from Eqs. (B.29)–(B.31) and (B.28):

$$\left[(ik_r)^2 + \mu_o \epsilon_o (i\omega_r)^2 \right] \mathcal{E}_{y1} = -i\mu_o \omega_r (\mathcal{J}_{int})_y - i\mu_o \omega_e (\mathcal{J}_{ext})_y e^{i\delta kx} e^{i\delta\omega t}, \tag{B.32}$$

where $\delta k = k_e - k_r$ and $\delta \omega = \omega_e - \omega_r$. In the slowly varying approximation, it is required that $\delta k \approx 0$ and $\delta \omega \approx 0$ [i.e. $\omega_e \approx \omega_r$].

Decomposing Eq. (B.32) into first and second order components:

$$(\mu_o \epsilon_o \omega_r^2 - k_r^2)\mathcal{E}_{y1} \approx -i\mu_o \omega_r (\mathcal{J}_{int})_{y1}, \tag{B.33}$$

$$(\mathcal{J}_{int})_{y2} \approx (\mathcal{J}_{ext})_{y2} e^{i\delta kx} e^{i\delta \omega t}; \tag{B.34}$$

where $(\mathcal{J}_{int})_{y1}$ and $(\mathcal{J}_{int})_{y2}$ are the first and second order components of Eq. (B.23).

Assuming weak dissipation in the plasma, $\sigma_T = \sigma_{Tr} + i\sigma_{Ti}$ (with $|\sigma_{Ti}| \gg |\sigma_{Tr}|$ and ordering σ_{Tr} with the slow variation of the fields), it is straight forward to find [from (B.23)]:

$$(\mathcal{J}_{int})_{y1} \approx \sigma_{Ti}(k_r, \omega_r)\mathcal{E}_{y1}(x_s, t_s), \tag{B.35}$$

$$(\mathcal{J}_{int})_{y2} \approx \sigma_{Tr}(k_r, \omega_r)\mathcal{E}_{y1}(x_s, t_s) + \frac{\partial \mathcal{E}_{y1}}{\partial x_s}\frac{\partial \sigma_{Ti}}{\partial k_r} + \frac{\partial \mathcal{E}_{y1}}{\partial t_s}\frac{\partial \sigma_{Ti}}{\partial \omega_r}; \tag{B.36}$$

and therefore [with (B.33)–(B.36)],

$$(\mu_o \epsilon_o \omega_r^2 - k_r^2)\mathcal{E}_{y1} \approx -i\mu_o \omega_r \sigma_{Ti}\mathcal{E}_{y1}, \tag{B.37}$$

$$\sigma_{Tr}\mathcal{E}_{y1} + \frac{\partial \mathcal{E}_{y1}}{\partial x_s}\frac{\partial \sigma_{Ti}}{\partial k_r} + \frac{\partial \mathcal{E}_{y1}}{\partial t_s}\frac{\partial \sigma_{Ti}}{\partial \omega_r} \approx (\mathcal{J}_{ext})_{y2} e^{i\delta kx} e^{i\delta \omega t}. \tag{B.38}$$

Equation (B.37) is simply the dispersion relation for dissipation-free electromagnetic waves (k_r, ω_r), and Eq. (B.38) determines the slowly varying amplitude of $\overline{E}$, due to a second order external excitation and weak dissipation.

Since $\epsilon_T = \epsilon_{Tr} + i\epsilon_{Ti} = \epsilon_o(1 + i\sigma_T/\omega_r \epsilon_o)$, then: $\epsilon_{Tr} = \epsilon_o(1 - \sigma_{Ti}/\omega_r \epsilon_o)$, $\epsilon_{Ti} = \sigma_{Tr}/\omega_r$; and Eq. (B.38) can also be written as:

$$\omega_r \epsilon_{Ti}\mathcal{E}_{y1} - \frac{\partial(\omega_r \epsilon_{Tr})}{\partial k_r}\frac{\partial \mathcal{E}_{y1}}{\partial x_s} + \frac{\partial(\omega_r \epsilon_{Tr})}{\partial \omega_r}\frac{\partial \mathcal{E}_{y1}}{\partial t_s} = -(\mathcal{J}_{ext})_{y2} e^{i\delta kx} e^{-i\delta \omega t}, \tag{B.39}$$

where (ω_r, k_r) satisfy the first order dispersion relation.

B.2 Equations for the Slowly Varying Amplitude of the Longitudinal Fields

In the longitudinal case, it is assumed that:

$$E_{x1} = \mathcal{R}e\{\mathcal{E}_{x1}(x_s, t_s)e^{i(k_r x - \omega_r t)}\}, \tag{B.40}$$

$$(J_{int})_x = \mathcal{R}e\{(\mathcal{J}_{int})_x(x_s, t_s)e^{i(k_r x - \omega_r t)}\}, \tag{B.41}$$

$$(J_{ext})_{x2} = \mathcal{R}e\{(\mathcal{J}_{ext})_{x2}(x_s, t_s)e^{i(k_e x - \omega_e t)}\}, \tag{B.42}$$

and $(\mathcal{J}_{int})_x$ given by (B.24). Then, from Poisson's Eq. (B.27):

$$-i\omega_r \epsilon_o \mathcal{E}_{x1}(x_s, t_s) + (\mathcal{J}_{int})_x(x_s, t_s) = -(\mathcal{J}_{ext})_{x2}(x_s, t_s)e^{i(\delta k x - \delta \omega t)}; \tag{B.43}$$

where $\delta k = k_e - k_r$, $\delta\omega = \omega_e - \omega_r$, and $(\mathcal{J}_{int})_x$ containing first and second order terms.

Again, assuming weak dissipation [$\sigma_L = \sigma_{Lr} + i\sigma_{Li}$, with $|\sigma_{Li}| \gg |\sigma_{Lr}|$, and ordering the weak dissipation with the slowly varying fields], a simple decomposition into first and second orders of Equation (B.43) leads to:

$$-i\omega_r \epsilon_o \mathcal{E}_{x1} = (\mathcal{J}_{int})_{x1}, \tag{B.44}$$

$$(\mathcal{J}_{int})_{x2} = -(\mathcal{J}_{ext})_{x2}; \tag{B.45}$$

where, using Eq. (B.24),

$$(\mathcal{J}_{int})_{x1} = \sigma_{Li}(k_r, \omega_r)\mathcal{E}_{x1}(x_s, t_s), \tag{B.46}$$

$$(\mathcal{J}_{int})_{x2} = \sigma_{Lr}(k_r, \omega_r)\mathcal{E}_{x1}(x_s, t_s) + \frac{\partial \mathcal{E}_{x1}}{\partial x_s}\frac{\partial \sigma_{Li}}{\partial k_r} + \frac{\partial \mathcal{E}_{x1}}{\partial t_s}\frac{\partial \sigma_{Li}}{\partial \omega_r}. \tag{B.47}$$

Therefore, [from (B.44)–(B.47)] to first and second order:

$$-i\omega_r \epsilon_o \mathcal{E}_{x1} \approx \sigma_{Li}(\omega_r, k_r)\mathcal{E}_{x1}, \tag{B.48}$$

$$\sigma_{Lr}(\omega_r, k_r)\mathcal{E}_{x1}(x_s, t_s) + \frac{\partial \mathcal{E}_{x1}}{\partial x_s}\frac{\partial \sigma_{Li}}{\partial k_r} + \frac{\partial \mathcal{E}_{x1}}{\partial t_s}\frac{\partial \sigma_{Li}}{\partial \omega_r} \approx -(\mathcal{J}_{ext})_{x2}e^{i\delta kx}e^{i\delta\omega t}. \qquad (B.49)$$

Again, Eq. (B.48) is the dispersion relation for dissipation-free electrostatic waves (ω_r, k_r), and Eq. (B.49) determines the electrostatic field slowly varying amplitude due to a second order external excitation.

Once more, with $\epsilon_{Lr} = \epsilon_o(1 - \sigma_{Li}/\omega_r\epsilon_o)$ and $\epsilon_{Li} = \sigma_{Lr}/\omega_r$, Eq. (B.49) becomes

$$\omega_r\epsilon_{Li}\mathcal{E}_{x1} - \frac{\partial(\omega_r\epsilon_{Lr})}{\partial k_r}\frac{\partial \mathcal{E}_{x1}}{\partial x_s} + \frac{\partial(\omega_r\epsilon_{Lr})}{\partial \omega_r}\frac{\partial \mathcal{E}_{x1}}{\partial t_s} = -(\mathcal{J}_{ext})_{x2}e^{i\delta kx}e^{-i\delta\omega t}. \qquad (B.50)$$

B.3 The slowly varying amplitude equation

In the slowly varying amplitude approximation, the electric field of a longitudinal (or transverse) linear mode, with real k_ℓ and real ω_ℓ, is (see Eq. B.15):

$$\overline{E}_\ell = \mathcal{R}e\left\{\overline{E}_{\ell o}u_\ell(x_s, t_s)e^{ik_\ell x}e^{-i\omega_\ell t}\right\}; \qquad (B.51)$$

where the slow modulation $[\overline{\mathcal{E}}_\ell(x_s, t_s)]$ is rewritten in terms of the unperturbed amplitude of the mode $[\overline{E}_{\ell o}]$ and the slowly varying complex amplitude due to the perturbation $[u_\ell(x_s, t_s)]$:

$$\overline{\mathcal{E}}_\ell(x_s, t_s) = \overline{E}_{\ell o}u_\ell(x_s, t_s). \qquad (B.52)$$

Equations (B.39) and (B.50) can be combined into:

$$\left[\frac{\partial(\omega_r\epsilon_r)}{\partial \omega_r}\frac{\partial}{\partial t_s} - \frac{\partial(\omega_r\epsilon_r)}{\partial k_r}\frac{\partial}{\partial x_s} + \omega_r\epsilon_i\right]\overline{E}_{\ell o}u_\ell(x_s, t_s) = -\overline{\mathcal{J}}_p(x_s, t_s)e^{i\delta kx}e^{-i\delta\omega t}, \quad (B.53)$$

where $\overline{E}$ is either the electrostatic or the electromagnetic field, ϵ is the approximate dielectric function, (k_ℓ, ω_ℓ) are the wavenumber and frequency that satisfy the first order dispersion relation for the unperturbed, dissipative-free mode, and $\overline{\mathcal{J}}_p$ is the external perturbation current, with characteristic frequency and wavenumber: ω_p, k_p. The dephasing is: $\delta k = k_p - k_\ell$ and $\delta\omega = \omega_p - \omega_\ell$.

Dot multiplying Eq. (B.53) by $\overline{E}_{\ell o}^*/4$, one obtains:

$$\left[\frac{\partial(\omega_r K_r)}{\partial \omega_r} \frac{\partial}{\partial t_s} - \frac{\partial(\omega_r K_r)}{\partial k_r} \frac{\partial}{\partial x_s} + \omega_r K_i \right] \frac{\epsilon_o |\overline{E}_{\ell o}|^2}{4} u_\ell(x_s, t_s) = -\frac{1}{4} \overline{E}_{\ell o}^* \cdot \overline{\mathcal{J}}_{p\ell}, \quad \text{(B.54)}$$

where $\overline{\mathcal{J}}_{p\ell} = \overline{\mathcal{J}}_p(x_s, t_s) e^{i\delta k x} e^{-i\delta \omega t}$, and $K = \epsilon/\epsilon_o$ is the linear permitivity function $K(k_r, \omega_r)$.

Then, separating out terms in ω_r and k_r from those in x_s and t_s, Equation (B.54) leads to the equation for the slowly varying amplitude:

$$w_{\ell o} \frac{\partial u_\ell}{\partial t_s} - s_{\ell o} \frac{\partial u_\ell}{\partial x_s} + 2 p_{\ell o} u_\ell = -\frac{\overline{E}_{\ell o}^* \cdot \overline{\mathcal{J}}_{p\ell}}{4}; \quad \text{(B.55)}$$

where one identifies (from conservation of energy [49]), the unperturbed linear mode average wave energy density ($w_{\ell o}$), average wave energy flow density ($s_{\ell o}$) and average wave dissipated power density ($p_{\ell o}$):[49]

$$w_{\ell o} = \frac{\mu_o}{4} |\overline{H}_{\ell o}|^2 + \frac{\epsilon_o}{4} |\overline{E}_{\ell o}|^2 + \frac{\epsilon_o |\overline{E}_{\ell o}|^2}{4} \left[\omega_r \frac{\partial K_r}{\partial \omega_r} \right]_{K_r=0}, \quad \text{(B.56)}$$

$$s_{\ell o} = \frac{1}{2} \mathcal{R}e \left\{ \overline{E}_{\ell o} \times \overline{H}_{\ell o} \right\} + \frac{\epsilon_o |\overline{E}_{\ell o}|^2}{4} \left[\omega_r \frac{\partial K_r}{\partial k_r} \right]_{K_r=0}, \quad \text{(B.57)}$$

and

$$p_{\ell o} = \frac{\epsilon_o |\overline{E}_{\ell o}|^2}{2} (\omega_r K_i)_{K_r=0}. \quad \text{(B.58)}$$

Finally, since the group velocity (of mode ℓ) is $v_{g\ell} = s_{\ell o}/w_{\ell o}$, and its damping rate is $\nu_\ell = p_{\ell o}/2 w_{\ell o}$, the equation for the slowly varying amplitude becomes:

$$\left(\frac{\partial}{\partial t_s} + v_{g\ell} \frac{\partial}{\partial x_s} + \nu_\ell \right) u_\ell(x_s, t_s) = -\frac{(1/4) \overline{E}_{\ell o}^* \cdot \overline{\mathcal{J}}_{p\ell}}{w_{\ell o}}. \quad \text{(B.59)}$$

The parameters in Eq. (B.59) have to be evaluated from the fluid equations, or in the case of the damping rate, from the plasma kinetic equations. Before these parameters are evaluated, the coupling of modes equations for three resonant modes are derived.

B.4 Equations for Three Resonant Modes

Consider the coupling between the three weakly coupled linear modes (ℓ, m and n), with real frequencies and wavenumbers (ω_ℓ, k_ℓ), (ω_m, k_m) and (ω_n, k_n):

$$\overline{E}_\ell = \mathcal{R}e\left\{\overline{E}_{\ell o} u_\ell(x_s, t_s) e^{-i(k_\ell x - \omega_\ell t)}\right\}, \tag{B.60}$$

$$\overline{E}_m = \mathcal{R}e\left\{\overline{E}_{mo} u_m(x_s, t_s) e^{-i(k_m x - \omega_m t)}\right\}, \tag{B.61}$$

$$\overline{E}_n = \mathcal{R}e\left\{\overline{E}_{no} u_n(x_s, t_s) e^{-i(k_n x - \omega_n t)}\right\}; \tag{B.62}$$

that satisfy approximately the resonance conditions [the subscript "r" in k and ω, indicating "real", is dropped from here on]:

$$\omega_\ell - \omega_m - \omega_n = \delta\omega \approx 0, \tag{B.63}$$

$$k_\ell - k_m - k_n = \delta k \approx 0. \tag{B.64}$$

The second order current density in the equation for the slowly varying amplitude of mode ℓ, Eq. (B.59), is assumed to be produced by the product of the resonant modes (m,n). Therefore,

$$\overline{\mathcal{J}}_{p\ell} = \overline{\mathcal{J}}_{mn} u_n(x_s, t_s) u_m(x_s, t_s) e^{i\Delta\psi}; \tag{B.65}$$

where $\overline{\mathcal{J}}_{mn}$ is proportional to the product of the unperturbed resonant field amplitudes $[\overline{\mathcal{J}}_{mn} \sim E_{om} E_{on}]$, and $\Delta\psi = (\delta k)x - (\delta\omega)t$.

Generalizing to the case of three resonant waves, the three coupled mode equations are:

$$\left(\frac{\partial}{\partial t_s} + v_{g\ell}\frac{\partial}{\partial x_s} + \nu_\ell\right) u_\ell(x_s, t_s) = -\frac{1}{4}\frac{\overline{E}_{\ell o}^* \cdot \overline{\mathcal{J}}_{mn}}{\mathrm{w}_{\ell o}} e^{i\Delta\psi} u_m u_n, \tag{B.66}$$

$$\left(\frac{\partial}{\partial t_s} + v_{gm}\frac{\partial}{\partial x_s} + \nu_m\right) u_m(x_s, t_s) = -\frac{1}{4}\frac{\overline{E}_{mo}^* \cdot \overline{\mathcal{J}}_{\ell n}}{\mathrm{w}_{mo}} e^{-i\Delta\psi} u_\ell u_n^*, \tag{B.67}$$

$$\left(\frac{\partial}{\partial t_s} + v_{gn} \frac{\partial}{\partial x_s} + \nu_n \right) u_n(x_s, t_s) = -\frac{1}{4} \frac{\overline{E}^*_{no} \cdot \overline{\mathcal{J}}_{\ell m}}{\mathrm{w}_{no}} e^{-i\Delta\psi} u_\ell u_m^*, \qquad (\text{B.68})$$

For convenience, the COM equations are written in terms of the wave amplitudes $a_\ell = |a_{\ell o}| u_\ell(x_s t_s)$, such that $|a_\ell|^2 = |\mathrm{w}_\ell| / \omega_\ell$ is the wave action density, and ω_ℓ is taken as positive:

$$\left(\frac{\partial}{\partial t_s} + v_{g\ell} \frac{\partial}{\partial x_s} + \nu_\ell \right) a_\ell(x_s, t_s) = -p_\ell K_\ell a_m a_n e^{i\Delta\psi}, \qquad (\text{B.69})$$

$$\left(\frac{\partial}{\partial t_s} + v_{gm} \frac{\partial}{\partial x_s} + \nu_m \right) a_m(x_s, t_s) = -p_m K_m a_\ell a_n^* e^{-i\Delta\psi}, \qquad (\text{B.70})$$

$$\left(\frac{\partial}{\partial t_s} + v_{gn} \frac{\partial}{\partial x_s} + \nu_n \right) a_n(x_s, t_s) = -p_n K_n a_\ell a_m^* e^{-i\Delta\psi}; \qquad (\text{B.71})$$

where, p_ℓ is the sign of the wave energy ($p_\ell = \mathrm{w}_{\ell o} / |\mathrm{w}_{\ell o}|$), and the coupling coefficient K_ℓ is:

$$K_\ell = \frac{\overline{E}^*_{\ell o} \cdot \overline{\mathcal{J}}_{mn} |a_{\ell o}|}{4 |\mathrm{w}_{\ell o}| |a_m a_n|} = \frac{(1/4) \overline{E}^*_{\ell o} \cdot \overline{\mathcal{J}}_{mn}}{\omega_\ell \cdot |a_{\ell o} a_{no} a_{mo}|}. \qquad (\text{B.72})$$

B.5 Conservative Coupling

In a conservative coupling system, the total variation of the energy density has to be zero:

$$\sum_{\ell, m, n} \left(\frac{\partial}{\partial t_s} + v_{g\ell} \frac{\partial}{\partial x_s} + 2\nu_\ell \right) \mathrm{w}_\ell(x_s, t_s) = 0. \qquad (\text{B.73})$$

Using (B.69)-(B.71), it can be shown, see [49], that this implies $K_m = K_n = -K_\ell^*$. This is:

$$\frac{\overline{E}^*_{\ell o} \cdot \overline{\mathcal{J}}_{m,n}}{\omega_\ell} = -\frac{\overline{E}^*_{mo} \cdot \overline{\mathcal{J}}_{\ell,-n}}{\omega_m} = -\frac{\overline{E}^*_{no} \cdot \overline{\mathcal{J}}_{\ell,-m}}{\omega_n} \equiv M. \qquad (\text{B.74})$$

Therefore, the three conservative COM equations are:

$$\left(\frac{\partial}{\partial t_s} + v_{g\ell} \frac{\partial}{\partial x_s} + \nu_\ell \right) a_\ell(x_s, t_s) = p_\ell K a_m a_n e^{i\Delta\psi}, \qquad (\text{B.75})$$

$$\left(\frac{\partial}{\partial t_s} + v_{gm} \frac{\partial}{\partial x_s} + \nu_m \right) a_m(x_s, t_s) = -p_m K^* a_\ell a_n^* e^{-i\Delta\psi}, \qquad (\text{B.76})$$

$$\left(\frac{\partial}{\partial t_s} + v_{gn} \frac{\partial}{\partial x_s} + \nu_n \right) a_n(x_s, t_s) = -p_n K^* a_\ell a_m^* e^{-i \Delta \psi}; \qquad \text{(B.77)}$$

where,

$$K = \frac{-M/4}{|a_{\ell o} a_{mo} a_{no}|}. \qquad \text{(B.78)}$$

B.6   Evaluation of the second order current density

The current densities and the coupling constant (K) are evaluated next, using the fluid equations (B.5)–(B.8), and Maxwell equations (B.1)–(B.4). In general, for a plasma in a magnetic field $(\overline{B}_o)$, this is carried out in [49]. Here again, we restrict ourselves to $\overline{B}_o = 0$ and the specific coupled waves of interest.

Considering the perturbation expansion, Eqs. (B.9)–(B.14), the fluid equations are first separated into orders of magnitude. With $v_{Ts}^2 = \kappa T_s / m_s$, $N_s = n_s / n_{so}$, and

$$N_s^{\gamma_s - 2} \nabla N_s \approx \nabla N_{s1} + \nabla N_{s2} + (\gamma_s - 2) \nabla \left(\frac{N_{s1}^2}{2} \right), \qquad \text{(B.79)}$$

the fluid equations [(B.7)–(B.8)] for the first order variables $[O(\xi)]$ are:

$$\frac{\partial N_{s1}}{\partial t} + \nabla \cdot \overline{v}_{s1} = 0, \qquad \text{(B.80)}$$

$$\frac{\partial \overline{v}_{s1}}{\partial t} + \gamma_s v_{Ts}^2 \nabla N_{s1} = \frac{q_s \overline{E}_1}{m_s}; \qquad \text{(B.81)}$$

and for the second order $[O(\xi^2)]$:

$$\frac{\partial N_{s2}}{\partial t} + \nabla \cdot \overline{v}_{s2} + \nabla \cdot (N_{s1} \overline{v}_{s1}) = 0, \qquad \text{(B.82)}$$

$$\frac{\partial \overline{v}_{s2}}{\partial t} + \gamma_s v_{Ts}^2 \nabla N_{s2} + \gamma_s (\gamma_s - 2) v_{Ts}^2 \nabla \frac{N_{s1}^2}{2} = -\overline{v}_{s1} \cdot \nabla \overline{v}_{s1} + \frac{q_s}{m_s} \overline{v}_{s1} \times \overline{B}_1. \qquad \text{(B.83)}$$

Before the current densities are evaluated, Equation (B.83) is simplified as in

Appendix A. Taking advantage of the vector identity:

$$\overline{v}_{s1} \cdot \nabla \overline{v}_{s1} = \nabla \frac{|\overline{v}_{s1}^2|}{2} - \overline{v}_{s1} \times (\nabla \times \overline{v}_{s1}), \tag{B.84}$$

Eq. (B.83) can be rewritten as:

$$\frac{\partial \overline{v}_{s2}}{\partial t} + \nabla \frac{|\overline{v}_{s1}^2|}{2} + \gamma_s v_{Ts}^2 \nabla N_{s2} + \gamma_s(\gamma_s - 2) v_{Ts}^2 \nabla \frac{N_{s1}^2}{2} = \frac{1}{m_s} \overline{v}_{s1} \times (\nabla \times \overline{P}_{s1}), \tag{B.85}$$

where, $\overline{P}_{s1} = m_s \overline{v}_{s1} + q_s \overline{A}_1$, and $\overline{A}_1$ is a vector potential such that $\overline{B}_1 = \nabla \times \overline{A}_1$ [i.e. $\nabla \cdot \overline{B}_1 = 0$].

Considering Farady's law [Eq. (B.1)], we know that $\nabla \times (\overline{E}_1 - i\omega \overline{A}_1) = 0$, so

$$\overline{A} = \overline{E}/i\omega + \nabla \phi / i\omega; \tag{B.86}$$

where ϕ is a scalar potential [i.e., $\nabla \times (\nabla \phi) = 0$]. From Eq. (B.81), we also know that:

$$\overline{v}_{s1} = \frac{1}{-i\omega} \left(\frac{q_s}{m_s} \overline{E} - \gamma_s v_{Ts}^2 \nabla N_{s1} \right). \tag{B.87}$$

Direct substitution of (B.86)–(B.87) into (B.85), gives $\nabla \times \overline{P}_{s1} = 0$ (because $\nabla \times (\nabla N_{s1}) = \nabla \times (\nabla \phi) = 0$); and the second order momentum conservation equation then reads as:

$$\frac{\partial \overline{v}_{s2}}{\partial t} + \nabla \frac{|\overline{v}_{s1}^2|}{2} + \gamma_s v_{Ts}^2 \nabla N_{s2} + \gamma_s(\gamma_s - 2) v_{Ts}^2 \nabla \frac{N_{s1}^2}{2} = 0. \tag{B.88}$$

Equations (B.80)–(B.81) relate order $O(\xi)$ quantities, while equations (B.82) and (B.88) order $O(\xi^2)$. Considering $\partial_y = \partial_z = 0$ and $\nabla \to \hat{x}\partial_x$, Maxwell equations for $O(\xi)$ variables and equations (B.80)–(B.81), one finds a set of linear partial differential equations that can be Fourier/Laplace transformed to obtain the dispersion relations for the linear plasma modes. In this way, for **electromagnetic waves**, neglecting ion dynamics and considering equations (B.1), (B.2), (B.6) and the $\hat{y}$ component of

(B.80)–(B.81), the dispersion relation is:

$$\omega^2 = c^2 k^2 + \omega_{pe}^2; \tag{B.89}$$

where ω_{pe} is the plasma frequency, and $c = (\epsilon_o \mu_o)^{-1/2}$ the speed of light. Using (a.56) and the cold plasma permitivity function, the wave energy density is given by w $= \epsilon_o |E|^2 / 2$.

For **electron plasma waves**, considering $\omega \approx \omega_{pe}$, $v_p^2 = (\omega/k)^2 \gg v_{Te}^2$ (i.e. $k\lambda_{De} \ll 1$, to avoid wave particle interaction effects), $\gamma_e = 3$ (for one degree freedom electrons) and neglecting ion dynamics (i.e., $\omega \gg \omega_{pi}$); equations (B.3) and the $\hat{x}$ component of (B.80) and (B.81) turn into the dispersion relation:

$$\omega^2 = 3v_{Te}^2 k^2 + \omega_{pe}^2, \tag{B.90}$$

where $v_{Te} = (\kappa T_e / m_e)^{-1/2}$ is the electron thermal velocity. Using (A.56) and the warm fluid electron permitivity function, the electron plasma wave energy density is given by w $= \epsilon_o |E|^2 / 2$.

Finally, for **ion acoustic waves**, considering electron and ion dynamics (i.e., $\omega \ll \omega_{pi}$), $k\lambda_{De} \ll 1$, $v_{Ti}^2 \ll (\omega/k)^2 \ll v_{Te}^2$, $\gamma_e = 1$ and $\gamma_i = 3$ (for isothermal electrons and one degree freedom ions), equations (B.3) and the $\hat{x}$ components of (B.80) and (B.81) give the dispersion relation:

$$\omega^2 = (1 + 3T_i / Z_i T_e) c_s^2 k^2, \tag{B.91}$$

where, $c_s = (Z_i \kappa T_e / m_i)^{-1/2}$ is the speed of sound in the plasma. When $T_e \ll T_i$, $\omega^2 \approx c_s^2 k^2$. The ion wave energy density is obtained using (A.56) and the warm fluid electron-ion permitivity function; it is given by w $= \epsilon_o |E|^2 / (2k^2 \lambda_{De}^2)$.

The **second order current density**, can then be evaluated using equations

(B.82), (B.88) and the second order components of (B.6):

$$\overline{J}_{s2} = q_s n_{so} \left[\overline{v}_{s2} + n_{s1} \overline{v}_{s1} / n_{so} \right] ; \tag{B.92}$$

where n_{s1} and $\overline{v}_{s1}$ can be considered as the s-particle density and velocity, produced by the superposition of linear modes [satisfying the dispersion relations (B.89)–(B.91)].

The second order particle velocity $(\overline{v}_{s2})$, obtained from Eqs. (B.82) and (B.88) [with the Fourier/Laplace transformation: $\partial_t \to -i\omega_\ell$ and $\nabla \to i\overline{k}_\ell$], is given by:

$$\overline{v}_{s2} = \left[1 - \frac{\gamma_s v_{Ts}^2 k_\ell^2}{\omega_\ell^2} \right]^{-1} \frac{\overline{k}_\ell}{\omega_\ell} \left\{ \gamma_s(\gamma_s - 2) v_{Ts}^2 \frac{N_{s1}^2}{2} + \frac{|\overline{v}_{s1}|^2}{2} + \gamma_s v_{Ts}^2 \frac{N_{s1}(\overline{k}_\ell \cdot \overline{v}_{s1})}{2} \right\} ; \tag{B.93}$$

where once again, $N_{s1} = n_{s1}/n_{so}$ and $\overline{v}_{s1}$ result from the superposition of linear modes.

In the particular case of the three interacting modes [with frequencies and wavenumbers (ω_ℓ, k_ℓ), (ω_m, k_m) and (ω_n, k_n)], the total first order particle density and velocity are:

$$n_{s1} = \mathcal{R}e \left\{ n_{\ell 1} e^{i(k_\ell x - \omega_\ell t)} + n_{m1} e^{i(k_m x - \omega_m t)} + n_{n1} e^{i(k_n x - \omega_n t)} \right\}, \tag{B.94}$$

$$v_{sx1} = \mathcal{R}e \left\{ v_{\ell x1} e^{i(k_\ell x - \omega_\ell t)} + v_{mx1} e^{i(k_m x - \omega_m t)} + v_{nx1} e^{i(k_n x - \omega_n t)} \right\}. \tag{B.95}$$

Evaluation of N_{s1}^2, $|\overline{v}_{s1}|^2$ and $n_{s1}\overline{v}_{s1}$; and selection of the terms that match the the resonant frequency and wavenumber (ω_ℓ, k_ℓ), leads to the amplitude of the second order current density, that is resonant with mode ℓ:

$$\overline{\mathcal{J}}_{s2}^{(\ell)} = \overline{\mathcal{J}}_{p\ell} = \frac{q_s n_{so}}{2} \left[1 - \frac{\gamma_s v_{Ts}^2 k_\ell^2}{\omega_\ell^2} \right]^{-1} \frac{\overline{k}_\ell}{\omega_\ell} \{ \overline{v}_{s1}^{(m)} \cdot \overline{v}_{s1}^{(n)} + \gamma_s(\gamma_s - 2) v_{Ts}^2 N_{s1}^{(m)} N_{s1}^{(n)} +$$
$$\gamma_s v_{Ts}^2 \left(N_{s1}^{(m)} \overline{v}_{s1}^{(n)} + N_{s1}^{(n)} \overline{v}_{s1}^{(m)} \right) \} + \frac{q_s n_{so}}{2} \left(N_{s1}^{(m)} \overline{v}_{s1}^{(n)} + N_{s1}^{(n)} \overline{v}_{s1}^{(m)} \right) \tag{B.96}$$

From the 1st order equation (B.81), the complex conjugate electric field of the unperturbed mode ℓ, is given by:

$$\overline{E}_\ell^* = i \frac{m_s}{q_s} \left[\omega_\ell \overline{v}_{s1}^{(\ell)*} - \gamma_s v_{Ts}^2 \overline{k}_\ell N_{s1}^{(\ell)*} \right] . \tag{B.97}$$

Then, after some algebra, substitution of (B.97) and (B.96) into Eq. (B.74) gives:

$$M = i\frac{n_{so}m_s}{2}\{N_{s1}^{(\ell)*}\left(\overline{v}_{s1}^{(m)}\cdot\overline{v}_{s1}^{(n)}\right) + N_{s1}^{(m)*}\left(\overline{v}_{s1}^{(\ell)*}\cdot\overline{v}_{s1}^{(n)}\right) + N_{s1}^{(n)*}\left(\overline{v}_{s1}^{(\ell)*}\cdot\overline{v}_{s1}^{(m)}\right) +$$
$$\gamma_s(\gamma_s - 2)v_{Ts}^2 N_{s1}^{(\ell)*}N_{s1}^{(m)}N_{s1}^{(n)}\}; \text{(B.98)}$$

and as shown before,

$$K = -\frac{M/4}{|a_{\ell o}a_{mo}a_{no}|}. \tag{B.99}$$

Equations (B.98)–(B.99) give the coupling coefficient in terms of the first order particle density and velocity, of the three resonant modes ℓ, m and n. The only part missing, in the derivation of K, is to determine the nature of the resonant modes (which could be ion acoustic, electron plasma or electromagnetic), and evaluate the first order particle densities and velocities in each particular case. The coupling coefficients for SRS and LDI are evaluated next.

B.7   Stimulated Raman Scattering

In SRS, the highest frequency electromagnetic wave (ℓ), interacts with a secondary electromagnetic wave (m) and an electron plasma wave (n). Therefore, $\omega_\ell^2 = \omega_{pe}^2 + c^2 k_\ell^2$, $\omega_m^2 = \omega_{pe}^2 + c^2 k_m^2$, and $\omega_n^2 = \omega_{pe}^2 + 3v_{Te}^2 k_n^2$ [where $(k_n\lambda_{De})^2 \ll 1$].

From the first order equations (B.80)-(B.81),

$$\overline{v}_1^{(\ell)} \approx \frac{iq_e}{\omega_\ell m_e}E_\ell\hat{e}_\ell, N_1^{(\ell)} \approx \frac{\overline{k}_\ell}{\omega_\ell}\cdot\overline{v}_{s1}^{(\ell)} = 0, \tag{B.100}$$

$$\overline{v}_1^{(m)} \approx \frac{iq_e}{\omega_m m_e}E_m\hat{e}_m, N_1^{(m)} \approx \frac{\overline{k}_m}{\omega_m}\cdot\overline{v}_{s1}^{(\ell)} = 0, \tag{B.101}$$

$$\overline{v}_1^{(n)} \approx \frac{iq_e}{\omega_n m_e}E_n\hat{e}_n, N_1^{(n)} \approx \frac{iq_e}{\omega_n m_e}\left(\frac{k_n}{\omega_n}\right)E_m; \tag{B.102}$$

where $\hat{e}_\beta$ [for $\beta = \ell$, m and n] are the unit vectors in the direction of $\overline{v}_\beta$, and (ω_β, k_β) satisfy the corresponding dispersion relation.

Direct substitution of (B.100)–(B.102) into equation (B.98), and some algebra,

leads to:

$$M_{max} \approx -\frac{1}{2}\left(\frac{n_{eo}q_e^2}{m_e\epsilon_o}\right)\left(\frac{q_e}{m_e}\right)\epsilon_o\frac{E_\ell^* E_m E_n}{\omega_\ell\omega_m\omega_n}\left(\frac{k_n}{\omega_n}\right); \qquad (B.103)$$

where only the resonant terms ($\omega \approx \omega_\ell$), from the nonlinear current density (B.91), have been considered. The subindex "max" stands for the assumption that the secondary electromagnetic wave propagates parallel (but in opposite direction), to the high frequency EM wave [$\hat{e}_m = -\hat{e}_\ell$]; which results in the maximum possible coupling.

Next, considering equation (B.56) and the linear dispersion relations (B.89)-(B.90) to find $|a_\beta| = \sqrt{\epsilon_o/2\omega_\beta}|E_\beta|$ (for $\beta = \ell, m, n$), the coupling coefficient [Eq. (B.99)] is found to be:

$$K_{max} \approx -\sqrt{\frac{2}{\epsilon_o}}\frac{e}{m_e}\frac{k_n}{4}\left(\frac{\omega_{pe}^2}{\omega_\ell\omega_m\omega_n}\right)^{1/2}; \qquad (B.104)$$

which is the same coupling coefficient obtained from the Zakharov equations in Appendix A (A.100).

The maximum parametric SRS growth rate (see Chapter 2), given by $(\gamma_{SRS})_{max} = |K_{max}a_\ell|$ can be evaluated right away:

$$(\gamma_{SRS})_{max} \approx \frac{k_n}{4}|v_{\ell o}|\sqrt{\frac{\omega_n}{\omega_m}}; \qquad (B.105)$$

where, $|v_{\ell o}| = e|E_\ell|/m_e\omega_\ell$ is the magnitude of the quiver velocity of the EM pump.

B.8 Langmuir Decay Interaction

In LDI, the highest frequency electron plasma wave (ℓ), resonantly interacts with a backscattered electron plasma wave (m) and an ion acoustic wave (n). Therefore, $\omega_\ell^2 = \omega_{pe}^2 + 3v_{Te}^2 k_\ell^2$, $\omega_m^2 = \omega_{pe}^2 + 3v_{Te}^2 k_m^2$, and $\omega_n^2 = c_s^2 k_n^2$; [where $(k_\beta\lambda_{De})^2 \ll 1$, for $\beta = \ell, m, n$; and $T_e \gg T_i$].

Again, from the first order equations (B.80)-(B.81),

$$\overline{v}_1^{(\ell)} \approx \frac{iq_e}{\omega_\ell m_e}E_\ell\hat{e}_\ell, N_1^{(\ell)} \approx \frac{iq_e}{\omega_\ell m_e}\left(\frac{k_\ell}{\omega_\ell}\right)E_\ell, \qquad (B.106)$$

$$\overline{v}_1^{(m)} \approx \frac{iq_e}{\omega_m m_e} E_m \hat{e}_m, \quad N_1^{(m)} \approx \frac{iq_e}{\omega_m m_e} \left(\frac{k_m}{\omega_m}\right) E_m, \tag{B.107}$$

$$\overline{v}_1^{(n)} \approx \frac{iq_e}{\omega_n m_e} E_n \hat{e}_n, \quad N_1^{(n)} \approx \frac{iq_i}{\omega_n m_i} \left(\frac{k_n}{\omega_n}\right) E_n. \tag{B.108}$$

Direct substitution of (B.106)–(B.108) into equation (B.98) [which contains only the resonant terms of the nonlinear current density], gives:

$$M_{max} \approx -\left(\frac{n_{eo} m_e}{2}\right) \left(\frac{q_e}{m_e}\right)^3 \frac{c_s}{v_{Te}^2} \frac{E_\ell^* E_m E_n}{\omega_\ell \omega_m \omega_n}. \tag{B.109}$$

Once again, only the largest nonlinear current combination and the maximum possible coupling is considered; which is obtained when $\hat{e}_m = -\hat{e}_\ell$ [i.e., the pump electron plasma wave couples to a backscattered secondary electron plasma wave]. In this approximation, it was also considered that $k_n/\omega_n \ll k_m/\omega_m \sim k_\ell/\omega_\ell$.

The coupling coefficient evaluated with (B.109) in Eq. (B.99), is:

$$K_{max} = -\frac{M_{max}(\omega_\ell \omega_m \omega_n)^{1/2}}{4\left(\frac{\epsilon_o}{2}\right)^{3/2} \frac{1}{k_n \lambda_{De}} |E_{\ell o} E_{mo} E_{no}|}. \tag{B.110}$$

Then, using equation (B.56) and the linear dispersion relations (B.90)-(B.91):

$$a_\ell = \sqrt{\frac{\epsilon_o}{2\omega_\ell}} |E_\ell|, \tag{B.111}$$

$$a_m = \sqrt{\frac{\epsilon_o}{2\omega_m}} |E_m|, \tag{B.112}$$

$$a_n = \sqrt{\frac{\epsilon_o}{2\omega_n}} \frac{|E_n|}{k_n \lambda_{De}}; \tag{B.113}$$

so the coupling coefficient reduces to (considering that $\omega_\ell \approx \omega_n \approx \omega_{pe}$):

$$K_{max} \approx -\sqrt{\frac{2}{\epsilon_o}} \frac{e}{m_e} \frac{\omega_{pe}}{4v_{Te}} \left(\frac{\omega_n}{\omega_\ell \omega_m}\right)^{1/2}; \tag{B.114}$$

which is just the same that (A.101).

The maximum parametric LDI growth rate (see Chapter 2), given by $(\gamma_{LDI})_{max} =$

$|K_{max}a_\ell|$ can also be evaluated at this time:

$$(\gamma_{LDI})_{max} \approx \frac{1}{4}\frac{v_{\ell o}}{v_{Te}}\sqrt{\omega_m\omega_n};$$ (B.115)

where once again, $|v_{\ell o}|$ is the quiver velocity of mode ℓ.

.

160

Appendix C

Numeric Approach

Two numerical techniques were used to integrate the coupled mode equations: 1) the method of characteristics with Runge-Kutta integration in time [72], and 2) the Lax-Wendroff integration scheme [73]. These numerical techniques, as well as the computer algorithms used to implement them, are explained in detail in the present Appendix.

C.1 Method of Characteristics

Each wave is transformed to its characteristic frame, $a_\ell(x,t) \rightarrow a_\ell(x - v_{g\ell}t, t)$, to reduce its envelope equation to an ODE in time. After the simple integration of the resulting wave amplitude equations, the envelopes are transformed back to the common frame of reference. This numerical technique is based on the one used by Reiman and Bers, in 1979, to integrate the conservative 3 COM equations.[72]

Considering no wave de-phasing and real wave envelopes only (as explained in Chapter 4), the computer algorithm provided in section C.4, is set to solve the following set of seven coupled mode equations:

$$\left(\frac{\partial}{\partial t} + v_{g1} \frac{\partial}{\partial x} + \nu_1 \right) a_1 = -K_{SRS} a_2 a_3, \tag{C.1}$$

$$\left(\frac{\partial}{\partial t} + v_{g2} \frac{\partial}{\partial x} + \nu_2 \right) a_2 = K_{SRS} a_1 a_3, \tag{C.2}$$

$$\left(\frac{\partial}{\partial t} + v_{g3} \frac{\partial}{\partial x} + \nu_3 \right) a_3 = K_{SRS} a_1 a_2 - K_{LDI} a_4 a_5, \tag{C.3}$$

$$\left(\frac{\partial}{\partial t} + v_{g4} \frac{\partial}{\partial x} + \nu_4 \right) a_4 = K_{LDI} a_3 a_5 - K_{casc} a_6 a_7, \tag{C.4}$$

$$\left(\frac{\partial}{\partial t} + v_{g5} \frac{\partial}{\partial x} + \nu_5 \right) a_5 = K_{LDI} a_3 a_4. \tag{C.5}$$

$$\left(\frac{\partial}{\partial t} + v_{g6} \frac{\partial}{\partial x} + \nu_6 \right) a_6 = K_{casc} a_4 a_7, \tag{C.6}$$

$$\left(\frac{\partial}{\partial t} + v_{g7} \frac{\partial}{\partial x} + \nu_7 \right) a_7 = K_{casc} a_4 a_6. \tag{C.7}$$

A transformation into the *characteristic* frames, $x'_\ell = x - v_{g\ell} t$ for $\ell = 1 \to 7$, eliminates the spatial derivatives and gives the simple ordinary differential equations:

$$\frac{d}{dt} a_\ell(x'_\ell, t) = -\gamma_\ell a_\ell(x'_\ell, t) \pm K a_m(x'_\ell, t) a_n(x'_\ell, t), \tag{C.8}$$

which can be integrated with a finite difference scheme:

$$a_\ell(x'_\ell, t + \Delta t) = a_\ell(x'_\ell, t) + \Delta t \left\{ -\gamma_\ell a_\ell(x'_\ell, t) \pm K a_m(x'_\ell, t) a_n(x'_\ell, t) \right\}. \tag{C.9}$$

In the source code, see Section C.4, Equation (C.8) is integrated with the IMSL ODE solver DIVPRK, which employs the Runge-Kutta-Verner fifth and sixth order method. These integration scheme gives much better accuracy than Eq.(C.9).

The source code stores the field amplitudes at time $t = TT$ $[a_\ell(x, t = TT)]$ in the vectors $V1 \to V7$, of length equal to the number of space grid points in the simulation box $(NX + 1)$. The ODE solver, however, requires that all the integrating variables are supplied in a single vector of unknowns, and the ODE equations in an external subroutine. To this purpose, the field amplitudes are combined in the vector V, of length $NN = 7 * (NX + 1)$, and the ODE equations (C.8) are defined in the external subroutine "FCN".
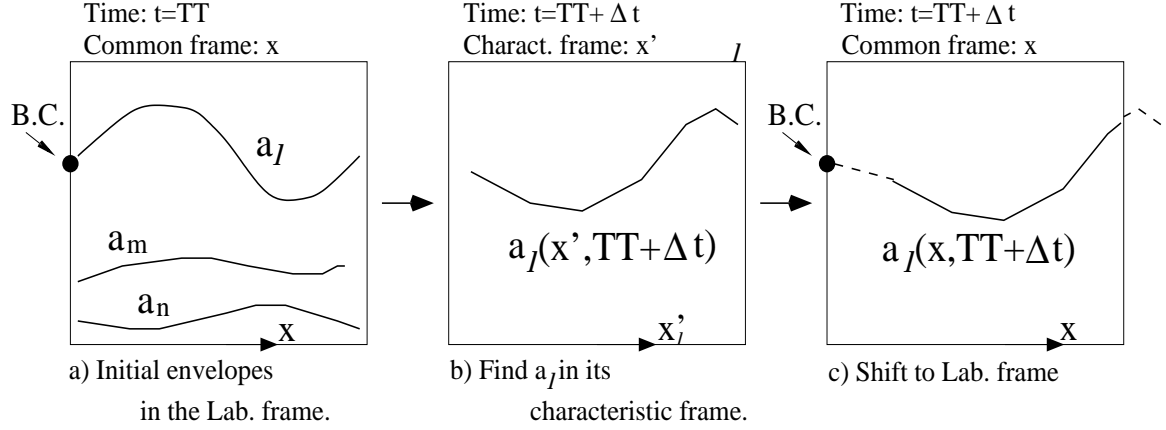
Figure C-1: Illustration of the numerical procedure.

Starting from the wave envelopes at time $t = TT$, the code finds the envelopes at $t = TT + \Delta t$, by direct integration of Equations(C.8). Then, the resulting envelopes (which are referred to x'_ℓ) are transformed back to the common frame of reference, as illustrated in Figure C-1. Iteration of this process allows to find the amplitudes for consecutive time steps.

The time step (Δt) is such that waves with group velocity of $v_g = 1$, propagate one spatial grid point each time step: $\Delta t = DELX$, where $DELX$ is the size of a space grid step. The value of $DELX$ is calculated from the length of the interaction box ($RLNGTH$) and the number of grid-points (NX), which must be provided in the input file.

As indicated with the dashed lines in Figure C-1, after the transformation to the reference frame, the wave amplitudes at few grid-points remain unknown. When the group velocity is $v_g = 1$, there is only one unknown, which corresponds to the boundary condition. However, when the group velocity is larger than one, the field amplitudes at $v_g - 1$ grid-points are not known, and they need to be estimated. In the source code, this is done with a linear fit to the boundary condition. This approximation gives rise to a small numerical error, which is manifested as small ripples in the field amplitudes, with a characteristic space scaling of v_g grid-points. The nature and implications of such ripples are discussed in section C.3.

A block diagram of the source code, provided in Section C.4, is given in Figure C-2. In this figure, the source code line numbers are provided for easy reference.
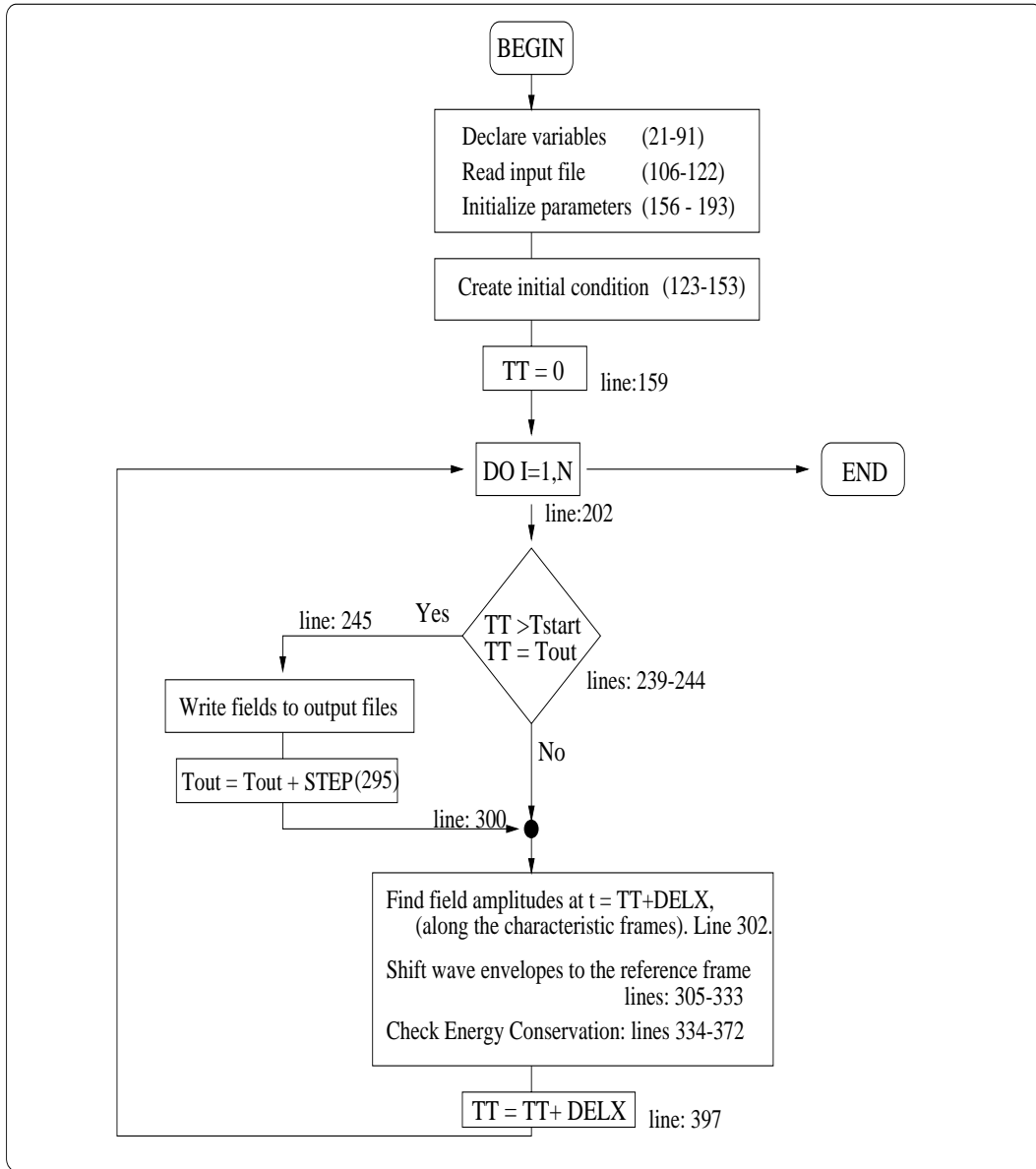
Figure C-2: Block diagram for the "method of characteristics" source code.

To generate the initial condition $[a_\ell(x, t = 0)$, for $\ell = 1...7]$, all the field amplitudes are set to a specified noise level within the box, except at the boundaries where the boundary conditions apply. The initial condition is then evolved in time for a given number of time steps (N), and the field amplitudes are written to an output file at

specified time intervals ($STEP$). Energy conservation is verified at every time step.

The block diagram in Fig. C-2, shows how the initial condition is set up, and the time variable TT is initialy set to zero. Then, in a simple loop, the wave equations are integrated N times, increasing the time variable TT by $\Delta t = DELX$ (in each loop). A decision point within the loop, determines whether the field amplitudes should be written to an output file. This occurs whenever TT is equal to T_{OUT} and larger than T_{STRAT}.

Conservation of Energy

To check the conservation of energy, the code evaluates the error in the following relations, which should be equal to zero (see Chapter 2):

$$Err1 = \frac{I_2}{\omega_2} + \frac{I_1}{\omega_1}, \tag{C.10}$$

$$Err2 = \frac{I_7}{\omega_7} + \frac{I_6}{\omega_6}, \tag{C.11}$$

$$Err3 = \frac{I_3}{\omega_3} + \frac{I_1}{\omega_1} + \frac{I_5}{\omega_5}, \tag{C.12}$$

$$Err4 = \frac{I_5}{\omega_5} + \frac{I_4}{\omega_4} + \frac{I_6}{\omega_6}, \tag{C.13}$$

$$Err5 = \frac{I_4}{\omega_4} + \frac{I_1}{\omega_1} + \frac{I_3}{\omega_3} + \frac{I_6}{\omega_6}. \tag{C.14}$$

The integrals I_ℓ, for $\ell = 1 \rightarrow 7$, are calculated as:

$$I_\ell = IF\ell - II\ell + IL\ell - IO\ell + E_{Dis\ell}, \tag{C.15}$$

where, the variables: $IF\ell$, $II\ell$, $IL\ell$, $IO\ell$ and $E_{Dis\ell}$, stand for the ℓ mode, total energy in the box at $t = TT$, total energy in the box at $t = TT + STEP$, energy that crossed the first boundary ($x = -L/2$) during $STEP$, energy that crossed the second boundary ($x = L/2$) during $STEP$, and the total energy dissipated in the

box during $STEP$. They are defined as:

$$IF\ell = \left|\int_{-L/2}^{L/2}|a_\ell(x,t)|^2 dx\right|_{t=TT+STEP}, \qquad (C.16)$$

$$II\ell = \left|\int_{-L/2}^{L/2}|a_\ell(x,t)|^2 dx\right|_{t=TT}, \qquad (C.17)$$

$$IL\ell = \int_{TT}^{TT+STEP} v_{g\ell}|a_\ell(x=L/2,t)|^2 dt \qquad (C.18)$$

$$IO\ell = \int_{TT}^{TT+STEP} v_{g\ell}|a_\ell(x=-L/2,t)|^2 dt, \qquad (C.19)$$

$$E_{Dis\ell} = 2\nu_\ell \int_{-L/2}^{L/2}\int_{TT}^{TT+STEP}|a_\ell(x,t)|^2. \qquad (C.20)$$

As reference for the curious reader, a list of the **input parameters**, and their description, is given in Table C.1. These parameters need to be supplied to the source code in the text file "tdatc_u".

Parameter	Description
$RLNGTH$	length of the simulation box
NX	number of grid points in space
N	No. of time steps to be calculated
$TSTART$	Initial time to start writing data to output file
$STEP$	Time step to write data to output file
$NOISE$	Initial nose amplitude
AMP_ℓ	Boundary amplitude of mode ℓ
GAM_ℓ	Damping rate of model ℓ
VEL_ℓ	group velocity of mode ℓ
KKK	SRS coupling coefficient
$Kcasc$	Cascading coupling coefficient
TOL	Tolerance in numerical error

Table C.1: Input parameters

The output files containing the amplitude of the fields in the simulation box, the time evolution of the envelopes at the boundaries, the error in the conservation relations, and other relevant parameters, are the text files: "aiajak1", "aiajak2",

"fields1", fields2", "power" and "conser". This files can be read with Matlab, to generate any desired plot.

As explained before, the provided source code is set to solve the seven coupled modes equations. However, it can be used to evolve the three and five wave interactions, by setting the proper parameters (coupling coefficients) to zero. The evolution of complex wave envelopes, with complex coupling coefficients or wave de-phasing, can be investigated with a very similar code. The main difference being that some variables need to be defined as complex, and the wave equations need to be separated into their real and imaginary parts. In this case, instead of seven equations in the FCN subroutine, there would be fourteen (seven for the real part of the wave envelopes, and seven for the imaginary parts).

Concerned by the numerical error (small ripples in the field amplitudes) that was explained before, I have pursued an alternative technique to integrate the coupled mode equations. This alternative technique lead to very similar numerical results. While the comparison between both techniques is left to Section C.3, the following Section describes in detail the Lax-Wendroff approach.

C.2 Lax-Wendroff Technique

In this technique, the wave envelopes are evolved in time and space, considering a Taylor series expansion (with respect to time) of the field amplitudes $a_\ell(x,t)$:[73]

$$a_\ell(x, t + \Delta t) = a_\ell(x,t) + \Delta t \left(\frac{\partial}{\partial t} a_\ell\right)_{x,t} + \frac{(\Delta t)^2}{2} \left(\frac{\partial^2}{\partial t^2} a_\ell\right)_{x,t} + \cdots \qquad \text{(C.21)}$$

In this expansion, the time derivatives (at time t) can be evaluated using the slowly varying amplitude equations [(C.1) – (C.7)], for $\ell = 1 \to 7$:

$$\frac{\partial}{\partial t} a_\ell = -v_{g\ell} \frac{\partial}{\partial x} a_\ell - \gamma_\ell a_\ell \pm K a_m a_n, \qquad \text{(C.22)}$$

$$\frac{\partial^2}{\partial t^2} a_\ell = -v_{g\ell} \frac{\partial}{\partial x} \left(\frac{\partial}{\partial t} a_\ell\right) - \gamma_\ell \frac{\partial}{\partial t} a_\ell \pm K \left(a_m \frac{\partial}{\partial t} a_n + a_n \frac{\partial}{\partial t} a_m\right). \qquad \text{(C.23)}$$

167

The spatial derivatives in Equations (C.22) and (C.23), can be easily evaluated with finite difference schemes. With accuracy of $O(\Delta x^2)$, the space derivatives are:

$$\left[\frac{d}{dx}u\right]_i = \frac{u_{i+1} - u_{i-1}}{2\Delta x}, \tag{C.24}$$

$$\left[\frac{d^2}{dx^2}u\right]_i = \frac{u_{i+1} - 2u_i + u_{i-1}}{(\Delta x)^2}. \tag{C.25}$$

The source code used to implement the Lax-Wendroff approach is provided in Section C.5. This code is very similar to the one used for the method of characteristics, with the main difference that instead of calling the ODE solver to find $a_\ell(x - v_{g\ell}t, t + \Delta t)$, now Equation (C.21) is applied to find $a_\ell(x, t + \Delta t)$ directly. For convenience, this is done in the "STP" subroutine, which substitutes the call to the ODE solver DIVPRK. Apart from the transformations to the reference frame, which is not necessary any more, both source codes are pretty much the same. To contrast with section C.4, the source code in section C.5 is set to solve only the five wave coupled mode equations:

$$\left(\frac{\partial}{\partial t} + v_{g1}\frac{\partial}{\partial x} + \nu_1\right)a_1 = -K_{SRS}a_2a_3, \tag{C.26}$$

$$\left(\frac{\partial}{\partial t} + v_{g2}\frac{\partial}{\partial x} + \nu_2\right)a_2 = K_{SRS}a_1a_3, \tag{C.27}$$

$$\left(\frac{\partial}{\partial t} + v_{g3}\frac{\partial}{\partial x} + \nu_3\right)a_3 = K_{SRS}a_1a_2 - K_{LDI}a_4a_5, \tag{C.28}$$

$$\left(\frac{\partial}{\partial t} + v_{g4}\frac{\partial}{\partial x} + \nu_4\right)a_4 = K_{LDI}a_3a_5, \tag{C.29}$$

$$\left(\frac{\partial}{\partial t} + v_{g5}\frac{\partial}{\partial x} + \nu_5\right)a_5 = K_{LDI}a_3a_4. \tag{C.30}$$

Considering that at early times in the simulation the pump wave (a_1) exhibits a sharp edge, the time step needs to be set so the pump wave propagates one grid-point each time step: $\Delta t = DELX/v_{g1}$. This improves the accuracy achieved with the method of characteristics, but makes the computation time significantly larger. A
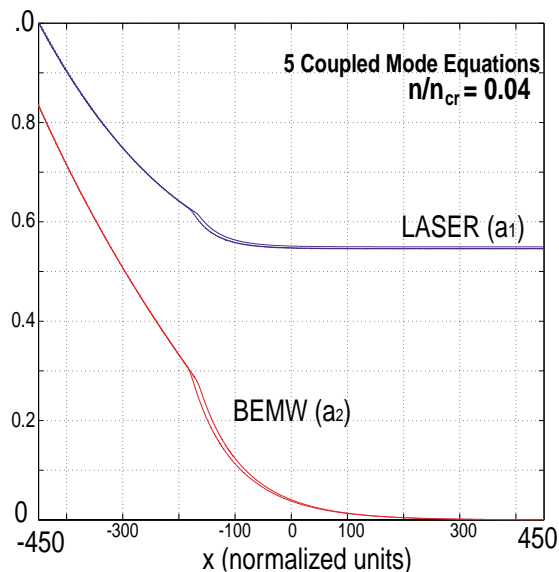
Figure C-3: Comparison between Lax-Wendroff and Method of Characteristics.

discussion on the advantages and disadvantages of both techniques is given in the following section.

C.3   Discussion

As explained already, two different numeric techniques have been used to solve the coupled mode equations, in a finite region of interaction. While both techniques give approximately the same results, the method of characteristics allow for faster calculations, and the Lax-Wendroff scheme for higher accuracy.

Figure C-3 compares the laser and SRS backscattering steady state wave envelopes, obtained with the method of characteristics and the Lax-Wendroff schemes. The parameters used to obtain such results, correspond to those in Chapter 4, with an electron plasma density of $n/n_{cr} = 0.04$. The wave envelopes through the box are almost identical (in the figure, both calculations almost fall on top of each other). is difficult to notice the difference . A similar error is observed in the other wave amplitudes, or when different plasma parameters are considered. Such cases however, are not shown, for brevity purposes. Instead, we take a closer look to the field am-
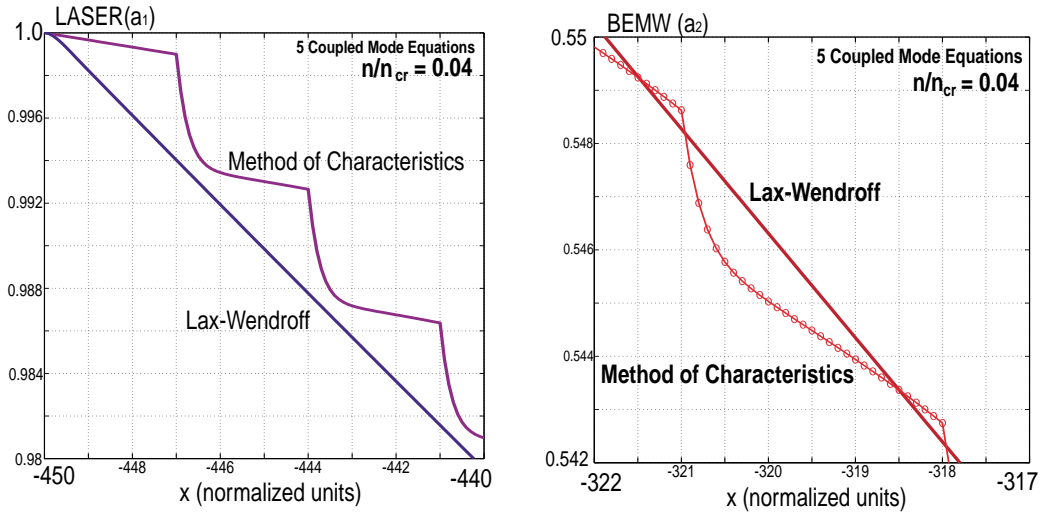
Figure C-4: Method of Characteristics vs. Lax-Wendroff (detailed view)

plitudes, to describe the "ripples" in the wave amplitudes that are obtained with the method of characteristics is applied.

Figure C-4 shows a detailed picture of the filed amplitudes (same data plotted in Figure C-3). Figure C-4.a shows the laser amplitude near the left boundary, and the Lax-Wendroff calculation can be observed to have a nice and smooth variation. The laser amplitude obtained with the method of characteristics, however, shows a series of ripples which arise from the inaccurate estimation of the field amplitude near its boundary condition (explained in Section C.1). This ripples have a periodicity of exactly 30 grid-points, which correspond to the laser group velocity considered in the simulation, and is independent of the spacing between the grid-points.

Figure C-4.b shows a detailed view of the field amplitude in the SRS backscattered electromagnetic wave. As it can be appreciated, the ripples observed in the laser also appear in the backscattered wave, which should not be surprising because both waves are coupled. The circles in the figure show the field amplitudes at the different grid-points, so the thirty grid-point periodicity can be clearly appreciated. Again, the amplitude calculated with the Lax-Wendroff scheme appears to be smooth and nice.

The amplitude of the numeric ripples appears to be small (compared to the field amplitudes) when the damping in the system is relatively large - as in the above

170

example. However, when the damping is relatively weak, the ripples can become unstable and the time evolution may not reach a steady state. To avoid this problem, a narrow window averaging (over few neighboring grid-points) can be implemented in the code. This would soften the sharp corners in the ripples and therefore prevent them from growing unstable. Such window averaging has been implemented and observed to be effective, as it prevents the ripples from growing and leads to a stable space/time evolution, which matches the one obtained with Lax-Wendroff scheme.

Apart from the "ripples" problem, both numeric techniques lead to almost identical results. Therefore, considering that the method of characteristics is much faster than the Lax-Wendroff approach, it is recommendable to use the first method to obtain a quick grasp of the wave envelopes behavior, before pursuing the accurate, but slow, simulations with the Lax-Wendroff scheme.

C.4   Source Code (Method of Characteristics)

Source code:

```
C       This program solves the 7COM equations,
C         based on Carson-Reiman algorithm.
C
C         Each equation is integrated in time, along its characteristic,
C         then shifted back to the common reference frame.
C
C         IMSL-ODE's solver (DIVPRK) is used to integrate in time.
C
C         Finite length plasma is considered, and one BC for each wave.
C                                                                              10
C         This code may be used to integrate the 7 COM equations.
C
C         7COM.f


        IMPLICIT NONE



C       DEFINITION OF VARIABLES
                                                                              20
        INTEGER*4 I, II, J, K, K1, K2, L ! Flags
        INTEGER*4 COUNT
        INTEGER*4 SHFPTS
        INTEGER*4 NX, N          ! No. of grid points in space & time
        INTEGER*4 NXD, MID
        INTEGER*4 MXSTEP, NN     ! For DIVPRK routine
        INTEGER*4 ISEED, NOUT    ! For random number generation
        INTEGER*4 DUM            ! dummy variable


        REAL*8 R(20010), DRNUNF ! For random number generation              30
        REAL*8 NOISE             ! Initial noise level
        REAL*8 RLNGTH, DELX      ! Box length & grid−size [Norm. space units]
        REAL*8 TT                ! Time [Norm. time units]
        REAL*8 AMP1, AMP2, AMP3, AMP4, AMP5 ! Boundary Conditions
        REAL*8 AMP6, AMP7
        REAL*8 GAM1, GAM2, GAM3, GAM4, GAM5 ! Damping rates
        REAL*8 GAM6, GAM7
        REAL*8 VEL1, VEL2, VEL3, VEL4, VEL5 ! Group velocities
        REAL*8 VEL6, VEL7
        REAL*8 KSRS              ! SRS coupling coefficient                  40
        REAL*8 KLDI              ! LDI coupling coefficient
        REAL*8 KCASC             ! Cascade coupling coefficient
```

172

```fortran
      REAL*8 X(20010)          ! Vector of space points.
      REAL*8 V1(20010), V2(20010), V3(20010) ! Field amplitudes
      REAL*8 V4(20010), V5(20010)
      REAL*8 V6(20010), V7(20010)
      REAL*8 V(200000)         ! Input/output for DIVPRK

      REAL*8 EOI1, EOF1, ELI1, ELF1 ! For energy conserv. check        50
      REAL*8 II1, IF1, IO1, IL1
      REAL*8 EOI2, EOF2, ELI2, ELF2
      REAL*8 II2, IF2, IO2, IL2
      REAL*8 EOI3, EOF3, ELI3, ELF3
      REAL*8 II3, IF3, IO3, IL3
      REAL*8 EOI4, EOF4, ELI4, ELF4
      REAL*8 II4, IF4, IO4, IL4
      REAL*8 EOI5, EOF5, ELI5, ELF5
      REAL*8 II5, IF5, IO5, IL5
      REAL*8 EOI6, EOF6, ELI6, ELF6                                    60
      REAL*8 II6, IF6, IO6, IL6
      REAL*8 EOI7, EOF7, ELI7, ELF7
      REAL*8 II7, IF7, IO7, IL7
      REAL*8 C1, C2, C3, C4, C5, C6, C7 ! Integ. Squared. Amps.
      REAL*8 I1, I2, I3, I4, I5, I6, I7
      REAL*8 ERR1, ERR2, ERR3, ERR4, ERR5, ERR6, ERR7
      REAL*8 DUMM1, DUMM2, DUMM3, DUMM4, DUMM5 ! Dummy variables

      REAL*8 TOUT, HH ! Vars. for plotting routine
      REAL*8 TSTART                                                    70

      INTEGER*4 IDO ! Vars. for DIVPRK
      REAL*8 PARAM(50)
      REAL*8 TEND, STEP
      REAL*8 TOL

C     External routines:

      EXTERNAL FCN ! Coupling of modes equations
      EXTERNAL DIVPRK, DSET ! IMSL solver                              80
      EXTERNAL RNSET, DRNUNF, UMACH ! Generation of random numbers

C     Shared variables:

      COMMON /VARS1/ NX
      COMMON /VARS2/ RLNGTH, DELX, GAM1, GAM2, GAM3, GAM4, GAM5
      COMMON /MORE/  KSRS, KLDI, VEL1, VEL2, VEL3, VEL4, VEL5
```

```fortran
      COMMON /MORE1/ Kcasc, VEL6, VEL7, GAM6, GAM7, AMP6, AMP7
      COMMON /AMPV/  AMP1, AMP2, AMP3, AMP4, AMP5

C       INPUT/OUTPUT files:

      OPEN (1, FILE='initial')
      !OPEN (2, FILE='aiajak1')
      !OPEN (3, FILE='aiajak2')
      OPEN (4, FILE='fields1')
      OPEN (5, FILE='fields2')
      OPEN (6, FILE='power')
      OPEN (7, FILE='conser')
      OPEN (8, FILE='plot_param')
      OPEN (9, FILE='tdatc_u', STATUS='OLD')
      !OPEN (10, FILE='tplot', FORM='UNFORMATTED')


C       Read input data:

      READ (9,*) AMP1, AMP2, AMP3, NOISE
      READ (9,*) AMP4, AMP5, RLNGTH, NX
      READ (9,*) STEP, N, TOL, DUMM1
      READ (9,*) TSTART, DUMM1
      READ (9,*) GAM1, DUMM1, GAM4, GAM5
      READ (9,*) GAM2, DUMM1, GAM3, DUMM3
      READ (9,*) DUMM1, VEL1, VEL2, VEL3
      READ (9,*) KLDI
      READ (9,*) MXSTEP
      READ (9,*) VEL4, VEL5
      READ (9,*) KSRS
      READ (9,*) Kcasc, VEL6, VEL7
      READ (9,*) GAM6, GAM7, AMP6, AMP7


C    Generate initial condition:
C     (Random number generation has been turned off)

      NXD = INT(NX/2.) ! Generate vector of space points
      DELX = RLNGTH/NXD/2.
      MID = NXD+1
      DO I=1,NX+1
         X(I) = (I-MID)*DELX
      ENDDO

      !CALL UMACH (2, NOUT)
      !ISEED = 123457
      !CALL RNSET (ISEED)
```

DO I=1,NX+1 ! Set all field amplitudes at noise level

    V1(I) = NOISE

    V2(I) = NOISE

    V3(I) = NOISE

    V4(I) = NOISE

    V5(I) = NOISE

    V6(I) = NOISE   140

    V7(I) = NOISE

ENDDO

V1(1) = AMP1 ! Fix boundary value for the pump

V2(NX+1) = AMP2 ! Fix boundary value for the BEMW

C   *!WRITE INITIAL CONDITION*

C   *DO I=1,NX+1*

C   *WRITE(1,26) x(I), V1(I), V2(I), V3(I), V4(I), V5(I)*

C   *ENDDO*

                                                         150

C   *INITIALIZATION OF other VARIABLES*

COUNT = 0   ! Counter for plotting routine

TT = 0.0   ! Time counter (in norm. time units)

NN = 7*(NX+1)   ! Total number of equations

DELX=RLNGTH/NX ! Grid spacing in space.

TEND = DELX   ! Time increment used in time integration:

                     ! A wave with group velocity vg = 1, shifts one gridpoint.   160

TOUT = TT   ! Vars. for plotting routine

HH = DELX/2   ! Vars. for plotting routine

C   *Initialization of variables for energy conservation check.*

IO1 = 0.d0   ! Squared field amplitudes integrated over box,

IL1 = 0.d0   ! used to check the conservation of energy.

IO2 = 0.d0   170

IL2 = 0.d0

IO3 = 0.d0

IL3 = 0.d0

IO4 = 0.d0

IL4 = 0.d0

IO5 = 0.d0

IL5 = 0.d0

```
      IO6 = 0.d0
      IL6 = 0.d0
      IO7 = 0.d0                                                                180
      IL7 = 0.d0


      C1 = 0.d0              ! Squared field amplitudes integrated over box,
      C2 = 0.d0              ! used to check the conservation of energy.
      C3 = 0.d0
      C4 = 0.d0
      C5 = 0.d0
      C6 = 0.d0
      C7 = 0.d0
                                                                               190
C     MAIN SOLVING ROUTINE
C     Starting from the initial condition, integrates the COM equations for N time steps

      CALL DSET (50, 0.d0, PARAM, 1) ! Initialize vars. for DIVPRK
      PARAM(4) = MXSTEP
      IDO = 1


      DO 38 I=1,N           ! Integrate COM equations N times

         DO J=1,NX+1        ! Generate V vector for DIVPRK,                     200
                            ! which combines all the field amplitudes at all points.
            II = 7 * (J−1)
            V (II+1) = V1(J)
            V (II+2) = V2(J)
            V (II+3) = V3(J)
            V (II+4) = V4(J)
            V (II+5) = V5(J)
            V (II+6) = V6(J)
            V (II+7) = V7(J)
         ENDDO                                                                  210


      EOI1 = V1(1)**2 ! Squared field amplitudes at the boundaries,
      ELI1 = V1(NX+1)**2 ! at time TT
      EOI2 = V2(1)**2 ! used to check the conservation of energy.
      ELI2 = V2(NX+1)**2
      EOI3 = V3(1)**2
      ELI3 = V3(NX+1)**2
      EOI4 = V4(1)**2
      ELI4 = V4(NX+1)**2
      EOI5 = V5(1)**2                                                           220
      ELI5 = V5(NX+1)**2
      EOI6 = V6(1)**2
```

176

```fortran
      ELI6 = V6(NX+1)**2
      EOI7 = V7(1)**2
      ELI7 = V7(NX+1)**2


      II1 = C1          ! Squared field amplitudes integrated over box,
      II2 = C2          ! used to check the conservation of energy.
      II3 = C3
      II4 = C4
      II5 = C5
      II6 = C6
      II7 = C7


C     Integrate the fields in the box and werite to an output file
C     only at selected moments in time: every "STEP" time units, after TT>TSTART
C     Note: Initial data is included in the file.


      IF (TT.GE.TSTART) THEN


        IF (TT.GE.(TOUT-HH)) THEN
          write(*,*) I, '/', N

          COUNT = COUNT+1 ! Counter for plotting routine

          C1 = 0.d0    ! Clean integrated squared field amplitudes
          C2 = 0.d0
          C3 = 0.d0
          C4 = 0.d0
          C5 = 0.d0
          C6 = 0.d0
          C7 = 0.d0


          !Integration with TRAPEZOIDAL RULE

          !Skip points, to match numeric errors in time & space integrations (switched off!!):
          !SHFPTS = NINT(DABS(VEL1)) !No. of points to skip.
          SHFPTS = 1M̂
          DUM = INT(NX/SHFPTS)


          DO K = 0,DUM
            K1 = K*SHFPTS
            K2 = (K+1)*SHFPTS
            DUMM1 = DELX*SHFPTS

            C1=C1+(DUMM1/2.d0)*(V(7*K1+1)**2 + V(7*K2+1)**2)
```

177

```fortran
            C2=C2+(DUMM1/2.d0)*(V(7*K1+2)**2 + V(7*K2+2)**2)
            C3=C3+(DUMM1/2.d0)*(V(7*K1+3)**2 + V(7*K2+3)**2)
            C4=C4+(DUMM1/2.d0)*(V(7*K1+4)**2 + V(7*K2+4)**2)          270
            C5=C5+(DUMM1/2.d0)*(V(7*K1+5)**2 + V(7*K2+5)**2)
            C6=C6+(DUMM1/2.d0)*(V(7*K1+6)**2 + V(7*K2+6)**2)
            C7=C7+(DUMM1/2.d0)*(V(7*K1+7)**2 + V(7*K2+7)**2)
      ENDDO


      ! Register the field amplitudes in an output file:
      OPEN (2, FILE='aiajak1')
      OPEN (3, FILE='aiajak2')
      DO J=1,NX+1
         WRITE(2,26) x(J), V1(J), V2(J), V3(J), V4(J), V5(J)           280
         WRITE(3,23) x(J), V6(J), V7(J)
      ENDDO
      CLOSE(2)
      CLOSE(3)


      ! Register integrated fields and boundary amplitudes
      WRITE(4,225) TT,V1(1),V2(1),V1(Nx+1),V2(Nx+1)
      WRITE(5,20) V3(1),V3(Nx+1)
      WRITE(6,26) TT, C1, C2, C3, C4, C5

                                                                       290
      TOUT = TOUT+STEP ! Flag update


      ENDIF
      ENDIF



C        Integrate COM equations in time (along each characteristic frame)
      CALL DIVPRK (IDO, NN, FCN, TT, TEND, TOL, PARAM, V)


                                                                       300

C        DIVPRK returns the integrated amplitudes in the V vector; here, we update the vectors: Vi
      DO J=1,NX+1
         II = 7 * (J-1)
         V1(J) = V(II+1)
         V2(J) = V(II+2)
         V3(J) = V(II+3)
         V4(J) = V(II+4)
         V5(J) = V(II+5)
         V6(J) = V(II+6)
         V7(J) = V(II+7)                                               310
      ENDDO
```

```fortran
C         All field amplitudes were found in their own characteristic frame,
C         now we shift them back to the lab. frame:

          CALL SHIFTER (NX+1, V1, X, VEL1, TT, YYS, AMP1)
          V1 = YYS
          CALL SHIFTER (NX+1, V2, X, VEL2, TT, YYS, AMP2)
          V2 = YYS
          CALL SHIFTER (NX+1, V3, X, VEL3, TT, YYS, AMP3)          320
          V3 = YYS
          CALL SHIFTER (NX+1, V4, X, VEL4, TT, YYS, AMP4)
          V4 = YYS
          CALL SHIFTER (NX+1, V5, X, VEL5, TT, YYS, AMP5)
          V5 = YYS
          CALL SHIFTER (NX+1, V6, X, VEL6, TT, YYS, AMP6)
          V6 = YYS
          CALL SHIFTER (NX+1, V7, X, VEL7, TT, YYS, AMP7)
          V7 = YYS
                                                                   330
C         Cheks of energy conservation:
          EOF1 = V1(1)**2 ! Squared amplitudes at the boundaries,
          ELF1 = V1(NX+1)**2 ! at time: TT+STEP
          IF1 = C1
          EOF2 = V2(1)**2
          ELF2 = V2(NX+1)**2
          IF2 = C2
          EOF3 = V3(1)**2
          ELF3 = V3(NX+1)**2
          IF3 = C3                                                 340
          EOF4 = V4(1)**2
          ELF4 = V4(NX+1)**2
          IF4 = C4
          EOF5 = V5(1)**2
          ELF5 = V5(NX+1)**2
          IF5 = C5
          EOF6 = V6(1)**2
          ELF6 = V6(NX+1)**2
          IF6 = C6
          EOF7 = V7(1)**2                                          350
          ELF7 = V7(NX+1)**2
          IF7 = C7


C         Error in energy conservation (should be zero)
          I1 = IF1−II1+IL1−IO1+DABS(2.d0*GAM1*DELX/2)*(IF1+II1)
          I2 = IF2−II2+IL2−IO2+DABS(2.d0*GAM2*DELX/2)*(IF2+II2)
          I3 = IF3−II3+IL3−IO3+DABS(2.d0*GAM3*DELX/2)*(IF3+II3)
```

179

$$I4 = IF4{-}II4{+}IL4{-}IO4{+}DABS(2.d0*GAM4*DELX/2)*(IF4{+}II4)$$

$$I5 = IF5{-}II5{+}IL5{-}IO5{+}DABS(2.d0*GAM5*DELX/2)*(IF5{+}II5)$$

$$I6 = IF6{-}II6{+}IL6{-}IO6{+}DABS(2.d0*GAM6*DELX/2)*(IF6{+}II6) \qquad 360$$

$$I7 = IF7{-}II7{+}IL7{-}IO7{+}DABS(2.d0*GAM7*DELX/2)*(IF7{+}II7)$$

ERR1 = I2 + I1

ERR2 = I7 + I6

ERR3 = I3 + I1 + I5

ERR4 = I5 + I4 + I6

ERR5 = I4 + I1 + I3 + I6

C   *Write the error in energy conservation relations:*   370

C   *WRITE(7,26) TT, IF1, II1, IL1, IO1,*

C &   *IF1-II1+IL1-IO1+DABS(2.d0*GAM1*DELX/2)*(IF1+II1)*

WRITE(7,26) TT, ERR1, ERR2, ERR3, ERR4, ERR5

C   *Energy crossing the boundary from TT to TT+dT*

IO1 = (VEL1*DELX/2)*(EOF1+EOI1)

IL1 = (VEL1*DELX/2)*(ELF1+ELI1)

IO2 = (VEL2*DELX/2)*(EOF2+EOI2)

IL2 = (VEL2*DELX/2)*(ELF2+ELI2)

IO3 = (VEL3*DELX/2)*(EOF3+EOI3)   380

IL3 = (VEL3*DELX/2)*(ELF3+ELI3)

IO4 = (VEL4*DELX/2)*(EOF4+EOI4)

IL4 = (VEL4*DELX/2)*(ELF4+ELI4)

IO5 = (VEL5*DELX/2)*(EOF5+EOI5)

IL5 = (VEL5*DELX/2)*(ELF5+ELI5)

IO6 = (VEL6*DELX/2)*(EOF6+EOI6)

IL6 = (VEL6*DELX/2)*(ELF6+ELI6)

IO7 = (VEL7*DELX/2)*(EOF7+EOI7)

IL7 = (VEL7*DELX/2)*(ELF7+ELI7)

390

C *Increase time mark and go to DIVPRK again*

TT = TEND

TEND = TEND + DELX

38 **CONTINUE**

C *Register the field amplitudes, at final time, in an output file:*

WRITE(*,*) TT   400

WRITE(4,225) TT,V1(1),V2(1),V1(Nx+1),V2(Nx+1)

```fortran
      WRITE(5,20) V3(1),V3(Nx+1)


      OPEN (2, FILE='aiajak1')
      OPEN (3, FILE='aiajak2')
      DO J=1,NX+1
         WRITE(2,26) x(J), V1(J), V2(J), V3(J), V4(J), V5(J)
         WRITE(3,23) x(J), V6(J), V7(J)
      ENDDO                                                           410
      CLOSE(2)
      CLOSE(3)


C     Write variables for the plotting routine
      WRITE(8,251) VEL4, VEL5, COUNT, RLNGTH, DELX, AMP1, STEP


C     Formatting rules


251   FORMAT(F8.5,1X,F8.5,1X,I4,1X,F12.5,1X,F12.5,1X,F8.5,1X,F8.5)
20    FORMAT(F12.6,1X,F12.6)                                          420
22    FORMAT(1PG15.7E2,1X,1PG15.7E2)
23    FORMAT(F8.3,1X,F12.6,1X,F12.6)
24    FORMAT(1PG15.7E2,1X,1PG15.7E2,1X,1PG15.7E2,1X,1PG15.7E2)
25    FORMAT(F12.6,1X,F12.6,1X,F12.6,1X,F12.6,1X,F12.6)
26    FORMAT(F8.3,1X,F12.6,1X,F12.6,1X,F12.6,1X,F12.6,1X,F12.6)
225   FORMAT(F12.6,1X,F12.6,1X,F12.6,1X,F12.6,1X,F12.6)


      CLOSE(1)
      !CLOSE(2)
      !CLOSE(3)                                                       430
      CLOSE(4)
      CLOSE(5)
      CLOSE(6)
      CLOSE(8)
      CLOSE(9)
      !CLOSE(10)


      STOP
      END
                                                                      440
C     ++++++++++++++++++++++++++++++++++++++++++++++
C
C     FCN subroutine
C
C     Time derivatives of the field amplitudes, along the characteristic frames
C     Called from DIVPRK, (IMSL - ODE's solver).
C
```

```fortran
      SUBROUTINE FCN (NN, TT, V, VPRIME)
                                                                          450
      IMPLICIT NONE

C     Definition of variables

      INTEGER*4 I, II   ! Flags
      INTEGER*4 NN    ! No. of simultaneous eqs.
      INTEGER*4 NX    ! No. of gridpoints
      REAL*8 V(200000), VPRIME(200000) ! Unknown vectors, dV/dt
      REAL*8 V1(20010), V2(20010), V3(20010) ! Field amplitudes
      REAL*8 V4(20010), V5(20010)                                        460
      REAL*8 V6(20010), V7(20010)


      REAL*8 RLNGTH  ! Simulation box length [Norm. space units]
      REAL*8 DELX      ! Gridspacing [Norm. space units]
      REAL*8 TT         ! Time [Norm. time units]
      REAL*8 GAM1, GAM2, GAM3, GAM4, GAM5 ! Damping rates
      REAL*8 GAM6, GAM7
      REAL*8 VEL1, VEL2, VEL3,VEL4, VEL5 ! Group velocities
      REAL*8 VEL6, VEL7
      REAL*8 KSRS, KLDI, Kcasc                                           470
      REAL*8 AMP1, AMP2, AMP3, AMP4, AMP5, AMP6, AMP7 ! BC.

C     Shared variables

      COMMON /VARS1/ NX
      COMMON /VARS2/ RLNGTH, DELX, GAM1, GAM2, GAM3, GAM4, GAM5
      COMMON /MORE/  KSRS, KLDI, VEL1, VEL2, VEL3, VEL4, VEL5
      COMMON /MORE1/ Kcasc, VEL6, VEL7, GAM6, GAM7, AMP6, AMP7
      COMMON /AMPV/  AMP1, AMP2, AMP3, AMP4, AMP5
                                                                          480
C     Conform vectors with field amplitudes.

      DO I=1,NX+1
         II = 7 * (I−1)
         V1(I) = V(II+1)
         V2(I) = V(II+2)
         V3(I) = V(II+3)
         V4(I) = V(II+4)
         V5(I) = V(II+5)
         V6(I) = V(II+6)                                                  490
         V7(I) = V(II+7)
      ENDDO
```

182

```
C       Time derivatives (along characteristic frames)

        DO I=1,NX+1

          II = 7 * (I−1)

          VPRIME(II+1) =  − KSRS*V2(I)*V3(I) + GAM1*V1(I)                          500
          VPRIME(II+2) =  + KSRS*V1(I)*V3(I) + GAM2*V2(I)
          VPRIME(II+3) =  + KSRS*V1(I)*V2(I) + GAM3*V3(I) − KLDI*V4(I)*V5(I)
          VPRIME(II+4) =  + KLDI*V3(I)*V5(I) + GAM4*V4(I) − Kcasc*V6(I)*V7(I)
          VPRIME(II+5) =  + KLDI*V3(I)*V4(I) + GAM5*V5(I)
          VPRIME(II+6) =  + Kcasc*V4(I)*V7(I) + GAM6*V6(I)
          VPRIME(II+7) =  + Kcasc*V4(I)*V6(I) + GAM7*V7(I)


C         SRS:
C         VPRIME(II+1) =  -  KSRS*V2(I)*V3(I) + GAM1*V1(I)
C         VPRIME(II+2) =  +  KSRS*V1(I)*V3(I) + GAM2*V2(I)                          510
C         VPRIME(II+3) =  +  KSRS*V1(I)*V2(I) + GAM3*V3(I)


C         LDI:
C         VPRIME(II+3) =  -  KLDI*V4(I)*V5(I) + GAM3*V3(I)
C         VPRIME(II+4) =  +  KLDI*V3(I)*V5(I) + GAM4*V4(I)
C         VPRIME(II+5) =  +  KLDI*V3(I)*V4(I) + GAM5*V5(I)


C         VPRIME(II+1) =  0.d0
C         VPRIME(II+2) =  0.d0
C         VPRIME(II+3) =  0.d0                                                      520
C         VPRIME(II+4) =  0.d0
C         VPRIME(II+5) =  0.d0
C         VPRIME(II+6) =  0.d0
C         VPRIME(II+7) =  0.d0

        ENDDO

        RETURN
        END
                                                                                   530


C       ++++++++++++++++++++++++++++++++++++++++++++
C
C       shifter subroutine
C
C       Shifting of functions is done here.
C       A linear fit to the Boundary Condition is fed in the shifting side.
```

C

```fortran
      SUBROUTINE SHIFTER (NX, YY, XX, VEL, TT, YYS, INI)              540

      IMPLICIT NONE
      INTEGER*4 I, J, K
      INTEGER*4 NX    ! No. of gridpoints
      INTEGER*4 SHFTPTS ! No. of shifted gridpoints
      REAL*8 VEL, INI  ! Wave velocity and Boundary value
      REAL*8 TT        ! TIME COUNTER
      REAL*8 XX(20010) ! Argument of YY
      REAL*8 YY(20010) ! Variables to be shifted
      REAL*8 YYS(20010) ! SHIFTED YY                                  550


      SHFTPTS = NINT(DABS(VEL))

      IF (VEL.GT.0.d0) THEN

        DO I=1,NX-SHFTPTS
          YYS(I+SHFTPTS) = YY(I)
        ENDDO
        DO I=1,SHFTPTS
          YYS(I) = INI - (INI-YY(1))/(SHFTPTS)*(I-1)                  560
          !YYS(I) = INI
        ENDDO
      ELSE

        DO I=1,NX-SHFTPTS
          YYS(I) = YY(I+SHFTPTS)
        ENDDO
        DO I=1,SHFTPTS
          YYS(NX-SHFTPTS+I) = YY(NX) + (INI-YY(NX))/(SHFTPTS)*I
          !YYS(NX-SHFTPTS+I) = YY(NX)                                 570
        ENDDO

      ENDIF

      RETURN
      END
```

184

C.5   Source Code (Lax-Wendroff Technique)

Source code:

```
C
C        This program solves the 5COM equations,
C        based on the Lax-Wendroff scheme.
C
C        A finite length plasma is considered, and on BC for each wave.
C
C        LaxWen.f (from: energy.f)
C

         IMPLICIT NONE                                              10


C        DEFINITION OF VARIABLES

         INTEGER*4 I, II, J, K, K1, K2, L ! Flags
         INTEGER*4 COUNT
         INTEGER*4 SHFPTS, DUM
         INTEGER*4 NX, N
         INTEGER*4 NXD, MID
         INTEGER*4 CW1, CW2 ! Indices to first and second
                            ! coupled waves                         20
C        INTEGER*4 CNT(20)

         REAL*8 RLNGTH, DELX
         REAL*8 DELT
         REAL*8 TT          ! Time [seconds]

         REAL*8 V(20,50010) ! FIELD AMPLITUDES
         REAL*8 X(50010)

         REAL*8 AMP(20), NOISE ! Initial Amplitude             30
         REAL*8 C(20)
         REAL*8 GAM(20)
         REAL*8 VEL(20)
         REAL*8 KKK         ! Ksrs/Kldi
         REAL*8 KCASC       ! Kcasc/KldI
         REAL*8 DUMM1, DUMM2, DUMM3, DUMM4 ! Dummy variables

         REAL*8 TOUT, HH ! Plotting parameters
         REAL*8 TSTART
                                                                    40
         REAL*8 TEND, STEP
         REAL*8 TOL
```

185

```fortran
      EXTERNAL STP

      COMMON /VARS1/ NX
      COMMON /VARS2/ RLNGTH, DELX, DELT
      COMMON /MORE/  VEL, GAM, AMP
      COMMON /MORE1/ KKK, Kcasc
```

```fortran
C     OPEN INPUT/OUTPUT FILES

      OPEN (1, FILE='fields2')
      !OPEN (2, FILE='datos')
      !OPEN (3, FILE='aiajak')
      !OPEN (4, FILE='SRSref')
      OPEN (5, FILE='fields1')
      OPEN (6, FILE='power')
      OPEN (8, FILE='plot_param')
      OPEN (9, FILE='tdatc_u', STATUS='OLD')
      !OPEN (10, FILE='tplot', FORM='UNFORMATTED')
```

```fortran
C     READ INITIAL DATA

      READ (9,*) AMP(1), AMP(2), AMP(3), NOISE
      READ (9,*) AMP(4), AMP(5), RLNGTH, NX
      READ (9,*) STEP, N, TOL, DUMM1
      READ (9,*) TSTART, DUMM1
      READ (9,*) GAM(1), DUMM1, GAM(4), GAM(5)
      READ (9,*) GAM(2), DUMM1, GAM(3), DUMM3
      READ (9,*) DUMM1, VEL(1), VEL(2), VEL(3)
      READ (9,*) DUMM1
      READ (9,*) MXSTEP
      READ (9,*) VEL(4), VEL(5)
      READ (9,*) KKKM̂
      READ (9,*) Kcasc, VEL(6), VEL(7)M̂
      READ (9,*) GAM(6), GAM(7), AMP(6), AMP(7)
```

```fortran
C     INITIAL CONDITION:

      NXD = INT(NX/2.)
      DELX = RLNGTH/NXD/2.
      MID = NXD+1
```

```fortran
      DO I=1,NX+1
        X(I) = (I−MID)∗DELX
```

```fortran
        V(1,I) = NOISE
        V(2,I) = NOISE
        V(3,I) = NOISE
        V(4,I) = NOISE
        V(5,I) = NOISE
        V(6,I) = NOISE
        V(7,I) = NOISE

      ENDDO
```

```fortran
      V(1,1) = AMP(1)
      V(2,NX+1) = AMP(2)
      V(3,1) = AMP(3)
      V(4,NX+1) = AMP(4)
      V(5,1) = AMP(5)

C     !WRITE INITIAL CONDITION
C     DO I=1,NX+1
C     WRITE(2,26) x(I), V1(I), V2(I), V3(I), V4(I), V5(I)
C     ENDDO
```

```fortran
C     INICIALIZATION OF other VARIABLES

      COUNT = 0         ! Count for plotting rout.
      TT = 0.0          ! Time counter (time units)
      DELX=RLNGTH/NX ! One step length (space u)

      DELT = DELX/VEL(1) !Assume V1 is the fastest wave
      TEND = DELT^M
```

```fortran
      TOUT = TT         ! For plotting criteria
      HH = DELX/2       ! For plotting criteria

C     MAIN SOLVING ROUTINE

      DO 38 I=1,N

C     Integrate the fields in the box and werite to an output file
```

```fortran
C      (only for selected moments in time)
C     Note: Initial data is written to file.
```

```fortran
      IF (TT.GE.TSTART) THEN

        IF (TT.GE.(TOUT-HH)) THEN

          write(*,*) I, '/', N

          COUNT = COUNT+1
```
                                                                          140
```fortran
          !COMPUTE AVERAGE ENERGY in pump and daughter waves
          DO L = 1,7
            C(L) = 0.d0
          ENDDO

          !SHFPTS = NINT(DABS(VEL1))
          SHFPTS = 1
          DUM = INT(NX/SHFPTS)
```

```fortran
          !Integration with TRAPEZOIDAL RULE                             150
          DO K = 0,DUM
            K1 = K*SHFPTS
            K2 = (K+1)*SHFPTS
            DUMM1 = DELX*SHFPTS
            DO L = 1,7
              C(L)=C(L)+(DUMM1/2.d0)*(V(L,K1+1)**2 + V(L,K2+1)**2)
            ENDDO
          ENDDO
```

```fortran
          ! Write fields in the box                                      160
          OPEN (3, FILE='aiajak')
          DO J=1,NX+1
            WRITE(3,26) x(J),V(1,J),V(2,J),V(3,J),V(4,J),V(5,J)
          ENDDO
          CLOSE(3)

          WRITE(6,26) TT, C(1), C(2), C(3), C(4), C(5)
          WRITE(5,225) TT,V(1,1),V(2,1),V(1,Nx+1),V(2,Nx+1)
          WRITE(1,20) V(3,1),V(3,Nx+1)
          TOUT = TOUT+STEP                                               170

        ENDIF
      ENDIF


C     CALL DIVPRK (IDO, NN, FCN, TT, TEND, TOL, PARAM, V)
C     intead: Now we call STP
```

```
            CALL STP (TT, V)


                                                                          180
C       Increase time mark and go to DIVPRK again
        TT = TEND
        TEND = TEND + DELT


 38     CONTINUE


        WRITE(5,225) TT,V(1,1),V(2,1),V(1,Nx+1),V(2,Nx+1)
        WRITE(1,20) V(3,1),V(3,Nx+1)


                                                                          190

C       WRITE FIELD AMPLITUED in SPACE at final time...
C       WRITE(*,*) TT
C       DO J=1,NX
C        WRITE(3,26) x(J), V1(J), V2(J), V3(J), V4(J), V5(J)
C       ENDDO


C       Write parameters for the plotting routine
        WRITE(8,251) VEL(4), VEL(5), COUNT, RLNGTH, DELX, AMP(1), STEP


                                                                          200

251     FORMAT(F8.5,1X,F8.5,1X,I4,1X,F12.5,1X,F12.5,1X,F8.5,1X,F8.5)
 20     FORMAT(F12.6,1X,F12.6)
 22     FORMAT(1PG15.7E2,1X,1PG15.7E2)
 23     FORMAT(F8.3,1X,F12.6,1X,F12.6)
 24     FORMAT(1PG15.7E2,1X,1PG15.7E2,1X,1PG15.7E2,1X,1PG15.7E2)
 25     FORMAT(F8.3,1X,F12.6,1X,F12.6,1X,F12.6,1X,F12.6)
 26     FORMAT(F12.6,1X,F12.6,1X,F12.6,1X,F12.6,1X,F12.6,1X,F12.6)
225     FORMAT(F12.6,1X,F12.6,1X,F12.6,1X,F12.6,1X,F12.6)


        CLOSE(1)                                                          210
C       !CLOSE(2)
C       !CLOSE(3)
C       !CLOSE(4)
        CLOSE(5)
        CLOSE(6)
        CLOSE(8)
        CLOSE(9)
        !CLOSE(10)


        STOP                                                              220
        END
```

```
C      +++++++++++++++++++++++++++++++++++++++++++++++++++++++++
C
C      Function STP
C        Defines the set of differential equations to be solved
C        The subroutine is called by DIVPRK, (ODE's solver).
C

       SUBROUTINE STP (TT, V)                                          230

       IMPLICIT NONE

C      DEFINITION OF VARIABLES
       INTEGER*4 I, II, J ! Flags
       INTEGER*4 NX    ! No. of gridpoints
       REAL*8 V(20,50010)
       REAL*8 DM(20,50010) ! FUNCTIONS TO BE INT.
       REAL*8 DV(20,50010), DDV(20,50010)
                                                                       240
       REAL*8 TT        ! Time (independent var.)
       REAL*8 GAM(20)   ! Damping for each wave
       REAL*8 RLNGTH    ! Window length, VELOCITY
       REAL*8 DELX, DELT ! Length of one space step [m]
       REAL*8 VEL(20)   ! Vel. in [m/sec]

       REAL*8 KKK, Kcasc, KLDI
       REAL*8 AMP(20)

C      External routines to evaluate the forward and backward derivatives  250
C      The only difference between Fwd. and Bkwd. is at the boundaries.
       EXTERNAL FDFF, FDDFF ! Forward 1st and 2nd derivative in x
       EXTERNAL BDFF, BDDFF ! Backward 1st and 2nd derivative in x

       COMMON /VARS1/ NX
       COMMON /VARS2/ RLNGTH, DELX, DELT
       COMMON /MORE/  VEL, GAM, AMP
       COMMON /MORE1/ KKK, Kcasc

       DELX = RLNGTH/NX                                                260
       KLDI = 1.D0

       CALL FDFF (1, VEL(1), GAM(1), V, DV(1,:), −KKK, 2, 3, 0.d0, 4, 5)
       CALL BDFF (2, VEL(2), GAM(2), V, DV(2,:), KKK, 1, 3, 0.d0, 4, 5)
       CALL FDFF (3, VEL(3), GAM(3), V, DV(3,:), KKK, 1, 2, −KLDI, 4, 5)
       CALL BDFF (4, VEL(4), GAM(4), V, DV(4,:), 0.d0, 1, 2, KLDI, 3, 5)
       CALL FDFF (5, VEL(5), GAM(5), V, DV(5,:), 0.d0, 1, 2, KLDI, 3, 4)
```

190

CALL FDDFF(1,VEL(1),GAM(1),V,DV,DDV(1,:), −KKK, 2, 3, 0.d0, 4, 5)

CALL BDDFF(2,VEL(2),GAM(2),V,DV,DDV(2,:), KKK, 1, 3, 0.d0, 4, 5)   270

CALL FDDFF(3,VEL(3),GAM(3),V,DV,DDV(3,:), KKK, 1, 2, −KLDI, 4, 5)

CALL BDDFF(4,VEL(4),GAM(4),V,DV,DDV(4,:), 0.d0, 1, 2, KLDI, 3, 5)

CALL FDDFF(5,VEL(5),GAM(5),V,DV,DDV(5,:), 0.d0, 1, 2, KLDI, 3, 4)

DO I=1,NX+1

   !5 Coupled Mode Equations
   DM(1,I) = V(1,I) + DELT*DV(1,I) + (DELT)**2*DDV(1,I)/2.d0
   DM(2,I) = V(2,I) + DELT*DV(2,I) + (DELT)**2*DDV(2,I)/2.d0   280
   DM(3,I) = V(3,I) + DELT*DV(3,I) + (DELT)**2*DDV(3,I)/2.d0
   DM(4,I) = V(4,I) + DELT*DV(4,I) + (DELT)**2*DDV(4,I)/2.d0
   DM(5,I) = V(5,I) + DELT*DV(5,I) + (DELT)**2*DDV(5,I)/2.d0

ENDDO

C   *DM(1,1) = AMP(1)*

C   *DM(2,NX+1) = AMP(2)*

V(1,:) = DM(1,:)   290
V(2,:) = DM(2,:)
V(3,:) = DM(3,:)
V(4,:) = DM(4,:)
V(5,:) = DM(5,:)

RETURN
END

C   *++* 30
C
C   *FORWARD First TIME Derivative*
C

SUBROUTINE FDFF (M,VEL,GAM,V,DV,K1,CW1,CW2,K2,CW3,CW4)

IMPLICIT NONE

C   *DEFINITION OF VARIABLES*
INTEGER∗4 I   ! Flags   310
INTEGER∗4 NX   ! No. of gridpoints
INTEGER∗4 M, CW1, CW2, CW3, CW4 ! Indices to main & cpled wvs.

191

```fortran
      REAL*8 V(20,50010)
      REAL*8 DV(50010)

      REAL*8 GAM        ! Damping for each wave
      REAL*8 RLNGTH  ! Window length, VELOCITY
      REAL*8 DELX, DELT ! Length of one space step [m]
      REAL*8 VEL                                                        320
      REAL*8 K1, K2

      COMMON /VARS1/ NX
      COMMON /VARS2/ RLNGTH, DELX, DELT

      DO I=2,NXM̂
         DV(I) = -VEL*(V(M,I+1)-V(M,I-1))/2.d0/DELX - GAM*V(M,I)
     &           + K1*V(CW1,I)*V(CW2,I)
     &           + K2*V(CW3,I)*V(CW4,I)
      ENDDO                                                             330

      DV(1) = 0.d0
      DV(NX+1) = -VEL*(3*V(M,NX+1)-4*V(M,NX)+V(M,NX-1))/2.d0/DELX
     &         - GAM*V(M,NX+1)
     &         + K1*V(CW1,NX+1)*V(CW2,NX+1)
     &         + K2*V(CW3,NX+1)*V(CW4,NX+1)

      RETURN
      END
                                                                        340


C     ++++++++++++++++++++++++++++++++++++++++++++++++++++++++++++++++++
C
C     BACKWARD First TIME Derivative
C

      SUBROUTINE BDFF (M,VEL,GAM,V,DV,K1,CW1,CW2,K2,CW3,CW4)

      IMPLICIT NONE
                                                                        350
C     DEFINITION OF VARIABLES
      INTEGER*4 I        ! Flags
      INTEGER*4 NX    ! No. of gridpoints
      INTEGER*4 M, CW1, CW2, CW3, CW4 ! Indices to main & cpled wvs.

      REAL*8 V(20,50010)
      REAL*8 DV(50010)
```

192

```fortran
      REAL*8 GAM        ! Damping for each wave
      REAL*8 RLNGTH ! Window length, VELOCITY                       360
      REAL*8 DELX, DELT ! Length of one space step [m]
      REAL*8 VEL
      REAL*8 K1, K2

      COMMON /VARS1/ NX
      COMMON /VARS2/ RLNGTH, DELX, DELT

      DO I=2,NX
         DV(I) = -VEL*(V(M,I+1)-V(M,I-1))/2.d0/DELX - GAM*V(M,I)
     &           + K1*V(CW1,I)*V(CW2,I)                             370
     &           + K2*V(CW3,I)*V(CW4,I)
      ENDDO

      DV(NX+1) = 0.d0
      DV(1) = -VEL*(-V(M,3)+4*V(M,2)-3*V(M,1))/2.d0/DELX
     &        - GAM*V(M,1)
     &        + K1*V(CW1,1)*V(CW2,1)
     &        + K2*V(CW3,1)*V(CW4,1)

      RETURN                                                        380
      END




C     +++++++++++++++++++++++++++++++++++++++++++++++++++++++++++++++++
C
C     FORWARD Second TIME Derivative
C

      SUBROUTINE FDDFF (M,VEL,GAM,V,DV,DDV,K1,CW1,CW2,K2,CW3,CW4)    390

      IMPLICIT NONE

C     DEFINITION OF VARIABLES
      INTEGER*4 I        ! Flags
      INTEGER*4 NX     ! No. of gridpoints
      INTEGER*4 M, CW1, CW2, CW3, CW4 ! Indices to main & cpled wvs.

      REAL*8 V(20,50010), DV(20,50010)
      REAL*8 DDV(50010)                                             400

      REAL*8 GAM        ! Damping for each wave
```

```fortran
      REAL*8 RLNGTH  ! Window length, VELOCITY
      REAL*8 DELX, DELT ! Length of one space step [m]
      REAL*8 VEL
      REAL*8 SGN1
      REAL*8 K1, K2


      COMMON /VARS1/ NX
      COMMON /VARS2/ RLNGTH, DELX, DELT                               410


      DO I=2,NX
        DDV(I) = VEL*VEL*( V(M,I+1)−2.d0*V(M,I)+V(M,I−1) )/DELX/DELX
        + 2.d0*VEL*GAM*(V(M,I+1)−V(M,I−1))/2.d0/DELX
     &        + GAM*GAM*V(M,I)
     &        + K1*( V(CW1,I)*DV(CW2,I)+V(CW2,I)*DV(CW1,I) )
     &        − VEL*K1*V(CW1,I)*(V(CW2,I+1)−V(CW2,I−1))/2.d0/DELX
     &        − VEL*K1*V(CW2,I)*(V(CW1,I+1)−V(CW1,I−1))/2.d0/DELX
     &        − GAM*K1*V(CW1,I)*V(CW2,I)
     &        + K2*( V(CW3,I)*DV(CW4,I)+V(CW4,I)*DV(CW3,I) )           420
     &        − VEL*K2*V(CW3,I)*(V(CW4,I+1)−V(CW4,I−1))/2.d0/DELX
     &        − VEL*K2*V(CW4,I)*(V(CW3,I+1)−V(CW3,I−1))/2.d0/DELX
     &        − GAM*K2*V(CW3,I)*V(CW4,I)
      ENDDO


      DDV(1) = 0.d0
      DDV(NX+1) = VEL*VEL*(
     &   35*V(M,NX+1)−104*V(M,NX)+114*V(M,NX−1)−56*V(M,NX−2)+11*V(M,NX−3)
     &   )/12/DELX/DELX
     &   + 2.d0*VEL*GAM*(3*V(M,NX+1)−4*V(M,NX)+V(M,NX−1))/2.d0/DELX     430
     &   + GAM*GAM*V(M,NX+1)
     &   + K1*( V(CW1,NX+1)*DV(CW2,NX+1)+V(CW2,NX+1)*DV(CW1,NX+1) )
     &   − VEL*K1*V(CW1,NX+1)*(3*V(CW2,NX+1)−4*V(CW2,NX)+V(CW2,NX−1))
     &   /2.d0/DELX
     &   − VEL*K1*V(CW2,NX+1)*(3*V(CW1,NX+1)−4*V(CW1,NX)+V(CW1,NX−1))
     &   /2.d0/DELX
     &   − GAM*K1*V(CW1,NX+1)*V(CW2,NX+1)
     &   + K2*( V(CW4,NX+1)*DV(CW4,NX+1)+V(CW4,NX+1)*DV(CW3,NX+1) )
     &   − VEL*K2*V(CW3,NX+1)*(3*V(CW4,NX+1)−4*V(CW4,NX)+V(CW4,NX−1))
     &   /2.d0/DELX                                                    440
     &   − VEL*K2*V(CW4,NX+1)*(3*V(CW3,NX+1)−4*V(CW3,NX)+V(CW3,NX−1))
     &   /2.d0/DELX
     &   − GAM*K2*V(CW3,NX+1)*V(CW4,NX+1)


      RETURN
      END
```

```
C      ++++++++++++++++++++++++++++++++++++++++++++++++++++++++++++++
C                                                                    450
C      BACKWARD Second TIME Derivative
C

       SUBROUTINE BDDFF (M,VEL,GAM,V,DV,DDV, K1, CW1, CW2, K2, CW3, CW4)


       IMPLICIT NONE


C       DEFINITION OF VARIABLES
       INTEGER*4 I      ! Flags
       INTEGER*4 NX    ! No. of gridpoints                           460
       INTEGER*4 M, CW1, CW2, CW3, CW4 ! Indices to main & cpled wvs.


       REAL*8 V(20,50010), DV(20,50010)
       REAL*8 DDV(50010)


       REAL*8 GAM       ! Damping for each wave
       REAL*8 RLNGTH  ! Window length, VELOCITY
       REAL*8 DELX, DELT ! Length of one space step [m]
       REAL*8 VEL
       REAL*8 K1, K2                                                 470


       COMMON /VARS1/ NX
       COMMON /VARS2/ RLNGTH, DELX, DELT



       DO I=2,NX
          DDV(I) = VEL*VEL*( V(M,I+1)−2.d0*V(M,I)+V(M,I−1) )/DELX/DELX
     &         + 2.d0*VEL*GAM*(V(M,I+1)−V(M,I−1))/2.d0/DELX
     &         + GAM*GAM*V(M,I)
     &         + K1*( V(CW1,I)*DV(CW2,I)+V(CW2,I)*DV(CW1,I) )          480
     &         − VEL*K1*V(CW1,I)*(V(CW2,I+1)−V(CW2,I−1))/2.d0/DELX
     &         − VEL*K1*V(CW2,I)*(V(CW1,I+1)−V(CW1,I−1))/2.d0/DELX
     &         − GAM*K1*V(CW1,I)*V(CW2,I)
     &         + K2*( V(CW3,I)*DV(CW4,I)+V(CW4,I)*DV(CW3,I) )
     &         − VEL*K2*V(CW3,I)*(V(CW4,I+1)−V(CW4,I−1))/2.d0/DELX
     &         − VEL*K2*V(CW4,I)*(V(CW3,I+1)−V(CW3,I−1))/2.d0/DELX
     &         − GAM*K2*V(CW3,I)*V(CW4,I)


       ENDDO                                                         490


       DDV(NX+1) = 0.d0
```

```
      DDV(1) = VEL*VEL*(
     &      11*V(M,5)−56*V(M,4)+114*V(M,3)−104*V(M,2)+35*V(M,1)
     &      )/12/DELX/DELX
     &      + 2.d0*VEL*GAM*(−V(M,3)+4*V(M,2)−3*V(M,1))/2.d0/DELX
     &      + GAM*GAM*V(M,1)
     &      + K1*( V(CW1,1)*DV(CW2,1)+V(CW2,1)*DV(CW1,1) )
     &      − VEL*K1*V(CW1,1)*(−V(CW2,3)+4*V(CW2,2)−3*V(CW2,1))/2.d0/DELX
     &      − VEL*K1*V(CW2,1)*(−V(CW1,3)+4*V(CW1,2)−3*V(CW1,1))/2.d0/DELX
     &      − GAM*K1*V(CW1,1)*V(CW2,1)
     &      + K2*( V(CW3,1)*DV(CW4,1)+V(CW4,1)*DV(CW3,1) )
     &      − VEL*K2*V(CW3,1)*(−V(CW4,3)+4*V(CW4,2)−3*V(CW4,1))/2.d0/DELX
     &      − VEL*K2*V(CW4,1)*(−V(CW3,3)+4*V(CW3,2)−3*V(CW3,1))/2.d0/DELX
     &  − GAM*K2*V(CW3,1)*V(CW4,1)


      RETURN
      END
```

196

Bibliography

[1] Nuckolls J. H., et al., *Nature* **239**, 139, 1972.

[2] Lindl J., *Physics Today*, September 1992.

[3] Lindl J., *Phys. Plasmas* **2** (11), 3933, November 1995.

[4] Fernández J. A., et al., *Phys. Rev. Lett.* **77**(13), 2702 (1996).

[5] Fernández J. A., et al., *Phys. Plasmas* **4**(5), 1849 (1997).

[6] Fernández J. A., et al., in *30th. Annual Anomalous Absorption Conf.*, Ocean City, MD, 2000.

[7] Fernández J. A., et al., in *Proc. 1st IFSA*, Bordeaux, France (1999), pp. 318-323.

[8] Labuane C., et al., in *Proc. 1st IFSA*, Bordeaux, France (1999), pp. 289–297.

[9] Young P. E., et al., in *Proc. 1st IFSA*, Bordeaux, France (1999), pp. 307–312.

[10] Focia R. J., MIT-Plasma Fusion Center, PSFC/JA-01-17. Submitted to *Phys. Rev. Lett.*.

[11] Cobble J. A., et al., *Phys. Plasmas* **7**(1), 323 (2000).

[12] Montgomery D. S., et al., in *30th. Annual Anomalous Absorption Conf.*, Ocean City, MD, 2000.

[13] Montgomery D. S., et al., *Laser & Particle Beams* **17**(3), 349 (1998).

[14] Labaune C., et al., *Phys. Plasmas* **5**(1), 1849 (1998).

[15] Kirkwood R. K., *Phys. Rev. Lett.* **77**(13), 2706 (1996).

[16] Baker K. L., et al., *Phys. Rev. Lett.* **77**(1), 67 (1996).

[17] Villanueve D. M., et al., *Phys. Rev. Lett.* **71**(3), 368 (1993).

[18] Drake R. P., et al., *Phys. Fluids* **31**, 3130 (1988); and *Phys. Fluids* **B1**, 1082 (1989).

[19] Drake R. P., et al., *Phys. Rev. Lett.* **60**, 1018 (1988).

[20] Villanueve D. M., et al., *Phys. Rev. Lett.* **59**(14), 1585 (1987).

[21] Phillion D. W., et al., *Phys. Rev. Lett.* **49**(19), 1405 (1982).

[22] Watt R. G., et al., *Phys. Rev. Lett.* **41**(3), 170 (1978).

[23] Karttunen S. J., *Plasma Phys* **22**, 151-162 (1980)

[24] Karttunen S. J., *Phys Rev A* **23**, 2006 (1981)

[25] Heikkinen J. A. and Karttunen S. J., *Phys. Fluids* **29**, 1291 (1986).

[26] Chow C. C., Ph.D. Thesis, M.I.T. (1992); and C. C. Chow, *Physica D* **81**, 237-270, (1995).

[27] Chow C. C., Bers A., Ram A. K., *Phys. Rev. Lett.* **68**, 3379 (1992); and *Plasma Phys. and Contr. Fusion* **34**, 1945 (1992).

[28] Chow C. C., Bers A., Ram A. K., in *Physics of Space Plasmas (1991)*, SPI Conference Proceedings and Reprint Series, No. 11, Scientific Publishers Inc., pp. 179-195.

[29] Ram A. K., Chow C.C., Bers A., *Saturation of SRS by Spatio Temporal Chaos in Coupled Langmuir Decay*, MIT-Plasma Fusion Center, PFC/JA-94-8-REV.

[30] Salcedo A., Bers A., and Ram A. K., in *Proc. 1st IFSA*, Bordeaux, France (1999).

[31] Salcedo A., et al., in *42nd Annual Meeting of the DPP-APS*, Bulletin of the American Physical Society, DPP/ICPP, **Vol. 45, No. 7**, abstract: WP1-43, pp. 357, Quebec City, Canada, 2000.

[32] Ghizzo A. and Bertrand P., *J. Comput. Physics*, Vol.90, No. 2 (1990).

[33] Reveille T., et al., *Phys. Fluids B* **4**(8), 2665-2668 (1992).

[34] Estabrook K., Kruer W. L. and Lasinsky B. F., *Phys. Rev. Lett.* **45**(17), 1399-1403, October 1980.

[35] Joshi C., Tajma T. and Dawson J. M., *Phys. Rev. Lett.* **47**(18), 1285-1288, November 1981.

[36] Vu H. X., et al., *J. Comput. Physics* **156**, 12-42 (1999).

[37] Bonnaud G., Pesme D., and Pellat R., *Phys. Fluids* **B2**, 1618 (1990).

[38] Rose H. A., et al., *Phys. Rev. Lett.* **58**, 2547 (1987).

[39] Rozmus W., et al., *Phys. Fluids* **30**(7), 2181 (1987).

[40] Bonnaud G., Pesme D., and Pellat R., *Phys. Fluids* B**2**(7), 1618 (1990).

[41] Drake R. P., et al., *Phys. Fluids* B**3**(11), 2936 (1991).

[42] Kolber T., Rozmus W., and Tikhonchuk V.T., *Phys. Fluids* **B5**, 138 (1993).

[43] Rozmus W., *Physica Scripta* **T30**, 64-68 (1990).

[44] Bezzerides B., DuBois D. F., and Rose H. A., *Phys. Rev. Lett.* **70**, 2569 (1993).

[45] Russell D. A., et al., *Phys. Plasmas* **6**(4), 1294 (1999).

[46] Chen F. F., *"Introduction to Plasma Physics & Controlled Fusion"*, Volume 1: Plasma Physics, 2nd ed., Plenum Press, NY, 1990.

[47] Kruer W. L., *"The Physics of Laser Plasma Interactions"*, Addison-Wesley, 1988.

[48] Bers A., in *Class Notes for Introduction to Plasma Physics - II*, M.I.T., CH.10, 1999.

[49] Bers A., in *Plasma Physics - Les Housches 1972*, edited by C. De Witt and J. Peyraud (Gordon and Breach, New York), 1975.

[50] Bers A., in *Handbook of Plasma Physics*, edited by M. N. Rosenbluth and R. Z. Sagdeev (North Holland, Amsterdam), Vol. 1, Chap. 3.2., 1983.

[51] Chambers F. W., Ph.D. Thesis, M.I.T. (1975).

[52] Watson D. C., Ph.D. Thesis, M.I.T. (1975).

[53] Kaup D. J., Reiman A., Bers A., *Rev. Mod. Phys.*, **51**, 915 (1979).

[54] Chambers D. C., Ph.D. Thesis, Chapter 6, M.I.T. (1975).

[55] Epperlin E. M., *Phys. Rev. Lett.* **65**, 2145, (1990).

[56] Rosenbluth M. N., *Phys. Rev. Lett.* **29** (9), 565–567, (1972).

[57] Liu C. S., Rosenbluth M. N. and White R. B., *The Physics of Fluids*, Vol 17, No. 6 (1974).

[58] Hohenberg and Shraiman, *Physica D* **37**, 109, (1989).

[59] Fried B. D. and Conte S. D., *"The Plasma Dispersion Function"*, Academic, NY, 1961.

[60] Fried B. D. and Gould R. W., *Phys. Fluids* **4** 1, 139 – 147 (1960).

[61] Williams E. A., et al., *Phys. Plasmas* **2**(1), 1294 (1995).

[62] Besnard D., Bonnaud G. & Schurtz G., in *La Fusion Thermonucléaire Inertielle Par Laser*, Partie 3, Volume II, Chaptitre XIII, pp. 1105 – 1115. Edited by Dautray R. & Watteau J. P., Eyrolles, Paris, 1993.

[63] Benney D. J. and Newell A. C., *J. Math. Phys.* **46**, 133 (1967).

[64] Haus H. A., *"Waves and Fields in Optoelectronics"*, Chapter 7, Prentice Hall, 1984.

[65] Gledhill I. M. and Hellberg M. A., *J. of Plasma Physics* **36**, part 1, 75-96 (1986).

[66] Berger R. L., Williams E. A. and Simon A., *Phys. Fluids* **B1**(2), 414-421 (February 1989).

[67] Oberman C. and Auer G., *Phys. Fluids* **17**(11), 1980-1982 (November 1974).

[68] Bekefi G., *"Radiation Processes in Plasmas"*, Jhon Wiley & Sons, London, 1975.

[69] Morales G. J. *The Physics of Fluids*, Vol 18, No. 9, pp. 1220 (September 1975).

[70] Morales G. J. and O'Neil T. M., *Phys. Rev. Lett.* **28** (7), 417–420, (February 1972).

[71] Lee A. and Pocobelli G., *The Physics of Fluids*, Vol 15, No. 12, pp. 2351-2355 (December 1972).

[72] Reiman A. and Bers A., in *Proceedings of the 7th Conference on Numerical Simulation of Plasmas*, pp. 188, Courant Institute, N.Y.U., June 1975.

[73] Ames W. F., *Numerical Methods for Partial Differential Equations*, 2nd Edition, Academic Press, NY, 1977.